



THE UNIVERSITY
of ADELAIDE

Environment Studies of Pulsar Wind Nebulae
and Their Interactions with the Interstellar Medium

Fabien Voisin
Faculty of Sciences
School of Physical Sciences
University of Adelaide

July 17, 2017

supervised by

A. Prof. Gavin ROWELL

Contents

Abstract	i
Declaration of Originality	ii
Acknowledgement	iii
1 Introduction	1
1.1 Structure of pulsar environments	1
1.1.1 The pulsar and its magnetosphere	2
1.1.2 The pulsar wind	3
1.1.3 The pulsar wind nebula	4
1.2 Dynamical aspects of the PWNe and their progenitor SNR	6
1.3 The PWN : Motivation and Challenges.	7
1.3.1 A laboratory for CRs and electrons study	7
1.3.2 Current challenge in our understanding of PWNe	7
1.3.3 Combining TeV gamma-ray astronomy with molecular gas study	9
2 Introduction to Gamma-ray astronomy	11
2.1 Cosmic-ray and Extensive air showers	11
2.1.1 How it all started	11
2.1.2 Extensive air showers	13
2.1.3 Means of cosmic-ray detections and CR observatories	17
2.1.4 The cosmic-ray flux	18
2.2 Gamma-ray astronomy	20
2.2.1 Space-Based telescopes	21
2.2.2 Ground based gamma-ray telescopes	22
2.2.3 VHE TeV sources	28

3	Tracing the interstellar medium	31
3.1	Basic radiation theory	31
3.1.1	Definitions	31
3.1.2	Black body radiation	34
3.2	Line emission	35
3.2.1	Einstein coefficients	36
3.2.2	Relation between Einstein coefficients under Local Thermal Equilibrium assumption	36
3.2.3	Critical Density	37
3.3	Tracing the ISM with Mopra and Nanten2	39
3.3.1	Acquiring the antenna temperature T_A^* and source temperature T_{src}	40
3.4	Physical parameters derived from the source temperature T_{src}	42
3.4.1	Column density	42
3.4.2	Optical depth	44
3.4.3	Temperature	44
3.4.4	Distance of the molecular cloud	45
3.4.5	Mass of the molecular cloud	45
3.4.6	Density	46
3.4.7	Turbulences in the molecular clouds	46
3.4.8	Useful transitions detectable by the Mopra and Nanten telescopes	47
3.5	HI 21cm radiation : tracer of atomic gas	51
3.6	Summary	52

4	On the evolution of cosmic-ray, high energy electron and gamma-ray energy distributions	53
4.1	Radiative losses	53
4.1.1	Impulsive Injector	54
4.1.2	Continuous injector	58
4.1.3	Numerical methods	60
4.1.4	Evolution of the gamma-ray emission	60
4.2	Particle Transport	62
4.2.1	Scattering of charged particles from perturbations of the magnetic fields	65
4.2.2	Diffusion equation	66
4.2.3	Diffusion coefficient	68
4.2.4	Propagation Effects on the energy distribution of CRs/electrons and gamma-rays	69
4.2.5	Propagation in molecular clouds	72
5	ISM Studies Towards TeV PWN HESSJ1825–137 and Northern Region (PAPER I)	75
6	Gamma-ray contribution of HESS J1825–137 towards HESS J1826–130	101
6.1	Progenitor SNR	102
6.1.1	Contribution from CRs	102
6.1.2	High energy electrons	105
6.2	Contribution from the PWN?	105
6.2.1	High energy electrons	106
6.2.2	Contribution from CRs?	106
6.3	Modelling particle diffusion from HESS J1825–137 and its progenitor SNR	107
6.3.1	Motivation	107
6.3.2	Solving the diffusion equation	107
6.3.3	Modelling scenarios and assumptions	109
6.3.4	Contribution from the progenitor SNR	112
6.3.5	Association with the PWN HESS J1825–137?	117
6.4	Summary, discussion what next?	123

7	ISM Studies Towards Seven PWNe and PWNe Candidates (PAPER II)	127
8	Summary and Future Works	167
8.1	Future work	168
8.1.1	Upgrading the numerical code	168
8.1.2	Towards a more detailed multi wavelength studies	169
8.1.3	Study of the SNRs in the Large Magellanic Cloud (LMC)	170
A	Diffusive shock acceleration	171
B	Probing Non-thermal emission	175
B.1	Synchrotron radiation	175
B.2	Inverse Compton	177
B.2.1	Bremsstrahlung	179
B.2.2	proton-proton interaction	179
B.3	SED modelling Code	180
B.4	Comparison of Results	181
C	Diffusion code	185
C.1	Numerical solution	185
C.1.1	Obtaining the time step Δt	187
C.1.2	Obtaining γ_0	187
C.1.3	Convergence to exact solution	189
C.1.4	Boundary condition	189
C.1.5	Obtaining the SED	189
C.1.6	test result	190
D	Additional gamma-ray modelled emission towards HESS 1826–130	193

Abstract

Pulsars, rapidly rotating neutron star born from the core-collapse of massive stars, convert a fraction of their rotational energy to accelerate electrons up to high energies. The generated pulsar wind eventually reaches the termination shock and creates a pulsar wind nebula (PWN). There, the particles' trajectories become randomized, and they produce radio to X-ray emission via synchrotron radiation; and TeV γ -ray emission from the interaction of high energy electrons with the Cosmic Microwave Background; and the infra-red emission from Galactic dust.

Although progress has been made towards the understanding of the structure of the pulsar environment, several issues, such as the composition of the pulsar winds, still need to be addressed. Indeed, no direct evidence of hadronic components have yet been discovered inside the PWN. However, nearby dense molecular clouds could provide sufficient target particles for the potential hadrons from the PWN and its progenitor supernova remnant (SNR) to produce significant TeV emission via proton-proton (p-p) interaction.

My work thus first consists of conducting interstellar matter (ISM) studies towards several PWNe using the 22-metre Mopra and the 4-metre Nanten radio telescopes. Among the studied PWNe, I particularly focus on HESS J1825–137 and its plausible association with the nearby unidentified TeV source HESS J1826–130. I have mapped the HESS J1826–130 region with Mopra in the 7 and 12 mm bands which, combined with the Nanten CO(1–0) survey and the GRS $^{13}\text{CO}(1-0)$, enable an accurate analysis of the morphological and physical properties of several dense molecular clouds found in the line of sight. Interestingly, I have found a massive molecular cloud adjacent to the PWN HESS J1825–137 and overlapping the HESS J1826–130 TeV emission. From our mass estimates, I suggest that the cosmic-rays originating from the progenitor SNR of the pulsar PSR J1826–1334 can significantly contribute to the TeV emission.

We then attempt to model and predict spectral and morphological properties of the TeV emission from the propagation of high energy CRs and electrons, originating from the progenitor SNR and potentially from the PWN. We find that the resulting spectral shape of the TeV γ -ray emission is very sensitive to the diffusion coefficient of high energy particles inside molecular clouds. I also find that only a ‘slow’ diffusion’ of CRs (diffusion coefficient $D(E) \sim 10^{26} \sqrt{E/10 \text{ GeV}} \text{ cm}^2 \text{ s}^{-1}$) results in a significant contribution of the gamma-ray emission towards HESS J1826–130 at all energies. We finally notice that the contribution from hypothetical CRs escaping the PWN HESS J1825–137 is expected to be overshadowed by the contribution of CRs escaping the progenitor SNR. As one expects the latter’s contribution to decrease as time evolves while the former’s contribution to remain somewhat constant, I thus argue that older PWNe may be more suitable candidates to obtain direct evidence of CRs inside PWNe. Among the studied PWNe, I find that, based on simplistic diffusion studies, the ISM surrounding HESS J1809–193 may be a good laboratory to detect CRs escaping the pulsar PSR J1809–1917.

Declaration of Originality

I certify that this work contains no material which has been accepted for the award of any other degree or diploma in my name, in any university or other tertiary institution and, to the best of my knowledge and belief, contains no material previously published or written by another person, except where due reference has been made in the text. In addition, I certify that no part of this work will, in the future, be used in a submission in my name, for any other degree or diploma in any university or other tertiary institution without the prior approval of the University of Adelaide and where applicable, any partner institution responsible for the joint-award of this degree.

I give consent to this copy of my thesis when deposited in the University Library, being made available for loan and photocopying, subject to the provisions of the Copyright Act 1968.

I acknowledge that copyright of published works contained within this thesis resides with the copyright holder(s) of those works.

I also give permission for the digital version of my thesis to be made available on the web, via the University's digital research repository, the Library Search and also through web search engines, unless permission has been granted by the University to restrict access for a period of time.

I acknowledge the support I have received for my research through the provision of an Australian Government Research Training Program Scholarship.

Fabien Voisin

Signature :

Date :

List of my published papers within this thesis

- Voisin, F., Rowell, G., Burton, M. G., Walsh, A., Fukui, Y., Aharonian, F., 2016, MNRAS, 458, 2813-2835.
- Voisin, F., Rowell, G., Burton, M. G., Fukui, Y., Sano, H., Aharonian, F., Maxted, N., Braiding, C., Blackwell, R., Lau, J., *forthcoming, to be published in PASA*

Acknowledgement

These PhD years have been rough, and I would like to thank a few important people that helped me succeed despite a great deal of challenges.

Firstly, I feel truly indebted to my supervisor and mentor Dr Gavin Rowell, who managed to channel my insatiable desire to answer every question in Astronomy, and subsequently taught me how to become a more productive researcher. He was also patient enough to guide me through the hardships, not only in my PhD, but also in my personal life, despite my chaotic, and sometimes unruly, behaviour. I would also like to thank Prof. Bruce Dawson and Emeritus Prof. Roger Clay, for kindly listening to all my nonsense and concerns and provide their moral support thorough the years.

I am also grateful to all my co-authors for their input in my paper drafts, with a special thanks to Prof. Michael Burton for his knowledge in radio-astronomy and his numerous feedbacks, making sure that the paper is as complete as possible. I am also especially thankful to Prof. Yasuo Fukui and Dr Hidetoshi Sano for their close collaborations, unconditionally sending me Nanten CO(1-0) data, useful to complete my various gas studies towards pulsar wind nebulae. They also included me in their multi wavelength studies towards supernova remnants in the Large Magellanic Cloud. I wish to continue this collaboration as they both are very productive and knowledgeable researchers.

On a more personal note, I would like to thank my fellow students in the TeV gamma-ray group : Rebecca Blackwell, Phoebe De Wilt, Jarryd Hawkes, James Lau, Andrew Curzons, Cameron Snowswell for their patience over my constant talks about cosmic-ray diffusion (whatever questions they asked always ended up in an awful lecture about the theory, the modelling, the code). I am especially grateful to Drs Nigel Maxted, Manuel Carrillo-Serrano and Gail Higginbottom who, on top of enduring the same fate as the others, had to cope with my worst when my level of exhaustion and frustration were reaching new heights (and additionally, offering me a few ice coffees to quench my cravings).

I would like to finish by thanking my parents, Denis Voisin and Brigitte Mouchel, for their sacrifices, their trust and their financial support contributed to this success. A special thanks to my mother for her motivational speeches when my morale was very low. Last but not least, I owe this achievement to my partner Anne Nguyen for her love and patience thorough this period. We have been though insurmountable challenges and have been able to conquer against all odds. Never, in my wildest dreams, I would have been able to learn and achieve in so little time alone. This thesis is, in some sense, a product of us.

Chapter 1

Introduction

Pulsars, discovered by Jocelyn Bell and Anthony Hewish in 1967, generated great interest due to the periodic nature of the radio emission. From the spatial association with supernova remnants (SNRs) and the pulse properties of the observed Crab and Vela pulsars, Gold (1969) confirmed that these phenomena are generated by rapidly rotating neutron stars, born from the core-collapse of high mass stars. These objects possess strong magnetic fields $B \sim 10^{12-13}$ G at their surface and can be approximated as a magnetic dipole. Among the more than 2000 pulsars currently identified, the ones associated with gamma-ray emission, the gamma-ray pulsars, have attracted a lot of interest in high energy astrophysics. At first, the number of identified gamma-ray pulsars was low, but the advance in gamma-ray astronomy led to the discovery of an increasing number of pulsars, notably in the last decade thanks to the increased sensitivity of Silicon-based detectors such as *AGILE* (Tavani et al., 2009) and *FERMI-LAT* (Atwood et al. 2009, see Fig. 1.1). These pulsars have been categorised into three different types : Radio-loud, radio-quiet, and millisecond pulsars, the latter being mostly detected by the *FERMI* telescope (see Caraveo 2014). Although the plasma is mostly co-rotating with the pulsar, a significant amount of accelerated particles – electrons/positrons pairs and, possibly, ions – escape the pulsar magnetosphere (see Fig. 1.2) and propagate outwards to form a *pulsar wind*. Eventually, the pressure of the expanding pulsar wind decreases and matches the supernova remnant cold ejecta pressure and forms a termination shock. Particles crossing the termination shock accelerate and produce broad-band electromagnetic (EM) emission, forming a pulsar wind nebula (PWN).

This chapter provides a brief introduction of the current knowledge of the dynamics, structure and electromagnetic (EM) emission properties of the different environment towards the pulsar and its PWN, and their association with the current major topics associated with PWN studies. I will also emphasize the current challenges regarding the evolution of the PWNe and the acceleration mechanism to accelerate the particles to high energies which is, in some models, linked to the composition of the PWNe. I will also stress how the ISM can unveil key information about PWNe and their progenitor SNR properties.

1.1 Structure of pulsar environments

The pulsar environment consists of several regions with very distinct properties. Figs. 1.2 and 1.3 describe the main regions which are briefly outlined below :

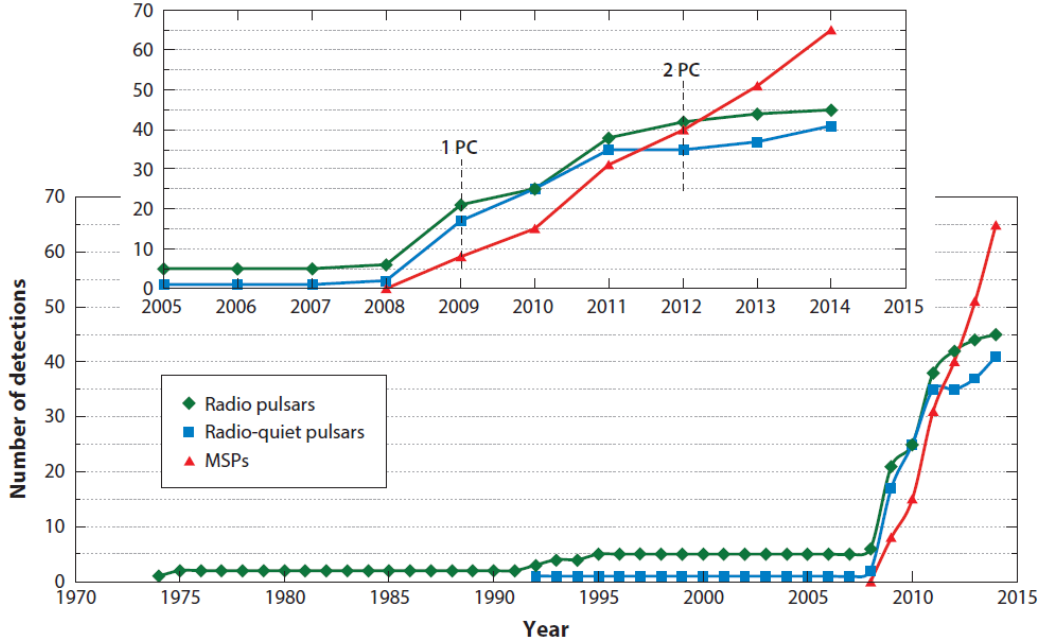


Figure 1.1: Evolution of the number of detections of radio-loud (green), radio-quiet (blue) and millisecond gamma-ray pulsars (red) as a function of time. The inset zooms over the last decade with the release of the 1st and 2nd *Fermi* catalogue marked PC1 and PC2 respectively (from Caraveo 2014).

1.1.1 The pulsar and its magnetosphere

The pulsar is a very dense compact object, a neutron star with density reaching $\sim 3 \times 10^{17} \text{ kg m}^{-3}$. Interestingly, the magnetic axis is not necessarily aligned with the rotation axis of the pulsar. Goldreich & Julian (1969) demonstrated that the near environment, or *magnetosphere*, of the pulsar cannot remain as a vacuum. Particles are ripped off the neutron star surface due to the enormous potential generated by the rotating magnetic field and co-rotate with the pulsar. A plasma is then formed with a number density $n_{\text{GJ}} = |\mathbf{\Omega} \cdot \mathbf{B}| / 2\pi e c$, with $\mathbf{\Omega}$ being the pulsar rotation vector, \mathbf{B} is the magnetic field, e being the elementary charge, and c is the speed of light in the vacuum. The magnetosphere of the pulsar extends up to the cylindrical region encompassing the particles co-rotating at sub-luminal speeds, the *light cylinder* with radius $r_{\text{LC}}(\theta) = c/\Omega \sin(\theta)$ where θ is the polar angle. Magnetic field lines past this region become predominantly toroidal and expands outwards. The particles, electrons/positrons pairs, travelling along these *open* lines are accelerated and eventually escape the magnetosphere. The energy transferred to this escaping wind equals the spin down power of the pulsar $L_{\text{SD}}(t) = -4\pi I \dot{P}_0 / P_0^3 \left(1 + (n-1) \dot{P}_0 t / P\right)^{-(n+1)/(n-1)}$ with n being the braking index of the pulsar ($n = 3$ for dipole magnetic field), P_0 and \dot{P}_0 are the initial period and period derivative respectively, and I is the moment of inertia of the neutron star.

In order to match the broadband observations of the PWNe, the plasma however requires a much higher density than n_{GJ} by a multiplicity factor $\kappa \sim 10^4$. The pulsar also emits pulsed radio and gamma-ray emission although they may originate from different regions. To match the lightcurve of these emission, Sturrock (1971) first developed the polar cap model where extracted electrons would produce high energy emission, which would interact with the magnetic field and produce electron/positron pair cascade. The resulting low energy pairs would then emit the observed coherent and beamed radio emission via the synchrotron process. The resulting emission is also expected to show a sharp cut-off at \sim a few GeV. Unlike the polar cap model whose acceleration mechanism occurs at low altitude above the pulsar (see green region in Fig. 1.2), the slot gap (Arons, 1983) and the outer gap (Cheng et al., 1986) models invoke

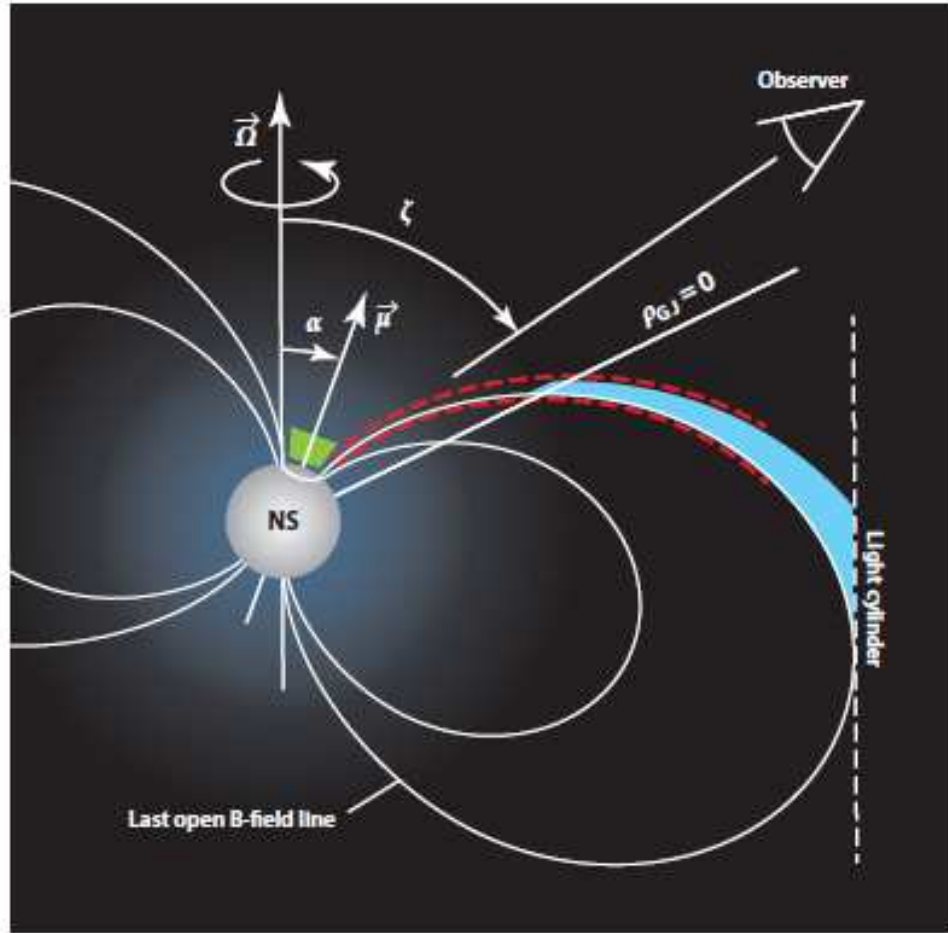


Figure 1.2: Illustration of the structure of the pulsar magnetosphere modelled as a dipole. The polar cap model acceleration site is shown in green while the slot gap region are encompassed within the red dashed lines and the outer gap region is shown in cyan (from Caraveo 2014).

a particle acceleration and pulsed radiation at high altitude (see Fig. 1.2). Indeed the slot gap model predicts acceleration towards the favourable magnetic field lines, delimited by the red dashed lines in Fig. 1.2, whereas the outer gap model argues for an acceleration site towards a low charge density regions between the $\Omega \cdot \mathbf{B} = 0$ regions and the light cylinder (shown in cyan in Fig. 1.2).

1.1.2 The pulsar wind

The particles escaping the magnetosphere travel outwards while following the toroidal magnetic field lines and the wind Lorentz factor reaches $\gamma_w \sim 10^6$. The pulsar wind is mostly confined inside the current sheet produced by the rotating pulsar, and is located at the equatorial plane. As a result of the plasma expansion, the plasma in this region is unperturbed and the acceleration of the particles of the pulsar winds become negligible. Consequently, synchrotron and bremsstrahlung radiation (dependent on the particle acceleration, see Appendix B) become inefficient. This is thought to explain why the pulsar wind zone is under luminous in X-rays.

In the case of an *oblique* pulsar, where the magnetic moment is not aligned with the rotation axis, the current sheet changes polarity in the magnetic field and becomes corrugated. As the distance increases, the separation between the two polarities becomes small and dissipation of the magnetic field is expected

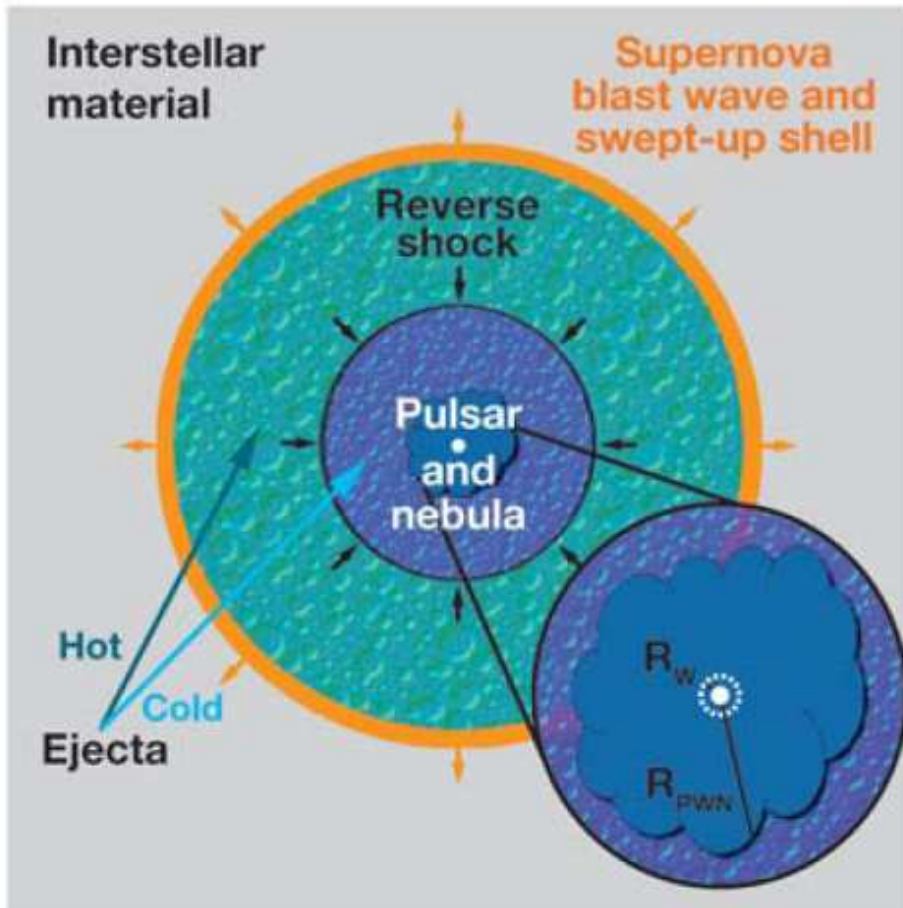


Figure 1.3: Sketch illustrating the structure of the pulsar environment. The white dot of the zoomed figure represents the magnetosphere while the dashed white circle indicates the position of the termination shock. The irregular blue shape highlights the morphology of the PWN. The surrounding region in purple shows the cold ejecta whereas the region delimited by the reverse shock in black and the front shock in orange is the re-thermalised ejecta (figure taken from Gaensler & Slane 2006)

to occur, resulting in the plasma to transition from being electromagnetically dominated to being kinematically dominated. From magnetic reconnection, particle acceleration might then occur in this region (Kirk et al., 2002). Inverse-Compton up-scattering of thermal and synchrotron photons originating from the pulsar magnetosphere (see previous section) may become efficient and consequently explain the origin of the pulsed gamma-ray emission found in the Crab nebula (Bogovalov & Aharonian, 2000).

1.1.3 The pulsar wind nebula

The pulsar wind nebula consists of confined shock-accelerated particles. Their flows have become randomized in time and direction, and is kinetically dominated (rather than magnetically dominated). The sudden acceleration of particles will lead to unpulsed and broadband non-thermal radiation from synchrotron (from radio to X-rays, see Fig. 1.4) and inverse-Compton (IC) up-scattering of cosmic microwave background (CMB) and infra-red (IR) soft photons to γ -ray energies. Kennel & Coroniti (1984) [KC90] first described the structure of the PWN as an onion layered region where particles would be tied to the travelling magnetic field. Earlier injected particles would then be positioned at a further distance from the pulsar. However, a uniform radio spectral index indicates efficient mixing of the particles inside the PWN. Recent X-ray observations illustrate the presence of a torus and jets (see Fig. 1.4, left panel), which

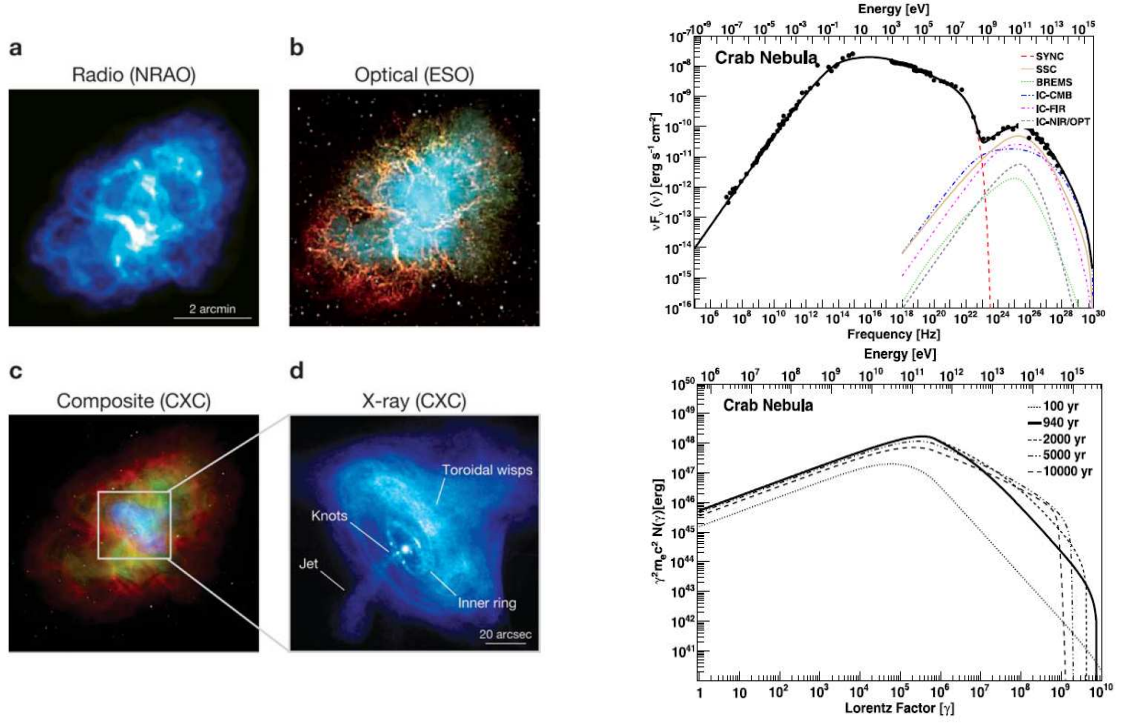


Figure 1.4: (*Left*) Morphology of the Crab nebula as seen in Radio (a.) in optical (b.) and in X-rays (c. and d.) (figure from Gaensler & Slane 2006). (*Top right*) Broadband spectral energy distribution (SED) of the Crab nebula. The synchrotron radiation (in red dashed lines) contributes to the total observed emission (in black solid line) up to energies of a few ~ 100 MeV, while the inverse-Compton up scattering of Cosmic Microwave Background (dashed blue line), far infra-red (red dotted line), optical/near infra-red (dotted grey line) and synchrotron photons (purple dashed line) as well as bremsstrahlung emission contribute to the observed emission in the MeV-TeV energy range. (*Bottom right*) Electron energy distribution required to produce the above SED. (figure from Torres et al. 2014)

illustrates the latitude dependent distribution of the density of electrons in the pulsar winds which was not predicted by the [KC90] model. As shown in Fig. 1.4, PWNe illustrates an uniform radio emission with a hard spectral index $\alpha = -0.3$ to 0.0 ($F(\nu) \propto \nu^\alpha$). The morphology of the X-ray emission also appears less extended compared to the radio and TeV emission because of the short synchrotron lifetime of the high energy electrons emitting those X-rays. Kargaltsev et al. (2013) also indicated that, as PWNe evolve, the gamma to X-ray luminosity ratio L_γ/L_X increases, likely caused by the reduction of the magnetic field strength from the PWN expansion (see Torres et al. 2014), leading to reduced synchrotron luminosity inside the PWN.

Middle-aged PWNe also exhibit steepening of the very high energy (VHE) γ -ray emission away from the pulsar caused by Synchrotron cooling, and an asymmetric TeV morphology caused by the reverse shock resulting from the interaction with the ISM. Although PWNe generally illustrate the aforementioned properties, each PWN is likely to have distinct features as their spectral and morphological properties of the emitted radiation are still heavily affected by the density distribution of the ISM. Gelfand et al. (2009) also indicated that the evolution of the multi-wavelength properties of the PWN drastically change at the different phases of the PWN (see next section). Indeed, energy losses from adiabatic expansion, synchrotron and inverse-Compton radiation may be dominant at distinct stages, thus affecting the electron energy distribution in a different fashion.

1.2 Dynamical aspects of the PWNe and their progenitor SNR

PWNe are ever-changing environments with strong changes in their morphological and radiative properties. Most of these changes highly depend on the distribution of the ISM and the physical properties of the progenitor SNR itself. I can list three main evolutionary phases of the SNR :

- *Free expansion phase* : Until the mass swept by the supernova roughly matches the mass of the ejecta M_0 , the shock, produced by a supernova with kinetic energy E_{SN} , travels linearly at constant velocity $v_{\text{SNR}} \propto \sqrt{E_{\text{SN}}/M_0} \sim$ a few 1000 km/s. The shock speed of the SNR allows efficient cosmic-ray acceleration via diffusive shock acceleration (see Appendix A). In this phase, young SNRs are X-ray bright due to the high temperature of the plasma and the synchrotron radiation of high energy electrons at the shock front. This phase generally last up for a few hundred years.
- *Sedov-Taylor phase* : In this phase, the mass swept by the SNR becomes larger than the Mass of the ejecta. As the radiative losses are still negligible, the SNR expands adiabatically and its radius $R_{\text{SNR}}(t)$ follows the Sedov-Taylor solution $R_{\text{SNR}}(t) \propto t^{2/5}$ (Sedov, 1959). The shock speed consequently decreases as a function of $t^{-3/5}$. The SNR eventually produces a reverse shock that will reheat the interior. The increasing density towards the shock front becomes non negligible and cosmic-rays might then produce significant γ -ray emission (see Dermer & Powale 2013). The ISM surrounding the SNR being generally inhomogeneous, the SNR structure becomes more irregular with shock speed stalling at ISM clouds. Interaction with these dense clouds leaves specific X-ray and γ -ray signatures (Slane et al., 2014). The Sedov-Taylor phase generally lasts for ~ 20000 years.
- *Snow-Plow Radiative phase* : Once the temperature of the SNR interior becomes less than 10^6 K, the ions from the plasma eventually recombines with the free electrons and enhance radiative losses via Lyman α radiation. A neutral dense shell behind the shock is then formed that can be visible in radio and infra-red (IR). As the temperature does not decrease uniformly inside the SNR interior, the front shock still expands due to the pressure inside the SNR. The shock enters a snow-plough phase where the momentum of the shock is conserved. Concerning the evolution of the SNR, Oort (1951) predicted an expansion $R_{\text{SNR}}(t) \propto t^{1/4}$ while Cioffi et al. (1988) claimed a slightly faster propagation $R_{\text{SNR}}(t) \propto t^{3/10}$. The shock eventually breaks down when the expansion velocity roughly equals the thermal velocity of particles in the ISM (~ 10 km/s). This phase thus lasts until the age of the SNR reaches ~ 500000 years.
- *Merging with surroundings* : Once the SNR expansion velocity slowly reaches the dispersion velocity inside the ISM, the SNR starts to break and merge with the ISM. The remaining kinetic energy of the SNR then contributes to the turbulence in the ISM.

Hydrodynamical simulations of the evolution of the PWN also shows similar phases (see Gaensler & Slane 2006 for detailed review)

- *Free expansion phase*: the PWN evolves in the SNR ejecta and the propagation is supersonic. For a young PWN, the spin down energy can be considered constant and the radius of the PWN evolves as a function of $t^{6/5}$. This phase lasts from several hundred to a few thousand years and ends when the SNR reverse shock meets the PWN (van der Swaluw et al., 2001).
- *Crushed PWN* : Once the reverse shock reaches the PWN, the pressure of the hot ejecta pushes the PWN inwards. The increasing pressure of the PWN eventually leads to a new subsonic expansion due to the higher speed of sound in the medium. This process keeps iterating until the PWN starts

to slowly expand once again in proportion to $t^{11/15}$. As the surrounding ISM generally illustrates irregular densities, it is expected that the PWN becomes crushed on one side, leading to an offset position of the pulsar within the PWN (Blondin et al., 2001) and an irregular morphology of the PWN.

- *Relic-PWN and bow shock* : If the pulsar leaves its PWN interior, the PWN does not receive injected electrons and becomes ‘relic’. The pulsar then creates a new PWN beside the former one. Finally, the pulsar, born with a proper motion, will leave the SNR interior and travel through the ISM. A bow shock geometry is thus generally expected.

1.3 The PWN : Motivation and Challenges.

1.3.1 A laboratory for CRs and electrons study

As will be emphasized in Chapter 2, understanding how cosmic-rays are created and where they come from remains a major topic in astrophysics. It is now well accepted that particles can be accelerated up to very high energy by several astrophysical objects. Among the acceleration mechanisms, the first order Fermi acceleration (diffusive shock acceleration) of a test particle within a strong shock appears favourable to explain the spectrum of CRs bombarding Earth.

As opposed to CRs whose trajectories are deflected by the Galactic magnetic field, gamma-rays produced by the accelerated high energy particles (see Appendix B) can help identify those CR accelerators. In Fig. 1.5 (Deil et al., 2015)¹, I note that PWNe represent the major fraction of identified TeV sources, and are consequently good laboratories to study the origin of cosmic-rays (see Chapter 2).

Another major topic to which the PWNe could provide answers is the origin of the positron excess announced by the *PAMELA* collaboration in 2009 (Adriani et al., 2009). Indeed, unlike the protons and electrons which are primary particles, the positrons can only be produced via inelastic processes. Due to the short synchrotron cooling time of high energy electrons, the presence of a nearby astrophysical source of positrons is thus required (Atoyan et al., 1995) and the Geminga PWN, located at $d \sim 200$ pc, may be a good candidate to explain this excess.

1.3.2 Current challenge in our understanding of PWNe

Recent progress has been made with models that attempt to reconcile the evolution of the PWN dynamics with the EM radiation from PWNe (Bucciantini et al., 2011; Torres et al., 2014). Although aspects of the structure and the spectral properties have mostly been understood, major challenges still remain to be addressed :

- The acceleration mechanism : Although the energy distribution of electrons roughly matches with that from the diffusive shock acceleration (DSA) $\propto E^{-2}$ (see Appendix A), MHD simulations indicate this mechanism may be inefficient for transverse relativistic shocks unless strong B field variations at small scales allow the particles to deflect back into the shock (see Blandford & Eichler 1987). This notably requires a small magnetization of the plasma (kinetically dominated) $\sigma =$

¹<http://tevcat.uchicago.edu/>

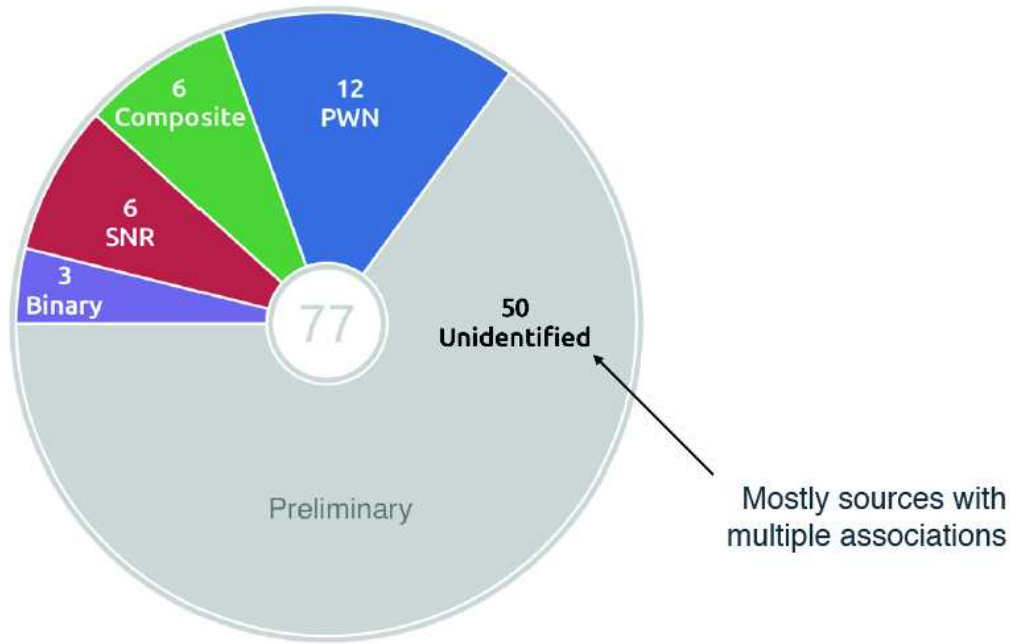


Figure 1.5: Diagram illustrating the different type of TeV sources currently identified in the Galactic plane. More than 60% of the detected sources remain unidentified. The TeV cat website (see footnote) keeps update of the list of TeV sources in the sky (Deil et al., 2015).

$B^2/4\pi n\gamma m_e c^2 < 0.01$ (n being the pulsar wind density). However, this condition contradicts with the large magnetization of the plasma leaving the magnetosphere ($\sigma \gg 1$). One way to avoid this σ paradox is to invoke the *striped current sheet* where magnetic dissipations, produced in the neutral sheet separating the two polarities, may occur (see Section 1.1.2). Spectral modelling of the Crab nebula across the entire electromagnetic spectrum indicated the intrinsic broken-power-law nature of the energy distribution of electrons (see Fig. 1.4), which suggests either several acceleration mechanisms (Bucciantini et al., 2011) or various population of electrons (see Meyer et al. 2010). Among the popular mechanisms, the *Resonant Cyclotron Acceleration* (Hoshino et al., 1992) notably invokes the presence of ions producing cyclotron radiation that would be absorbed by the shocked electrons (see e.g Amato 2014 for further review). This mechanism has already been used to explain the observed wisps of the Crab nebula and the X-ray arcs of PSR B1509–58 (Gaensler et al., 2002). However, recent one-zone modelling of young and old PWNe seem to infer the energy transferred to hadronic components would be quite small (Bucciantini et al., 2011). The relatively low ambient density prevents the protons/ions to be directly observed via proton-proton interaction. Consequently, whether they can attain very high energies still remain to be addressed.

- The dark TeV sources : From the HESS Galactic Plane Survey (HGPS), a growing a number of *dark sources*, γ -ray sources with no visible counterparts at other wavelengths, have been detected and may be associated with PWNe. This challenge links to the evolution of the PWN luminosity as it evolves through the different stages. One evident factor coming to play is that the magnetic field of the PWN decreases with time, and the PWN may become X-ray and radio quiet due to the lack of synchrotron radiation. HESS J1303–631 is a prominent example where the multi-wavelength counterparts of the TeV source are very faint or not detected. However, energy dependent morphology of the TeV emission confirmed its association with the pulsar PSR J301–6305 (H.E.S.S. Collaboration et al., 2012).
- Confinement of high energy electrons : It is thought that the toroidal magnetic field lines of young PWNe are thought to confine the particles efficiently. However, at later epochs, the pressure inside

PWN eventually match the pressure of the ISM and the PWN breaks. The escaping high energy electrons propagating along the Galactic magnetic field lines could explain the observed electron energy spectrum on Earth. It has also been noted that the reverse shock crushing the PWN could also disrupt its magnetic field lines and allow high energy particles to escape (de Jager & Djannati-Ataï, 2009).

1.3.3 Combining TeV gamma-ray astronomy with molecular gas study

As discussed in the last section, further evidence of CRs inside PWNe could help provide important answers about the acceleration mechanisms inside PWNe. It is known that the gamma-rays produced by CRs is proportional to the target density of the surrounding ISM (see appendix B). Consequently, dense molecular clouds with particle densities of 10^{2-4} cm^{-3} , can then increase the gamma-ray emission by a few orders of magnitude and help search for CRs not only from the progenitor SNR but also from the PWN itself, as suggested by Bednarek (2007). Aharonian & Atoyan (1996) has, however, noted the differences in the evolution of the TeV spectral and morphological properties between an impulsive source, a good approximation for SNR, and a continuous source, for PWN, assuming the CRs uniformly diffuse inside the molecular clouds. Therefore, evidence of a physical interaction between the progenitor SNR and the molecular cloud is the first step to argue the subsequent physical association between the molecular cloud and the PWN itself. To do so, I can use the anti-correlation between hard X-ray emission with molecular emission tracing diffuse gas (e.g CO(1-0)) to highlight the interface between the CR source and the nearby molecular clouds. Shock tracers (see chapter 3) may also provide additional evidences of the SNR-Molecular cloud interaction. Consequently, combining ISM studies with TeV gamma-ray astronomy would not only provide valuable information about the nature of several TeV emission, but also give answers concerning the composition of high energy particles inside PWNe.

In this thesis, I focus on the study of eight TeV sources which may have been produced by nearby PWNe. To provide an accurate view of the ISM towards these TeV sources, I make use of the 4 metre Nanten telescope CO(1-0) large scale survey (Mizuno & Fukui, 2004), which traces the diffuse molecular gas, and combine it with our recent Mopra 7mm and 12mm observations, which indicates the dense molecular clouds, star forming regions and also post-shocked molecular gas with arcmin resolution (see Chapter 3 for further details). The SGPS/GASS HI (McClure-Griffiths et al., 2005, 2009) surveys are also used to obtain information concerning the spatial distribution of the atomic gas.

Among the TeV source, I particularly look at HESS J1825-137, a large PWN (Aharonian et al., 2006b) powered by the pulsar PSR J1826-1334 located at $d = 4 \text{ kpc}$. The significant offset of the pulsar with respect to the TeV peak (see Fig. 1.6) suggests the PWN has been crushed by the progenitor SNR reverse shock due to its interaction with a nearby molecular cloud. Interestingly, the newly announced TeV source HESS J1826-130 (Deil et al., 2015) overlaps the large molecular cloud. Consequently, this region is a good laboratory to study the diffusion of protons and electrons for the PWN and its progenitor SNR with the molecular cloud, and to provide key information on how the PWN interacts with the ISM.

In Chapter 2, I introduce the concept of γ -ray astronomy and the detection techniques. I follow up by reviewing radiative concepts useful for atomic and molecular lines study of the surrounding gas in Chapter 3. I then review in Chapter 4 how the propagation of CRs/high energy electrons and their interactions with the surrounding ISM will affect their energy distribution, and consequently the spectral and morphological properties of the resulting gamma-ray emission. Chapter 5, in a form of a journal paper, I provide an accurate view of the ISM towards HESS J1825-137 while in Chapter 6, I make use of these information to model the possible contribution of CRs/high energy electrons the PWN

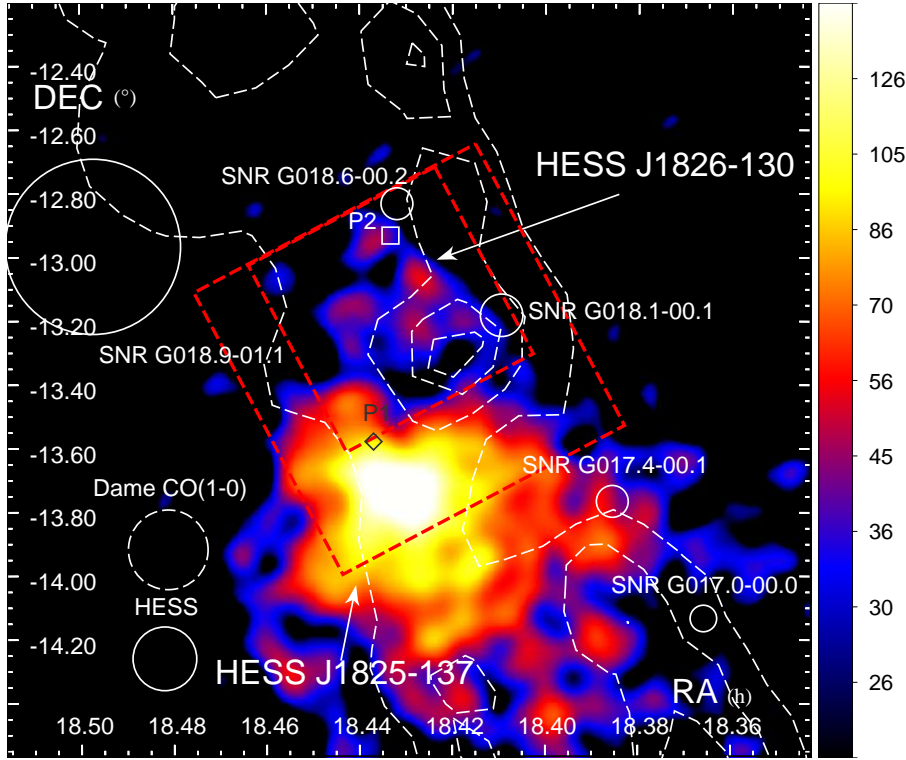


Figure 1.6: TeV gamma-ray excess count above $E_\gamma = 270$ GeV towards the PWN HESS J1825–137 and the unidentified TeV source HESS J1826–130 overlaid by the Dame CO(1–0) integrated intensity (20,40,60,80 K km/s) in white dashed contours. The red dashed boxes represent the 7mm (small box) and the 12mm (large box) Mopra surveys, probing dense molecular clouds as well as star forming regions and post-shocked gas (see chapters 3 and 5 for further details). P1 and P2 indicate the position of the pulsars PSRs J1826–1334 and J1826–1256 respectively. The white circles indicate the location and size of the SNRs catalogued by Brogan et al. (2006)

HESS J1825–137 and its progenitor SNR to the HESS J1826–130 emission and study its association with the aforementioned PWN and its progenitor SNR. Finally, I study the environment of several PWN candidates using molecular lines to provide additional distance constraint in chapter 7.

Chapter 2

Introduction to Gamma-ray astronomy

Over the last decades, gamma-ray astronomy has been developed to locate sources capable of accelerating particles to very high energies. Gamma-rays are generally produced from the interaction of these high energy particles with a target atom/molecule or photon. Notably as photons travel in straight lines and can be readily detected, gamma-rays appear to be a reliable method to search for particle accelerators. Space-based gamma-ray astronomy was launched with the start of the SAS-2 (Fichtel et al., 1975) and COS-B (Bignami et al., 1975) experiments. Gamma-ray detections were notably found towards the Crab nebula and Cen A. Ground based gamma-ray telescopes (e.g Whipple : Kildea et al. 2007, HEGRA : Daum et al. 1997) were also designed to detect gamma-rays up to TeV energies. Unlike space-based gamma-ray telescopes, which looked at gamma-ray primaries, the concept of ground-based gamma-ray astronomy was to detect the Čerenkov light produced by the extensive air showers (Cocconi, 1960) from the interactions between the astrophysical gamma-ray and an air atom/molecule. Although the larger effective area allowed more detections of very-high energy (VHE) gamma-rays, the major challenge has been to remove the background of cosmic-ray showers. Nowadays, more than a hundred VHE gamma-ray sources have been detected, and helped to obtain key information about Galactic and extra Galactic particle accelerators.

In this chapter, I first briefly review the history of the science of cosmic-rays, and explain the basic physics of extensive air showers (EAS). We then discuss the flux and spectral properties of the cosmic-ray flux bombarding Earth, and the main scenarios used to explain how cosmic-rays are created. We then elaborate on the processes of space-based and ground based gamma-ray astronomy and list the different types of Galactic TeV sources identified so far.

2.1 Cosmic-ray and Extensive air showers

2.1.1 How it all started

Cosmic-rays, as named by Millikan (Hillas, 1972), are high energy particles such as protons, Helium and heavier nuclei, whose origins are extra-terrestrial. It all started when Coulomb first noticed some loss of



Figure 2.1: Victor Hess about to ascend to discover cosmic-rays. Credit goes to *VF Hess Society, Schloss Pöllau/Austria*

electric charge during his experiments although his apparatus was isolated. Later on, in the twentieth century, soon after the establishment of Einstein's relativity theory, the birth of quantum mechanics and radioactivity, several experiments investigated the ionization occurring in the air that was responsible for the loss of charge.

The ionization of the atmosphere was reported by Geitel and Wilson (Hillas, 1972) who conducted experiments using an isolation apparatus. Observing no decrease in ionization even by placing the apparatus inside the Caledonian Railway tunnel, he first concluded that ionization was a property of the air itself. From several experiments, Rutherford noted that the charge loss rate could be reduced if he placed a lead shield around the electroscope. Because of the penetrating power of gamma-rays when they propagate through material, it was soon believed that most of the ion production was due to gamma-rays emitted from radioactive elements from Earth. Under this hypothesis, it was suggested that the ionization rate should decrease with altitude.

However, Victor Hess ascended up to 5000 metres in several balloon flights (see Fig. 2.1) to observe the evolution of the ionization rate as a function of altitude, and indicated that although the radiation was at first decreasing, it rapidly increased. Consequently, he discovered the radiation was coming from outer-space (Hess, 1913) and the lack of radiation drop during a solar eclipse indicated that the sun was not the main source of the radiation.

Unfortunately, not all physicists were convinced about the veracity of the discovery as there were serious result variations between different balloon flights. In order to disprove at first the extraterrestrial origin of radiations, Millikan and Cameron set up an experiment in Lake Muir in 1925 where they measured the ionization rate at the surface and bottom of the lake (Millikan & Cameron, 1926). The rapid decrease of radiation at the bottom of the lake gave the final proof that the radiation was of extra-terrestrial origin.

However, the nature of these cosmic-rays was still unclear. Millikan was convinced that cosmic-rays consisted of gamma-rays because of their penetrating power compared to α or β radiation. The discovery that the ionization rate depended on the latitude and thus the geomagnetic distribution on Earth made it clear that cosmic-rays consisted of charged particles.

Another major leap in cosmic-ray physics was the discovery of extensive air showers (EAS). Skobelzyn observed several tracks in his photographs and after the advance of quantum electrodynamics, Bruno Rossi understood that the interaction of cosmic-rays with the surrounding walls of his laboratory were creating new particles and the *secondary particles* would have a common origin.

Several studies using coincidence detectors followed and in 1938, Pierre Auger and Roland Maze performed an experiment tracking the temporal coincidence as a function of distance between two detectors and spotted coincidences at a separation of ~ 300 metres at high altitude (Auger et al., 1939). Auger concluded that a primary particle interacting with the atmosphere was generating a cascade of secondaries and the primary particle's energy must have been at least $\sim 10^{15}$ eV.

Studies of cosmic-rays have been of great importance for particle physicists as the interaction between a high energy particle and a target particle could lead to the creation of new elementary particles, e.g enabling the discovery of the positron. Regarding hadronic interactions, the energetic collision would overcome the binding forces inside a nucleus and enable the observation of subatomic particles (Auger, 1941). Therefore, before the launch of colliders, extensive air showers were the only particle source available to particle physicists.

2.1.2 Extensive air showers

When primary CRs, high energy electrons, or high energy gamma-rays interact with a target particle in our atmosphere, they produce extensive air showers (EAS) consisting of secondary particles (e.g muons, electrons, photons). In this section, I review the properties of the two types of cascade encountered : the electromagnetic and hadronic air shower.

Electromagnetic air shower

Electromagnetic air showers consist of the interaction of an energetic electron/positron or gamma-ray with an air particle. They produce a cascade of photons and electron/positron pairs via the two following interactions.

$$e^{\pm} + N = e^{\pm} + N + \gamma \quad (2.1)$$

$$\gamma + N = e^{+} + e^{-} + N \quad (2.2)$$

The first interaction describes the production of gamma-ray from the interaction of an electron/positron with a target nucleus N , called *Bremsstrahlung*, and the second shows the production of an electron/positron pair from the interaction of an energetic gamma-ray with a target particle N . Their cross sections σ_{pair} and σ_{br} are linked by the following relation (see Stanev 2010) :

$$\sigma_{\text{pair}}(k, E) \sim \frac{7}{9} \sigma_{\text{br}}(E, k) \text{ cm}^2 \quad (2.3)$$

where E is the energy the charged particle and k is the resulting photon energy.

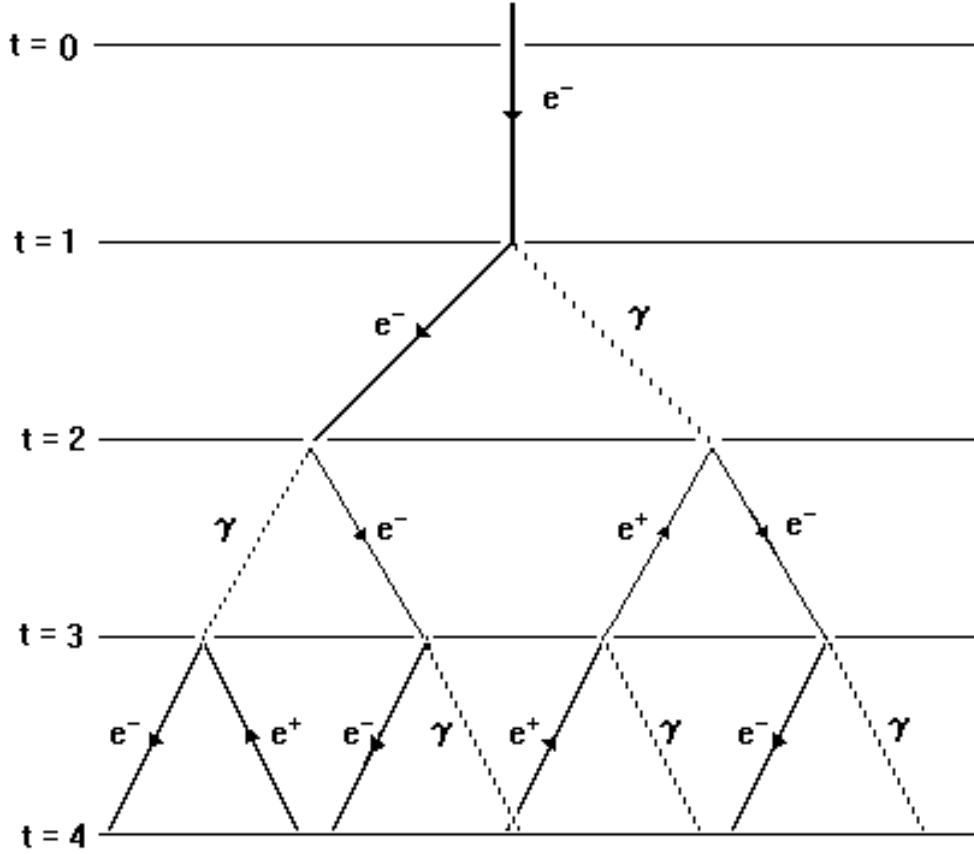


Figure 2.2: Sketch representing the Heitler's model of the electromagnetic cascade. n indicates the n^{th} generation of particles (Heitler, 1954).

The electromagnetic air shower was first modelled by Heitler (1954). Facing the complexity of the problem, Heitler made the following assumption in order to derive the key features of an electromagnetic air shower. For simplicity, the radiation length $\langle \lambda_r \rangle$ is assumed to be the same for both Bremsstrahlung and pair production so it becomes easy to associate the generation of a given particle to a specific distance (see Fig. 2.2).

The radiation length needed for a particle to lose half of its energy is $\langle \lambda' \rangle = \langle \lambda_r \rangle \ln 2$. Therefore, in one unit of $\langle \lambda' \rangle$, one particle will interact and generate two particles of half its energy. The shower consisted of layers separated in unit of $\langle \lambda' \rangle$. Let's define the atmospheric depth X as the integral of the mass density of the atmosphere ρ that the cosmic-ray has crossed before reaching the altitude h :

$$X = \int_h^\infty \rho(l) dl \text{ g cm}^{-2} \quad (2.4)$$

The particle energy $E(X)$ at generation n and therefore at atmospheric depth $X = n \langle \lambda_r \rangle \ln 2$ can be described as follows :

$$E(X) = \frac{E_0}{2^n} = E_0 e^{-X/\langle \lambda_r \rangle} \quad (2.5)$$

where E_0 is the energy of the primary particle. The particles multiply and the cascade expands as it propagates through the atmospheric depth X . However, the respective energy of each particle is halved

at every interaction and eventually reaches a critical energy where the ionization energy loss becomes dominant (Heitler, 1954) and the multiplication of particles inside the EAS eventually stops. The averaged energy of each particle at the maximum of the shower is κE_c , κ being a constant of order unity and E_c being the critical energy dependent on the properties of the medium. The air shower reaches maximum development at depth X_{max} given by the following equation :

$$X_{max} = \langle \lambda_r \rangle \ln \left(\frac{E_0}{\kappa E_c} \right) \quad (2.6)$$

and the number of particles of particles N_m found at X_{max} is :

$$N_m = \frac{2}{3\kappa} \frac{E_0}{E_c} \quad (2.7)$$

Heitler noted the model overestimated the total number of electrons approaching X_{max} . By comparing with simulations of cascade events, Matthews (2005) deduced that the total number of electron N_e computed using Heitler's simple model should be divided by 10 in order to reach better agreements with experimental data.

$$N_e = \frac{N_m}{10} \quad (2.8)$$

Another useful feature that can be derived from Heitler's model is the derivation of the elongation rate for an electromagnetic shower Λ_γ , which is the variation of X_{max} as a function of the primary particle energy E_0 .

$$\Lambda_\gamma = \frac{dX_{max}}{d \log(E_0)} = 2.3 \langle \lambda_r \rangle \text{ per decade of energy} \quad (2.9)$$

The elongation rate for electromagnetic shower in the atmosphere is $\Lambda_\gamma = 85 \text{ g cm}^{-2}$ per decade of energy. Finally, the lateral width of the electromagnetic cascade tends to be quite small. Indeed, for a gamma-ray induced shower of a few TeV generated at $\sim 20 \text{ km}$ altitude, the width of the shower does not exceed a few tens of metres. The large momentum of the primary in the direction of travel leads to small angle scattering.

Therefore, although the Heitler model cannot perfectly describe the evolution of the electromagnetic shower in detail, it does reproduce important key features :

- X_{max} agrees well with Monte-Carlo simulations of cascade showers and is *logarithmically* proportional to the primary particle energy E_0
- The maximum number of photons and electron/positron pairs is proportional to the primary particle energy E_0

Hadronic air shower

When a proton or nucleus interact with an air molecule, a hadronic air shower will be generated, consisting of secondary particles as well as electromagnetic sub-cascades (with details as described previously).

The proton-proton inelastic interaction produces pions. On one hand, the charged pions π^+ and π^- have a life time of $2.6 \times 10^{-8} \text{ s}$ before decaying into muons and muonic neutrinos:

$$\pi^+ \rightarrow \mu^+ + \nu_\mu \quad (2.10)$$

$$\pi^- \rightarrow \mu^- + \nu_\mu \quad (2.11)$$

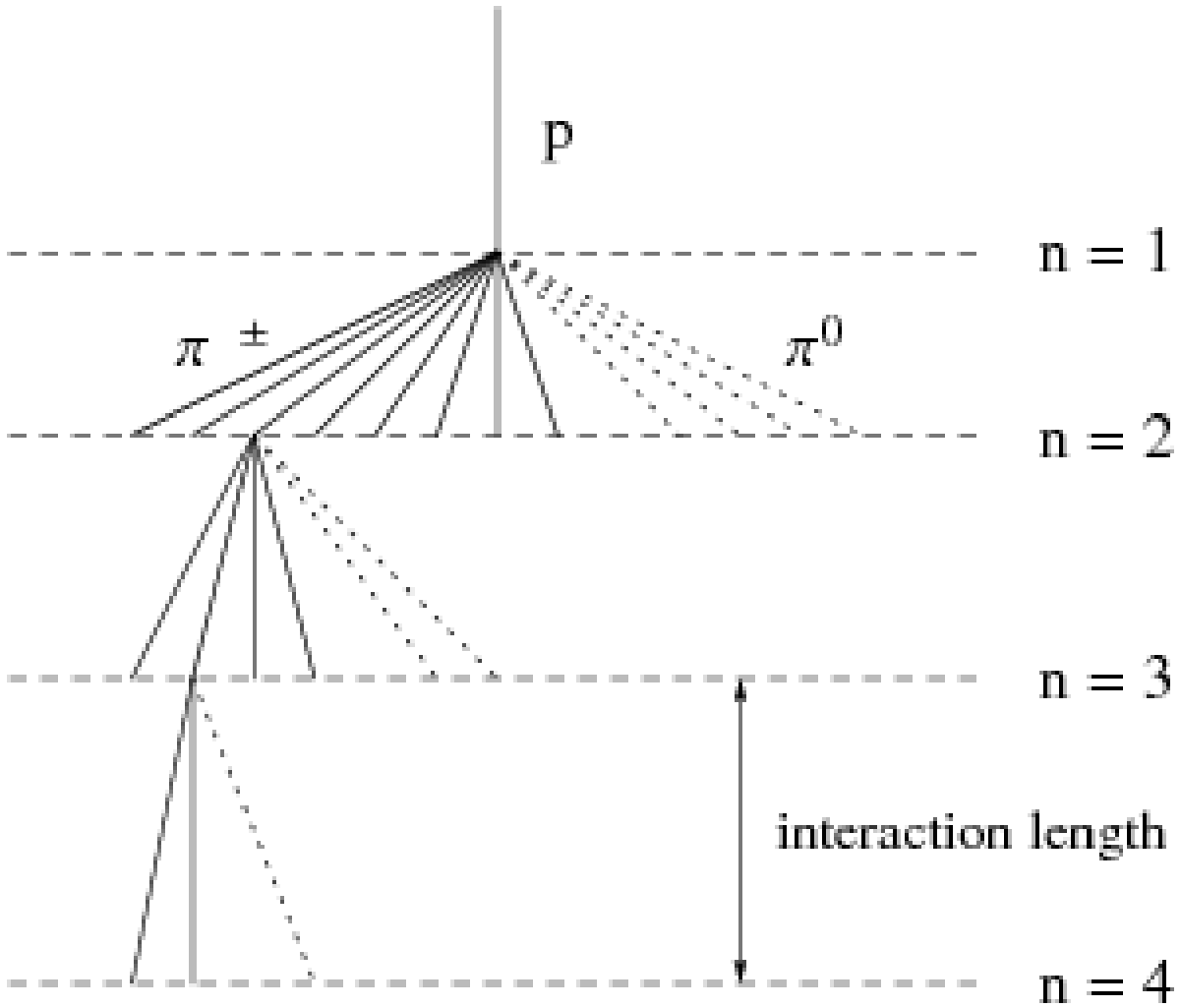


Figure 2.3: The model of Matthews (2005) for hadronic air shower where a nucleus interacts with an air molecule. The cascade will produce neutral pions which will generate gamma-rays while the charged pions π^\pm will eventually decay to charged muons μ^\pm .

On the other hand, neutral pion π^0 has a lifetime of 8.4×10^{-17} s and will decay into gamma-rays after their production:

$$\pi^0 \rightarrow 2\gamma \quad (2.12)$$

The much larger lifetime of the charged pions compared to neutral pions means they are likely to interact with other air nuclei and produce further pions before decaying into muons. The hadronic cascade is consequently a mix of electromagnetic sub showers plus muonic components.

Matthews (2005) generalised Heitler's model to hadronic showers (see Fig. 2.3). He divided the atmosphere in several layers of length equal to $\lambda_I \ln 2$, where λ_I represented the interaction length. After reaching this layer the particles split into $N_{ch} - 1$ charged pions and $N_{ch}/2$ neutral pions. Two-thirds of the previous particle energy would then be shared amongst the charged pions. While the neutral pions create electromagnetic sub showers, the charged pions keep multiplying and their energy drops to :

$$E_\pi = \frac{2^n E_0}{(3N_{ch})^n} \quad (2.13)$$

¹Matthews (2005) used $N_{ch}=10$ which agreed quite well with the simulations.

after n interactions. We define the critical energy E_c^p as the energy of the pion when it decays into a muon. Indeed, the secondary particles decay after several interactions and thus the production of new pions eventually ceases. The critical number of interactions n_c is thus given by the following relation:

$$n_c = \frac{\ln(E_0/E_c^p)}{\ln(3N_{ch}/2)} \quad (2.14)$$

At the maximum of the shower development, the hadronic shower mainly consists of muons and electron pairs. Electrons represent the main fraction of the cascade shower. We note that the muons which have a lifetime of 2.1×10^{-6} s, may end up decaying into electrons/positrons and all may not reach detectors on the ground.

$$\mu^- \rightarrow e^- + \bar{\nu}_e + \nu_\mu \quad (2.15)$$

$$\mu^+ \rightarrow e^+ + \nu_e + \bar{\nu}_\mu \quad (2.16)$$

Finally, Matthews (2005) was able to estimate the depth of maximum development for an hadronic shower X_{max}^p , although he noted the underestimation of the value compared to simulations.

$$X_{max}^p = X_0 + \langle \lambda_r \rangle \ln \left(\frac{E_0}{3N_{ch}E_c^\gamma} \right) \quad (2.17)$$

The derived elongation rate for hadronic showers in air is 58 g cm^{-2} , somewhat less than the elongation rate from showers initiated with gamma-rays or leptons. Finally, its lateral distribution and the presence of muons are unique features and become important means to distinguish them from electromagnetic air showers. These features turn out to be very important for ground based high energy gamma-ray observatories as I discuss later.

2.1.3 Means of cosmic-ray detections and CR observatories

A better understanding of cosmic-rays and their interactions improved the methods used to observe them at higher energies. While low energy primaries (up to 10^{14} eV) can be detected from balloons at high altitude, the number of higher energy cosmic-ray is too low to be detected. Several techniques have however been developed using information from EAS to reconstruct the energy of the primary particle and its arrival direction.

Cosmic-ray observatories may consist of scintillator counters, made of high density inorganic material, and able to count the number of secondary particles reaching the detectors. The mass and charge of the particle can be obtained by placing a magnet between two scintillators (e.g PAMELA), in which the time of flight is measured - and thus the velocity- and the charge of the particle by computing the deviation of the incident particle due to the magnetic field.

Čerenkov ground detectors detect the light produced by the particles exceeding the speed of light in a polarizable medium (e.g water). A collection of these Čerenkov detectors record the quantity of incoming EAS particles and provide useful information about the lateral distribution of particles in the shower. This method has notably been used by the Pierre Auger Observatory (Pierre Auger Collaboration, 2015), consisting of ground based Čerenkov detectors (see Fig. 2.4 top left panel) which measure the time of flight of the cascade, combined with 4x6 air fluorescence detectors measuring the total energy deposited by the cascade in the atmosphere and to obtain the energy of the primary particle. Ultra high energy cosmic-rays

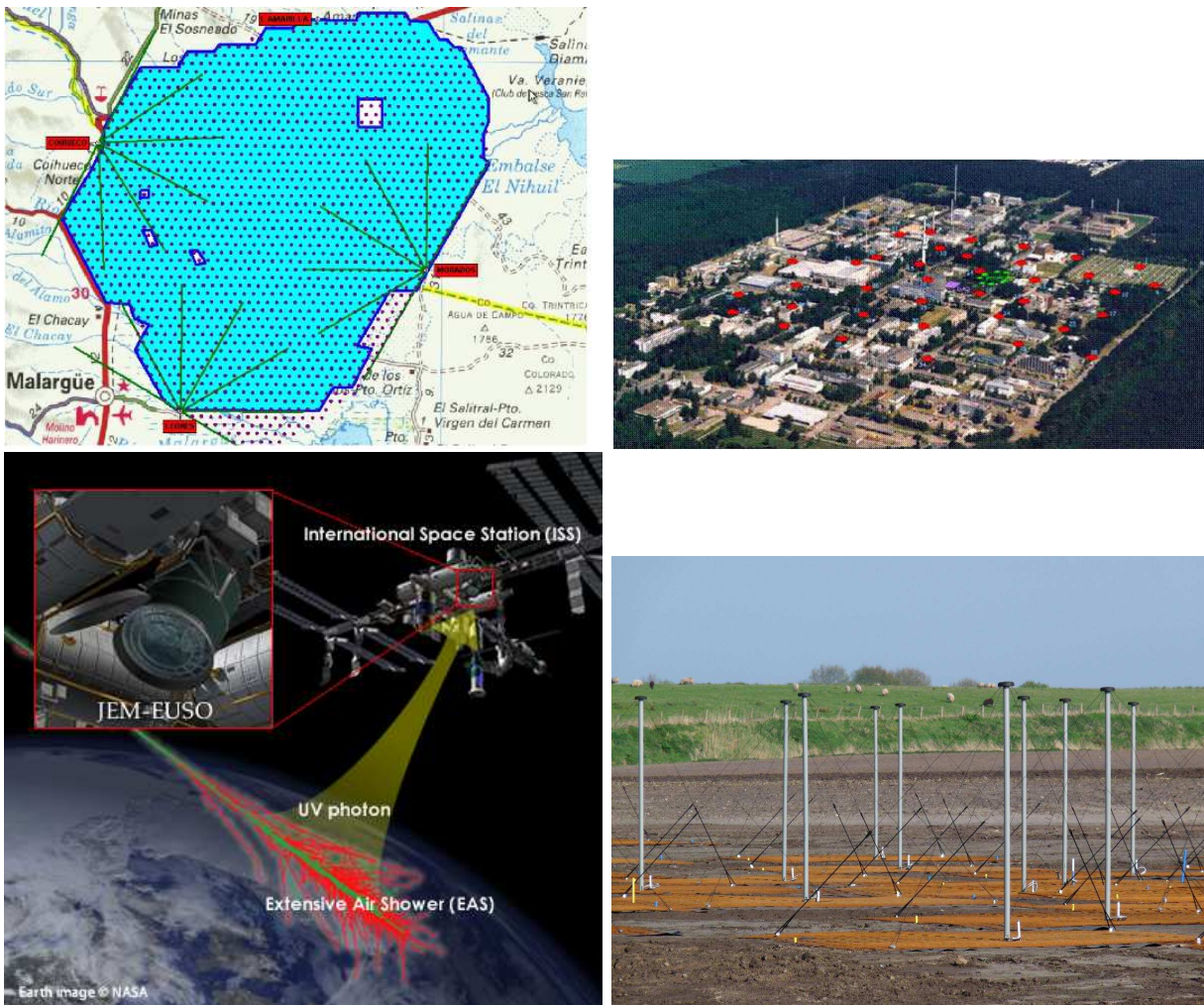


Figure 2.4: (Top left) Map showing the coverage of the Pierre Auger Observatory (Pierre Auger Collaboration, 2015) necessary to detect UHE cosmic-rays. (Top right) KASCADE Grande observatory (Apel et al., 2010) coverage. (Bottom left) Sketch of the JEM-EUSO telescope (Takahashi & JEM-EUSO Collaboration, 2009), located at the ISS, and detecting EAS from UHE cosmic-rays entering the atmosphere. (Bottom right) Low band antennae from the LOFAR observatory (van Haarlem et al., 2013).

are notably able to produce up to 10^6 particles and the fluorescence can therefore be detected up to 30 km away by the fluorescence detectors (FD). The combination of the surface and fluorescence detectors allow better reconstruction of the arrival direction and the total energy of the shower.

KASCADE GRANDE (Apel et al., 2010) consists of muon detectors, an array of scintillators and a central high tuned hadron calorimeter (see Fig. 2.4 top right panel) which measures the arrival angle and the energy of individual hadrons within an air shower, enabling the study of high energy hadronic interactions. Another means of observation is to detect the radio emission coming from the extensive air shower (EAS) using the radio telescope LOFAR (see Fig. 2.4, bottom right panel, van Haarlem et al. 2013). Finally, the next generation cosmic-ray observatory JEM-EUSO (Takahashi & JEM-EUSO Collaboration, 2009) is expected to detect UHECR from space at the International Space Station (see Fig. 2.4 bottom left panel).

2.1.4 The cosmic-ray flux

Fig. 2.5 displays the cosmic-ray flux as a function of energy and the most striking feature is the approximate consistency of the power-law distribution $F(E) \sim E^{-\alpha}$ over 13 decades of energy (see Fig. 2.5). Two

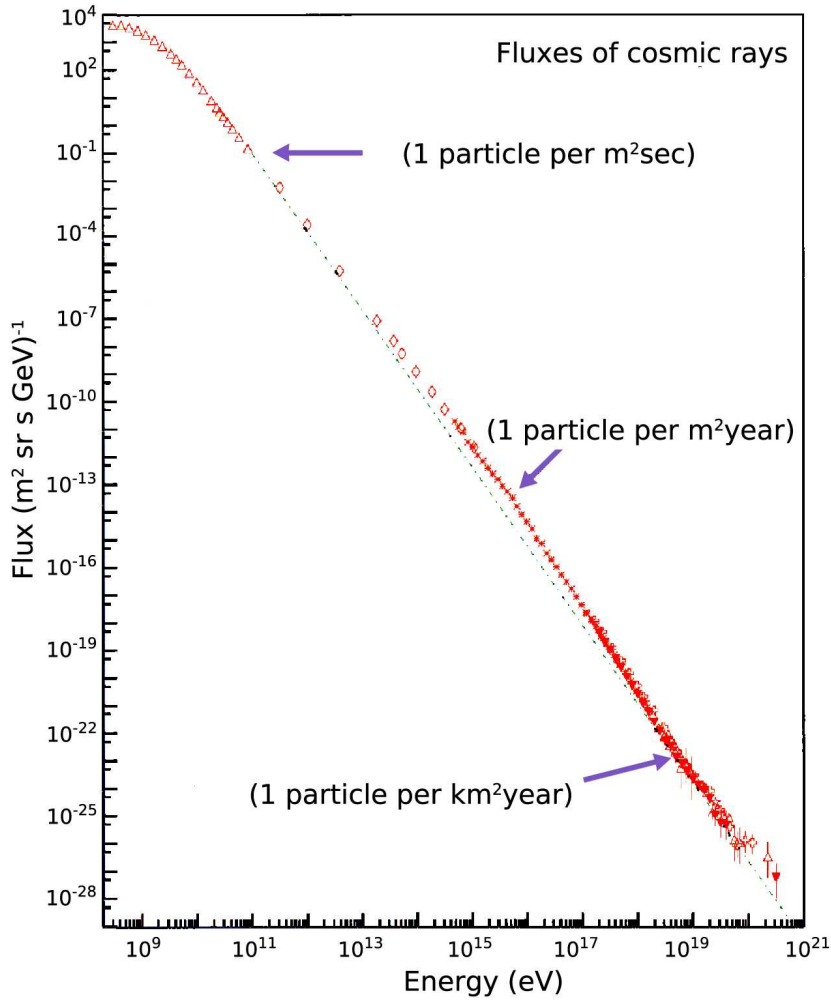


Figure 2.5: Differential flux of cosmic-rays reaching Earth.

spectral breaks can however be noticed : the presence of a knee at $E \sim$ a few 10^{15} eV where the spectrum steepens and the *ankle* located at $E \sim 10^{18}$ eV where the cosmic-ray flux flattens. The presence of cosmic-rays attaining such energies is remarkable and one ponders about what mechanisms could cause such a feature. Acceleration of protons, electrons and nuclei to high energies (bottom-top) is a well established explanation. Among the possible sources of acceleration, first order Fermi acceleration is a well known scenario capable of explaining such behaviour (see Appendix A). In our Galaxy, SNRs are known to accelerate CRs via this mechanism (Reynolds & Keohane, 1999). However, stringent conditions are required to accelerate particles up to energies above 100 TeV in SNRs. The magnetic field strength and scale have to be large enough in order to prevent the particles from escaping from the shock (Bell, 1978a). Indeed, as particles gain energy, their gyroradii grow larger and become less sensitive to small scale variation of the magnetic field. Due to their higher charge number Z resulting in a smaller gyroradius, heavier nuclei (e.g Fe) may however attain energies up to 5 PeV in a SNR.

Other mechanism of acceleration from electromagnetic forces also requires extreme conditions in order to produce ultra-high energy cosmic-rays (UHECR). Hillas (1984) commented that the magnetic field strength and the size of the acceleration site were thus the major requirements to accelerate particles to such energies. Fig. 2.6 shows the *Hillas plot* which places the different acceleration sites according to their size and magnetic field. Among with neutron stars (already mentioned in Chapter 1), extragalactic objects such as AGN jets, Galactic clusters, radio Galaxies are found to be major candidates to produce UHECRs. It has also been observed that the detection of UHECRs appeared far from the Galactic plane. As our Galactic magnetic field is too weak (\sim a few μG) to deflect potential UHECRs from the Galactic

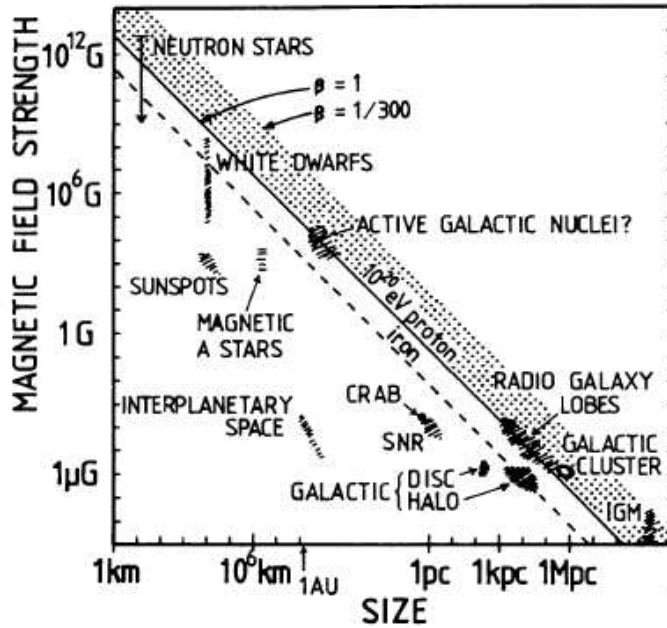


Figure 2.6: Hillas plot illustrating the potential candidates to produce ultra high energy cosmic-rays ($\sim 10^{20}$ eV). Each sources are positioned according to their surrounding magnetic field and their size. (Hillas, 1984)

Center, it is thus thought that the origin of the particles with energy above the *ankle* are of extragalactic origin.

However, after the discovery of the CMB radiations, Greisen (1966) and Zatsepin & Kuz'min (1966) (GZK) claimed that a 10^{20} eV proton coming from distant galaxies would interact with the background radiation and thus deduced that a spectral *GZK* cutoff would be expected at energies above 5×10^{19} eV. However, a 3×10^{20} eV shower has been observed from the *Fly eye's* experiment (Bird et al., 1994). Nowadays, the Pierre Auger observatory currently searches for astrophysical sources capable of generating cosmic-rays above 10^{18} eV. UHECR astronomy is indeed made possible because the very large Larmor radius of UHECR makes them relatively unaffected by the magnetic fields. An alternative possible explanation for the origin of UHECR is that they originate from the decay of massive X particles (Top-down, see Barbot & Drees 2003 and references therein) decaying into high energy neutrinos, CRs and gamma-rays.

To summarize, understanding the origin of cosmic-rays, their composition, their sources, and the various mechanisms of acceleration are the major motives to study our universe at high energies. By interacting with the surrounding ISM, CRs and high energy electrons produce gamma-ray photons (see Appendix B), which are not deflected by Galactic magnetic fields. Consequently, gamma-ray sources can also help identify various high energy sources. In the following section, I will review the various methods used to detect gamma-rays and identify gamma-ray sources.

2.2 Gamma-ray astronomy

The development of gamma-ray astronomy has opened a new window to the study of the violent universe. By providing a complementary view at high energies of the different objects already studied at other wavelengths, one can thus obtain important constraints on the energy distribution and composition

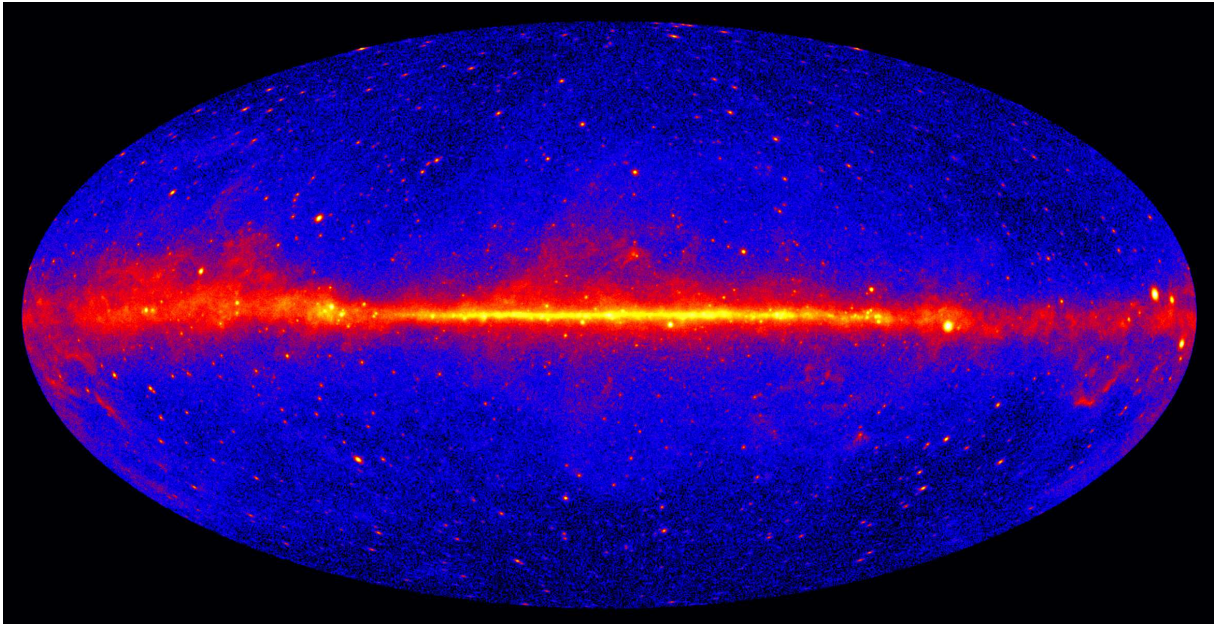


Figure 2.7: gamma-ray sky above 10 GeV seen by the Fermi-LAT telescope after 5 years of observation (Credit : NASA/DOE/Fermi LAT Collaboration).

of particles (CRs/high energy electrons) inside the astrophysical object. Also, from the combination of spaced-based gamma-ray telescopes with ground based Čerenkov observatories, it has thus become possible to map the gamma-ray universe over several decades of energy (\sim a few MeV to a few tens of TeV). In this section, I briefly review the different techniques used to detect gamma-ray sources from spaced-based and ground-based observatories.

2.2.1 Space-Based telescopes

Low energy gamma-ray primary photons (MeV range) can be directly detected by space-based telescopes. The main advantage of the gamma-ray satellites is the complete coverage of the sky at the expense of the relatively small collective area. Nonetheless, the number of detected photons (and sensitivity) gradually increases with time. SAS-2 (Fichtel et al., 1975) and COS-B (Bignami et al., 1975) experiments with respective energy ranges $E_\gamma = 20$ MeV to 16 GeV and $E_\gamma = 30$ MeV to 5 GeV were the first experiments to detect gamma-ray sources. Scintillators were used to discriminate gamma-rays from charged particles, and gas filled spark chambers were used to obtain the arrival direction and total energy of the incoming photons. Later, the launch of EGRET (Kanbach et al., 1988) with energy range $E_\gamma = 20$ MeV to 30 GeV enabled the discovery of many more gamma-ray sources, notably gamma-ray pulsars (see Caraveo 2014 and references therein) and provided a detailed map of the gamma-ray sky above 100 MeV. The significant hardware improvement used by FERMI-LAT (Atwood et al., 2009) and AGILE (Tavani et al., 2009) (notably the arrival of the silicon-stripe detector) allowed gamma-ray observations with greater sensitivity. Due to this increased sensitivity, it however becomes difficult to isolate gamma-ray sources from the diffuse gamma-ray emission produced by the ambient cosmic-rays propagating in our Galaxy. To circumvent this, the package `Galprop` (Strong & Moskalenko, 1998) has been used to model the distribution of CRs in our Galaxy and subsequently model the gamma-ray background emission. Fig. 2.7 shows the gamma-ray sky seen by FERMI-LAT after five years of observations where the Galactic plane shows strong emission.

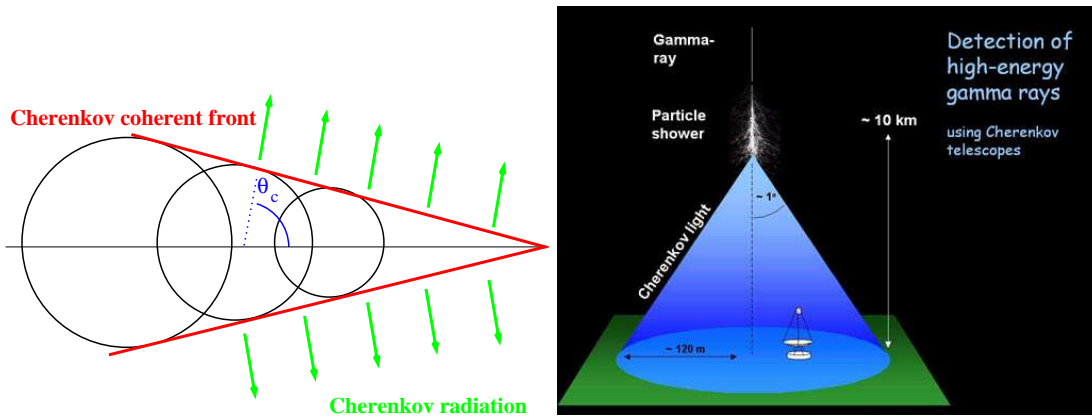


Figure 2.8: (Left panel) Illustration of the Čerenkov front (in red) from the propagation of a charged particle with speed exceeding the speed of light in the medium. The black circles indicate the spheres of propagating light generated at various epochs. θ_c represents the angle between the charged particle propagation direction and the shock front (see text). (Right panel) Diagram illustrating the cone of Čerenkov radiation generated by the extensive air showers, and consequently the effective area for the observation of the extensive air shower (Credit : HESS website).

2.2.2 Ground based gamma-ray telescopes

Predictions made by Cocconi (1960) regarding possible detections of TeV gamma-rays towards the Crab nebula have launched the idea of detecting high energy gamma-rays produced by sources of cosmic-rays. Galbraith & Jelley (1953) notably previously showed that extensive air showers could be detected from observations of intense Čerenkov radiation pulses produced by secondary particles in the cascade. Imaging Atmospheric Čerenkov Telescopes (IACTs) make use of that Čerenkov pulse to reconstruct the arrival direction and the energy of a primary particle. Alternatively, ground-based water Čerenkov detectors array (e.g HAWC Abeyssekara et al. 2013) located at high altitude can record the energy of secondary particles crossing water Čerenkov tanks to obtain useful information about the orientation of the shower and its total energy. In the following, I will first focus on the properties of the Čerenkov radiation, and the imaging techniques and analyses used by HESS to detect gamma-ray sources.

Čerenkov Emission

A charged particle travelling inside a dense dielectric medium provokes the polarisation of the surrounding molecules. After the passage of that charged particle, the surrounding polarised molecules oscillate back to their initial state and emit electromagnetic (EM) radiation. In the case where the crossing particle is slower than the speed of light in the medium $c^* = c/n$ (with n being the refractive index of the medium), the produced radiation will not be coherent. However when the particle travels faster than the speed of light in the medium $v_{\text{particle}} > c^*$, the EM radiation forms a coherent front and thus Čerenkov radiation can be observed (see Fig. 2.8). Knowing that the light propagates at a speed c/n and the particle crosses the medium at $v_{\text{particle}} = \beta c$, the angle θ_c of the Čerenkov front with respect to the particle direction is :

$$\cos(\theta_c) = \frac{1}{\beta n} \quad (2.18)$$

We note from Eq. 2.18 that, for ultra relativistic particles ($\beta \sim 1$), the Čerenkov photons (green arrows in Fig. 2.8 left panel) are propagating at an angle $\theta_c \sim \cos^{-1}(1/n)$. As the refractive index of air is quite low ($n \sim 1.0002$, dependent on altitude), the Čerenkov coherent photons are expected to be beamed around the particle. The EAS evolves and produces secondary particles which keep emitting Čerenkov radiation until

the produced secondaries eventually fall below the Čerenkov threshold energy. That threshold energy is given by the following equation :

$$E_{\text{thres}} = \frac{mc^2}{\sqrt{1 - (1/n)^2}} \quad (2.19)$$

From the evolution of the EAS, a cone of coherent Čerenkov light (see Fig. 2.8 right panel) is thus formed and propagates until it reaches the IACTs. Therefore it is possible to track the evolution of the EAS and restore information about the nature, energy and arrival direction of the primary particle. From the simulation of air showers, the expected radius of the Čerenkov cone as it reaches the ground is ~ 120 m (Patterson & Hillas, 1983). For this reason, IACTs offer an effective area five orders of magnitude larger compared to space-based gamma-ray telescopes. However, IACTs suffer from great contamination caused by hadronic air showers, which strongly dominates over gamma-ray induced air showers. We will thus summarize the various techniques used by HESS to isolate gamma-ray induced EAS and increase the sensitivity and thus detect gamma-ray sources.

H.E.S.S

The High Energy Stereoscopic System (H.E.S.S) is located in Namibia at 1800m altitude above sea level. Its moderate altitude enables the detection of lower energy gamma-rays with shallower X_{max} (see section 2.1.2) which would otherwise be undetectable at sea level. H.E.S.S consists of four 12 metre Čerenkov telescopes for a total mirror area of 108 m² positioned in a square geometry, and an extra 28 metre telescope, added in 2012, located at the centre of the geometry in order to achieve greater sensitivity at the lower energy (> 30 GeV). The great sensitivity given by the H.E.S.S and H.E.S.S II combination allows a 5σ significance detection of a gamma-ray source with a flux down to 1% of the Crab flux within 25 hours. Observations with HESS occur during moonless nights in order to reduce the night sky background noise (NSB) and to consequently increase the sensitivity to record the Čerenkov emission from the generated EAS. The basic method of observation consists of recording at the ON position (ON) and comparing it with a OFF region where no gamma-ray emission is expected to be detected. However, considering the limited amount of observation time, one instead uses the *wobble mode* where both the ON and OFF position shares the same field of view (FoV). During a 28 minute run, events will be recorded when three pixels of each camera have been triggered inside a 8×8 pixel map, and the coincidence of the triggers from each cameras has occurred within a time window of 80 ns (Aharonian et al., 2006a).

Cleaning events

Once all the runs have been recorded, the first analysis step consists of cleaning each events by removing the noise produced by the *Night Sky Background* (NSB) and isolating the Čerenkov signals. To do so, a *tail-cut* procedure is applied : each pixel with intensity above 10 photo-electrons (p.e) and surrounded by pixels with intensity above 5 p.e, or each pixel with intensity reaching 5 p.e next to a pixel with intensity above 10 p.e are accepted. Signals which do not meet these requirements are considered as noise and are removed from the image.

Obtaining important information with Hillas Parameters

Now that the various images have been cleaned, the zero, first and second moments of the image will be used to obtain the total image intensity, the center of gravity and the dispersion of the intensity distribution. From these image parameters, Hillas (1985) demonstrated that the position and size of the Čerenkov photons emitted by air showers could be parametrised by geometrical parameters that could

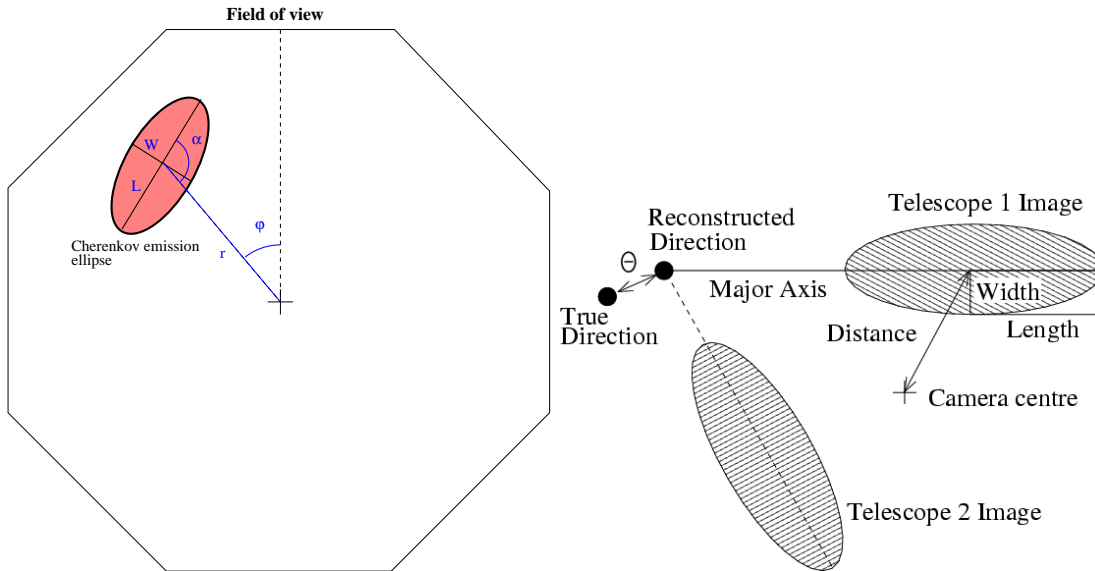


Figure 2.9: (*Left panel*) Sketch presenting the parametrisation of the Čerenkov radiation (pink ellipse) by the various Hillas parameters L , W , r , ϕ and α (see text for details) useful to determine the total energy of the primary particle and its arrival direction. (*Right panel*) Illustration of the stereoscopic reconstruction in order to constrain the arrival direction θ of the primary particle (Aharonian et al., 2006b).

provide useful information about the energy, size, and arrival direction of the air showers (I will later emphasize how this can be used to reject cosmic-ray induced air showers) As seen in Fig. 2.9, the observed Čerenkov image observed can be described by the following set of *Hillas parameters* : The Čerenkov image can first be modelled by an ellipse (see Fig. 2.9 left panel) whose length and width are obtained from the image second moments. The other parameters consist of the total amplitude of the ellipse which is given by the total number of photo-electrons detected, the angular distance between the centre of the camera and the ellipse centre (here labelled r in Fig. 2.9 left panel), the azimuthal angle ϕ and finally the angle α between the semi-major axis of the ellipse and this radial line.

The Hillas parameters parametrise the different morphological properties of the EAS observed by the IACTs, and thus provide important constraints regarding the total shower energy, its arrival direction θ and other important properties that will be used to discriminate gamma-ray from hadronic air showers. This parametrisation have in fact been used by various IACTs arrays such as Whipple (Kildea et al., 2007), HEGRA (Daum et al., 1997), VERITAS (Weekes et al., 2002) and HESS (Hinton & the HESS Collaboration, 2004). In the case of IACTs consisting of more than one telescope (e.g HESS), the arrival direction θ can be further constrained from the stereoscopic reconstruction of the air shower (see Fig. 2.9 right panel).

Cosmic-ray/Gamma-ray separation

An important task required to increase sensitivity is to reduce the number of background events caused by hadronic air showers. As discussed in Section 2.1.2 hadronic EAS has a more irregular lateral distribution compared to the more compact gamma-ray showers. Consequently, the geometrical properties defined by the Hillas parameters are found to be a rather efficient and robust methods to discriminate gamma-ray events from cosmic-ray events. Notably the width of the Čerenkov image has shown to be quite a powerful discriminant parameter. In the HESS analysis, one first compares in each camera i the width W_i of the shower with the expected width $\langle W_i \rangle$ and the distribution variance σ_i , both obtained from Monte-Carlo simulated gamma-ray events with a given zenith angle, to obtain the *Reduced Scaled Width* (RSW) :

$$\text{RSW}_i = \frac{W_i - \langle W_i \rangle}{\sigma_i} \quad (2.20)$$

Configuration	MRSL	MRSL	MRSW	MRSW	θ_{cut}^2	Image Amp	Distance
	Min	Max	Min	Max	Max (degree ²)	Min (p-e)	Max (degree)
Standard	-2.0	2.0	-2.0	0.9	0.0123	80	2.0
Hard	-2.0	2.0	-2.0	0.7	0.01	200	2.0
Loose	-2.0	2.0	-2.0	1.2	0.04	40	2.0
Extended	-2.0	2.0	-2.0	0.9	0.16	80	2.0

Table 2.1: Parameters used for selection cuts where MRSL, MRSW are the Mean reduced scaled length and width respectively, θ is the angular distance from the source, and the ‘distance’ represents the separation between the ellipse COG and the FOV center. The *Standard*, *Hard*, *Loose* and *Extended* rows are the different selection cut methods which are optimised for specific sources (Aharonian et al., 2006b).

The *Mean Reduced Scaled Width* parameter can thus be obtain via the following equation :

$$\text{MRSW} = \frac{1}{N_{\text{tel}}} \sum_{i=0}^{N_{\text{tel}}} \text{RSW}_i \quad (2.21)$$

Note that the *Mean Reduced Scaled Length* (MRSL) are also obtained from this method.

Table 2.1 illustrates the parameter cuts used to discriminate gamma-ray events from hadronic events. The aforementioned MRSL and MRSW are the shape cuts. θ_{cut} indicates the maximum angular distance between the position of the reconstructed event and the trial source position while a cut on the total Čerenkov image amplitude is also applied. Finally, a cut on the angular distance between the centre of the field of view and the centre of gravity of the ellipse helps filter out poor fits due to the Čerenkov images being on the edge of the camera.

In order to pass the selection cuts, each events must pass the conditions listed in Table 2.1. However, various types of cuts can be applied to increase the sensitivity and consequently the chance of detections for sources with distinct properties :

- *Standard cuts* best suit the detection of a gamma-ray source with similar spectral power-law index compared to the Crab nebula.
- *Hard cuts* can be applied to detect weaker sources but with harder spectra (e.g. $\Gamma = 2.0$). The tighter cut on the image amplitude considerably reduces the number of low energy events. However, it is at the expense of the minimal energy threshold observed by HESS.
- The lower threshold applied on the image amplitude for *Loose cuts* is advantageous to detect a strong source with very a steep spectrum (e.g $\Gamma = 3.0$). As opposed to the *hard-cuts*, the *Loose-cuts* improves the sensitivity of HESS at low energies at the cost of a higher number of background events.
- *extended cuts* increases the directional cut threshold θ_{cut} useful to detect gamma-ray events from extended sources (i.e. larger than the HESS point spread function).

This method using the Hillas parameters is a fast and robust method to reduce the number of non gamma-ray events. However, further progress has recently been made in the analysis which uses more parameters to discriminate gamma-ray from cosmic-rays events.

The *Paris-MVA* approach combines a 3D fit of the Čerenkov light image with a multivariate approach to further discriminate the gamma-ray events from hadronic events (Lemoine-Goumard et al., 2006). The tool for multivariate analysis package (TMVA) notably combines the various discriminant parameters into one to optimise the separation of cosmic-ray events from gamma-ray events. A set of decision trees, obtained from the same training sample, are used to quantify how likely an event to be a gamma-ray event or a hadron event (see Ohm et al. 2009).

Finally, the *model-analysis* method consists of fitting an uncleaned event with an analytical model describing the expected Cherenkov emission from an gamma-ray air shower at a given zenith angle and energy (de Naurois & Rolland, 2009). The *goodness of fit* derived is a powerful parameter to discriminate gamma-ray events from background events, but at the expense of computational time.

Modelling the Background events and obtaining the significance of detection

After the selection cuts, there are still a limited (but non zero) number of non gamma-ray events (that I hereby call background events). For instance, it is difficult to discriminate gamma-ray induced showers against high energy electron induced showers as they both only produce electromagnetic air showers. Modelling the background is the next step to obtaining an estimate of the real number of gamma-ray events towards the trial (ON) position. Most of the following methods require an OFF position where all the events are thus assumed to be background events. We mentioned that OFF observations (see Fig. 2.10 top left panel) considerably reduce the time allocated for a trial source, and one instead uses *wobble* mode to observe the ON position and define an OFF position both at the same time. In order to mitigate fluctuations of the number of background events N_{OFF} , it is common practice that the region defined as OFF must be larger than the ON position. We thus define α as the ratio between the effective areas of the ON and OFF position in order to appropriately scale down the number of background events. We can thus obtain the number of gamma-ray events by estimating the excess number of events N_{excess} obtained from the following equation :

$$N_{\text{excess}} = N_{\text{ON}} - \alpha N_{\text{OFF}} \quad (2.22)$$

where N_{ON} and N_{OFF} represent the number of events recorded (and passing the selection cuts) at the ON and OFF positions respectively. I list here three methods used to determine the background level :

- *Reflected background model* : The ON position is offset with respect to the centre of the FoV and the OFF regions are chosen equidistant to the FoV centre with respect to the ON position (see Fig. 2.10 top right panel) so that each OFF position has the same exposure time as the ON position. Assuming the chosen OFF regions have the same size as the ON regions, the exposure ratio α is thus related to the number of OFF positions chosen n_{OFF} (e.g. $\alpha = 1/7$ if $n_{\text{OFF}} = 7$). However, the more extended the source is, the fewer OFF positions can be taken.
- *Ring background model* : As per the reflected background model, the ON position is also located offset with respect to the centre of the FoV. The OFF position consists of a ring surrounding the ON position (see Fig. 2.10 bottom panels). The size of the ring is chosen so that the area ratio between the ON and OFF regions is $1/7$. In order to obtain α , a small correction factor must be added in order to account for the variation of the system acceptance function $A(r)^2$. This method is mostly suitable for small sources.
- *Template background* : Designed by Rowell (2003), the template background does not use the various cuts (see previous section) to discriminate gamma-ray showers from hadronic showers. As CR induced air showers mostly have larger MRSW values than gamma-ray induced air showers,

²Function which translates the ability of the telescope to accept event and decreases with respect to increasing radius

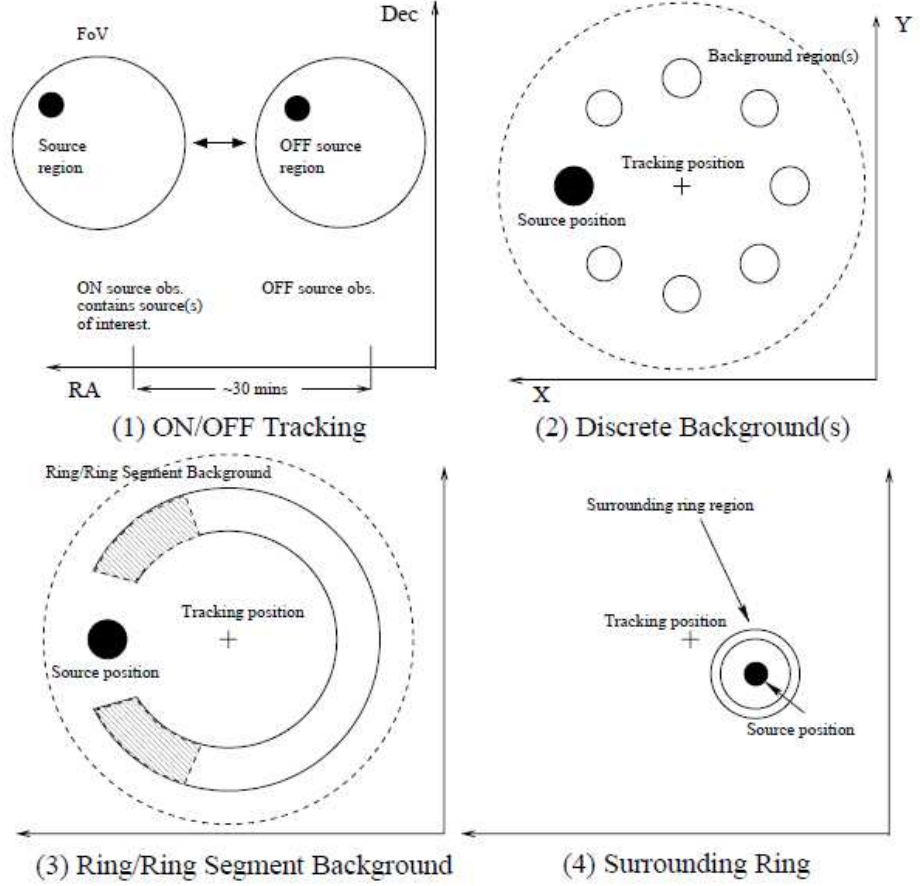


Figure 2.10: Illustration of the ON/OFF method (top left), the reflected background model (top right), and the ring (bottom left) and surrounding ring (bottom right) model in order to obtain an estimate of the number of background events that must be subtracted in order to obtain the total number of gamma-ray events in the ON region (Rowell, 2003).

events with $-2 < \text{MRSW} < \sim 0.6$ are in this case defined as signal (ON) events whereas events with $\sim 3.5 < \text{MRSW} < \sim 8.0$ are classified as background (OFF) events. Therefore, instead of a region in the FoV being used as a OFF position, the number of background events is here obtained at each position in the FoV. We obtain the normalisation factor $\alpha = P_s/P_b$ where P_s and P_b represents the total number of signal and background events obtained in the FoV. Additionally, to account for differences in the system acceptance response for gamma-ray like and CR-like events in the FoV, a 8th order polynomial is used to fit the normalised distribution of both signal $p_s(r^2)$ and background $p_b(r^2)$ as a function of the angular distance θ between the event and the FoV. This method is most suitable for morphological studies as the template background method is less restricted by the possible extension of the TeV source as N_{OFF} values are found for every pixel in the FoV.

Once the number of excess events N_{excess} is obtained, the significance a detection can be determined using the Li & Ma (1983) equation :

$$S = \sqrt{2} \left(N_{\text{ON}} \ln \left[\frac{1 + \alpha}{\alpha} \left(\frac{N_{\text{ON}}}{N_{\text{ON}} - N_{\text{OFF}}} \right) \right] + N_{\text{OFF}} \ln \left[(1 + \alpha) \left(\frac{N_{\text{OFF}}}{N_{\text{ON}} + N_{\text{OFF}}} \right) \right] \right)^{1/2} \quad (2.23)$$

Obtaining the differential flux $\Delta F/\Delta E_\gamma$

The differential photon flux $\Delta F/\Delta E_\gamma$ between energies E and $E + \Delta E$ is defined by

$$\frac{\Delta F}{\Delta E_\gamma} = \frac{N_{\text{excess}}}{A \times T \times \Delta E} \quad (2.24)$$

where N_{excess} represent the number of gamma-ray event, A is the effective area of the gamma-ray telescope, T the duration of the observation and ΔE the width of the energy bin.

In our case, the effective area A_{reco} is obtained from Monte-Carlo simulations and is dependent on the reconstructed energy of the gamma-ray event E_{reco} . In order to obtain the photon flux each ON and OFF event is thus weighted by the effective area A_{reco} . Eq. 2.24 becomes :

$$\frac{dF}{dE_\gamma} = (T\Delta E)^{-1} \left(\sum_{j=0}^{j=N_{\text{ON}}} (A_{\text{reco}_j})^{-1} - \alpha \sum_{k=0}^{k=N_{\text{OFF}}} (A_{\text{reco}_k})^{-1} \right) \quad (2.25)$$

2.2.3 VHE TeV sources

As of 2015, 77 TeV sources have been detected in the Galactic plane (Deil et al., 2015). However, only a fraction of these TeV sources have been firmly identified. In this section, I list the high energy objects which have been or could be associated various TeV sources :

- **Supernova Remnants** : Cosmic-ray are known to be confined and accelerated inside the SNR front shock during its free expansion phase (see chapter 1 for brief description). Notably, young SNRs are expected to produce CRs attaining PeV energies before they escape into the ISM (see Ptuskin & Zirakashvili 2005 and references therein). Due to large synchrotron losses electrons can only attain energies up to $\sim 50 - 100$ TeV (Reynolds & Keohane, 1999; Ohira et al., 2012). Young SNRs may produce leptonic TeV emission associated with strong non thermal X-ray emission. As SNRs are at first expected to expand in a cavity caused by the stellar winds of the progenitor star, the density of target particles is likely to be too low to produce hadronic TeV emission. However, as the SNR expansion becomes adiabatic, CRs and high energy electrons start to escape the front shock and diffuse into the ISM. While the escaping electrons will rapidly lose energy from non thermal radiation, CRs cross nearby dense molecular regions and produce hadronic TeV emission. Among the SNR shells observed at TeV energies by HESS, W28 showed spatial overlaps with molecular clouds, and could suggest hadronic emission (Aharonian et al., 2008).
- **Pulsar Wind Nebulae** : PWNe represent a major fraction of the identified TeV sources (see Fig 1.5 in Chapter 1) The relativistic electrons from the pulsar are being accelerated when they reach the termination shock. They will then produce TeV emission from the Inverse-Compton process. The mechanism of acceleration remains unclear as the conditions for efficient acceleration via 1st order Fermi acceleration do not match with the observed structure of the PWN (see Chapter 1). An important question is whether PWN accelerate protons and produce cosmic-rays.
- **X-ray binaries** : They consist of a high mass star orbiting around a dense compact object (e.g pulsar or black hole). Several binaries have been associated with TeV sources (e.g LS 5039, Aharonian et al. 2006c). The key feature of these objects is the modulation of the TeV emission depending on the orbital phase. Photon-photon absorption via e^+e^- pair production and a variation of the maximum energy attained by CRs/high energy electrons are amongst the possible cause of this variation of the TeV flux (see Bednarek & Sobczak 2014).

- Clusters : Globular clusters (GC) are thought to contain up to a few hundred milliseconds pulsars (Tavani, 1993). Leptons may be accelerated to high energies inside their magnetosphere (see chapter 1 for further detail) and/or at the shock caused by the collisions of the pulsar winds in the globular cluster (Bednarek & Sitarek, 2007). Single energetic sources embedded inside the globular cluster are also potential sources of CRs/high energy electrons. High energy electrons are then thought to produce leptonic TeV gamma-ray emission from inverse-Compton up-scattering of the Cosmic Microwave Background (CMB) fields and stellar photon fields. TeV gamma-ray emission was actually found towards the globular cluster Ter5, however with little spatial correspondence (H.E.S.S. Collaboration et al., 2011). However, Bednarek & Sobczak (2014) argued that globular clusters evolving in quite dense environments are likely to show irregular morphology and the offset peak TeV emission. Alternatively, the shock resulting from the colliding winds from massive stars are also thought to be a viable site to produce high energy particles from diffusive shock acceleration. This scenario has notably been used to explain the TeV emission towards Westerlund 2 (Aharonian et al., 2007).
- The Galactic Centre : HESS Collaboration et al. (2016) reported the detection of a PeVatron, a high energy source capable of accelerating CRs up to PeV energies, towards the Galactic Centre. The large extended morphology and the strong spatial correlation with the molecular gas suggest a hadronic origin. In fact, HESS Collaboration et al. (2016) indicated that the diffusion of CRs away from a continuous source could explain the spatial distribution of the gamma-ray emission. CRs accelerated by the super massive black-hole in its active phase is thought to provide the required energy input to provide such a gamma-ray flux.
- Dark TeV sources : These observed TeV sources represent a major part of the unidentified TeV sources. Their main feature is the lack of detections at other wavelengths. Some of these dark TeV sources are located nearby energetic pulsars and are thus thought to be older PWNe (e.g HESS J1303–631).

As a conclusion, it has become obvious that the study of the surrounding ISM and the propagation of particles (CRs/high energy electrons) can help unveil the origin of the unidentified gamma-ray sources. In the next chapters, I will thus explain the methods used in this thesis to obtain an accurate description of the ISM and how the surrounding environment can affect the distribution of CRs/high energy electrons.

Chapter 3

Tracing the interstellar medium

In the previous chapters, I highlighted that several types of high energy sources can produce very high energy (VHE) gamma-ray emission in our Galaxy. However, in the case where several high energy astrophysical objects are located nearby the TeV source, it becomes difficult to reveal which ones do actually contribute to the gamma-ray VHE emission. Additionally, one cannot obtain the distance of the VHE gamma-ray source in our Galaxy without the detections of its counterparts at various wavelengths (e.g optical, X-rays). Fortunately, one does know that the interstellar medium (ISM) surrounding high energy sources is expected to affect the morphology of the TeV emission. Notably, the ISM can help distinguish the hadronic/leptonic nature of the TeV emission as the energy distribution of cosmic-rays (CRs) is expected to differ from the energy distribution of high energy electrons inside/nearby dense molecular clouds (see Chapter 4 for further details). Consequently, an accurate description of the ISM can be vital to unveil additional information such as the origin, the nature and the distance of a TeV source.

There are several means to study the ISM. For instance, observation of continuum radiation emitted by dust grains can help determine the temperature, or highlight enhanced disruption in the ISM (e.g. star forming regions or SNR shocks). In this chapter, I however focus on the line emission emitted by atoms/molecules in an *excited* state. This method has the advantage to provide a 3D view of the ISM in our Galaxy. Particularly, line emissions produced by the various molecules can also constrain the physical properties (e.g particle density, Temperature) of dense molecular clouds, useful to model the gamma-ray emission from CRs/high energy electrons escaping high energy sources.

After a brief review of the basics of radiation theory, I explain the various techniques and approximation used in single-dish radio astronomy to obtain important information about the ISM distribution. Finally I provide a list of useful atomic/molecule transitions which can highlight key information about the studied gas (e.g. shocked clouds, presence of star forming regions).

3.1 Basic radiation theory

3.1.1 Definitions

Specific intensity I_ν and Flux F_ν

Let S be an astrophysical source with angular diameter $d\Omega_s$, located at distance ds from the telescope

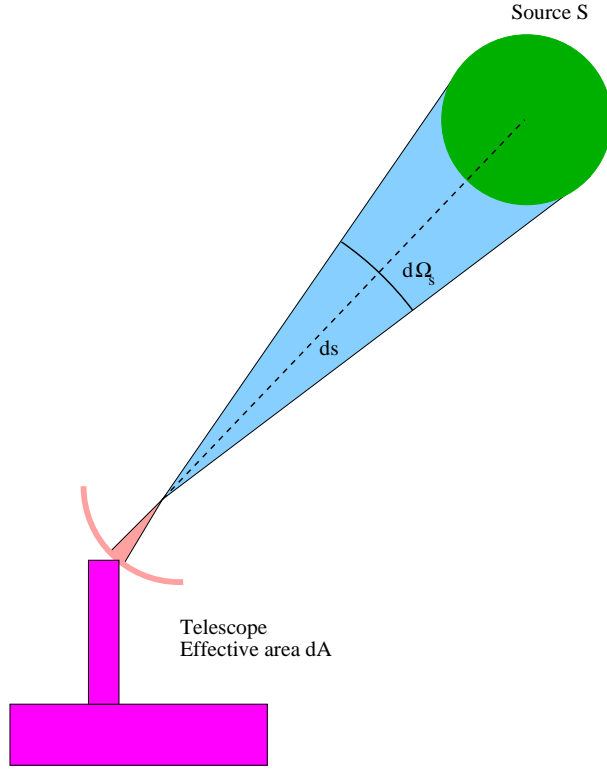


Figure 3.1: Basic illustration of the radiation produced by a source S, with angular diameter $d\Omega_s$, and located at a distance ds from our telescope with effective area dA .

(see Fig. 3.1). I also assume I use a telescope with effective are dA , that is sensitive to a specific frequency range $d\nu$. From the power dE/dt received from the source, the specific intensity I_ν is defined by the following equation :

$$I_\nu = \frac{dE}{dt dA d\nu d\Omega_s} \text{ W m}^{-2}\text{Hz}^{-1}\text{str}^{-1} \quad (3.1)$$

In other words, the specific intensity I_ν represents the power emitted by the source per unit frequency, area, and source angular size. I can also derive the expected specific flux F_ν by integrating I_ν over the entire source :

$$F_\nu = \int_{d\Omega_s} I_\nu(\Omega) d\Omega \text{ W m}^{-2}\text{Hz}^{-1} \quad (3.2)$$

The specific flux is also commonly expressed in Jansky (Jy) or in $\text{erg cm}^{-2} \text{s}^{-1} \text{Hz}^{-1}$.

If the intensity is uniform across the entire source, then Eq. 3.2 can be approximated as follow:

$$F_\nu = I_\nu \Delta\Omega_s \text{ W m}^{-2}\text{Hz}^{-1} \quad (3.3)$$

Emission and absorption coefficient

Let j_ν be the emission coefficient (in $\text{W m}^{-3} \text{Hz}^{-1}$) which indicates the power emitted at a frequency ν by an infinitesimal volume of a medium (pink cylinder in Fig. 3.2) with depth Δs . in the case of negligible absorption, the net variation of intensity dI_ν follows :

$$dI_\nu = j_\nu ds \text{ W m}^{-2}\text{Hz}^{-1}\text{str}^{-1} \quad (3.4)$$

In the absence of absorption, I note from Eq. 3.4 that the specific intensity I_ν is bound to increase linearly

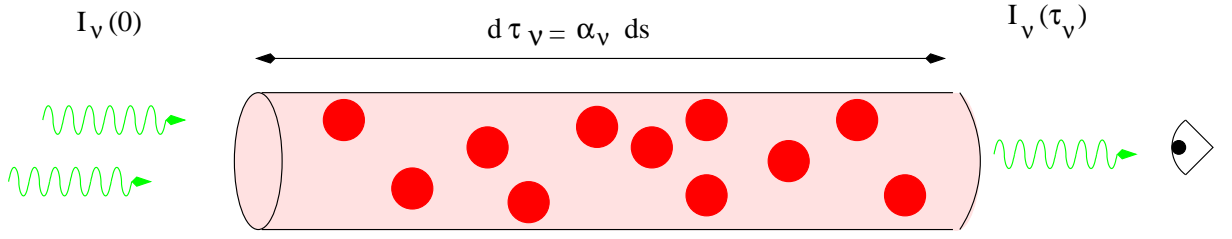


Figure 3.2: Sketch describing the effect of optical depth τ_ν due to the presence of a medium between the background (pink) source and the observer. The optical depth is dependent on the density of the medium. The red circles represent the atoms/molecules in the line of sight, ready to interact with the incoming photons.

with the depth of the medium Δs . Assuming a background source with specific intensity I_0 , I obtain :

$$I_\nu = \int_{\Delta s} j_\nu ds + I_0 \quad \text{W m}^{-2}\text{Hz}^{-1}\text{str}^{-1} \quad (3.5)$$

In a more realistic case, radiation is also expected to be absorbed by atoms/molecules in the medium (see Fig. 3.2). Let us introduce the absorption coefficient α_ν (m^{-1}) which represents the number of interactions per unit distance (inverse of the *mean free path*), dependent on the ambient particle density n and the cross section $\sigma(\nu)$:

$$\alpha_\nu = n\sigma(\nu) \quad \text{m}^{-1} \quad (3.6)$$

Over an infinitesimal distance ds , the resulting intensity loss can be expressed as follow:

$$dI_\nu = -\alpha_\nu I_\nu ds \quad (3.7)$$

Radiation transfer equation and optical depth τ_ν

It is known that particles in a medium both emit and absorb photons. Combining Eqs. 3.4 and 3.7, I thus derive the net intensity gain/loss dI_ν over a given infinitesimal distance ds .

$$\begin{aligned} \frac{dI_\nu(s)}{ds} &= j_\nu - \alpha_\nu I_\nu(s) \\ \frac{dI_\nu(s)}{\alpha_\nu ds} &= \frac{j_\nu}{\alpha_\nu} - I_\nu(s) \end{aligned} \quad (3.8)$$

I now introduce the optical depth $\tau_\nu = \int \alpha_\nu ds$, which is a measure of the opacity of the medium. For instance, a region that is optically thick ($\tau_\nu \gg 1$) will be opaque to any radiation at this frequency located behind that region. I also define the source function $S_\nu = j_\nu/\alpha_\nu$, which indicates the ratio between photons, with frequency ν , emitted and absorbed by the particles inside the medium. Eq. 3.9 thus becomes:

$$\frac{dI_\nu(\tau_\nu)}{d\tau_\nu} = S_\nu(\tau_\nu) - I_\nu(\tau_\nu) \quad (3.9)$$

Consequently, the analytical solution of this differential equation is:

$$I_\nu(\tau_\nu) = I_\nu(0) \exp(-\tau_\nu) + \exp(-\tau_\nu) \int_0^{\tau_\nu} S_\nu(\tau'_\nu) \exp(\tau'_\nu) d\tau'_\nu \quad (3.10)$$

where $I_\nu(0)$ is the observed specific intensity in the case where the medium is completely transparent (i.e. $\alpha_\nu = 0$, see Fig. 3.5). The second term indicates the contribution of the source function S_ν . In the

case where S_ν does not depend on the optical depth, Eq. 3.10 becomes :

$$\begin{aligned} I_\nu(\tau_\nu) &= I_\nu(0) \exp(-\tau_\nu) + S_\nu \exp(-\tau_\nu) \int_0^{\tau_\nu} \exp(\tau'_\nu) d\tau'_\nu \\ &= I_\nu(0) \exp(-\tau_\nu) + S_\nu \exp(-\tau_\nu) (\exp(\tau_\nu) - 1) \\ &= I_\nu(0) \exp(-\tau_\nu) + S_\nu (1 - \exp(-\tau_\nu)). \end{aligned} \quad (3.11)$$

I now study how the optical depth may affect the intensity after crossing the medium. In the case where the medium is optically thin ($\tau_\nu \ll 1$), Eq. 3.11 becomes :

$$I_\nu(\tau_\nu) = (1 - \tau_\nu) I_\nu(0) \quad (3.12)$$

Very little fraction of the intensity has been absorbed by the atoms/molecules inside the medium. The observer is consequently able to observe radiation from background sources. However, if the medium is *optically thick* ($\tau \gg 1$), Eq. 3.11 becomes :

$$I_\nu(\tau_\nu) = S_\nu(\tau_\nu) \quad (3.13)$$

The medium then becomes opaque and the observer are only able to detect photons emitted from the envelope of the medium.

3.1.2 Black body radiation

It was discovered that the intensity of the radiation emitted by an object in thermal equilibrium is mostly dependent on its temperature. For the case of a black body, idealised object capable to absorb all incoming radiation, thermal equilibrium means that the incoming intensity received must equal to the intensity produced by the black body $B_\nu(T)$, which notably follow the Planck distribution :

$$I_\nu = B_\nu(T) = \frac{2h\nu^3}{c^3} \frac{1}{\exp(h\nu/kT) - 1} \quad (3.14)$$

where h represents the Plank constant, c the speed of light and k the Boltzmann constant. As the surface of a black body absorbs all incoming radiation, the following equation must be satisfied for it to be in thermal equilibrium (see Fig. 3.3 left panel) :

$$\frac{dI_\nu}{d\tau_\nu} = S_\nu - B_\nu = 0 \quad (3.15)$$

Consequently, I obtain the *Kirchoff's law* which links the intensity of the thermal emission with the emissivity j_ν and the absorption coefficients α_ν :

$$B_\nu(T) = S_\nu = \frac{j_\nu}{\alpha_\nu} \quad (3.16)$$

A black body is a special case as it is an ideal absorber. I now study the case of a medium in thermal equilibrium (i.e. $B_\nu(T) = S_\nu$) which however does not absorb off the incoming light (see Fig. 3.3 right panel). Consequently $dI_\nu/ds \neq 0$, and Eq. 3.15 becomes :

$$\frac{dI_\nu(\tau_\nu)}{d\tau_\nu} = B_\nu(T) - I_\nu(\tau_\nu) = 0 \quad (3.17)$$

The general solution of Eq. 3.17 is :

$$I_\nu(\tau_\nu) = B_\nu(T) [1 - \exp(-\tau_\nu)] + I_0 \exp(-\tau_\nu) \quad (3.18)$$

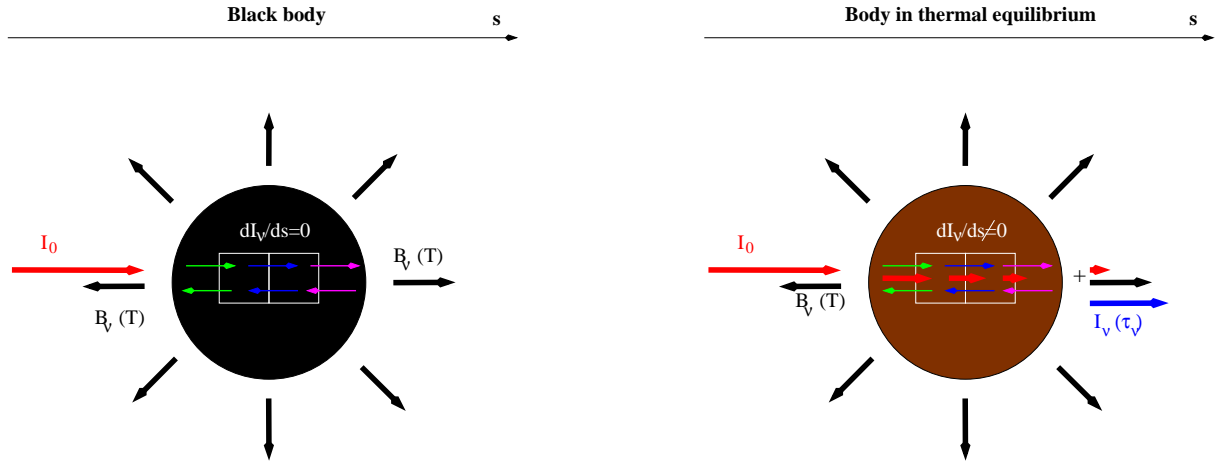


Figure 3.3: Illustration of the radiative transfer for a ideal black body (left panel) and a more transparent medium (right panel) in thermal equilibrium, both emitting black body radiation $B_\nu(T)$ shown in black. The green, purple and pink arrows represent the heat transfer between regions within the medium in thermal equilibrium, while the red arrows the evolution of a background radiation as it propagates through the medium. The resulting observed specific intensity I_ν is shown on the right hand side of each panel.

From the previous section, optically thick medium ($\tau_\nu \gg 1$) in thermal equilibrium approaches an ideal black body. In the radio band where $h\nu \ll kT$ (Rayleigh-Jeans approximation), the temperature of a black body in thermal equilibrium is given by :

$$T = \frac{c^2}{2\nu^2 k} B_\nu(T) \quad (3.19)$$

It is thus common practice to convert the observed intensity in brightness temperature T_b using :

$$T_b = \frac{c^2}{2\nu^2 k} I_\nu \quad (3.20)$$

Combining Eqs. 3.18, 3.19, and 3.20 I thus obtain :

$$T_b = T + \exp(-\tau_\nu) (T_b^0 - T) \quad (3.21)$$

where T_b^0 represents the brightness temperature in the case $\tau_\nu = 0$ (where both the background radiation and our medium contributes, see Eq. 3.5). Finally I note that the medium does not have to be strictly in thermal equilibrium for this solution to hold. A medium in local thermal equilibrium might still have net energy transfer within our medium, but the population might still have net energy transfer, but the population of atoms/molecules inside this medium still follows the Boltzmann distribution (which depends on T), and the radiation should still follow the Kirchoff relation (see Eq. 3.16). Although many astrophysical object are not black bodies, they are assigned a brightness temperature T_b which would indicate the expected temperature to produce such intensity I_ν if the system were to be a black body.

3.2 Line emission

It is learnt from quantum mechanics that atoms and molecules can be found in discrete energy states. Atoms/molecules emit photons by transitioning from an energy state j to a lower energy state k . The frequency of the photon radiated equals :

$$\nu_{jk} = \frac{E_j - E_k}{h} \quad (3.22)$$

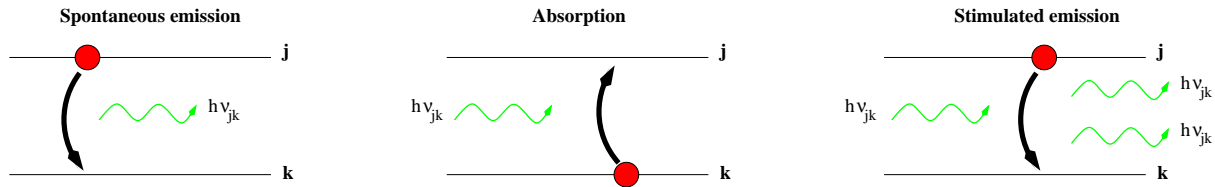


Figure 3.4: Illustration of the various mechanisms associated with radiation, resulting in the atom/molecule to change energy state (see 3.2.1).

where h is the Planck constant. A photon can also be absorbed by an atom/molecule provided the photon energy in the rest frame of this atom/molecule equals the difference in energy between the current energy state k and a higher energy state j . These radiations occurring at discrete frequencies are called line emission. Detection of such emission helps to obtain information about the distribution of the population of atoms/molecules among the various energy states. In the following section, I will explain the various radiation mechanisms which affect population of atoms/molecules at all energy states and thus the resulting intensity produced at a given frequency ν .

3.2.1 Einstein coefficients

I list here the various mechanisms related to line emission occurring in the ISM, which can change the population of atom/molecules in a given energy state. The Einstein coefficients define the rate to which these mechanisms occur :

- Spontaneous emission: One photon is spontaneously radiated from the atom/molecule (see Fig. 3.4 left panel). The rate of spontaneous transition of an atom/molecule from energy state j to energy state k is given by the Einstein coefficient A_{jk} (s^{-1}) and is proportional to the dipole moment of a molecular transition μ_{jk} ($A_{jk} \propto |\mu_{jk}|^2$).
- Absorption: the atom/molecule absorbs a photon and transition to a higher energy state (see Fig. 3.4 right panel). This process is dependent on the specific intensity I_ν and the Einstein coefficient B_{kj} .
- Stimulated emission or negative absorption: If an atom/molecule at energy state k could absorb a photon of frequency ν_{jk} and reach energy state j , an atom/molecule at energy state j can also interact with a photon of frequency ν_{jk} and transition to the lower energy state k . It will thus emit another photon with the same frequency (see Fig. 3.4 middle panel). The resulting stimulated emission depends on the specific intensity I_ν of the radiation and the Einstein coefficient B_{jk} ($\text{W}^{-1} \text{cm}^2 \text{sr Hz s}^{-1}$).

3.2.2 Relation between Einstein coefficients under Local Thermal Equilibrium assumption

As mentioned in Section 3.1.2, local thermal equilibrium (LTE) is achieved when the density of atoms/molecules over a state i , with energy E_i , follows the *Boltzmann* distribution :

$$n_i = g_i \exp\left(-\frac{E_i}{kT}\right) \quad (3.23)$$

where g_i denotes the degeneracy of the state i (e.g. from symmetry). For the sake of simplicity, I now assume an hypothetical atom/molecule with only two energy states E_1 and E_2 . The ratio between the densities n_1 and n_2 is defined by the following equation :

$$\frac{n_2}{n_1} = \frac{g_2}{g_1} \exp\left(-\frac{(E_2 - E_1)}{kT_X}\right) \quad (3.24)$$

where T_X is defined as the excitation temperature of the transition. In the absence of collisions, atoms in the state 1 can only transition to the energy state 2 by absorbing a photon of energy $h\nu_{21}$. Atoms in the state 2 can however transition to the energy state 1 by spontaneous and stimulated emission. The atoms is therefore in LTE if the number of atoms/molecules entering the state 2 equals the number of atoms/molecules leaving the state 2. The emitted and absorbed radiation then follow the following equation:

$$n_2 A_{21} + n_2 B_{21} B_\nu(T) = n_1 B_{12} B_\nu(T) \quad (3.25)$$

Combining Eq. 3.24 and Eq. 3.25 and using Rayleigh-Jeans approximation, I obtain:

$$\frac{2\nu^2}{c^2} kT = \frac{A_{21}/B_{21}}{[B_{12}g_1/B_{21}g_2] \exp(h\nu/kT_X) - 1} \quad (3.26)$$

If the system is in LTE ($T_X = T$), I thus obtain the following relations between the Einstein's coefficients :

$$A_{21} = B_{21} \frac{2h\nu^3}{c^2} \quad (3.27)$$

$$g_2 B_{21} = g_1 B_{12} \quad (3.28)$$

In reality, an atom/molecule owns multiple energy states, defined by various quantum numbers such as the angular momentum \mathbf{J} , consisting of the orbital momentum number \mathbf{L} and the various spins states of electrons and atoms \mathbf{S} (see Fig. 3.5). For the case of rigid linear molecules (e.g. Carbon monoxide CO), the photon, with spin $s = 1$, can only change the total angular momentum can only change by $\Delta J = \pm 1$, based on the conservation of angular momentum. Consequently, a two level state approximation definitely hold for such molecules.

3.2.3 Critical Density

As mentioned in section 3.2, collisions also contribute to the change of energy state inside an atom/molecule. In our two-level system, let C_{12} and C_{21} represent the collision rates, which bring a particle to transition from state 1 to state 2 and vice-versa. The collision rates follow the relation:

$$C_{21} = \langle \sigma v_2 \rangle \quad (3.29)$$

$$C_{12} = \langle \sigma v_1 \rangle \quad (3.30)$$

where σ is the collision cross section and v_1, v_2 indicate the velocity of atoms/molecules within the energy state E_1 and E_2 respectively. In the absence of background radiations, Eq. 3.25 becomes:

$$n_2 n C_{21} + n_2 A_{21} = n_1 n C_{12} \quad (3.31)$$

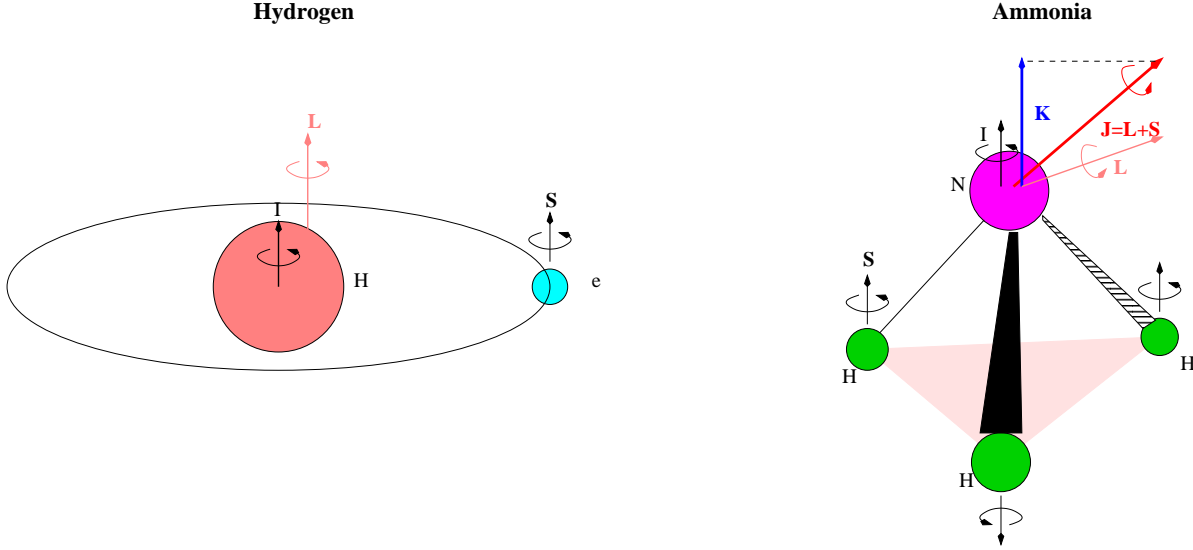


Figure 3.5: Illustration of the various angular momentum used to describe the various angular states of an atom/molecule using the hydrogen atom (*left panel*) and ammonia molecule (*right panel*). \mathbf{L} represents the orbital angular momentum of the atom/molecule, \mathbf{S} indicates the spin of an electron or atom, $\mathbf{J} = \mathbf{L} + \mathbf{S}$ denotes the total angular momentum. Finally, for the case of the ammonia, \mathbf{I} indicates the spin of the ammonia atom, located on the axis of the electric dipole moment (see text).

with n being the density of the target atom/molecule (e.g. H_2 in molecular clouds). In the case where collisions are dominant compared to the other types of interaction, then:

$$\frac{n_2}{n_1} = \frac{C_{12}}{C_{21}} \quad (3.32)$$

$$\frac{C_{12}}{C_{21}} = \frac{g_2}{g_1} \exp\left(-\frac{h\nu_{21}}{kT}\right) \quad (3.33)$$

However, I prove now that the conditions for the atoms/molecules distribution to become thermalised can be useful in providing constraints on the studied cloud. Combining Eqs. 3.31 and 3.33, I obtain :

$$\frac{n_2}{n_1} = \frac{C_{12}}{C_{21}} \frac{1}{1 + A_{21}/C_{21}n} \quad (3.34)$$

I now define the critical density such that $n_c = A_{21}/C_{21}$. Eq. 3.34 becomes :

$$\frac{n_2}{n_1} = \frac{1}{1 + n_c/n} \frac{g_2}{g_1} \exp\left(-\frac{h\nu_{21}}{kT}\right) \quad (3.35)$$

In the case where $n \ll n_c$, the spontaneous emission is dominant and the population is sub thermal. It is then unlikely to observe an emission line (in the absence of background radiation) in this scenario. In the case where $n \gg n_c$, the population of atoms/molecules becomes thermalised and the chances of detecting this transition are consequently maximised. Therefore, the critical density offers an estimate of the density required to detect such transitions. As the gas is thermalised, $v \propto \sqrt{T}$ and the critical density thus decreases with increasing temperature.

As mentioned earlier, molecules and atoms have multiple energy states. When collisions are included, the radiation equation in LTE becomes quite complex, and the critical density n_c for the $2 \rightarrow 1$ transition is then defined as :

$$n_c = \frac{A_{21}}{C_{21} + \sum_{i>2} C_{i2} g_i / g_2 \exp\left(-\frac{h\nu_{2i}}{kT}\right)} \quad (3.36)$$

Molecule	upper state j	lower state j	A_{jk} [s ⁻¹]	n_c [cm ⁻³]
CO	$J = 1$	$J = 0$	7.2×10^{-8}	5.0×10^2
¹³ CO	$J = 1$	$J = 0$	6.3×10^{-8}	5.0×10^2
CS	$J = 1$	$J = 0$	1.7×10^{-6}	2.0×10^4
NH ₃ *	$J, K = 1, 1$	$J, K = 1, 1$	1.0×10^{-7}	1.0×10^3

*Inversion transition of NH₃ (see Section 3.4.8).

Table 3.1: Einstein coefficients A_{jk} and resulting critical density n_c for the molecular transitions CO(1–0), ¹³CO(1–0), CS and NH₃.

Table 3.1 shows the Einstein coefficient A_{ij} and the critical density n_c obtained for useful molecular transitions. Notably, I remark that the critical density of CO and its isotopologues ¹³CO($J=1-0$) are quite low ($n_c \sim 5 \times 10^2 \text{ cm}^{-3}$, which thus allows the detection of diffuse molecular gas, while the higher critical density of CS($J=1-0$) enables the detection of embedded dense clumps. For linear molecules such as CO and CS, the dipole moments and the Einstein coefficient A_{jk} increases higher energy states. Consequently, higher critical density are expected for higher transitions.

3.3 Tracing the ISM with Mopra and Nanten2

In this thesis, most of our ISM observations come from the Mopra and Nanten2 telescopes. Mopra is a 22 metre diameter radio dish, located at Coonabarabran in NSW, Australia. This radio telescope can notably switch receivers and perform observations in the 12mm (22 – 24GHz), 7mm (42 – 48 GHz) and 3mm (90 – 110 GHz) with a beam full with half maximum (FWHM) $\theta_{12\text{mm}} \sim 2'$, $\theta_{7\text{mm}} \sim 1'$ and $\theta_{3\text{mm}} \sim 0.5'$ respectively. As shown in Table 3.2, the various transitions available allow to highlight diffuse and dense molecular gas, star forming regions, post-shocked gas (which will be discussed in section 3.4.8). The digital spectrometer MOPS can simultaneously observe up to 16 frequency ranges (Zoom mode), each consisting of a 137.5 MHz bandwidth divided into 4096 channels. Mopra can perform *on the fly* mapping where a region of the sky (*ON* position) is Nyquist sampled with respect to the aforementioned beam FWHM, and compared to a reference (*OFF*) position to obtain the antenna temperature T_A^* , which represents the power of the signal received expressed in terms of brightness temperature (see next section). Alternatively, deep *ON/OFF* observations can also be performed to considerably increase the exposure at a specific location and detect weaker sources.

To reduce the OTF data, I first use `Livedata`¹ to compare our *ON* spectral observations with the reference position *OFF* in order to obtain T_A^* . A linear fit is then used to remove the baseline from the spectra. I then use `Gridzilla`² to obtain a map illustrating the evolution of T_A^* as a function of position and line of sight velocity v_{lsr} in the local standard rest frame (lsr), obtained from the relative Doppler shift in frequency $v_{\text{lsr}} = c(\nu_0 - \nu)/\nu_0$.

I also make use of the Nanten2, a radio telescope located at the Atacama desert in Chile. The telescope was at first only equipped with low frequency receivers at 110 GHz and 220 GHz useful to detect CO(1–0) and CO(2–1) tracers. It notably carried out the under sampled Nanten CO(1–0) survey of the Galactic plane with a beam FWHM of 2.6' and a sampling grid of 4' (Mizuno & Fukui, 2004). Recent upgrades on the telescopes allow observations at frequencies in the 460-490 GHz and 809-880 GHz frequency ranges, which not only hosts higher CO (CO(4–3) and CO(7–6)) but also atomic carbon CI, which enable the study of the ‘dark gas’ (i.e not detected by the CO(1–0) or HI tracer, see Burton et al. 2015) .

¹<http://www.atnf.csiro.au/computing/software/livedata/>

²<http://www.atnf.csiro.au/computing/software/Gridzilla/>

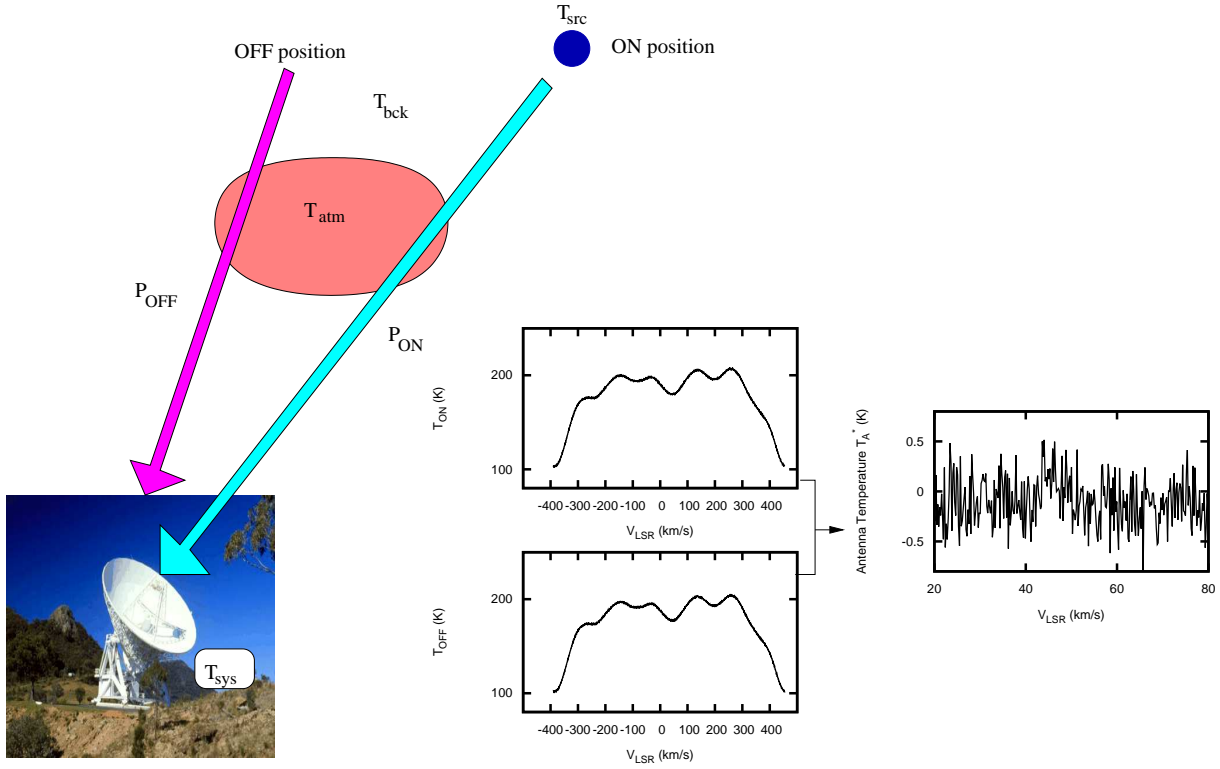


Figure 3.6: Sketch showing the ON and OFF position observation. it is shown that the extraterrestrial signal will be affected by the atmosphere with temperature T_{atm} and the system temperature of the telescope T_{sys} . The plot on the right hand side represents the temperature observed across the kinematic velocity in the local standard rest frame v_{LSR} during the ON and OFF position, and the resulting antenna temperature T_A^* derived from Eq. 3.41.

In the following section, I will explain the basics of single dish radio spectroscopy, and what useful information can be obtained. I will also provide a list of useful tracers observed by Mopra and Nanten which can help understand the structure and dynamics of molecular clouds.

3.3.1 Acquiring the antenna temperature T_A^* and source temperature T_{src}

Single dish radio telescopes such as Mopra record the antenna temperature T_A^* from a given region in the sky. During the *ON* observations (see Fig 3.6), the radio-telescope detects the antenna temperature T_A^* within the beam combined background radiation T_{bck} (usually the cosmic microwave background). This emission is attenuated due to the absorption of photons by the particles in the atmosphere with brightness temperature T_{atm} . Finally, the electronics with brightness temperature T_{rx} also contributes to the total power received by the dish. During the *OFF* observations, one does not expect any signal to be observed (i.e. $T_A^* = 0$). If P_{ON} and P_{OFF} represent the power received by the telescope during the *ON* and *OFF* positions respectively, I obtain the following equations :

$$P_{\text{ON}} = C (T_A^* \exp(-\tau_\nu) + T_{\text{bck}} \exp(-\tau_\nu) + T_{\text{atm}} (1 - \exp(-\tau_\nu)) + T_{\text{rx}}) \quad (3.37)$$

$$P_{\text{OFF}} = C (T_{\text{bck}} \exp(-\tau_\nu) + T_{\text{atm}} (1 - \exp(-\tau_\nu)) + T_{\text{rx}}) \quad (3.38)$$

where C is a constant converting the brightness temperature in power received. From the subtraction of Eq. 3.37 with Eq. 3.38, I obtain

$$T_A^* = \frac{P_{\text{ON}} - P_{\text{OFF}}}{C} \exp(\tau_\nu) \quad (3.39)$$

I now define T_{sys} represent the system temperature during our observation

$$T_{\text{sys}} = P_{\text{OFF}} \frac{\exp(\tau_\nu)}{C} \quad (3.40)$$

The system temperature reflects the noise caused by the electronics and the conditions of observations. For instance high precipitable water vapour (PWV) and low elevations are likely to increase the system temperature. Combining Eq 3.39 and Eq 3.40, The antenna temperature T_A^* is estimated via :

$$T_A^* = \frac{P_{\text{ON}} - P_{\text{OFF}}}{P_{\text{OFF}}} T_{\text{sys}} \quad \text{K} \quad (3.41)$$

The radio telescope may consist of a main beam and several side lobes and only a fraction η_{mb} of the total power received by the radio telescope is in fact transferred to the main beam. Consequently, in the case where the source angular diameter is less or comparable to the beam size, one needs to account for this main beam coefficient η_{mb} to obtain the true antenna temperature :

$$T_A^{*'} = \frac{T_A^*}{\eta_{\text{mb}}} \quad (3.42)$$

However, in the case, where the source angular diameter θ_s is much greater than the antenna beam diameter θ_{FWHM} , the side lobes will also receive a portion of the power emitted by the source. In this case, one must instead use the *extra beam* coefficient η_{xb} and obtain the true antenna temperature T_A^* via the following equation :

$$T_A^{*'} = \frac{T_A^*}{\eta_{\text{xb}}} \quad (3.43)$$

Now that I have the correct antenna temperature, I demonstrate how I recover the brightness temperature of the source. I first define gain pattern of the main beam $P(\theta, \phi)$, which depends on the azimuth ϕ and elevation θ . Let $A_e = c^2 / \Delta\Omega_A \nu^2$ be the effective area of the telescope which depends on the frequency ν and the effective beam area $\Delta\Omega_A = \int P(\theta, \phi) d\Omega$ of the radio telescope. The antenna temperature $T_A^{*'}$ obtained from a source emitting black body radiation $B_\nu(T)$ follows this equation :

$$T_A^{*' } = \frac{A_e(\nu)}{2k} \int B_\nu(T) P(\theta, \phi) d\Omega \quad (3.44)$$

It is common practice to assume the source intensity to be uniform. If the angular area of the source $\Delta\Omega_s$ is relatively small compared to the angular area of the beam $\Delta\Omega_A$, then :

$$T_A^* = \frac{c^2}{2\nu^2 k} B_\nu \left(\frac{\Delta\Omega_s}{\Delta\Omega_a} \right) \quad (3.45)$$

Combining Eq.3.21 and Eq.3.45, I obtain the brightness temperature of the source T_{src} :

$$T_{\text{src}} = T_A^* \frac{\Delta\Omega_a}{\Delta\Omega_s} \quad (3.46)$$

Therefore, both the antenna temperature and the source angular area is needed to recover the brightness temperature. I also note that, in the case where $\Delta\Omega_s \ll \Delta\Omega_a$, the observed antenna temperature are much smaller than its true brightness temperature. Consequently, telescopes with large beam size are less sensitive to small clumps and cores. If I approximate the main beam pattern as a Gaussian, then the beam size of the antenna can be described as follow:

$$\Delta\Omega_a = \int_{\phi=0}^{\phi=2\pi} \int_{\theta=0}^{\infty} \exp\left(-\frac{4\theta^2}{\theta_{\text{FWHM}}^2} \ln 2\right) \theta d\theta d\phi \quad (3.47)$$

$$\Delta\Omega_a = \frac{\pi \theta_{\text{FWHM}}^2}{4 \ln 2} \quad (3.48)$$

The source can be described as a disk with angular area $\Delta\Omega_s = \pi\theta_s^2/4$, with θ_s representing the angular diameter of the source. I then define the beam dilution factor f as the ratio between $\Delta\Omega_a$ and $\Delta\Omega_s$:

$$f = \frac{\Delta\Omega_a}{\Delta\Omega_s} = \frac{\theta_{\text{FWHM}}^2}{\theta_s^2 \ln 2} \quad (3.49)$$

The beam dilution factor f is therefore needed to convert the antenna temperature to the brightness temperature of a *point-like* source. However, in the case where $\Delta\Omega_s$ is not negligible compared to $\Delta\Omega_a$, the gain pattern distribution across the beam has to be accounted for³. Eq. 3.46 thus becomes :

$$T_A^* = T_{\text{src}} \frac{1}{\Delta\Omega_a} \int_{\phi=0}^{\phi=2\pi} \int_{\theta=0}^{\theta_s} \exp\left(-\frac{4\theta^2}{\theta_{\text{FWHM}}^2} \ln 2\right) \theta d\theta d\phi \quad (3.50)$$

If I combine Eqs. 3.48 and 3.50, I obtain a more general solution linking $T_A^{*'}$ and T_{src} :

$$T_A^{*'} = T_{\text{src}} \frac{4 \ln 2}{\pi \theta_{\text{FWHM}}^2} \times \frac{\pi \theta_{\text{FWHM}}^2}{4 \ln 2} \left(1 - \exp\left(-\frac{\theta_s^2}{\theta_{\text{FWHM}}^2} \ln 2\right)\right) \quad (3.51)$$

$$T_A^{*'} = T_{\text{src}} \left(1 - \exp\left(-\frac{\theta_s^2}{\theta_{\text{FWHM}}^2} \ln 2\right)\right) \quad (3.52)$$

In the limiting case $\theta_s \rightarrow 0$ I retrieve the solution from Eq. 3.49. I now define the correction factor K as follow :

$$K = \frac{f^{-1}}{(1 - \exp(-f^{-1}))} \quad (3.53)$$

Consequently, in the more general case, I obtain the source temperature T_{src} from the antenna temperature $T_A^{*'}$ by applying the correction factors f and K :

$$T_{\text{src}} = T_A^{*'} f K \quad (3.54)$$

Values of the correction factors f and K have been published by Ladd et al. (2005) (3mm Mopra observations) and Urquhart et al. (2010) (7mm and 12 mm Mopra observations).

3.4 Physical parameters derived from the source temperature

T_{src}

From the various line emission detections, I now list various methods used to constrain physical parameters such as the H_2 column density N_{H_2} , the optical depth τ_ν , the kinetic temperature of the gas T , the mass and density of the molecular cloud.

3.4.1 Column density

From LTE assumption

If I assume negligible background radiation and that the molecular cloud is in LTE, I obtain from Eq. 3.18 the following relation:

$$T_{\text{src}} = B_\nu(T) (1 - \exp(-\tau_\nu)) \quad (3.55)$$

$$T_{\text{src}} = \frac{h\nu}{k} \frac{1}{\exp\left(\frac{h\nu}{kT}\right) - 1} (1 - \exp(-\tau_\nu)) \frac{\tau_\nu}{\tau_\nu} \quad (3.56)$$

³which is mostly relevant for deep ON/OFF observation

It is possible, in this case, to link the optical depth of a transition τ_ν with the various Einstein's coefficients. First, I remind that the emissivity of a line emission j_ν is defined by the power emitted by an infinitesimal volume of the cloud per steradians. However, some of the spontaneous emission (characterized by the Einstein coefficient A_{jk}) are Doppler shifted due to the thermal motions of the population of atoms/molecules producing these radiation. I thus also define a normalised line shape function $\phi(\nu)$ which indicates the emitted radiation as a function of frequency. j_ν is then described by the following equation :

$$j_\nu = \frac{h\nu_{jk}}{4\pi} n_j A_{jk} \phi(\nu) \quad (3.57)$$

By using the Einstein relation given in Eq. 3.27 and Eq. 3.28, and the kirchoff's law, I then derive the absorption coefficients α_ν :

$$\alpha(\nu) = \frac{h\nu_{jk}}{4\pi} B_{jk} n_j \left(\exp\left(\frac{h\nu}{kT}\right) - 1 \right) \phi(\nu) \quad (3.58)$$

I now define the column density of the upper state j $N_j = \int n_j ds$. By integrating Eq. 3.58 along the line of sight s , I finally obtain the link between optical depth and column density :

$$\tau_\nu = \frac{h\nu_{jk}}{4\pi} B_{jk} N_j \left(\exp\left(\frac{h\nu}{kT}\right) - 1 \right) \phi(\nu) \quad (3.59)$$

By combining Eq. 3.56 and Eq. 3.59 I obtain the relationship between the observed source temperature T_{src} and the column density of the upper state N_j :

$$T_{\text{src}} = \frac{h\nu}{k} \frac{(1 - \exp(-\tau_\nu))}{\tau_\nu} \frac{h\nu_{ud}}{4\pi} B_{ud} N_u \phi(\nu) \quad (3.60)$$

$$T_{\text{src}} = \frac{h\nu_{ud} c^2 N_u}{8\pi k \nu_{jk}^2} A_{ud} \frac{(1 - \exp(-\tau_\nu))}{\tau_\nu} \phi(\nu) \quad (3.61)$$

$$(3.62)$$

By assuming an averaged optical depth over the line emission $\langle \tau \rangle$ (or assuming the optical depth to be constant over the frequency range of the line emission), I link the integrated intensity of the line emission with the column density of the upper state via the following equation :

$$\int_{-\infty}^{\infty} T_{\text{src}} d\nu = \frac{h\nu_{jk} c^2 N_j}{8\pi k \nu_{jk}^2} A_{jk} \frac{(1 - \exp(-\langle \tau \rangle))}{\langle \tau \rangle} \quad (3.63)$$

The source temperature of the spectra is often shown in unit of line of sight velocity v_{lsr} , which follows the relation $dv_{\text{lsr}}/c = d\nu/\nu_{ud}$. As a consequence, Eq. 3.63 becomes :

$$N_u = \frac{8\pi k \nu_{ud}^2}{hc^3 A_{ud}} \frac{\langle \tau \rangle}{(1 - \exp(-\langle \tau \rangle))} \int_{-\infty}^{\infty} T_{\text{src}} dv \quad (3.64)$$

Provided e kinetic temperature of the molecular cloud is known (see later sections for discussions on how to obtain the temperature of the molecular cloud) and assuming the cloud is optically thin at this frequency $\tau_\nu = 0$, the column density of the molecule N_{mol} is derived from the integrated intensity of the line emission and using the Boltzmann distribution :

$$N_{\text{mol}} = N_j g_j \sum_{i=0}^{i=\infty} \frac{g_i}{g_j} \exp\left(-\frac{(E_i - E_j)}{kT}\right) \quad (3.65)$$

It is finally possible to obtain the column density N_{H_2} by using the abundance ratio $\chi_{\text{mol}} = [\text{mol}] / [\text{H}_2]$ between the molecule and H_2 . A list of abundance ratios of various molecules used in our ISM study of our Galaxy can be found from Irvine et al. (1987) which studied molecular line emission towards several

regions (e.g. Orion nebula). As will be discussed later, the abundance ratio may differ significantly from one region to another. The abundance ratio is thus generally the main source of uncertainties in our H_2 column density estimates.

Consequently, by assuming an optically thin scenario, I was able to obtain the total column density from the integrated intensity of the line emission. However, in several cases, the cloud may be optically thick at these frequencies. One will see in section 3.4.2 a method to independently derive the optical depth.

From a conversion factor X

Estimates of the H_2 column density can be derived using a conversion factor linking the conversion factor linking the integrated intensity if the transition to N_{H_2} . X factors are generally obtained from various methods, for instance by comparing line emission of a wide range of clouds with the IR emission (e.g Leroy et al. 2011). The transitions where a conversion factor is commonly used are CO(1-0) and HI 21cm radiation (see Sections 3.4.8 and 3.5). X_{CO} is generally assumed to be fairly constant although its value may actually evolve as a function of the galactocentric radius (Strong et al., 2004).

3.4.2 Optical depth

If I assume two thermal line emission B_{ν_1} and B_{ν_2} with similar rest frequencies and negligible background radiation, I obtain from Eq. 3.55 :

$$T_{A_1}^* = B_{\nu_1}(T)(1 - \exp(-\tau_{\nu_1})) \quad (3.66)$$

$$T_{A_2}^* = B_{\nu_2}(T)(1 - \exp(-\tau_{\nu_2})) \quad (3.67)$$

If the the two studied frequencies are relatively close to one another, I have $B_{\nu_1} \sim B_{\nu_2}$ and it is therefore possible to derive the optical depth of a given transition by numerically solving the following equation :

$$\frac{T_{A_1}^*}{T_{A_2}^*} = \frac{1 - \exp(-\tau_{\nu_1})}{1 - \exp(-\tau_{\nu_2})} \quad (3.68)$$

I now define the ratio $R\tau_{\nu_2}/\tau_{\nu_1}$. R represents the expected ratio of line strength between the two transitions. R can either be two hyperfine transitions (NH_3 , see Section 3.4.8) or the abundance ratio between the two isotopologues (e.g CS, C^{34}S , see Section 3.4.8). It should also be noted that the structure of a molecular cloud can be further understood from the evolution of the optical depth across the velocity space. For instance, the cold dense gas in the center of the molecular cloud may show greater optical depth effects compared to the diffuse gas located at the edge. This may result in an apparent broadening of the line emission or, in some cases, self-absorption features.

3.4.3 Temperature

To estimate the kinematic temperature T of the molecular gas, two transitions of the same molecule must be detected. From the LTE approximation, I assume that the kinetic temperature equals the excitation temperature T_X which can be derived from the column density ratio between two energy states j and k :

$$T_X = \frac{h\nu_{jk}}{\ln\left(\frac{g_j N_k}{g_k N_j}\right)} \quad (3.69)$$

It should be noted that for rotational transition, T_X is referred as the rotational temperature T_{rot} while for spin state transition (e.g HI 21cm radiation), T_X is then defined as the spin temperature T_s . In the case where $h\nu_{jk}/k$ is quite small, it then requires a small temperature to achieve $n_j/n_k \sim g_j/g_k$. As a result, the excitation temperature obtained from the column density ratio may not be accurate. From Section 3.2.3, the H_2 density n_{H_2} must exceed the critical density for the two energy states to reach LTE. If the population ratio is however sub-thermal, one is required to use the radiative transfer equation Eq. 3.31 and use the following equation to obtain T :

$$T = \frac{T_X}{1 - kT_X/\Delta E [\ln(1 + f(T))]} \quad (3.70)$$

where $f(T)$ is an empirical function obtained from gas studies (e.g Tafalla et al. 2004).

Finally, in the case where more than two transitions of the same molecule are detected, it is possible to test whether the system is in LTE and obtain the kinematic temperature T by plotting $\ln(N_i/g_i)$ as a function of the energy state E_i . The system is in LTE if it can be fitted by the linear fit :

$$\ln\left(\frac{N_i}{g_i}\right) = -\frac{E}{kT} \quad (3.71)$$

The slope of this linear fit is then directly associated with the kinematic temperature T .

3.4.4 Distance of the molecular cloud

In order to obtain the physical size of a molecular cloud, one must, at first, obtain its distance. One important information obtained from a line emission detection is the radial velocity of the molecular cloud v_{lsr} (in the local solar rest reference). Brand & Blitz (1993) used HII regions to determine the velocity field in our Galaxy. From the position of the molecular transition in the v_{lsr} velocity space, I can use Brand & Blitz (1993) to estimate the distance. However the model usually predicts two solutions labeled the *near* and *far* distances. This degeneracy leads, in some case, to large uncertainties about the distance of some sources. If there exists a continuum background source in the line of sight, the HI absorption study (discussed in Section 3.5) enables to break the degeneracy of the solutions (Anderson & Bania, 2009; Roman-Duval et al., 2010).

3.4.5 Mass of the molecular cloud

From the column density

The total mass can be derived from the derived column density N_{H_2} via the following equation :

$$M = \mu m_{\text{H}} N_{\text{H}_2} A \quad (3.72)$$

where A represents the physical area of the source, m_{H} the mass of the hydrogen atom, $\mu = 2.8$ the weight factor assuming 20% of the molecular gas consist in Helium He. The mass obtained has the advantage not to rely on any geometrical assumptions. The main source of uncertainties however comes from the abundance ratio used to obtained N_{H_2} .

Virial mass

The virial mass M_{vir} is another method to constraint the mass of a molecular cloud. Indeed, in the case where thermal motions compensate the gravitation force, I obtain the following equation :

$$\frac{U}{2} = \text{P.E} \quad (3.73)$$

where $P.E$ is the potential energy generated by gravitation and U is the thermal energy of the molecular gas. Depending on the density distribution inside the molecular cloud, the virial mass can change by a few factor. Protheroe et al. (2008) derived the virial mass for a molecular cloud with a Gaussian density distribution

$$M_{\text{vir}} = 444 \left(\frac{\sigma}{1 \text{ pc}} \right) \left(\frac{\Delta v_{\text{FWHM}}}{1 \text{ km/s}} \right)^2 \quad (3.74)$$

where $\sigma\sqrt{2\ln 2}$ indicates the effective diameter of the cloud and Δv_{FWHM} is the FWHM of the line emission. This virial mass is ~ 2 greater than the one assuming a constant density and a factor of $2\sqrt{\pi}$ greater compared to the $1/r^2$ distribution.

3.4.6 Density

Based on our mass estimates, I obtain the H_2 density using the following relation

$$n_{H_2} = \frac{M}{V\mu m_H} \quad (3.75)$$

where V is the assumed volume occupied by the gas. I can also deduce the proton density $n_H = \mu n_{H_2}$ which indicates the total target density inside a molecular cloud. The derived density shows uncertainties due to the lack of information about the geometry of the observed molecular cloud.

3.4.7 Turbulences in the molecular clouds

Aside from obtaining physical parameters which constrain the structure of the molecular clouds, line emission study can also help to understand the dynamics of molecular clouds. As mentioned in section 3.2.2, the frequency emitted by the transition is Doppler shifted due to the thermal motions of the radiation. In this case, the line shape function $\phi(\nu)$ can be described as a Gaussian :

$$\phi(\nu) = \sqrt{\frac{mc^2}{2\pi kT\nu_0^2}} \exp\left(-\frac{(\nu - \nu_0)^2 mc^2}{2kT\nu_0^2}\right) \quad (3.76)$$

where ν_0 is the transition frequency, m is the mass of the emitting molecule and T is the kinetic temperature inside the cloud. By applying $v_{\text{lsr}} = c(\nu - \nu_0)/\nu_0 + v_{\text{cent}}$ (v_{cent} being the velocity of the peak emission), Eq. 3.77 becomes :

$$\phi(v_{\text{lsr}}) = \sqrt{\frac{mc^2}{2\pi kT\nu_0^2}} \exp\left(-\frac{m(v - v_{\text{cent}})^2}{2kT}\right) \quad (3.77)$$

In general, most emission can be well fitted with a Gaussian :

$$f(v_{\text{lsr}}) \propto \exp\left(-\frac{4(v_{\text{lsr}} - v_{\text{cent}})^2}{\Delta v_{\text{FWHM}}^2} \ln 2\right) \quad (3.78)$$

with Δv_{FWHM} being the full with half maximum of the line emission. If I assume that the linewidth of the emission is caused by the thermal motions of the molecules in the region, I obtain :

$$\Delta v_{\text{FWHM}} = \sqrt{\frac{8kT \ln 2}{m}} \quad (3.79)$$

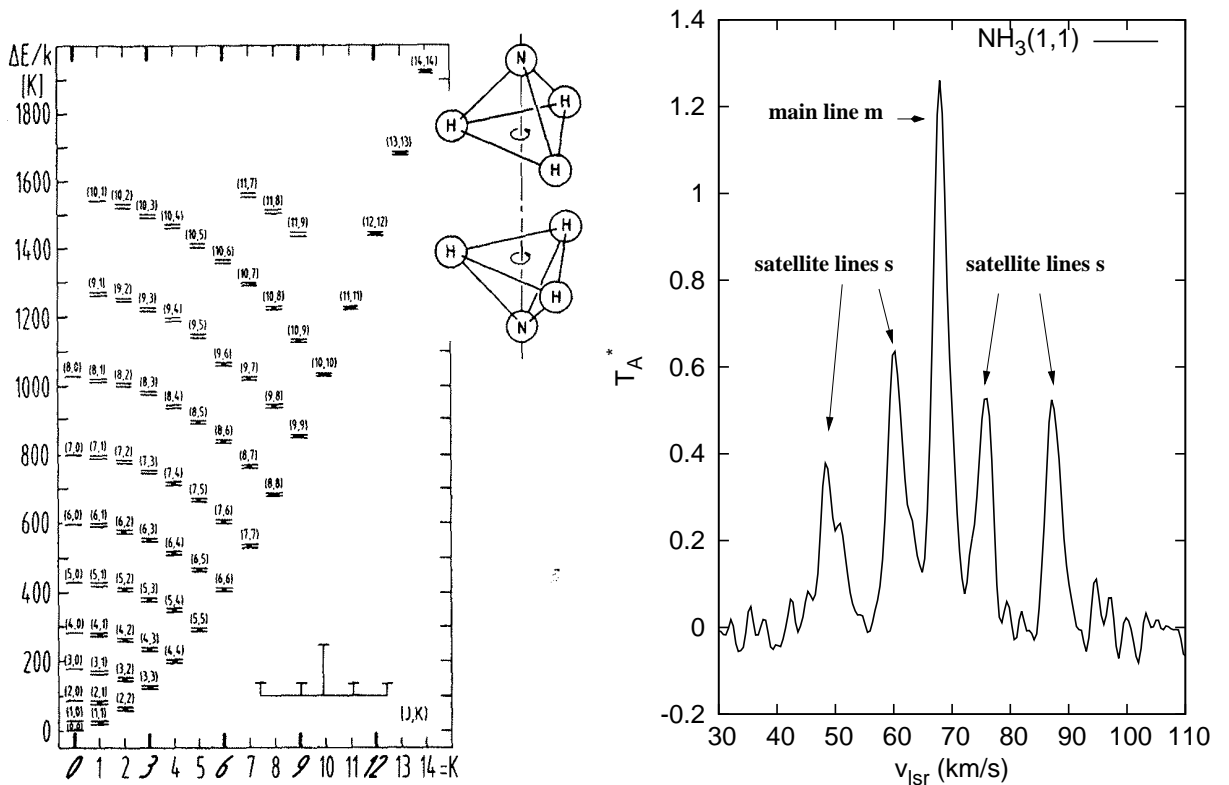


Figure 3.7: (*Left*) Rotational diagram of the ammonia NH_3 . The selection rules only allow molecular transition in the J ladder, thus making the $J=K$ energy state the rotational backbone of the molecule. (Wilson et al., 1993) The five vertical lines show the morphology of the observed NH_3 emission in velocity space. (*Right*) Example of $\text{NH}_3(1,1)$ emission. The emission main line is surrounded by four satellite lines which results from the quadrupole moment (see text).

For comparison, the FWHM of the $\text{CS}(1-0)$ transition at 20 K is expected to reach $\Delta v_{\text{FWHM}} \sim 0.06$ km/s, while the FWHM of the recombination line $H62\alpha$ emitted by hydrogen atoms is expected to reach $\Delta v_{\text{FWHM}} \sim 14$ km/s at 10000 K.

However, it is also possible to observe $\text{CS}(1-0)$ emission with FWHM exceeding $\Delta v_{\text{FWHM}} > 10$ km/s, which would output unreasonable temperature T . Enhanced micro-turbulence caused by nearby star forming regions or external shocks is then likely to explain the broadness of this emission.

Aside from micro turbulences, it is possible that various clumps inside molecular clouds may also move at different radial velocity v_{lsr} . Disruptions can indeed be found on a larger scale. Such phenomenon is called macro-turbulence. Cloud-cloud collisions are likely to produce such features resulting in differences in peak velocity v_{cent} between various clumps and regions (Habe & Ohta, 1992; Torii et al., 2015).

3.4.8 Useful transitions detectable by the Mopra and Nanten telescopes

The Mopra and Nanten2 telescopes are able to map a great variety of molecular transitions which allow to probe different environments of the ISM. In this section, I examine the properties of some line transitions important for our TeV gamma-ray studies.

Carbon monoxide CO and isotopologues

Carbon monoxide $^{12}\text{C}^{16}\text{O}$ (hereafter labeled CO) is the second most abundant molecule (after H_2) found in the ISM with an abundance ratio $\chi_{\text{CO}} \sim 10^{-4}$. CO is a linear rotor with a weak dipole moment $\mu = 0.122 D$, which results in a quite low spontaneous emission rate (see Table 3.1). As a consequence, the CO(1–0) transition has a low critical density $n_c \sim 5 \times 10^2 \text{ cm}^{-3}$ which enables the detection of diffuse molecular gas. However, due to the quite large abundance of CO in molecular clouds, radiative trapping usually becomes non negligible and the transition easily becomes optically thick. Detections of its isotopologues $^{13}\text{CO}(1-0)$ and $\text{C}^{18}\text{O}(1-0)$ can circumvent the problem. Indeed, the much reduced abundances of these isotopologues $\chi_{\text{CO}}/\chi_{^{13}\text{CO}} \sim 20 - 90$ and $\chi_{^{16}\text{O}}/\chi_{^{18}\text{O}} \sim 490$ (see Garden et al. 1991 and references therein) means their transitions are likely to be optically thin and thus observe inner regions of the molecular cloud. Provided the emission from isotopologues are detected, the optical depth of the transition can also be obtained using Eq. 3.68. In this case, the variable R defined in section 3.4.2 refers to the relative abundance ratio between CO and its isotopologue.

Due to the very low precipitable water vapour (PWV) in the Atacama desert, Nanten2 is able to map the CO(2–1) transition with a beam size similar to the Mopra CO(1–0) beam size. Assuming the cloud is in LTE, I use Eq. 3.69 to map the kinetic temperature distribution across the molecular cloud. This method is useful to claim physical associations between various CO(1–0) emission with distinct v_{lsr} and understand the dynamics of the molecular cloud (e.g. the molecular cloud towards NGC 3603, Fukui et al. 2014).

The LTE approximation also allows us to determine the column density. However, CO tends to ‘freeze out’ onto dust grains at low temperature ($T \sim 10 \text{ K}$) and high density environments ($n_{\text{H}_2} \sim 10^5 - 10^6 \text{ cm}^{-3}$). Tafalla et al. (2004) in fact noticed a drop of χ_{CO} by a factor of 3–10 towards the star less dense core L1517B.

As discussed in section 3.4.1, the conversion factor X_{CO} is also used to obtain the column density $N_{\text{H}_2} = X_{\text{CO}} W_{\text{CO}}$ from the CO(1–0) integrated intensity W_{CO} . Several methods have been used to derive the X_{CO} factor in our Galaxy (see Bolatto et al. 2013 and references therein). For instance, the X_{CO} factor were obtained from the comparison between the CO column density with the dust emission assumed optically thin. Comparison between the gamma-ray emission with the gas distribution has also been an alternative method to obtain X_{CO} (Strong & Mattox, 1996). Most of the studies reveal that the CO conversion factor converges towards $X_{\text{CO}} = 2.0 \pm 0.3 \times 10^{20} \text{ cm}^{-2}/(\text{K km/s})$ across the Galaxy. One must however remain cautious as this value could show large scale fluctuations. For instance Strong et al. (2004) argued that X_{CO} varies as a function of a galactocentric radius to explain differences between the observed gamma-ray emissivity and the distribution of SNRs and pulsars.

Carbon monosulphide CS and isotopologues

Carbon monosulphide $^{12}\text{C}^{32}\text{S}$ (labelled CS hereafter) has a high dipole moment ($\mu = 1.9 D$), which results in a high spontaneous emission rate (see Table 3.1). Consequently, CS(1–0) emission occurs at a density $n_{\text{H}_2} > 5 \times 10^4 \text{ cm}^{-3}$. CS(1–0) and CS(2–1) help to probe dense molecular clumps located inside molecular clouds. Despite its much lower abundance ratio (Irvine et al., 1987), CS has also been found to be optically thick. In the case where the isotopologue $\text{C}^{34}\text{S}(1-0)$ and/or $^{13}\text{CS}(1-0)$, I use Eq. 3.68 to obtain the optical depth (as per the CO analysis). The variable R defined in section 3.4.2 then refers to relative abundance ratio between CS and the isotopologue. From the small difference in energies between the states 2 and 1, it is however difficult to accurately constrain the temperature of the gas

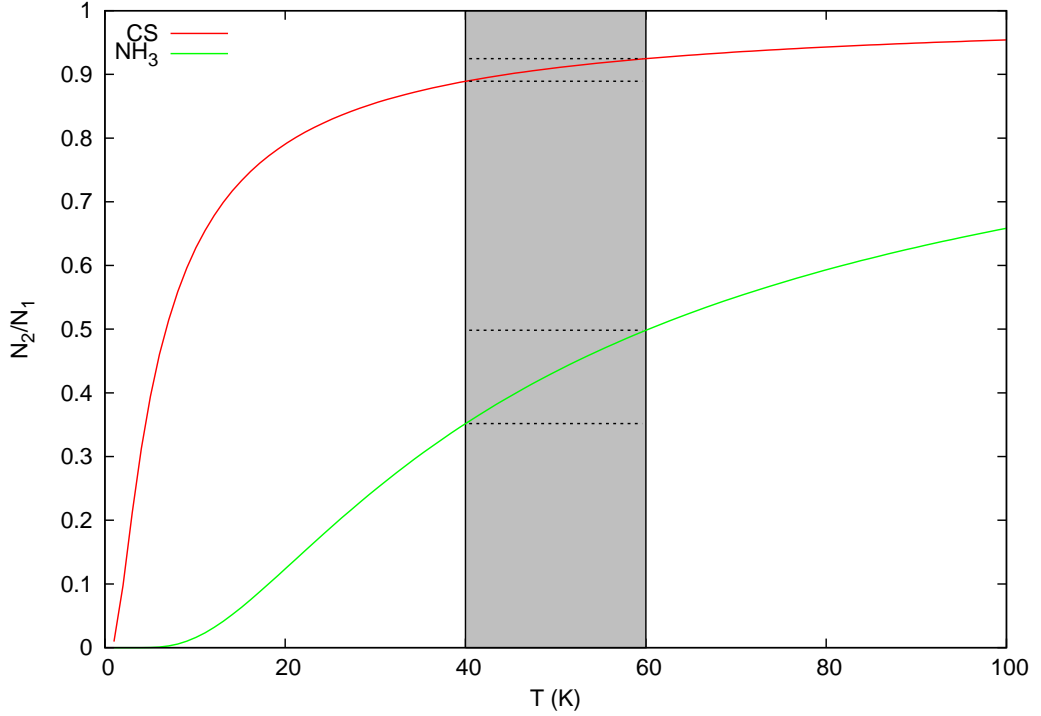


Figure 3.8: Evolution of the column density ratio $N_2^{\text{CS}}/N_1^{\text{CS}}$ (in red) and $N_{2,2}^{\text{NH}_3}/N_{1,1}^{\text{NH}_3}$ as a function of the kinematic temperature T

for temperature exceeding ~ 20 K (see Fig. 3.8). In this thesis, in the case where ammonia NH_3 is also detected (see next section), I may assume that NH_3 and CS trace the same gas, and use the kinetic temperature obtained from the analysis of the NH_3 transitions. In the case where NH_3 transitions have not been detected, I assume a kinetic temperature of the cloud $T = 10 - 20$ K.

The H_2 column density is then derived using LTE approximation. The abundance ratio χ_{CS} is however the major source of uncertainties. Indeed, from the studies of dense molecular regions, χ_{CS} is found to vary from 10^{-9} to 10^{-8} (Irvine et al., 1987). Also, as per CO, CS is also found to freeze-out onto dust grains in cold and very dense cores (Tafalla et al., 2004). As per a few studies of molecular clouds with CS (e.g. Zinchenko et al. 1994; Larionov et al. 2006; Nicholas et al. 2011), I use $\chi_{\text{CS}} = 4 \times 10^{-9}$ and thus expect our column density estimates to vary by a factor of 2.

Ammonia NH_3

Ammonia (NH_3) is a symmetric top molecule where the nitrogen N is located at the apex of the molecule. Unlike CS and CO, NH_3 does not freeze-out and can be observed in various regions (e.g dense cores, star forming regions). The rotational transitions of the NH_3 molecule can be described by the total angular momentum J and its projection on the dipole axis K (see Fig. 3.5). NH_3 can be divided into two sub-species : *ortho*- NH_3 where all the hydrogen spins are parallel ($K=3n$ with n being an integer) and *para*- NH_3 for $K \neq 3n$. From the symmetric top configuration, the dipole moment μ is located on the axis linking the atom N to the centre of the hydrogen H plane. From selection rules, spontaneous emission can not change K (i.e. $\Delta K = 0$) and $\Delta J = \pm 1$). NH_3 transitions thus occurs in ladder with fixed K (see Fig. 3.7). Notably, the energy states with $J = K$ are considered *metastable* and the ammonia populations are expected to fill these energy states.

The nitrogen atoms is located either above (top position) or underneath (bottom position) the hydrogen plane. The potential distribution of ammonia is represented as a double well, with a finite potential barrier at the hydrogen plane position. From this configuration, the J, K states are split into doublets (parity \pm) with distinct energies, and the nitrogen atom can quantum tunnel through the hydrogen plane and produce *inversion transition* which can be observed at mm wavelengths (e.g. $\text{NH}_3(1,1)$, $\text{NH}_3(2,2)$ and $\text{NH}_3(3,3)$). The uneven distribution of electrons results in a quadrupole moment from the interaction between the N atom and the electric fields. Each chiral state is then split into three (see Ho & Townes 1983 for further details). As a result, the shape of the NH_3 inversion transition consists in a main line (labelled m) emission surrounded by four satellite line emissions (labelled s , see Fig.,3.7). The relative strength of each resulting line emission and their separation in velocity space can be found from Wilson et al. (1978).

From the peak intensity of each line emission, it is then possible to first derive the optical depth of the main line emission $\tau(J, K, m)$ using Eq. 3.68. The variable R defined in section 3.4.2 is, in this case, defined as the ratio between the theoretical line intensity ratio between the main line $f(J, K, m)$ and the surrounding satellite line $f(J, K, s)$ (i.e. $R = f(J, K, m) / f(J, K, s)$). In order to obtain the total optical depth of the J, K transition $\tau(J, K)$ (hereafter labeled $\tau_{J,K}$), I use :

$$\tau_{J,K} = \frac{\tau(J, K, m)}{f(J, K, m)} \quad (3.80)$$

It is quite common to derive the optical depth of the $\text{NH}_3(1,1)$ transition as the satellite lines are often detected. Although it is difficult to detect the satellite lines of higher transitions (e.g. $\text{NH}_3(2,2)$ and $\text{NH}_3(3,3)$), one can still estimate the optical depth of other transitions $\tau_{J,K}$, from $\tau_{1,1}$ via the following equation (Ungerechts et al., 1986) :

$$\tau_{J,K} = \frac{1}{f(J, K, m)} \ln \left[1 - \frac{T_{\text{A}}^*(J, K, m)}{T_{\text{A}}^*(1, 1, m)} (1 - \exp(-\tau_{1,1,m})) \right] \quad (3.81)$$

In order to provide temperature estimates, one can first obtain the rotational temperature from the population studies of NH_3 transition states (e.g. $\text{NH}_3(1,1)$ and $\text{NH}_3(2,2)$). Using Quasi-LTE approximation for a dipole molecule (see Eq. 3.34 and Goldsmith 1972 for further discussion), Tafalla et al. (2004) obtained an empirical model which links the rotational temperature T_{rot} to the kinetic temperature T of the molecular cloud, namely :

$$T = \frac{T_{\text{rot}}}{1 - T_{\text{rot}}/42 \ln [1 + 1.1 \exp(-16/T_{\text{rot}})]} \quad (3.82)$$

Eq. 3.82 is particularly agreeing with simulations for $T = 5 - 20$ K. I finally assume the Boltzmann distribution to obtain the total NH_3 column density N_{NH_3}

$$N_{\text{NH}_3} = N_{1,1} \left[1 + \frac{1}{3} \exp\left(\frac{E_{(1,1)} - E_{(0,0)}}{kT}\right) + \frac{5}{3} \exp\left(\frac{E_{(1,1)} - E_{(2,2)}}{kT}\right) + \dots \right] \quad (3.83)$$

The abundance ratio χ_{NH_3} is thought to vary between 10^{-8} and 10^{-7} (Irvine et al., 1987) and thus becomes the major source of uncertainties in our N_{H_2} estimates.

Tracers of star forming regions and shocks

Recombination lines

Molecular clouds generally host star forming regions and the presence of new active stars reshape the structure of the molecular gas. The temperature generated by newborn stars are sufficient to ionise the

surrounding gas. HII regions are commonly observed regions inside molecular clouds. The electrons eventually recombine with their atoms and produce broad recombination line radiations. The recombination lines $H51\alpha$, $H62\alpha$, $H65\alpha$ and $H69\alpha$ could then be detected with Mopra (see Table 3.2).

Methanol CH_3OH

Another important tracer of star forming regions is the methanol maser emission obtained from population inversions among the energy states. Methanol shows two classes of masers: *Class I* where the source of population inversion comes from high collisions rates and *Class II* where radiation is the cause. Voronkov et al. (2014) stated that CH_3OH *class I* maser emission occur in the outskirts of active star-forming regions compared to class II which are generally coincident. H_2O masers are also a good signpost of star-forming regions and generated by shocks. As shown in Table 3.2, various CH_3OH masers can be detected with Mopra.

Silicon Monoxide SiO

Dust particles, bombarded by heavy molecules (e.g CO) in the presence of shocks, release silicate atoms in gas phase. Silicates are eventually eroded by the oxygen atoms and produce SiO molecules (Gusdorf et al., 2008). Silicon monoxide emission $SiO(1-0)$ have generally been observed behind weak shocks with velocity $v_s=25$ km/s and ambient density $n_{H_2} \sim 10^{4-5} \text{ cm}^{-3}$. Although weak shocks may originate from star forming regions, SNRs are also expected to produce weak shocks when crossing dense molecular regions. Therefore, silicon monoxide emission can be a good signpost to claim physical association between molecular cloud and nearby SNRs (e.g Nicholas et al. 2011).

3.5 HI 21cm radiation : tracer of atomic gas

So far, I focused on methods to obtain physical properties of molecular gas. However, atomic gas has also proven to be relevant for the study of the ISM nearby TeV sources. The main observational tool to probe atomic gas is the HI 21cm emission. This emission occurs when the spin of the proton and electron transition from parallel to anti parallel (see Fig. 3.5). The quite low spontaneous transition rate $A = 2.85 \times 10^{-15} \text{ s}^{-1}$ results in a very low critical density $n_c \sim 10^{-3} \text{ cm}^{-3}$. As a result, all the emission emitted from diffuse atomic gas can be observed.

In the presence of background radiation, strong HI absorption features, caused by the presence of dense molecular clouds in the line of sight, can be observed. Provided the location of these continuum radiation is known, these absorptions lines have been used to discriminate the near-far kinematic distance of a molecular cloud obtained with the Brand & Blitz (1993) model (see Roman-Duval et al. 2010 for further details on this method). In the case where HI 21cm emission is optically thin, I use the conversion factor $X_{HI} = 1.8 \times 10^{18}$ to convert our integrated intensity into hydrogen column density N_H .

Another major application is to compare the total column density $N_H = N_{HI} + 2N_{H_2}$ with the required column density used to fit X-ray source spectrum (which can be counterparts to the TeV emission), which could help to constrain the distance of the high energy source.

Finally, it has been found that HI emission self absorbs from the presence of cold HI gas in the line of sight. By correcting the self absorbing HI emission, Fukuda et al. (2014) has, in fact, found compelling correlation between the spatial distribution of the column density N_H and the TeV emission towards HESS J1731–347. Consequently, it proves that HI studies is required to complete an ISM description nearby TeV sources.

Table 3.2: Non exhaustive list of important molecular tracers which can be observed in 3mm, 7mm and 12mm with Mopra.

3mm		7mm		12mm	
Transition	Frequency (MHz)	Transition	Frequency (MHz)	Transition	Frequency (MHz)
HCO ⁺ (1-0)	89188.526	SiO(1-0, $\nu=3$)	42519.373	H69 α	19591.110
¹³ CS(2-1)	92494.720	SiO(1-0, $\nu=2$)	42820.582	CH ₃ OH(II)	19967.396
C ³⁴ S(2-1)	96412.950	SiO(1-0, $\nu=1$)	43122.079	H ₂ O	22235.253
CS(2-1)	97980.953	SiO(1-0, $\nu=0$)	43423.824	H65 α	23404.280
C ¹⁸ O(1-0)	109781.176	CH ₃ OH(I)	44069.476	NH ₃ (1,1)	23694.471
¹³ CO(1-0)	110201.354	HC ₃ N(5-4, F=4-3)	45090.264	NH ₃ (2,2)	23722.634
CO(1-0)	115271.202	H51 α	45453.720	NH ₃ (3,3)	23870.127
		¹³ CS(1-0)	46247.580	NH ₃ (6,6)	25056.025
		C ³⁴ S(1-0)	48206.946	H62 α	26959.170
		CS(1-0)	48990.957	NH ₃ (9,9)	27477.943

3.6 Summary

The different line transitions mentioned in the earlier sections help to understand the composition and morphology of the ISM next to the TeV source. Although the carbon monoxide CO(1-0) transition traces most of the ISM molecular gas across the galaxy, its emission is generally optically thick and consequently the CO(1-0) transition wont be sensitive to dense clumps inside the GMC. CS(1-0) and NH₃(1,1) thus complement the survey by locating the dense gas. However, their abundance ratios show variations dependent on the physical conditions of the molecular cloud (e.g temperature). Consequently, studies using multiple molecules and transitions must be used to constrain the physical parameters of the cloud. If one molecular cloud proves to be associated (e.g from a shock tracer) with the nearby TeV source, it is then possible to constraint the distance of the TeV source. The dense molecular clouds provides also good target for high energy cosmic-rays to produce γ -ray emission (see next section) and generally is also useful to understand the morphology of TeV sources (see Chapter 4).

Chapter 4

On the evolution of cosmic-ray, high energy electron and gamma-ray energy distributions

Cosmic-rays (CRs) and high energy electrons are accelerated inside high energy astrophysical sources (e.g. SNRs, PWNe). As they propagate into the ISM, they emit gamma-ray emission from inverse Compton, bremsstrahlung (for high energy electrons), and from p-p interactions (for CRs). In this chapter, I thus study the effects of the diffusion of CRs and high energy electrons accounting for energy losses and the resulting evolution of broadband photon spectral energy distribution (SED) at various locations.

I first briefly review the effects of radiation losses on the energy distribution of CRs and high energy electrons injected by impulsive and continuous sources, and their effects on the evolution of the photon broadband SED. I then describe the mechanism of propagation of charged particles (CRs/high energy electrons) in the ISM. Finally, assuming an isotropic diffusion, I provide useful information about the variation of the energy distribution of CRs and high energy electrons (and thus the photon SED) as we move away from the injectors. By doing so, I will be able to find key differences between the gamma-ray morphologies produced by CRs and high energy electrons.

4.1 Radiative losses

CRs/high energy electrons lose energy as they interact with the surrounding ISM. Although non-radiative losses (e.g. adiabatic) may also have a significant impact on the evolution of the energy distribution of CRs and electrons, I here focus on the radiative losses. On the one hand, high energy electrons will emit radio to X-ray photons while gyrating along magnetic field lines (synchrotron radiation), up-scatter background photons to high energies (inverse Compton), and interact with ISM particles and emit Bremsstrahlung emission. On the other hand, CRs predominantly lose energy from p-p interactions which create gamma-rays, secondary muons and electrons. Further details concerning these interactions can be found in Appendix B. Assuming they lose energy continuously, particles (cosmic-ray/high energy electrons) with initial Lorentz factor $\gamma_0 = E_0/mc^2$ will end up with a Lorentz factor $\gamma(t) = E/mc^2$ after time t . In this section, I provide basic analytical results to explain various effects of radiation losses

on the energy distribution of CRs/high energy electrons. The energy distribution of CRs and electrons $n(\gamma, t) = dN(t)/d\gamma$ evolves as particles lose their energy from non thermal radiations. The equation of the evolution of their energy distribution with Lorentz factor γ at time t is :

$$\frac{\partial n(\gamma, t)}{\partial t} = \frac{\partial}{\partial \gamma} (\dot{\gamma}(\gamma) n(\gamma, t)) + S(\gamma, t) \quad (4.1)$$

where $S(\gamma, t)$ is the source term and $\dot{\gamma}(\gamma)$ indicates the energy loss rate (in Lorentz factor unit) of a particle with Lorentz factor γ . I define the variable $Q(\gamma, t) = \dot{\gamma}(\gamma) n(\gamma, t)$ as the net loss rate of particles with Lorentz factor γ . Eq. 4.1 thus becomes :

$$\frac{\partial Q(\gamma, t)}{\partial t} = \dot{\gamma} \frac{\partial Q(\gamma, t)}{\partial \gamma} + \dot{\gamma} S(\gamma, t) \quad (4.2)$$

I now define the variable

$$\tau(\gamma', \gamma) = \int_{\gamma}^{\gamma'} \frac{d\gamma''}{\dot{\gamma}(\gamma'')} \quad (4.3)$$

which describes the time required for a CR/high energy electron to transition from a Lorentz factor γ' to γ . Notably, I can associate $t = \tau(\gamma_0, \gamma)$, with γ_0 being the initial Lorentz factor (see Fig. 4.1). I thus obtain the following equation :

$$\frac{\partial Q(\gamma, t)}{\partial t} = \frac{\partial Q(\gamma, t)}{\partial \tau} + \dot{\gamma} S(\gamma, t) \quad (4.4)$$

I note that $Q(\gamma, t) = Q(\gamma', t - \tau(\gamma', \gamma))$ is the solution of the homogeneous equation ($S(\gamma, t) = 0$). Assuming an impulsive source term $S(\gamma, t) = \delta(\gamma - \gamma') \delta(t - t')$, one can also obtain the Green's function $G(\gamma, \gamma', t, t')$ which satisfies Eq. 4.4 (Berezinskii et al., 1990) :

$$G(\gamma, \gamma', t, t') = \frac{1}{\dot{\gamma}} \delta(t - t' - \tau(\gamma', \gamma)) \quad (4.5)$$

where δ is here the Dirac function. In the case of an arbitrary source term, the solution $Q(\gamma, t)$ becomes :

$$Q(\gamma, t) = \int_{\gamma}^{\infty} \int_0^t G(\gamma, \gamma'', t, t'') \dot{\gamma} S(\gamma'', t'') dt'' d\gamma'' + Q(\gamma_0, 0) \quad (4.6)$$

Therefore, I now obtain the analytical solution of Eq. 4.1 :

$$Q(\gamma, t) = \int_{\gamma}^{\infty} \int_0^t \frac{1}{\dot{\gamma}} \delta(t - t'' - \tau(\gamma'', \gamma)) \dot{\gamma} S(\gamma'', t'') dt'' d\gamma'' + Q(\gamma_0, 0) \quad (4.7)$$

$$Q(\gamma, t) = \int_{\gamma}^{\infty} \mathcal{H}(t - \tau(\gamma'')) S(\gamma'', t - \tau(\gamma'', \gamma)) d\gamma'' + Q(\gamma_0, 0) \quad (4.8)$$

$$n(\gamma, t) = \frac{1}{\dot{\gamma}} \int_{\gamma}^{\infty} \mathcal{H}(t - \tau(\gamma'')) S(\gamma'', t - \tau(\gamma'', \gamma)) d\gamma'' + \frac{\dot{\gamma}_0}{\dot{\gamma}} n(\gamma_0, 0) \quad (4.9)$$

$$n(\gamma, t) = \frac{1}{\dot{\gamma}} \int_{\gamma}^{\gamma_0} S(\gamma'', t - \tau(\gamma'', \gamma)) d\gamma'' + \frac{\dot{\gamma}_0}{\dot{\gamma}} n(\gamma_0, 0) \quad (4.10)$$

with \mathcal{H} being the Heaviside step function. In the following section, I will discuss basic analytical results for the impulsive and continuous cases, for both CRs and electrons.

4.1.1 Impulsive Injector

For the case of an impulsive injector, I will use $S(\gamma, t) = 0$ and an initial power-law distribution $n(\gamma, 0) = A\gamma^{-\alpha}$

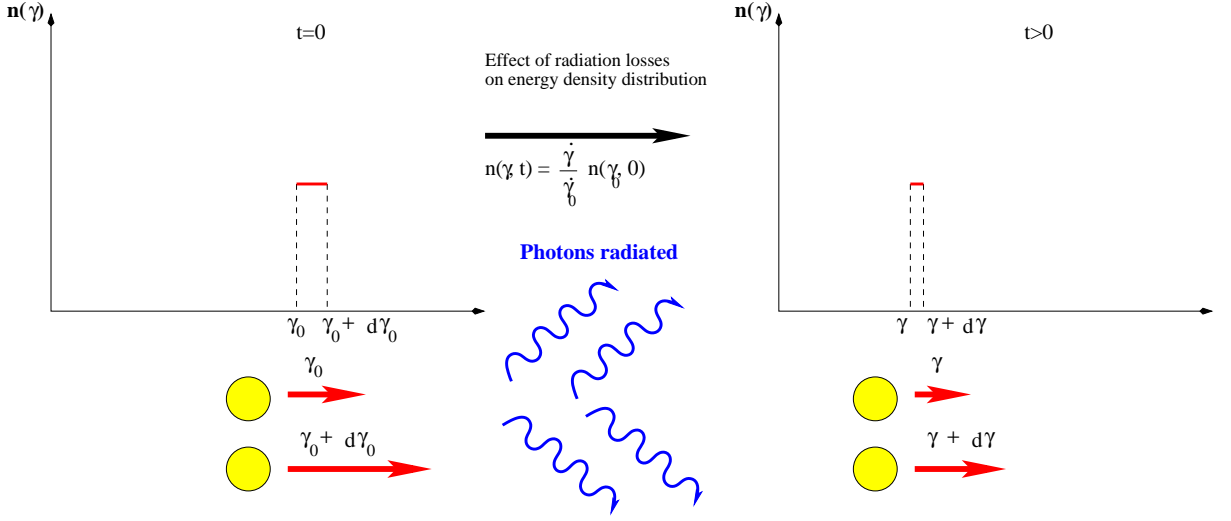


Figure 4.1: Sketch illustrating the evolution of the energy distribution of particles with initial Lorentz factor between γ_0 and $\gamma_0 + d\gamma_0$ (left panel) transition to a Lorentz factor between γ and $\gamma + d\gamma$ (right panel) due to radiative losses after time t

High energy CRs

High energy CRs mostly lose their energies via inelastic p-p interactions (see Appendix B). The inelastic p-p cross section σ_{inel} being weakly dependent on energy for CRs with energies $E_p > \text{a few GeV}$ (see Eq. B.32 in Appendix B), I approximate here the energy loss rate as $\dot{\gamma}(\gamma) = \gamma/\tau_{\text{pp}}$ with τ_{pp} being the p-p interaction timescale. Consequently, the evolution of the Lorentz factor with time becomes :

$$\frac{\gamma}{\gamma_0} = \exp\left(-\frac{t}{\tau_{\text{pp}}}\right) \quad (4.11)$$

Combining Eqs. 4.10 and 4.11 , I obtain :

$$n(\gamma, t) = A\gamma^{-\alpha} \exp\left(-\frac{(\alpha-1)t}{\tau_{\text{pp}}}\right) \quad (4.12)$$

In this model, the density of CRs with Lorentz factor between γ and $\gamma + d\gamma$ decreases exponentially with time. However, I remark from Fig. 4.2 that the shape of the energy distribution of CRs remains the same. A more realistic model of the CR energy distribution towards high energy sources requires the use of an exponential cut-off term dominant at Lorentz factor $\gamma > \gamma_c$. Eq. 4.12 then becomes :

$$n(\gamma, t) = A\gamma^{-\alpha} \exp\left(-\frac{(\alpha-1)t}{\tau_{\text{pp}}} - \frac{\gamma \exp(t/\tau_{\text{pp}})}{\gamma_c}\right) \quad (4.13)$$

As represented by the blue lines in Fig. 4.2 (top panel), the exponential cutoff shifts very quickly towards lower energy when $t > \tau_{\text{pp}}$ (see dotted line) and thus hadronic γ -ray emission at very high energies is expected to decrease rapidly once the age of the system evolves past the p-p cooling time τ_{pp} .

High energy electrons

As opposed to CRs, high energy electrons lose energy through three dominant processes : synchrotron, inverse-Compton and bremsstrahlung. In appendix B, Eqs B.9, B.24 and B.31 show the energy losses caused by each of these processes. If I include these three type of radiation losses, then Eq. 4.10 must be solved numerically.

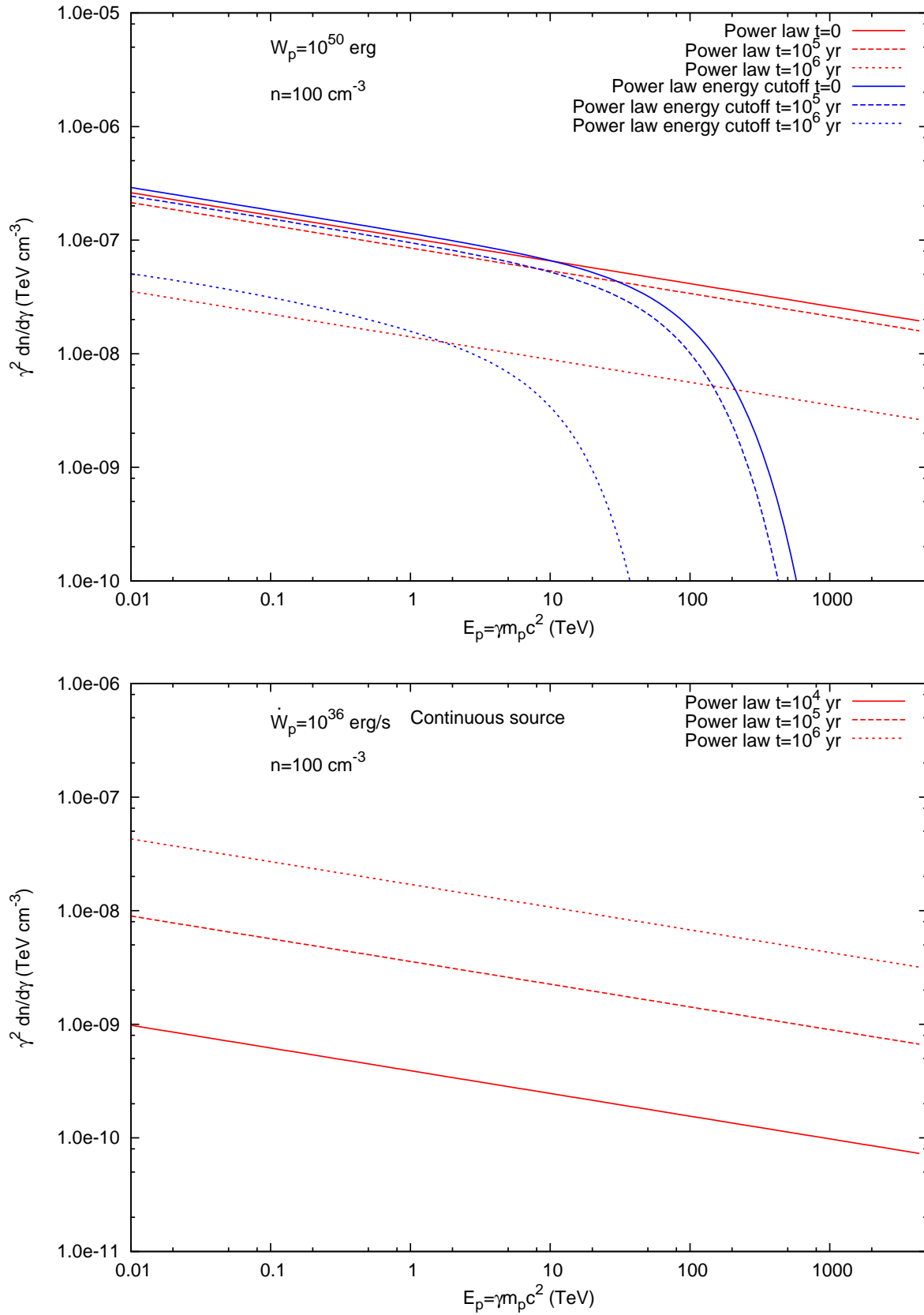


Figure 4.2: Energy distribution of CR $n(\gamma, t) = dn/d\gamma$ at various time epochs for an impulsive (top panel) and continuous source (bottom panel). In the top panel, the red lines represent the case of an initial power-law distribution whereas the blue lines include an energy cutoff at $E_c = 100$ TeV.

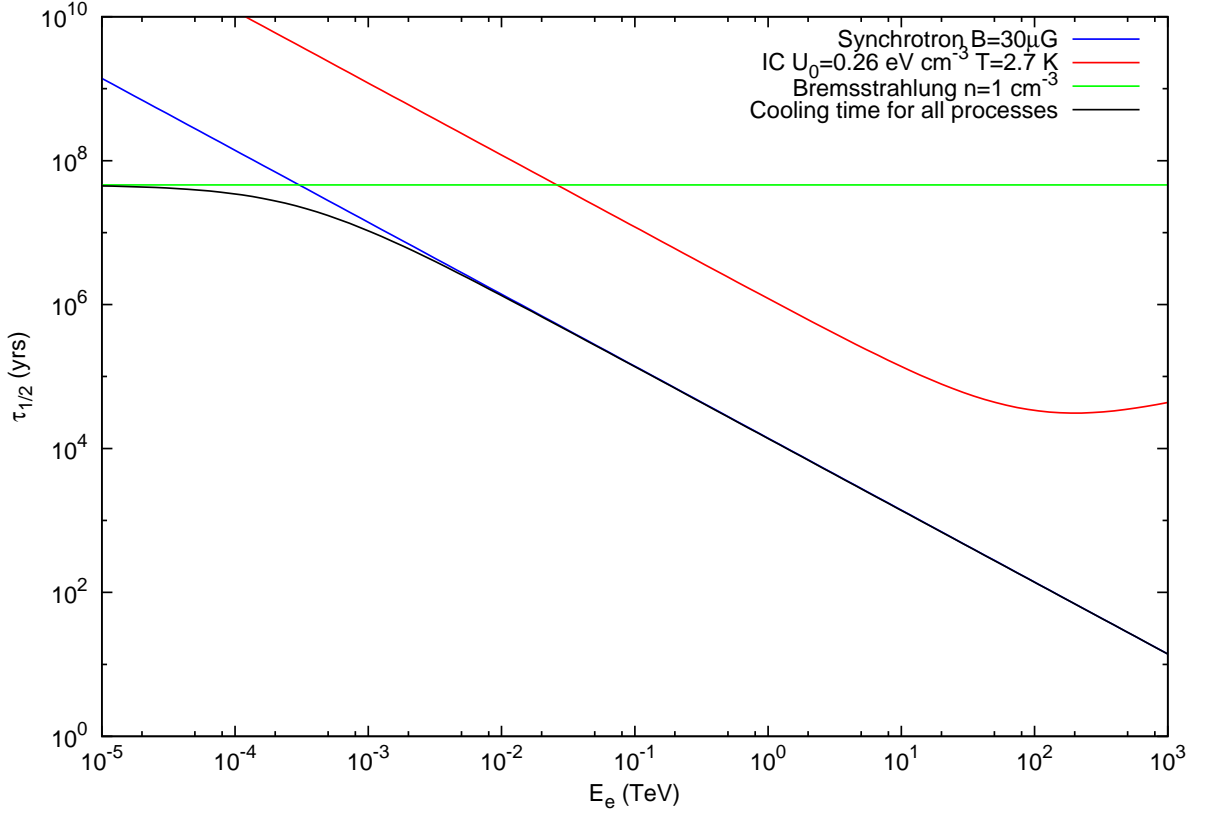


Figure 4.3: Evolution of the electron cooling time-scale $t_{1/2}$ as a function of energy for Synchrotron (blue line), inverse Compton (red line) and bremsstrahlung (green) and the cooling timescale accounting for all the aforementioned radiative processes is shown in black.

From Fig. 4.3, which shows the evolution of the time-scale $\tau_{1/2}$ for the various radiation mechanisms as a function of the particle (CR/high energy electron) energy, I first note that bremsstrahlung losses are likely to be dominant for low energy electrons in dense molecular regions. In this section however, I am mostly interested in key features for high energy electrons as this would affect the gamma-ray TeV emission. I observe that Synchrotron radiation is likely to be the dominant cause of energy losses for high energy electrons. For $E > 1$ TeV, I can use the synchrotron cooling rate $\dot{\gamma} = b_s \gamma^2$ with $b_s = 1.292 \times 10^{-15} (B_{\text{mG}})^2$ (see Manolakou et al. 2007). Using Eq. 4.3, the ratio between the initial Lorentz factor γ_0 and γ at time t is :

$$\frac{\gamma}{\gamma_0} = 1 - \gamma b_s t \quad (4.14)$$

Consequently, I can obtain γ_0 as a function of γ , b_s , and t

$$\gamma_0 = \frac{\gamma}{1 - \gamma b_s t} \quad (4.15)$$

Eqs. 4.14 and 4.15 provide two important points.

- As opposed to high energy protons, the fraction of energy loss of high energy electrons increases with the Lorentz factor γ
- After a time t , the Lorentz factor of a given particle injected at $t = 0$ cannot exceed $\gamma_{\text{crit}} = (b_s t)^{-1}$.

Consequently, combining Eqs. 4.10 and 4.15 and assuming the case where synchrotron losses are dominant at all energies, I obtain :

$$n(\gamma, t) = A \gamma^{-\alpha} (1 - \gamma b_s t)^{\alpha-2} \text{ for } \gamma < \gamma_{\text{crit}} \quad (4.16)$$

Fig. 4.4 (top panel) shows an example of the evolution of the energy distribution of electrons as a function of time as they lose energy from synchrotron radiation. In both cases, there are no electrons with energies above $E_{\text{crit}} = \gamma_{\text{crit}} m_e c^2$ ($E_{\text{crit}}(10^3 \text{ yr}) = 13 \text{ TeV}$ and $E_{\text{crit}}(10^4 \text{ yr}) = 1.5 \text{ TeV}$), due to the synchrotron and inverse Compton. In the case where $\alpha > 2$ I observe a decrease of the energy distribution as I reach closer to E_{crit} due to the bottom-heavy energy (low energy electrons contribute to most of the total energy budget) configuration of the initial electron distribution. On the contrary, in the case where $\alpha < 2$ the increase of the energy distribution as I reach closer to E_{crit} is caused this time by the top-heavy configuration of the initial distribution (high energy electrons contribute to most of the total energy budget).

4.1.2 Continuous injector

In the case of a continuous injector, I assume that there are no existing CRs/high energy electrons at $t = 0$, thus $n(\gamma, t) = 0$. Eq. 4.10 becomes :

$$n(\gamma, t) = \frac{1}{\dot{\gamma}(\gamma)} \int_{\gamma}^{\gamma_0} S(\gamma', t - \tau(\gamma', \gamma)) d\gamma' \quad (4.17)$$

Particles (CRs/high energy electrons) with Lorentz factor $\gamma < \gamma'' < \gamma_0$, injected at time $0 < \tau(\gamma'', \gamma) < t$ here contribute to $n(\gamma, t)$. In the following section, I will focus on a steady continuous injector with a power-law distribution.

High energy CRs

By combining Eqs. 4.11 and 4.17, I obtain the following analytical solution :

$$n(\gamma, t) = \frac{\tau_{\text{pp}} Q(\gamma, 0)}{\alpha - 1} \left(1 - \exp\left(-\frac{(\alpha - 1)}{\tau_{\text{pp}}}\right) \right) \quad (4.18)$$

As shown in Fig. 4.2 (bottom panel), the normalisation of energy distribution of CRs between increases before converging towards a constant value $\propto \tau_{\text{pp}}$. As per the impulsive injector, the spectral index of the CR energy distribution remains unchanged.

High energy electrons

As per the impulsive injector, I also assume that synchrotron radiation is the dominant cause of the electron energy losses at all energies. From Eq. 4.15, I have indicated that high energy electrons with Lorentz factor $\gamma_{\text{crit}} = (b_s t)^{-1}$ at time t have an initial Lorentz factor $\gamma_0 \rightarrow \infty$. Consequently, high energy electrons with current Lorentz factor $\gamma > \gamma_{\text{crit}}$ have been injected at a later time. Thus, in order to solve Eq. 4.17, two cases should be accounted for :

$$n(\gamma, t) = \begin{cases} \frac{1}{\dot{\gamma}(\gamma)} \int_{\gamma}^{\gamma_0} S(\gamma', t - \tau(\gamma', \gamma)) d\gamma' & \text{for } \gamma < (b_s t)^{-1} \\ \frac{1}{\dot{\gamma}(\gamma)} \int_{\gamma}^{\infty} S(\gamma', t - \tau(\gamma', \gamma)) d\gamma' & \text{for } \gamma \geq (b_s t)^{-1} \end{cases} \quad (4.19)$$

$$n(\gamma, t) = \frac{A\gamma^{-\alpha}}{(\alpha - 1)\gamma} \begin{cases} \left(1 - (1 - \gamma b_s t)^{\alpha-1}\right) & \text{for } \gamma < (b_s t)^{-1} \\ 1 & \text{for } \gamma \geq (b_s t)^{-1} \end{cases} \quad (4.20)$$

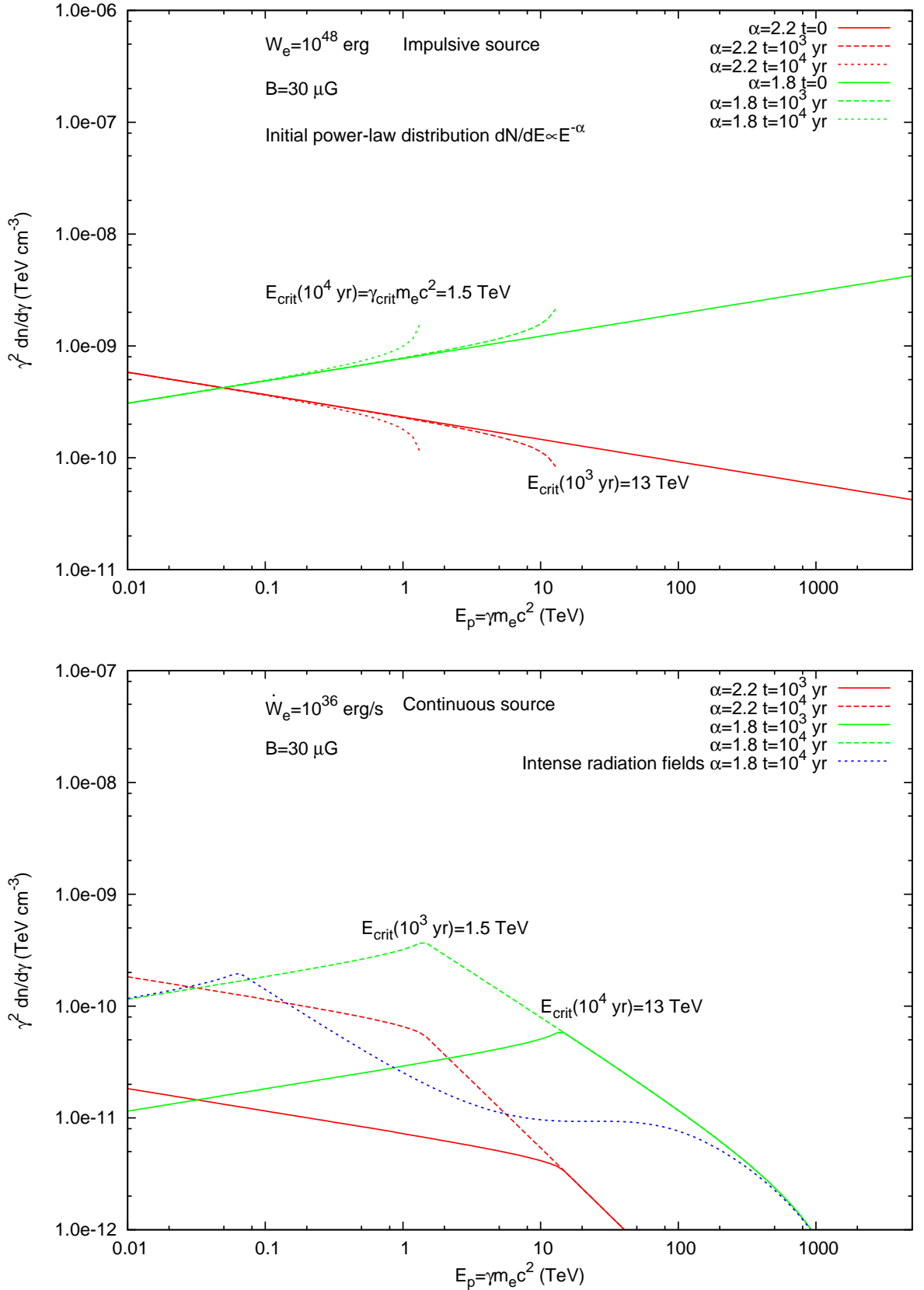


Figure 4.4: Evolution of the energy distribution of electrons as a function of time for the case of an impulsive (top panel) and continuous source (bottom panel). In both cases, a pure power-law with spectral index $\alpha = 2.2$ (red lines) and $\alpha = 1.8$ (green lines) is assumed. Finally, the dotted blue line highlights the effect of IC losses in the Klein-Nishina regime (see Blumenthal & Gould 1970 and references therein), caused by intense infra-red radiation fields (see text), on the final energy distribution of electrons.

Fig. 4.4 (bottom panel) illustrates the evolution of the energy density of electrons at various times. The striking features are that the initial pure power-law becomes broken at $\gamma = \gamma_{\text{crit}}(t)$ and the spectrum becomes steeper beyond $\gamma > \gamma_{\text{crit}}(t)$.

4.1.3 Numerical methods

In the previous sections, I showed simple cases and obtained analytical solutions which will later explain key features in the gamma-ray spectrum.

Obviously, the actual situation is generally more complex than these simplistic approximations. For instance, in the case of a source of relativistic particles surrounded by intense radiation fields, the IC scattering in the Klein-Nishina regime ($\gamma\epsilon_\gamma \sim m_e c^2$ with ϵ_γ being the initial energy of the target photon) considerably modifies the energy distribution of high energy electrons (see blue dotted lines in the bottom panel of Fig. 4.4).

Also, the initial energy distribution of the injected particles may not necessarily be described as a single power-law. For instance, in the case of the PWN, an initial broken power law with an energy cutoff may be required to account for various mechanisms of accelerations for low energy electrons (see Amato 2014, Bucciantini et al. 2011 and chapter 1 for further details) and for the spectral break caused by Synchrotron losses (see Fig. 4.4 bottom panel). The density of particles injected also depends on time. Although the aforementioned analytical solution provides a good overview of the general spectral features in which one generally observes in the CR/electron energy distributions, Eq. 4.1 must be solved numerically in order to provide accurate descriptions of the proton/electron energy distributions and their resulting gamma-ray spectra.

I have built a numerical modelling code which derives the evolution of an arbitrary energy distribution of CRs and electrons from an impulsive/continuous injector, accounting for radiation losses, and then reproduces the spectral energy distribution of photons (see Appendix B). As shown in Appendix C, this SED code will be used to obtain the spectral energy distribution of photons for a given position with an arbitrary distribution of CRs/electrons.

4.1.4 Evolution of the gamma-ray emission

For both impulsive and continuous injectors, I now review how the evolution of the energy distribution of CRs and high energy electrons can affect the photon SED. In the following, I used my numerical code to evolve the energy distribution of CRs/high energy electrons, accounting for all of the aforementioned radiation losses.

In the hadronic scenario, I have already mentioned that the energy distribution of CRs mostly depends density of target particles n_H . In Fig. 4.5 (top panel), I show the resulting SED photon produced by CRs from an impulsive source, with total energy budget $W_p = 10^{50}$ erg, as a function of time t in a region with particle density $n_H = 100 \text{ cm}^{-3}$. As discussed in Appendix B, the photon spectral index Γ roughly matches the CRs spectral index α between $E_\gamma = 10 \text{ GeV}$ to 10 TeV. I note that the normalisation of the gamma-ray spectrum significantly decreases at $t \gg \tau_{pp} \sim 6 \times 10^7 / n_H \text{ yr}$. The spectral index Γ does not vary until $t \geq 10^6 \text{ yr}$ (purple curve), which then reveals the cross section σ_{pp} being (weakly) dependent on the CR energy.

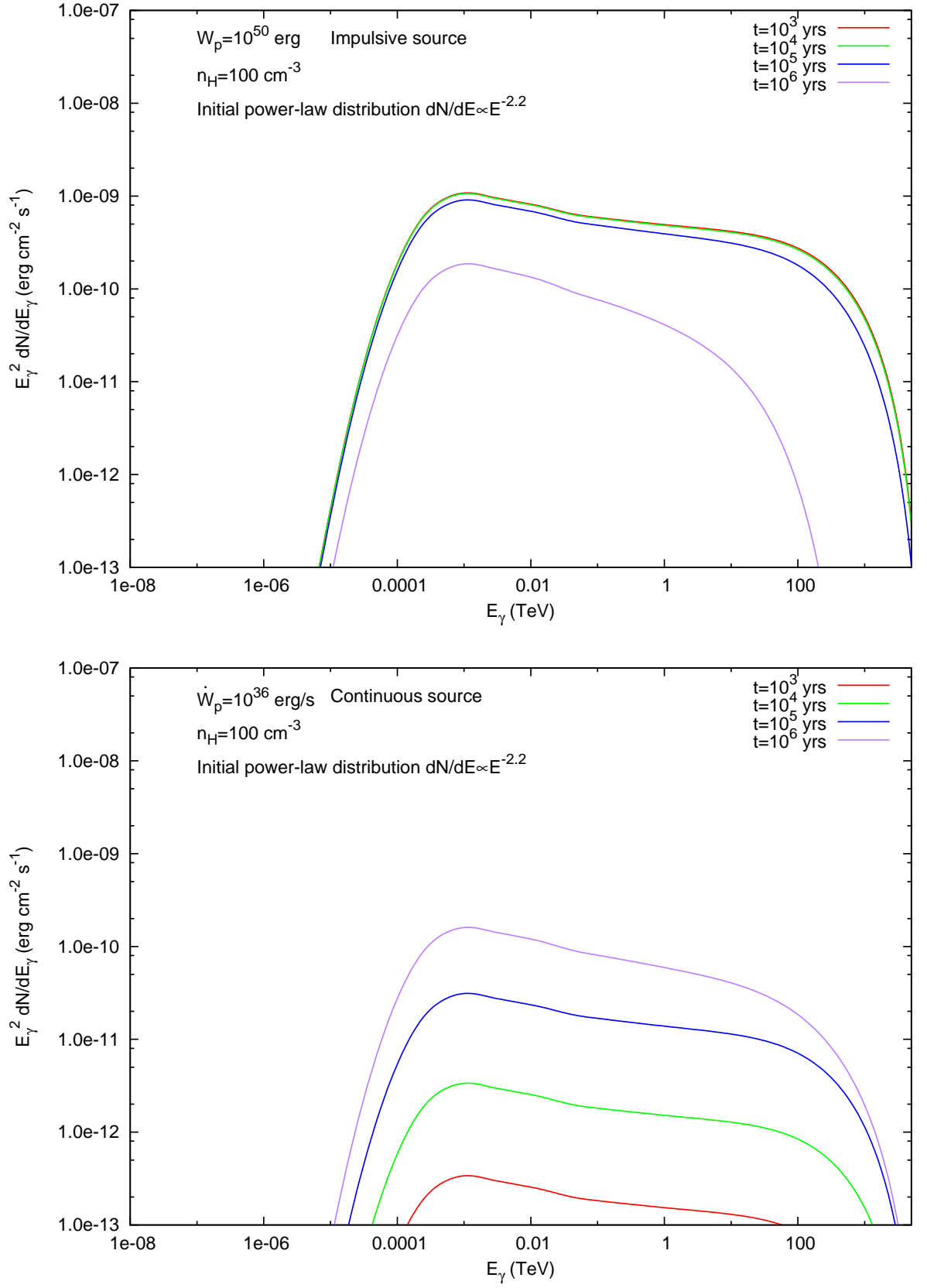


Figure 4.5: Evolution of the photon SED at various epochs for an impulsive (top panel) and continuous (bottom panel) hadronic injectors.

I also illustrate in Fig. 4.5 (bottom panel), the evolution of the SED produced by CRs injected by a continuous source with energy rate $\dot{W}_p = 10^{36}$ erg/s at various epochs. The gamma-ray normalisation increases linearly at early stage ($t \ll \tau_{pp}$) as shown by the green and blue spectrum in Fig. 4.5. Once the age of the system reaches $t \geq 10^6$ yr, the gamma-ray spectrum becomes quite steeper.

In the case of electrons, the case is far more complex because of the three competing radiation mechanisms. I first look at the effect of synchrotron dominated losses on the SED at various time epochs.

For the case of the impulsive source, I observe in Fig. 4.6 (top panel) that the cut-off energy of both the synchrotron contribution (solid lines) and inverse-Compton contribution (dashed lines) swiftly decreases with time. Similar features are found if I fix the time but vary the magnetic field (see Fig. 4.7). However, while IC decreases with increasing magnetic field due to larger radiative losses, the synchrotron emission peak increases. Consequently, a larger magnetic field increases the ratio between the synchrotron and IC total emitted power. In the Thompson limit ($\gamma E_\gamma \ll m_e c^2$), the power ratio is, in fact, defined as follows (Aharonian et al., 1997) :

$$\frac{P_{\text{sync}}}{P_{\text{IC}}} = \frac{B^2}{U_{\text{CMB}}} \quad (4.21)$$

with $U_{\text{CMB}} = 0.26 \text{ eV/cm}^{-3}$ being the energy density of the cosmic microwave background (CMB) radiation. I finally observe from Fig. 4.6 (bottom panel) that both synchrotron and inverse-Compton components become softer due to the steeper electron spectrum at high energies.

In this thesis, I aim to model the gamma-ray emission in dense molecular regions. therefore, it is important to describe the impact of the bremsstrahlung contribution to the gamma-ray spectrum. The bremsstrahlung contribution is softer than that for IC for the same distribution of electrons. From Fig. 4.8, which illustrates the SED produced by high energy electrons which have been continuously injected into a medium with density $n_H = 300 \text{ cm}^{-3}$ (within the range of densities inside molecular clouds), I observe that although Bremsstrahlung becomes dominant at energies up to $E_\gamma \sim$ a few TeV at this density, inverse-Compton eventually dominates at high energies for a fixed B field.

4.2 Particle Transport

In the absence of an electric field, the Lorentz force $\mathbf{F}_{\text{Lorentz}}$ acting on a charged particle is :

$$\mathbf{F}_{\text{Lorentz}} = q\mathbf{v} \times \mathbf{B} \quad (4.22)$$

where \mathbf{v} is the particle velocity and \mathbf{B} is the magnetic field. In the case of a uniform magnetic field (see Fig. 4.9), the charged particle gyrates along magnetic field lines. The helical motion is defined by the particle Larmor radius $r_L = E/Zq|B|c$ (with Zq being the total charge of the particle) and α the pitch angle between \mathbf{v} and \mathbf{B} .

The transport of CRs and high energy electrons is expected to be collisionless. Consequently, in the absence of perturbation in the magnetic fields, CRs and high energy electrons travel along the magnetic field lines.

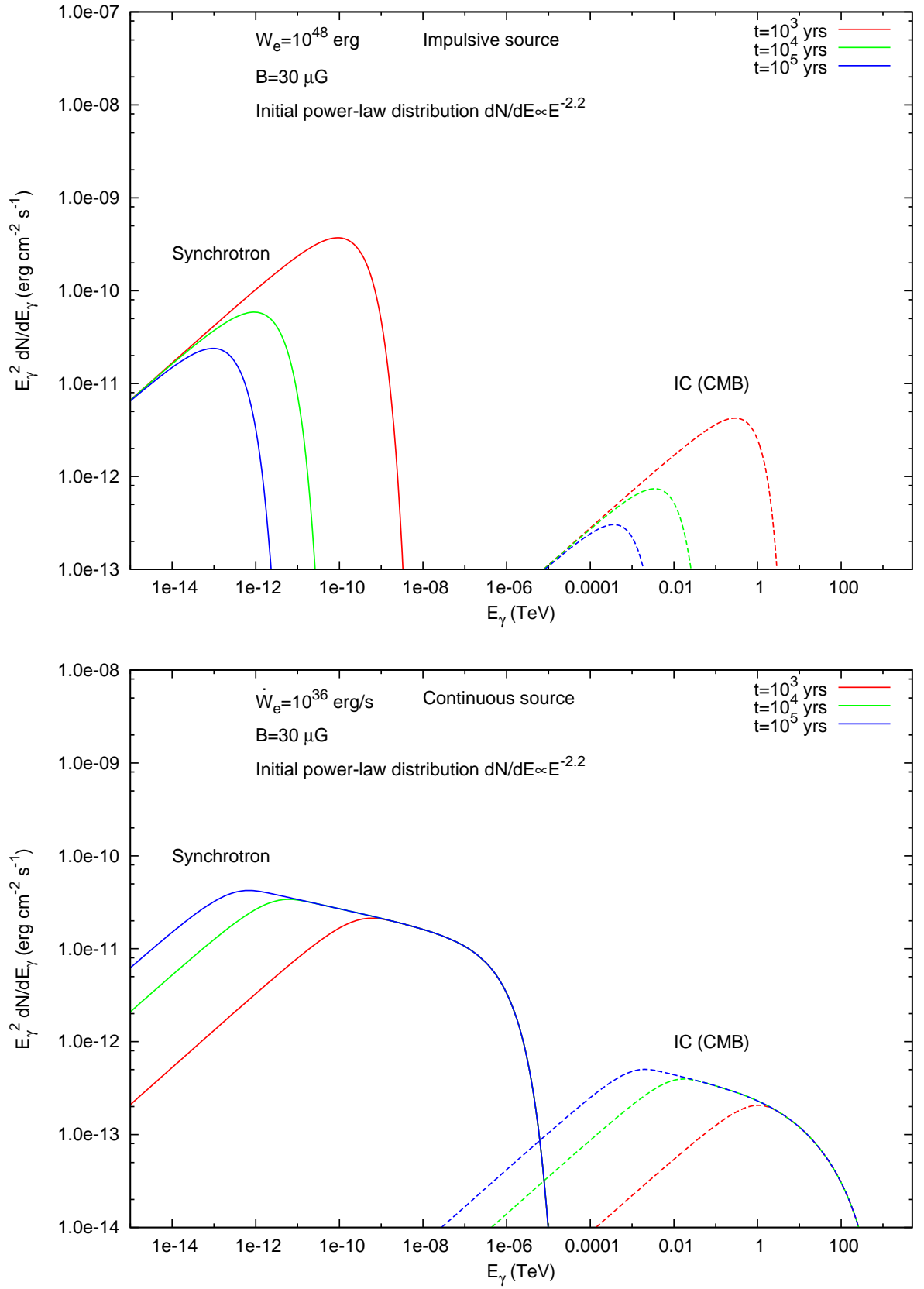


Figure 4.6: SED of photons produced by high energy electrons from an impulsive (top panel) and a continuous (bottom panel) injectors at various epochs. The solid lines and dashed lines represent synchrotron and IC (CMB) radiation respectively.

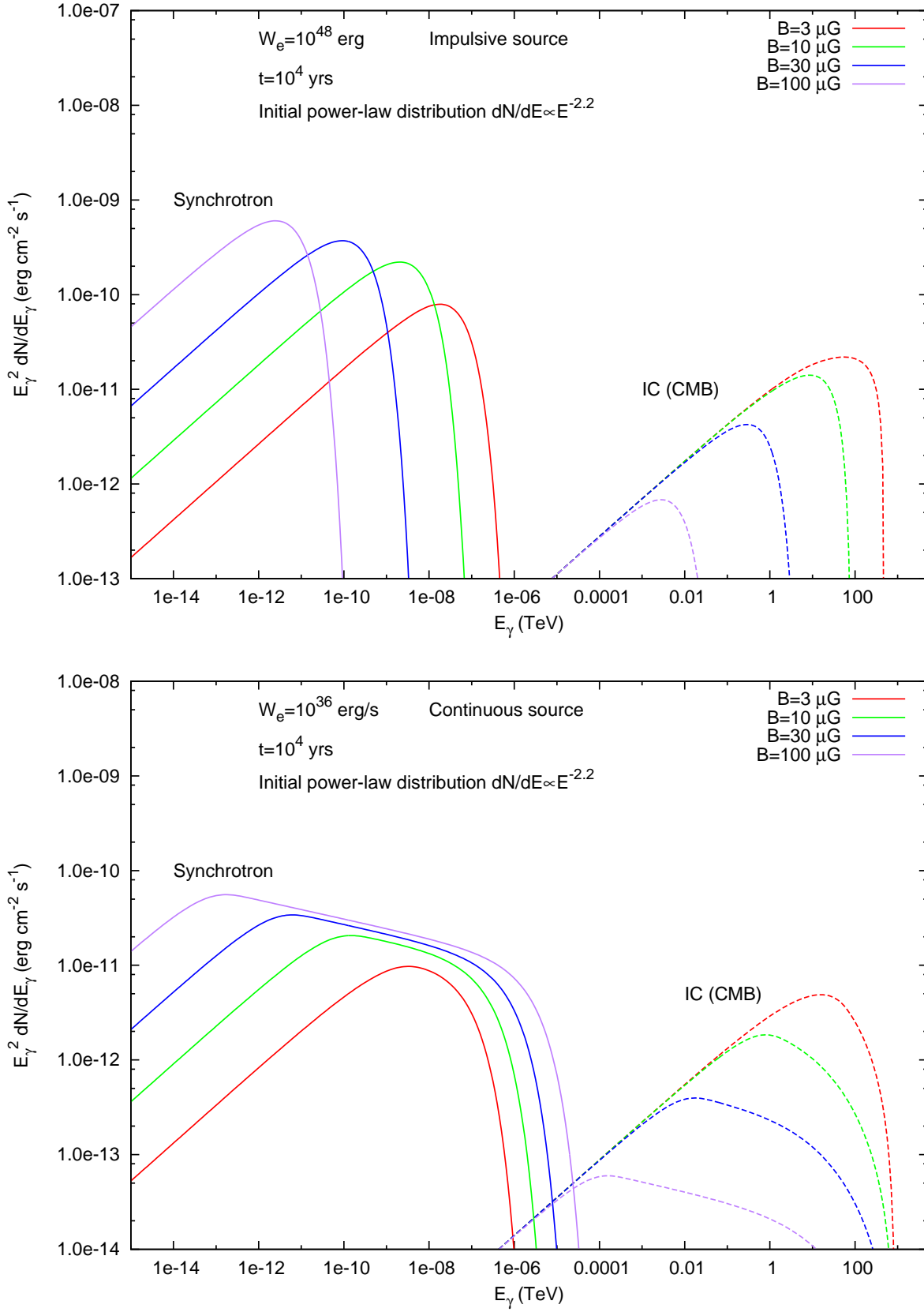


Figure 4.7: SED of photons produced by high energy electrons from an impulsive (top panel) and continuous (bottom panel) injector evolving in environments with various magnetic field strengths. The solid lines and dashed lines represent synchrotron and IC (CMB) radiation respectively.

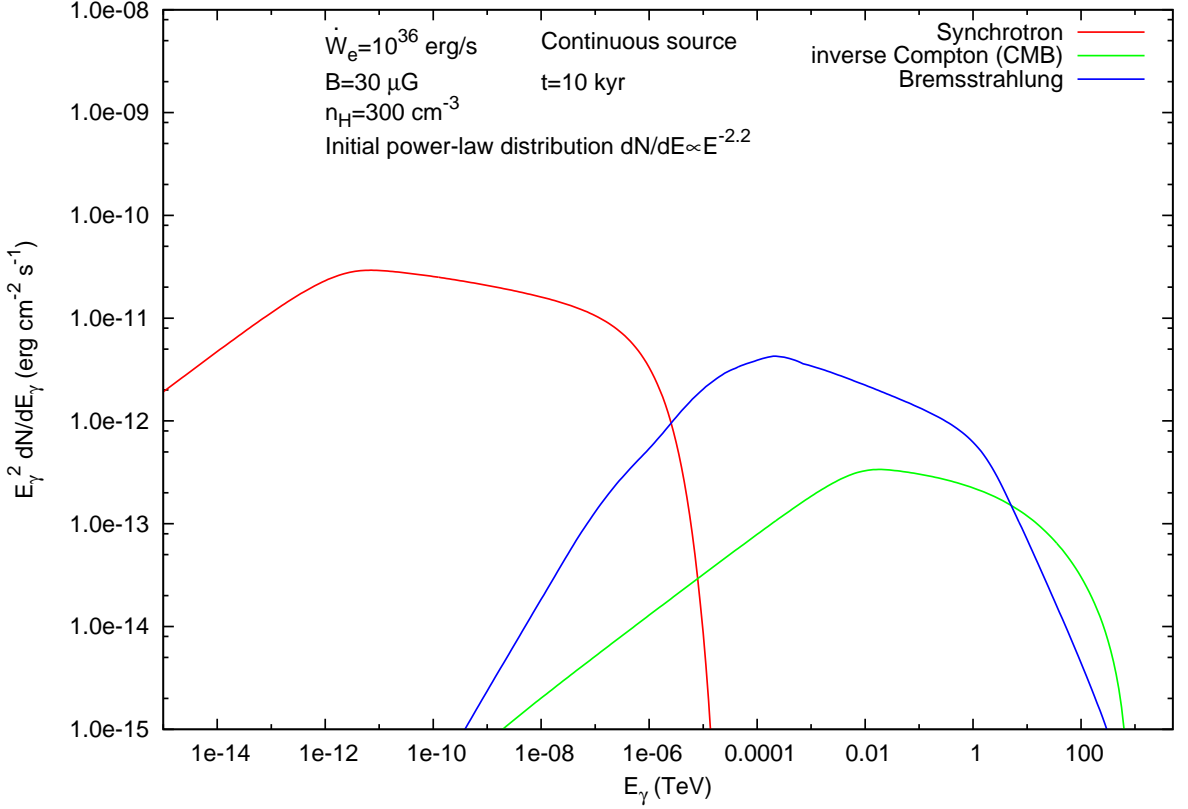


Figure 4.8: SED of photons at $t = 10^4$ yrs produced by continuously injected electrons with initial spectral index $\alpha = 2.2$, accounting for radiation losses and propagating in a dense environment ($n_H = 300 \text{ cm}^{-3}$). Synchrotron, inverse-Compton (CMB) and bremsstrahlung radiation are shown in red, green, and blue respectively.

4.2.1 Scattering of charged particles from perturbations of the magnetic fields

In our Galaxy, various mechanisms produce a spectrum of perturbation in the magnetic fields. Indeed, astrophysical shocks (e.g SNRs) enhance turbulence in the surrounding ISM (Malkov et al., 2013; Nava et al., 2016). Precursor high energy CRs are also expected to excite Alfvén waves surrounding the SNRs (see Skilling 1975). In this section I briefly introduce the effect of the magnetic field turbulence on the propagation of CRs and high energy electrons.

In the following example (see Fig. 4.10), a charged particle propagates along primary magnetic field lines orientated along the x axis. A perturbation of scale b in the y direction is implemented at $x = 0$. In Fig. 4.10a., I follow the propagation of three charged particles with initial pitch angle $\alpha = 50^\circ$ but with different velocities, and consequently three distinct Larmor radii. In the case where $r_L \ll b$ (purple curve), the charged particle follows the magnetic field lines. The total net impulse gained by the particle $\int F dt = 0$ and its motion thus remains unchanged after crossing the perturbation. In the case where $r_L \gg b$ (blue curve), the charged particle is not affected by the impulse generated by the perturbations and its motion also remains unaltered. However, in the specific case where $r_L \sim b$ (green curve), I notice that the particle motion is changed and the pitch angle α differs after crossing the perturbation.

From the case where $r_L \sim b$, I illustrated in Fig. 4.10b. the effect of the initial pitch angle on the motion of the charged particle after crossing the perturbation. In all cases, I find that the pitch angle has varied after crossing the perturbation. In fact, in the case where $\alpha = 80^\circ$ (cyan curve), the charged

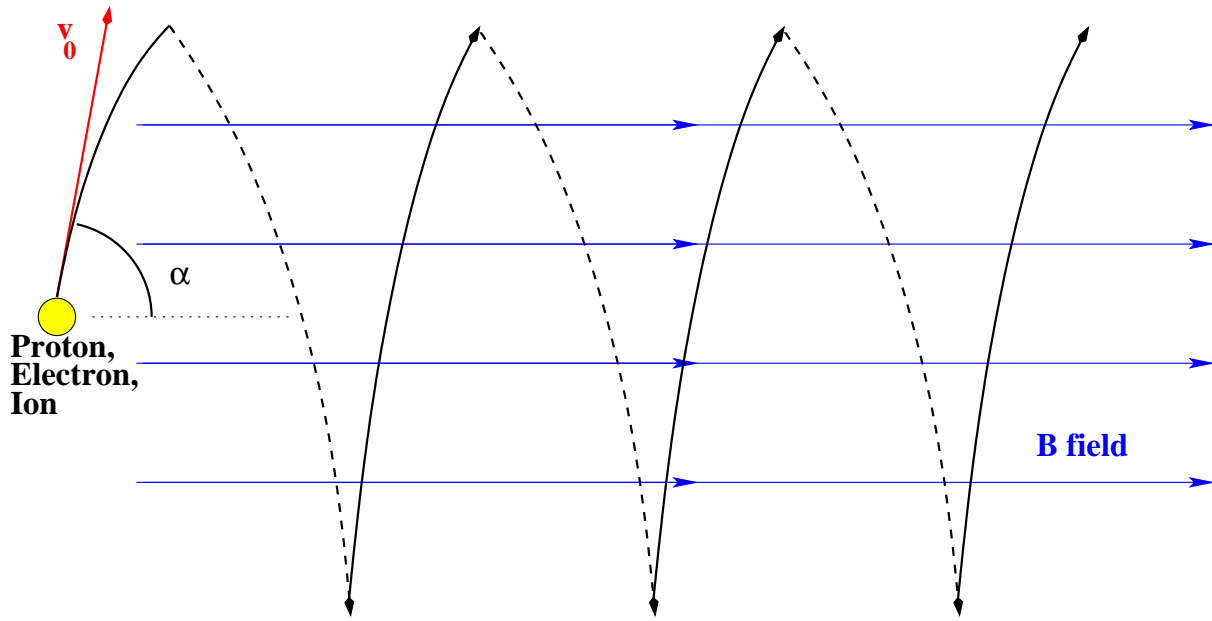


Figure 4.9: Sketch illustrating the helical motion of a charged particle with velocity $|\mathbf{v}| = v_0$ and pitch angle α in the presence of magnetic field.

particle has actually been reflected back to the opposite direction. From this example, I understand that efficient scattering of the pitch angle occurs when the Larmor radius roughly equals the scale of the turbulence b .

The magnetic field turbulence can be described as a series of perturbations $\delta\mathbf{B}(k) \propto \exp(i\mathbf{k}\cdot\mathbf{x})$ with wave number $k = 2\pi/b$. The energy density of the turbulence can also be expressed as follows (see Nava et al. 2016 and references therein):

$$\frac{(\delta B)^2}{8\pi} = \frac{B_0^2}{8\pi} \int_{k_0}^{\infty} W(k) dk \quad (4.23)$$

with B_0 being the primary magnetic field and $W(k) = d(\delta B^2(k)/B_0^2)/dk$ being the energy distribution of the turbulence with wave number k . Consequently, the scattering of CRs and high energy electrons thus depend on energy, and the energy density distribution of the magnetic turbulence $W(k)$.

Although the motion of these particles is, at first, in a ballistic regime, multiple scattering makes it eventually change to a diffusive regime (see Prosekin et al. 2015 and references therein). In our previous example where a primary magnetic field B_0 dominates over the turbulence, the charged particles thus diffuse along the magnetic field lines direction (see Nava & Gabici 2013 for more detailed study). However, in the case where the magnetic field is turbulent in all direction ($\delta B(k) \sim B_0$), their diffusion eventually becomes isotropic.

4.2.2 Diffusion equation

Due to the intrinsic relationship between charged particles (CRs/high energy electrons) and the magnetic fields, a full magnetohydrodynamics (MHD) description would be required to predict their spatial distribution. Alternatively, a stochastic description of the energy distribution of CRs/high energy electrons $n = n(\gamma, \mathbf{r}, t)$ can be obtained via the Fokker-Planck equation (see Cesarsky & Voelk 1977) :

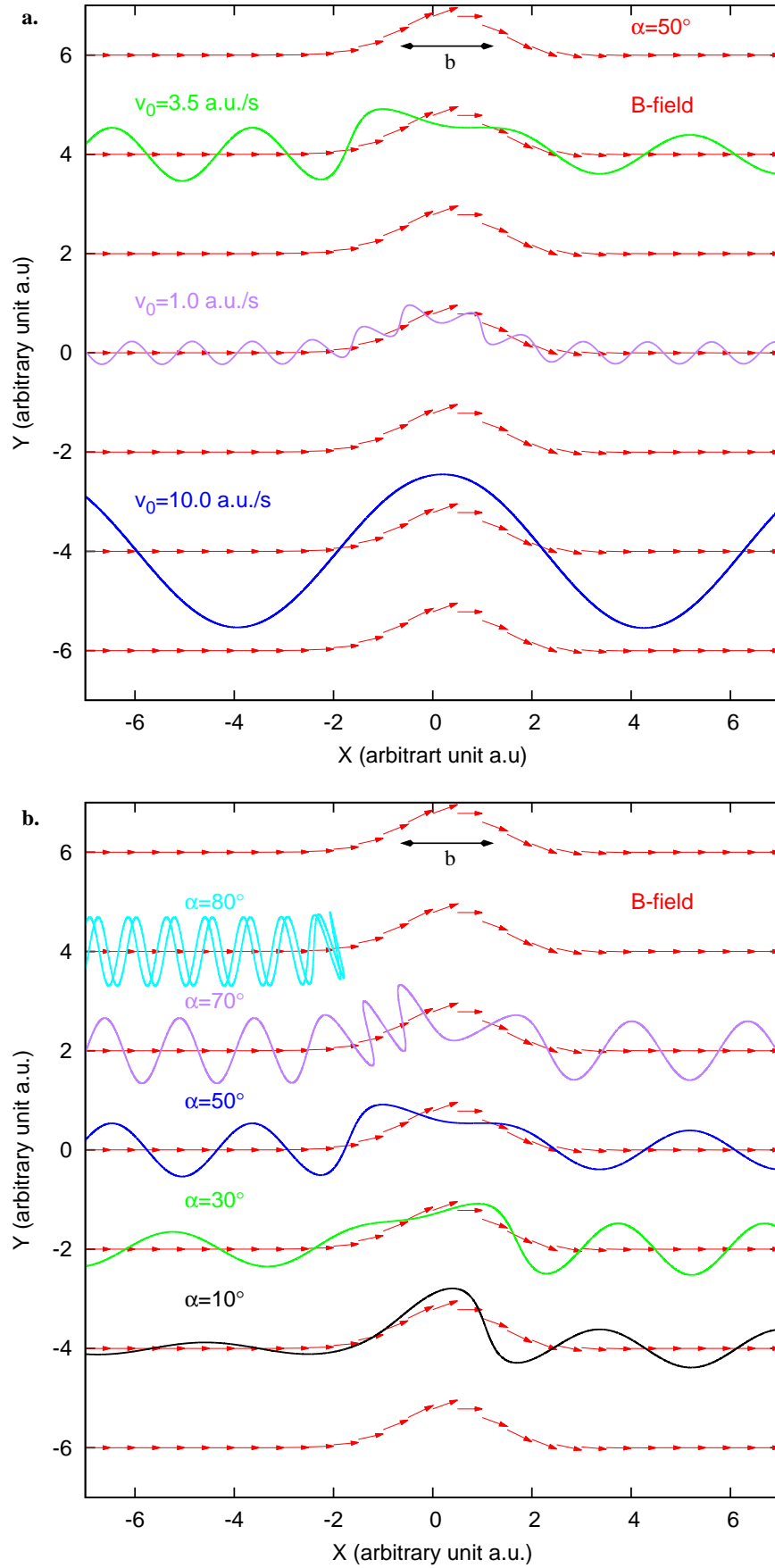


Figure 4.10: In the top panel, the various curves illustrate the motion of charged particles with different initial velocities v_0 and initial pitch angle $\alpha = 50^\circ$ in the presence of a perturbation of the magnetic fields. In the bottom panel, I indicate how the initial pitch angle will be affected due to the turbulences for the case $v_0 = 3.5$ a.u./s ($r_L \sim b$, see green curves in top panel).

$$\begin{aligned} \frac{\partial n}{\partial t} = & -\nabla \cdot (n\mathbf{v}_A) - \nabla \cdot (\overline{\overline{D}} \cdot \nabla n) + \frac{\partial}{\partial \gamma} \left(\dot{\gamma} n - \frac{\gamma}{3} (\nabla \cdot \mathbf{v}_A) \right) \\ & + \frac{\partial}{\partial \gamma} \left(\gamma^2 D_{\gamma\gamma} \frac{\partial}{\partial \gamma} \left(\frac{n}{\gamma^2} \right) \right) + S(\gamma, \mathbf{r}, t) \end{aligned} \quad (4.24)$$

Eq. 4.24 describes the evolution of the density of CRs/high energy electrons at various position and Lorentz factor. On the right hand side, the first term represents the advection of CRs/high energy electrons by a co-moving fluid with velocity \mathbf{v}_A . The advection term notably becomes significant when the bulk velocity \mathbf{v}_A is important (e.g jets) or when CRs/high energy electrons are confined by local magnetic fields. The second term represent the diffusion of CRs/high energy electrons. If the diffusion is preferred for a particular direction (e.g along the magnetic field lines), the diffusion coefficient $\overline{\overline{D}}$ is described as a second rank tensor. If the diffusion is however assumed to be isotropic, then D is described as a scalar¹. The third term describes the energy losses from various radiative processes and adiabatic expansion. The fourth term indicates diffusion in the energy space with diffusion coefficient $D_{\gamma\gamma}$, resulting from stochastic reacceleration of CRs/high energy electrons in the ISM (e.g. second order Fermi acceleration). Finally, the last term introduces the source function.

In the following sections, I use the simple case of an isotropic diffusion of CRs/high energy electrons to reveal features of the energy distribution of CRs/high energy electrons from diffusion. In chapter 6, the enhanced turbulence adjacent to particle accelerators (e.g SNRs) (see previous section for brief discussion), and the estimated age of HESS J1825–137 (4×10^4 yr), may justify this approximation. I will also assume that the advection term is negligible nor do I account for adiabatic losses or stochastic reacceleration. Eq. 4.24 becomes :

$$\frac{\partial n}{\partial t} = -\nabla \cdot (D(\mathbf{r}, \gamma) \cdot \nabla n) + \frac{\partial}{\partial \gamma} (\dot{\gamma} n) + S(\gamma, \mathbf{r}, t) \quad (4.25)$$

4.2.3 Diffusion coefficient

In the previous section, I commented on how the scattering of CRs/high energy electrons is dependent on the Larmor radius and consequently its energy and that the propagation of CRs/high energy electrons is, in our case, sensitive to the diffusion coefficient D . The diffusion coefficient parallel to the magnetic field lines is defined as :

$$D_{\parallel} = \frac{r_L c}{3} \frac{1}{I(k)} \quad (4.26)$$

$$\int I(k) d \ln(k) = \left(\frac{\delta B}{B_0} \right)^2 \quad (4.27)$$

where $I(k)$ is the normalised energy density spectrum of the magnetic turbulence with wave number k . The diffusion coefficient perpendicular to the magnetic field lines is found to be (see Drury 1983):

$$D_{\perp} = D_{\parallel} \left(\frac{\delta B}{B_0} \right)^4 \quad (4.28)$$

which quickly illustrates the anisotropic diffusion case where $\delta B \ll B_0$ (as explained previously).

For the following, I however assume that the turbulence is non negligible and approximate the transport of CRs as an isotropic diffusion, I have $D_{\parallel} = D_{\perp} = D$. It is generally assumed that the distribution of

¹The value of the diffusion coefficient may however spatially vary and be dependent on the particle energy

the turbulence follow a power-law $I(k) \propto k^{-s}$. Three special cases have been used in the literature while describing the motion of CRs/high energy electrons : The Kolmogorov spectrum $s = 5/3$, the Kraichnan spectrum $s = 3/2$ and the Bohm diffusion $s = 1$. It leads to a diffusion coefficient $D(E) \propto E^{1/3}$ for the case of Kolmogorov turbulence, $D(E) \propto E^{1/2}$ for the Kraichnan turbulence and $D(E) \propto E$ for the Bohm diffusion limit, respectively. Recent studies have in fact indicated that a diffusion power-law spectrum $D(E) \propto E^\delta$ with $\delta = [0.5 - 0.7]$ seems to agree with observations (see Strong et al. 2007 for further details).

Measurements of the ratio between bore (B) and carbon (C) cosmic-rays also lead to a general value of the diffusion coefficient $D_{1\text{GeV}} \sim 10^{28} \text{ cm}^2 \text{ s}^{-1}$ for particles with rigidity $E/Ze = 1 \text{ GV}$ (i.e 1 GeV=1GV rigidity for protons and electrons, see Gaisser 1990). However, as the magnetic turbulence is enhanced towards high energy sources such as SNRs (see Malkov et al. 2013; Nava et al. 2016 and references therein) or CR precursors which already escaped the shock (Skilling, 1975), I may therefore expect, based on Eq. 4.27, that the diffusion coefficient will be significantly suppressed. Notably, in the extreme case where $\delta B \sim B_0$, the mean free path of CRs/high energy electrons becomes their Larmor radius r_L and their propagation thus follows the Bohm diffusion limit $D(E) = r_L c/3$.

Accounting for possible suppression of the diffusion of CRs, Gabici et al. (2007) parametrised the diffusion coefficient as follow :

$$D(E) = 3 \times 10^{27} \chi \left(\frac{E}{1 \text{ GeV}} \right)^{1/2} \left(\frac{B}{3 \mu\text{G}} \right)^{-1/2} \quad (4.29)$$

where χ is a suppression factor accounting for the enhanced turbulences nearby shocks. χ values of 0.01 and 1 notably represent the ‘slow’ and ‘fast’ diffusion defined by Aharonian & Atoyan (1996) near high energy sources. Based on the GeV gamma-ray studies towards W28, and analysis of the TeV emission from adjacent molecular clouds, suppression factors of $\chi = 0.01$ (Giuliani et al., 2010), $\chi = 0.06$ (Gabici et al., 2010) were suggested, while Li & Chen (2010) adopted $\chi = 0.1$. From the study of molecular cloud towards Sgr B2, Protheroe et al. (2008) also indicated that a suppression factor $\chi = 0.07$ would require a cosmic-ray density 7 times higher than the averaged Galactic cosmic-ray density. Consequently, I will focus on a diffusion coefficient suppression factor $\chi = 0.01$ to 0.1. Nonetheless, the value of χ and may vary from a region to another.

To summarize this section, the diffusion coefficient is energy dependent and is sensitive to the spectrum of turbulence enhanced by nearby shocks. In the next section, I will thus provide a more quantitative analysis on how the diffusion of CRs/high energy electrons affect their energy density distribution by solving Eq. 4.25.

4.2.4 Propagation Effects on the energy distribution of CRs/electrons and gamma-rays

From the propagation of CRs/high energy electrons, the energy distribution is now dependent on the position $n(\gamma, \mathbf{r}, t)$. In the case of an impulsive source located at the center of the molecular cloud and assuming an uniform diffusion coefficient, the solution for the case of an impulsive source $S(\gamma, \mathbf{r}, t) = \delta(r) \delta(t)$ is :

$$n(\gamma, r, t) = \frac{\dot{\gamma}_0}{\dot{\gamma}} \frac{n(\gamma, 0, 0)}{\pi^{3/2} R_{\text{diff}}(\gamma, t)^3} \exp\left(-\frac{r^2}{R_{\text{diff}}(\gamma, t)^2}\right) \quad (4.30)$$

$$R_{\text{diff}}(\gamma, t) = \sqrt{4 \int_{\gamma}^{\gamma_0} D(\gamma') \frac{d\gamma'}{\dot{\gamma}}} \quad (4.31)$$

where R_{diff} is the diffusive radius of a particle with initial Lorentz factor γ_0 reaching γ at epoch t . In the following case, I assume an initial power-law distribution $n(\gamma, 0, 0) = n_0 \gamma^{-\alpha}$.

High energy CRs

Impulsive source

Combining Eq. 4.11 with Eqs. 4.30 and 4.31, I obtain :

$$n(\gamma, r, t) = \frac{n_0 \gamma^{-\alpha}}{\pi^{3/2} R_{\text{diff}}^3} \exp\left(-\frac{(\alpha-1)t}{\tau_{\text{pp}}} - \frac{R^2}{R_{\text{diff}}^2}\right) \quad (4.32)$$

$$R_{\text{diff}} = \sqrt{4D(\gamma)t \frac{(\exp(\delta t/\tau_{\text{pp}}) - 1)}{\delta t/\tau_{\text{pp}}}} \quad (4.33)$$

Fig. 4.11 (top panel) illustrates the CR energy distribution at $R = 0$ pc (solid red line), $R = 10$ pc (solid green line) and $R = 20$ pc (solid blue line) at $t = 40$ kyr. For the case where $R_{\text{diff}} \ll R$ ($E_p < 0.1$ TeV at $R = 20$ pc, see dashed lines), I observe in Fig. 4.11 (bottom panel) that the CR energy spectrum is much harder than the initial spectrum as the low energy CR have not reached this region. In the opposite case where $R_{\text{diff}} \gg R$ (above the dashed lines in Fig. 4.11), the spectrum however becomes much softer with spectral index $\alpha' = \alpha + 3\delta/2$. As discussed in the previous section, I do not expect any spectral change from radiative cooling of CRs as the radiative cooling time is weakly dependent on γ for high energy CRs.

Continuous source

For the case of a continuous source, Eq. 4.25 must be solved numerically. Nonetheless, an analytical solution can be derived for the limiting case $t \ll \tau_{\text{pp}}$ by convolving Eq 4.30 with the source function (Aharonian & Atoyan, 1996). I thus obtain :

$$n(\gamma, r, t) = \frac{S(\gamma)}{4\pi D(\gamma) R} \text{erfc}\left(\frac{r}{R_{\text{diff}}}\right) \quad (4.34)$$

In Fig. 4.11 (bottom panel), the CR energy spectrum is hard at the energy range satisfying $R_{\text{diff}} \ll R$. However for the case $R_{\text{diff}} \gg R$, the spectral index becomes $\alpha' = \alpha + \delta$ which is slightly harder than for the impulsive case. Indeed, the loss of high energy CRs escaping the region is compensated by recently injected CRs.

Consequently, as the spectral index Γ of the gamma-ray SED roughly equals the CR spectral index at $E_\gamma = 10$ GeV to 10 TeV (Kelner et al., 2006), I do expect the gamma-ray spectrum to be harder than the one obtained from the initial CR spectrum for distances greater than R_{diff} and becomes steeper once the bulk of CRs crossed this region.

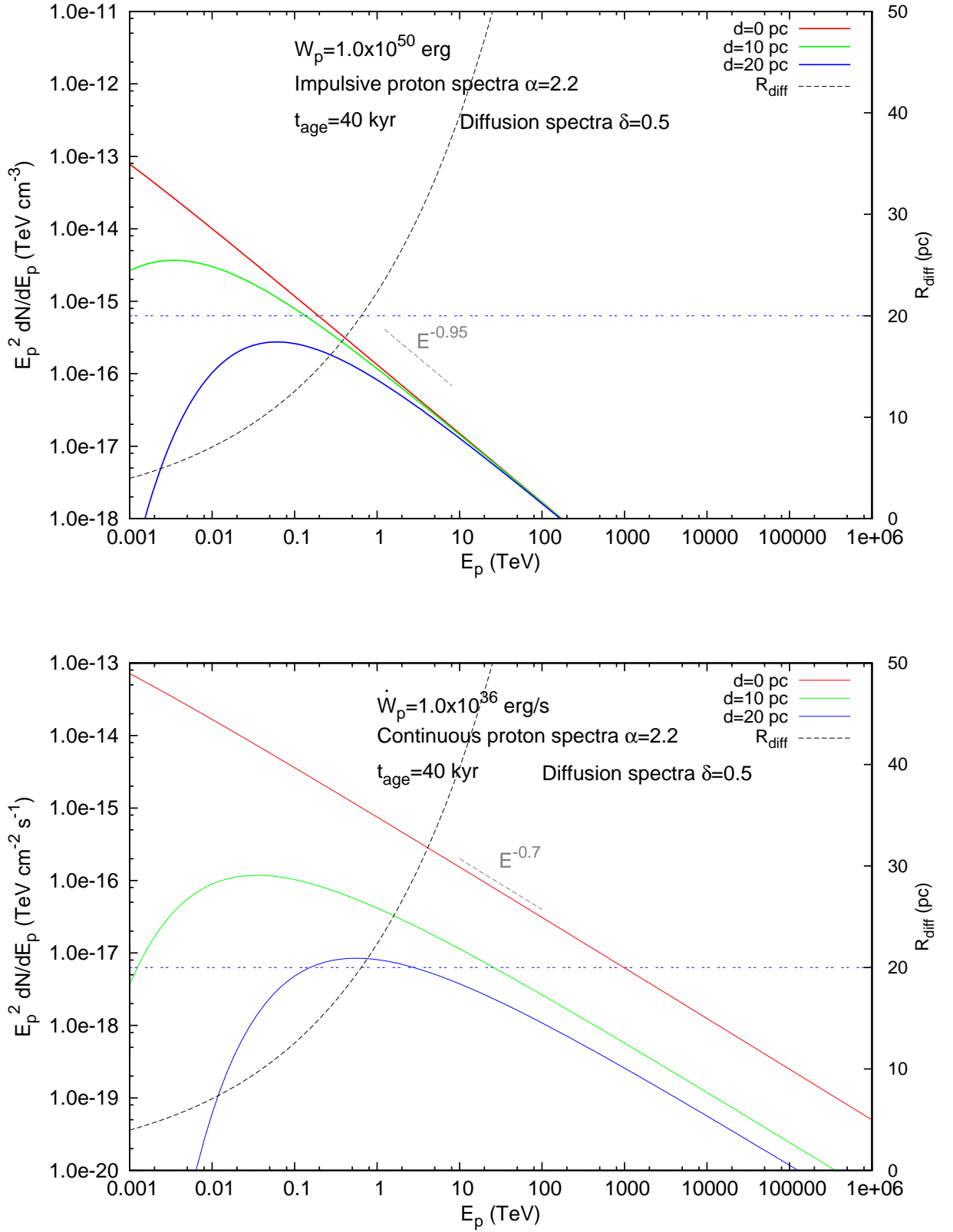


Figure 4.11: Energy distribution of CRs escaping an impulsive (top panel) or continuous source at $t = 40$ kyr at distance $d = 0$ pc (red line), $d = 10$ pc (green line), $d = 20$ pc (blue line). The black dashed line indicate R_{diff} . The horizontal blue dashed dotted line at $R = 20$ pc is here for clarity.

High energy electrons

Impulsive source

In the case of electrons injected by an *impulsive* source with synchrotron dominated cooling, I combine Eq. 4.30 with Eq. 4.20 and obtain for :

$$n(\gamma, r, t) = \frac{n(\gamma, 0, 0)}{\pi^{3/2} R_{\text{diff}}(\gamma, t)^3} (1 - \gamma b_s t)^{2-\alpha} \exp\left(-\frac{R^2}{R_{\text{diff}}(\gamma, t)^2}\right) \quad (4.35)$$

$$R_{\text{diff}}(\gamma, t) = \sqrt{4 \frac{D(\gamma)}{b_s \gamma (1-\delta)} \left(1 - (1 - \gamma b_s t)^{1-\delta}\right)} \quad (4.36)$$

Fig. 4.12 (top panel) illustrates the variation of the energy distribution of electrons at $R = 0$ pc (solid red line), $R = 10$ pc (solid green line) and $R = 20$ pc (solid blue line) at $t = 40$ kyr. As represented by the dashed line, R_{diff} does diverge at $E_c = \gamma_c m_e c^2 \sim 5$ TeV. At energies satisfying the condition $R_{\text{diff}} \ll R$, the spectrum of the electrons energy distribution is harder than its initial energy distribution. In this case, the photon SED is to show a harder spectrum for $R_{\text{diff}} \ll R$ but as time increases, the cutoff energies of both Synchrotron and IC radiation are expected to lower significantly as shown in Fig. 4.6.

Continuous source

In the case of a *continuous* source, the equation can only be solved numerically. I remind that only electrons injected between the time $t - t_c$ and t contribute to the energy distribution of electrons with Lorentz factor γ at time $t = 10$ kyr. From Fig. 4.12 (bottom panel), I finally remark that lower energy electrons reach higher R_{diff} (before diverging). Consequently, although I still observe a hard electron spectrum at energies satisfying $R_{\text{diff}} \gg R$, I also note a striking steepening of the electron energy spectrum as I increase distance from the continuous injector (as opposed to the CR case). Therefore the gamma-ray spectrum is also expected to steepen at high energies as I move away from the impulsive/continuous source.

4.2.5 Propagation in molecular clouds

Molecular clouds are expected to have a stronger magnetic field than the surrounding ISM (Crutcher et al., 2010), which not only leads to a slower diffusion of CRs/high energy electrons but also provokes severe energy losses for high energy electrons via synchrotron radiation (if the magnetic field is turbulent). Consequently, extended dense molecular clouds could potentially filter CRs from high energy electrons. The study of the gamma-ray morphology of the gamma-ray emission nearby molecular clouds could help determine the composition of high energy particles towards high energy sources.

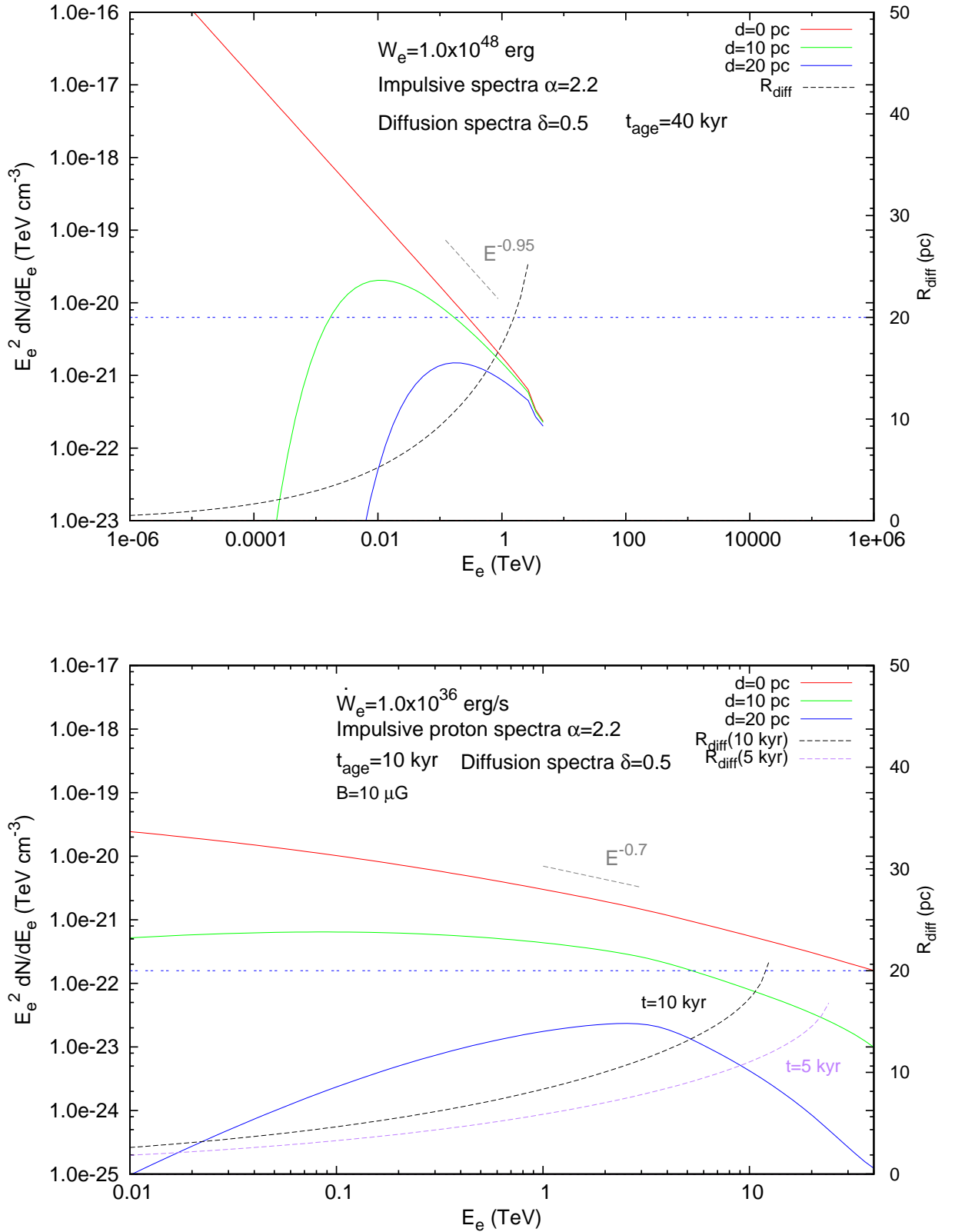


Figure 4.12: Energy distribution of high energy electrons escaping an impulsive (top panel) or continuous source (bottom panel) at $t = 40$ kyr and $t = 10$ kyr respectively and at distance $d = 0$ pc (red line), $d = 10$ pc (green line), $d = 20$ pc (blue line). The purple and black dashed line indicate R_{diff} for particles injected 5 kyr and 10 kyr ago respectively. The horizontal blue dashed dotted line at $R = 20$ pc is here for clarity.

Chapter 5

ISM Studies Towards TeV PWN HESSJ1825–137 and Northern Region (PAPER I)

Statement of Authorship

Title of Paper	ISM gas studies towards the TeV PWN HESS J1825-137 and northern region		
Publication Status	<input checked="" type="checkbox"/> Published	<input type="checkbox"/> Accepted for Publication	
	<input type="checkbox"/> Submitted for Publication	<input type="checkbox"/> Unpublished and Unsubmitted work written in manuscript style	
Publication Details	Voisin F., Rowell G., Burton M. G., Walsh A., Fukui Y., Aharonian F., 2016, MNRAS, 458, 2813		

Principal Author

Name of Principal Author (Candidate)	Fabien Voisin		
Contribution to the Paper	7mm-12mm Mopra data observations, molecular line analysis, ISM and high energy interpretation. Writing paper.		
Overall percentage (%)	58%		
Certification:	This paper reports on original research I conducted during the period of my Higher Degree by Research candidature and is not subject to any obligations or contractual agreements with a third party that would constrain its inclusion in this thesis. I am the primary author of this paper.		
Signature		Date	11/08/16

Co-Author Contributions

By signing the Statement of Authorship, each author certifies that:

- i. the candidate's stated contribution to the publication is accurate (as detailed above);
- ii. permission is granted for the candidate to include the publication in the thesis; and
- iii. the sum of all co-author contributions is equal to 100% less the candidate's stated contribution.

Name of Co-Author	Gavin Rowell		
Contribution to the Paper	ISM analysis- ISM/ High energy interpretation – Review (15%)		
Signature		Date	11/8/16

Name of Co-Author	Michael Burton		
Contribution to the Paper	ISM analysis – ISM interpretation - Review (10%)		
Signature		Date	11/8/16

Please cut and paste additional co-author panels here as required.

Name of Co-Author	Andrew Walsh		
Contribution to the Paper	HOPS Data (5%) n n		
Signature		Date	12/8/16

Name of Co-Author	Yasuo Fukui		
Contribution to the Paper	Nanten CO(1-0) data - ISM analysis -ISM interpretation (7%)		
Signature		Date	12/8/16

Name of Co-Author	Felix Aharonian		
Contribution to the Paper	High energy interpretation (5%)		
Signature		Date	11/08/2016



ISM gas studies towards the TeV PWN HESS J1825–137 and northern region

F. Voisin,^{1★} G. Rowell,^{1★} M. G. Burton,² A. Walsh,³ Y. Fukui⁴ and F. Aharonian^{5,6}¹*School of Physical Science, Adelaide university, North Terrace, Adelaide, SA 5005, Australia*²*School of Physics, University of New South Wales, Sydney, NSW 2052, Australia*³*International Centre for Radio Astronomy Research, Curtin University, GPO Box U1987, Perth, WA 6845, Australia*⁴*Department of Physics, University of Nagoya, Furo-cho, Chikusa-ku, Nagoya 464-8601, Japan*⁵*Max-Planck-Institut für Kernphysik, PO Box 103980, D-69029 Heidelberg, Germany*⁶*Dublin Institute for Advanced Studies, 31 Fitzwilliam Place, Dublin 2, Ireland*

Accepted 2016 February 25. Received 2016 January 14

ABSTRACT

HESS J1825–137 is a pulsar wind nebula (PWN) whose TeV emission extends across ~ 1 deg. Its large asymmetric shape indicates that its progenitor supernova interacted with a molecular cloud located in the north of the PWN as detected by previous CO Galactic survey (e.g. Lemièrre, Terrier & Djannati-Ataï). Here, we provide a detailed picture of the interstellar medium (ISM) towards the region north of HESS J1825–137, with the analysis of the dense molecular gas from our 7 and 12 mm Mopra survey and the more diffuse molecular gas from the Nanten CO(1–0) and GRS $^{13}\text{CO}(1–0)$ surveys. Our focus is the possible association between HESS J1825–137 and the unidentified TeV source to the north, HESS J1826–130. We report several dense molecular regions whose kinematic distance matched the dispersion measured distance of the pulsar. Among them, the dense molecular gas located at (RA, Dec.) = (18^h421m, –13[°]28′) shows enhanced turbulence and we suggest that the velocity structure in this region may be explained by a cloud–cloud collision scenario. Furthermore, the presence of a H α rim may be the first evidence of the progenitor supernova remnant (SNR) of the pulsar PSR J1826–1334 as the distance between the H α rim and the TeV source matched with the predicted SNR radius $R_{\text{SNR}} \sim 120$ pc. From our ISM study, we identify a few plausible origins of the HESS J1826–130 emission, including the progenitor SNR of PSR J1826–1334 and the PWN G018.5–0.4 powered by PSR J1826–1256. A deeper TeV study however, is required to fully identify the origin of this mysterious TeV source.

Key words: molecular data – pulsars: individual: PSR J1826–1334 – ISM: clouds – cosmic rays – gamma-rays: ISM.

1 INTRODUCTION

HESS J1825–137 is one of the brightest and most extensive pulsar wind nebulae (PWNe) detected in TeV γ -rays (Aharonian et al. 2006). It is powered by the high spin-down power ($\dot{E}_{\text{SD}} = 2.8 \times 10^{36}$ erg s^{–1}) pulsar PSR J1826–1334 with a dispersion measure distance of 3.9 ± 0.4 kpc and characteristic age $\tau_c \sim 20$ kyr.

PWNe represent a significant fraction of the Galactic TeV γ -ray source population. They convert a varying fraction of their pulsars’ spin-down energy \dot{E}_{SD} into high-energy electrons. The electron flow is temporally randomized and re-accelerated at a termination shock resulting from pressure from the surrounding interstellar medium

(ISM). Inverse-Compton up-scattering of soft photons then leads to TeV γ -rays, and associated synchrotron radio to X-ray emission.

The morphology of PWNe can be heavily influenced by the ISM. The interaction of the progenitor supernova shock with adjacent molecular clouds can lead to a reverse shock propagating back into the PWN (Blondin, Chevalier & Frierson 2001), giving rise to an asymmetry in the radio, X-ray and γ -ray emission that can trail away from the pulsar along the pulsar-molecular cloud axis.

HESS J1825–137 is an excellent example of this situation. The morphology of HESS J1825–137 (Fig. 1) displays a clear asymmetry with respect to PSR J1826–1334, and a molecular cloud to the north revealed by Lemièrre et al. (2005), with the bulk of the TeV γ -ray extending up to a degree south of the pulsar.

Interestingly, the weak TeV γ -ray emission component to the north labeled HESS J1826–130 (Deil et al. 2015) appears to

*E-mail: fabien.voisin@student.adelaide.edu.au (FV); growell@physics.adelaide.edu.au (GR)

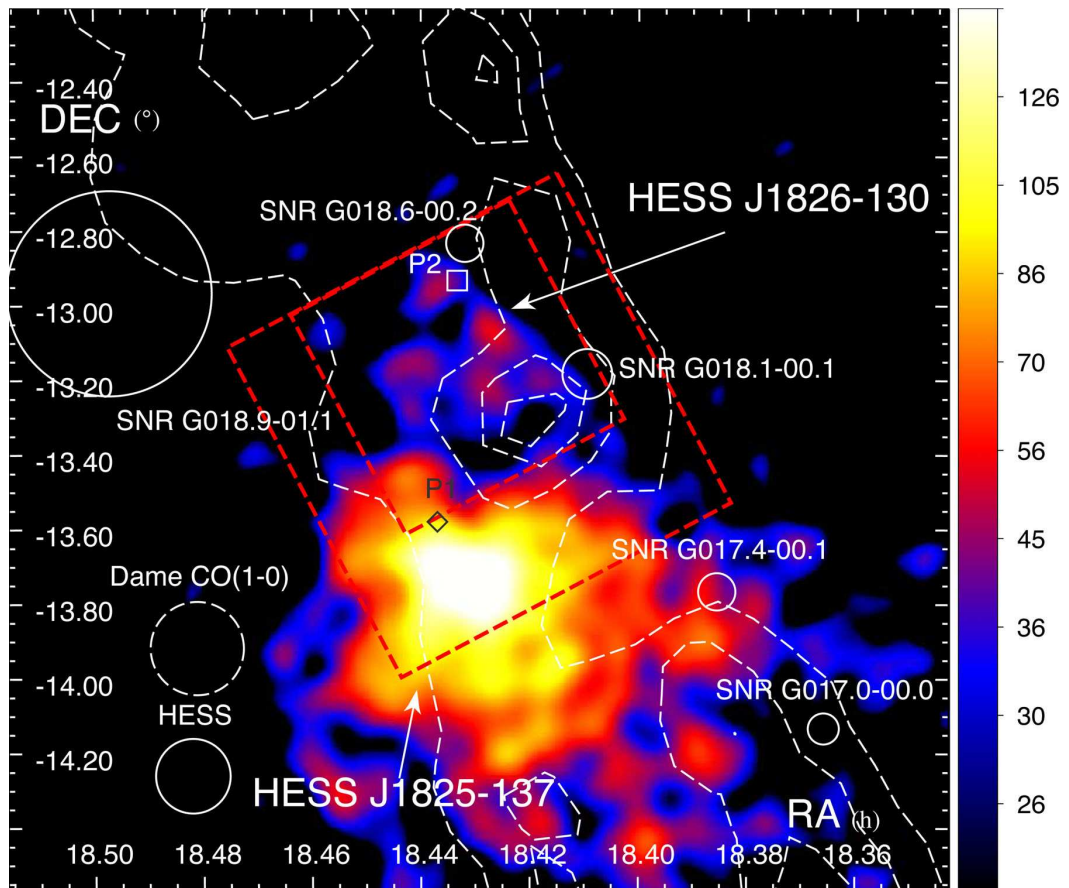


Figure 1. HESS excess counts image (>100 GeV) towards HESS J1825–137 overlaid by the CO(1–0) integrated intensity contour ($40, 60, 80, 100$ K km s $^{-1}$) between $v_{\text{lsr}} = 40$ and 60 km s $^{-1}$ from Dame, Hartmann & Thaddeus (2001) as revealed by Lemièrre et al. (2005). The white circles represent the different SNRs detected (Brogan et al. 2006). P1 indicates the pulsar PSR J1826–1334’s location while P2 shows the position of PSR J1826–1256. The small and large red dashed boxes (see online version) represent our 7 and 12 mm Mopra coverage, respectively.

spatially overlap this northern molecular cloud (see Fig. 1). Such an overlap could result from the interaction of multi-TeV cosmic rays with molecular clouds, and thus raises the possibility of cosmic ray acceleration in the vicinity, notably from HESS J1825–137’s progenitor supernova remnant (SNR).

We also note the presence of two additional SNRs in the region : G018.1–0.1 and G018.6–0.2 (Brogan et al. 2006) as shown in Fig. 1. Ray et al. (2011) also discovered the radio quiet pulsar PSR J1826–1256 (P2 in Fig. 1) with a spin-down luminosity $\dot{E}_{\text{SD}} = 3.6 \times 10^{36}$ erg s $^{-1}$, a period $P = 100$ ms and a characteristic age $\tau_c = 13$ kyr and powering the PWN G018.5–0.4 observed in X-rays by Roberts et al. (2007). Although no dispersion measure could be derived, Wang (2011) argues that the pulsar is located at a distance $d = 1.2$ – 1.4 kpc. Consequently, it is possible each of these sources could also contribute to the TeV emission inside HESS J1826–130.

To further investigate this issue, higher resolution mapping (improving that of the 8 arcmin resolution of the CO(1–0) data used by Lemièrre et al. 2005) of the molecular cloud and surrounding region is needed to probe the density and dynamics of the gas. In this paper, we made use of CO, and ^{13}CO survey data (from the Nanten telescope and the Galactic Ring Survey – GRS) plus new mapping of dense gas tracers such as carbon monosulphide (CS) and ammonia (NH_3) with the Mopra telescope in Australia.

In Section 2, we review the properties of the Mopra and Nanten telescopes, and the GRS as well as the methodology used to reduce our Mopra observations. Then, in Section 3, we briefly introduce the different gas tracers that we detected towards HESS J1826–130 and their physical properties. We present the results of our observations and provide gas parameter estimates for various regions using our CO, CS and NH_3 analysis in Section 4. Finally, in Section 5, we discuss the dynamics of the dense gas and finally discuss a few possible counterparts to the HESS J1826–130 emission.

2 DATA OBSERVATION AND REDUCTION

2.1 Mopra

We observed a 60 arcmin \times 60 arcmin region (large red dashed box in Fig. 1) centred at (RA,Dec.) = ($18^{\text{h}}425$, $-13^{\circ}3$) in the 12 mm band from the 2012 January 19 to 27 with the 22 m Mopra telescope. We combined our observations with the HOPS survey (Walsh et al. 2011), which covered the Galactic plane within the Galactic latitude $b = -0.5$ to $b = 0.5$ to achieve better sensitivity (see Table 1). Additionally, we observed a 40 arcmin \times 40 arcmin subsection (small red dashed box in Fig. 1) centred at (RA,Dec.) = ($18^{\text{h}}427$, $-13^{\circ}17$) in the 7 mm band. Four 7 mm ON–OFF switched deep pointings

Table 1. List of all gas tracers detected during our Mopra 7 and 12 mm observations towards HESS J1826–130, their respective rest frequencies, and the achieved mapping T_{rms} of the data cubes where these emission are found.

Tracer	Frequency (GHz)	T_{rms} (K/channel)
7 mm		
SiO(1–0, $v = 2$)	42.820 582	0.05
SiO(1–0, $v = 0$)	43.423 864	0.05
CH ₃ OH(7 ₀ –6 ₁)	44.069 476	0.06
H51 α	45.453 720	0.06
HC ₃ N(5–4, $F = 4-3$)	46.247 580	0.06
C ³⁴ S(1–0)	48.206 946	0.08
CS(1–0)	48.990 957	0.08
12 mm		
H69 α	19.591 110	0.05
H65 α	23.404 280	0.05
NH ₃ (1,1)	23.594 470	0.05
NH ₃ (2,2)	23.722 634	0.05
NH ₃ (3,3)	23.870 127	0.05
H62 α	26.939 170	0.05

were taken at (RA, Dec.) = (18^h419, –13[°]38), (18^h423, –13[°]34), (18^h419, –13[°]31) and (18^h420, –13[°]27) from the 13th until the 21st of April to search for additional emission from the isotopologue C³⁴S(1–0). Unfortunately, our observations were not sensitive enough to detect such emission. Finally, another 7 mm deep pointing was taken in 2014 August towards the position (RA, Dec.) = (18^h419, –14[°]04) towards a molecular cloud south of HESS J1825–137.

For these observations, we used the Mopra spectrometer MOPS in ‘zoom’ mode, which allowed the recording of sixteen sub-bands, each consisting of 4096 channels and a 137.5 MHz bandwidth, simultaneously. The Mopra on the fly (OTF) mapping fully sampled the region with a beam size of 2 arcmin (12 mm) and 1 arcmin (7 mm), a velocity resolution of 0.4 km s^{–1} (12 mm) and 0.2 km s^{–1} (7 mm). For the reduction of our OTF observations, we first used LIVEDATA¹ which outputs the spectra of each scan using an OFF position as reference. We used a first-order polynomial fit to subtract the baseline. Then, we used GRIDZILLA² to produce 3D cubes of each sub-bands in antenna temperature T_A^* (K) as a function of RA, Dec. and line-of-sight velocity. We used a 15 arcsec grid to map our region and the data were finally smoothed via a Gaussian with 1.25 arcmin FWHM in order to smooth out fluctuations. The T_{rms} /channel of each map in which detections have been found are listed in Table 1.

Finally, we used the ASAP³ software to reduce our ON-OFF deep pointing observations. The OFF position measurement was used to obtain the antenna temperature T_A^* of each scans. The achieved T_{rms} /channel ranges from 0.05 to 0.1 K. The beam temperature T_{mb} of maps and ON/OFF pointings were obtained using the main beam conversion factor η_{mb} determined by Urquhart et al. (2010, see Appendix A).

2.2 Nanten and GRS

To probe the more extended diffuse gas, we made use of more recent CO observations. The 4 m Nanten telescope carried out a

ISM studies towards HESS J1825–137 2815

CO(1–0) survey over the Galactic plane with a 2.6 arcmin beam size and a sampling grid of 4 arcmin, a velocity resolution $\Delta v = 1.0$ km s^{–1} (Mizuno & Fukui 2004) and a typical T_{rms} /channel value of ~ 0.35 K. The GRS ¹³CO(1–0) mapped the Galactic ring in our Galaxy using the Five College Radio Astronomy Observatory. It has a beam FWHM of 44 arcsec, a sampling grid of 22 arcsec, a velocity resolution $\Delta v \sim 0.2$ km s^{–1} and an averaged T_{rms} /channel ~ 0.36 K (Jackson 2004).

3 OVERVIEW OF DETECTED LINES

Table 1 indicates the various spectral lines detected in our analysis of Mopra data. The following sections review the properties of the major spectral tracers.

3.1 Carbon monosulfide CS(1–0) and isotopologues

A major 7 mm line in our study is the $J = 1-0$ emission from the carbon monosulfide (CS) molecule. CS is commonly found inside dense cores. Its critical density, n_c , at $T_k = 10$ K is $\sim 2 \times 10^4$ cm^{–3} and thus allows study of dense clumps located inside molecular clouds. The isotopologues of CS namely C³⁴S, and C¹³S are generally assumed to be optically thin given their abundance ratio [CS]/[C³⁴S] ~ 24 and [CS]/[¹³CS] ~ 75 based on terrestrial measurements (see e.g. Frerking et al. 1980). Their detection can provide estimates of optical depth and thus robust mass estimates of dense cores.

3.2 Ammonia NH₃

Ho & Townes (1983) outlined the properties of the ammonia molecule. The NH₃(J,K) structure consists of ladders where J is the total momentum and K is the momentum from the quadrupole axis. Only energy states where $J = K$ are metastable and thus can be populated easily. NH₃(1,1) spectra consist of one main line surrounded by four satellite lines whose expected relative strength compared to the main component is ~ 25 per cent. However, the ratio depends on optical depth, and so this enables an efficient estimation of the dense molecular gas opacity. Finally, the relative strength of the NH₃(2,2) and NH₃(3,3) satellite lines relative to their main components are ~ 5 per cent and ~ 3 per cent, respectively, and it is therefore unlikely to detect these satellite lines.

3.3 SiO(1–0)

Silicates can be released from dust grains into the gas phase from the crossing of a weak shock inside the molecular clouds (Schilke et al. 1997; Gusdorf et al. 2008). Silicon monoxide is then produced behind the shock and the non-vibrational SiO(1–0, $v = 0$) emission can be detected. Its detection becomes optimal for a shock speed $v_s = 25-50$ km s^{–1} and a target density $n_{\text{H}} = 10^4$ cm^{–3} (Gusdorf et al. 2008). Our 7 mm settings also enabled a search for SiO(1–0, $v = 1-3$), and their non-vibrational isotopologues ²⁹SiO(1–0, $v = 0$) and ³⁰SiO(1–0, $v = 0$).

3.4 Other spectral tracers

The 12 and 7 mm recombination lines H62 α , H65 α and H69 α and H51 α indicate ionized gas by UV radiation from nearby stars in H II complexes. Thus, these are important tracers of star formation and photodissociation regions where newborn stars radiate inside molecular clouds.

¹ <http://www.atnf.csiro.au/computing/software/livedata/>

² <http://www.atnf.csiro.au/computing/software/Gridzilla/>

³ <http://svn.atnf.csiro.au/trac/asap>

Cyanoacetylene (HC_3N) can be detected in warm molecular clouds and can be associated with star forming regions. This line emission is typically assumed optically thin and the large number of transitions available in the millimetre band allow the computation of physical parameters of molecular clouds (Morris et al. 1976).

Also, the methanol transition $\text{CH}_3\text{OH}(7_0-6_1)$ is a class I maser and generally traces star formation outflows. Weak shocks also tend to release CH_3OH from the grain mantle and collisionally pump the molecule from increased interaction with H_2 (see Voronkov et al. 2014 and references therein).

4 RESULTS AND ANALYSIS

4.1 Overview

Figs 2 and 3 show the $\text{CO}(1-0)$, $^{13}\text{CO}(1-0)$, $\text{CS}(1-0)$ and $\text{NH}_3(1,1)$ integrated intensity maps over three different velocity spans.

As shown in the top panel of Fig. 4, we noticed that the velocity distribution of all detections inside the region covered by our 7 mm survey mostly peaked in four velocity regions: $v_{\text{lsr}} = 40 \text{ km s}^{-1}$, $v_{\text{lsr}} = 45 \text{ km s}^{-1}$, $v_{\text{lsr}} = 50 \text{ km s}^{-1}$ and $v_{\text{lsr}} = 68 \text{ km s}^{-1}$ and the $^{13}\text{CO}(1-0)$ emission showed distinct structures at each velocities. We identified six bright regions, that we labeled R1 to R6 (see Figs 2 and 3). Each region showed bright emission from CO, CS and NH_3 listed above (see Fig. 5 for spectral plots), with the exception of R6 whose $\text{NH}_3(1,1)$ averaged emission over the region was too weak. The composition of these regions will be discussed in detail in order to provide a better understanding about the complex morphology of the observed emission.

Fig. 6 shows the $8 \mu\text{m}$ continuum image from the *Spitzer* GLIMPSE survey (Churchwell et al. 2009). The spectra of the different tracers of star-forming region are also shown in Fig. 7. We observed various infra-red (IR) features spatially coincident with dense molecular gas from some the aforementioned regions. Anderson et al. (2014) indicated that these IR sources were mostly H II regions (see red diamonds in Fig. 3). We detected several star-forming region tracers that were spatially coincident with these IR sources (which will be detailed in the next section). Association between these IR regions and the aforementioned molecular gas regions indicate likely source for driving the gas motion.

4.2 $\text{CO}(1-0)$ and $^{13}\text{CO}(1-0)$ analysis

The $\text{CO}(1-0)$ and its isotopologue $^{13}\text{CO}(1-0)$ averaged emission in the selected regions R1–R6 were fitted with a single Gaussian. The components from each region were labeled from ‘a’ to ‘f’ according to the velocity group they belonged to. For example, ‘a’ represents the velocity range $v_{\text{lsr}} = 46\text{--}55 \text{ km s}^{-1}$ matching the pulsar P1’s kinematic distance, whilst ‘b’, ‘c’, ‘d’, ‘e’ and ‘f’ indicate the range $v_{\text{lsr}} = 44\text{--}46 \text{ km s}^{-1}$, $39\text{--}44 \text{ km s}^{-1}$, $55\text{--}62 \text{ km s}^{-1}$, $62\text{--}75 \text{ km s}^{-1}$ and $30\text{--}35 \text{ km s}^{-1}$, respectively. The total mass was also determined using the $\text{CO}(1-0)$ averaged integrated intensity W_{CO} and the conversion factor $X_{\text{CO}} = 2.0 \times 10^{20} \text{ cm}^{-2}/(\text{K km s}^{-1})$. The conversion factor is generally assumed to be constant across the Galactic plane although its value may slightly vary as a function of the galactocentric radius (Strong et al. 2004). Finally, we used a prolate geometry to provide H_2 density, n_{H_2} , estimates via equation (G12). The total proton density n_{H} can be deduced using $n_{\text{H}} = 2.8 n_{\text{H}_2}$ which accounts for 20 per cent He fraction. We also used the full width half-maximum (FWHM) of the isotopologue $^{13}\text{CO}(1-0)$, less prone to optical depth effects (e.g. broadening), to obtain the Virial mass M_{vir} of the selected regions. We used the

inverse-squared r^{-2} and Gaussian density distribution (see Protheroe et al. 2008) as lower and upper-range of the Virial masses, respectively.

Among the observed clouds, the one located at $v_{\text{lsr}} = 45\text{--}60 \text{ km s}^{-1}$ is at a kinematic distance $d = 4 \text{ kpc}$ which is similar to that of the pulsar PSR J1826–1334, is adjacent to HESS J1825–137 (see red dashed circle in the middle-right panel of Fig. 2). Assuming the molecular cloud to be spherical with radius $R_{\text{MC}} \sim 18 \text{ pc}$ and centred at (RA,Dec.) = ($18^{\text{h}}431, -13^{\circ}26$), we obtain from our $\text{CO}(1-0)$ observations an averaged density over the region $n_{\text{H}} \sim 6.1 \times 10^2 \text{ cm}^{-3}$ and a total mass $M_{\text{H}_2} \sim 3.3 \times 10^5 M_{\odot}$. The density distribution is not uniform as shown by the presence of several molecular clumps (e.g. as in sub-regions labeled R1 to R5) seen in $\text{CO}(1-0)$ and $\text{CS}(1-0)$.

We also detected via the $\text{CO}(1-0)$ and $^{13}\text{CO}(1-0)$ molecular transitions a diffuse molecular cloud at $v_{\text{lsr}} = 18 \text{ km s}^{-1}$ as shown in Fig. D1. Its kinematic distance $d = 1.7 \text{ kpc}$ is similar to the pulsar PSR J1826–1256’s estimated distance and it sits between the pulsar and the SNR G018.6–0.2. We derived a total mass $M_{\text{H}_2} = 5.3 \times 10^3 M_{\odot}$ and an averaged density over the region $n_{\text{H}} = 5.9 \times 10^2 \text{ cm}^{-3}$ (within the red circle in Fig. D1). At $v_{\text{lsr}} = 60\text{--}80 \text{ km s}^{-1}$ (see Fig. 2 bottom panel), we also observed that the molecular gas appears adjacent to the pulsar P2 and the SNR G018.6–0.2 with the bulk of the molecular gas located north of the pulsar P2.

4.3 CS analysis

From the different spectra shown in Fig. 5, $\text{CS}(1-0)$ components were also fitted with a single Gaussian and the fit parameters have been listed in Tables 2 and 3. In order to derive physical parameters of the different regions, we used the local thermal equilibrium assumption (LTE). In the case where the isotopologue $\text{C}^{34}\text{S}(1-0)$ were also detected, we estimated of the averaged optical depth $\tau_{\text{CS}(1-0)}$ using equation (G1). An optically thin scenario $\tau_{\text{CS}(1-0)} = 0$ would otherwise be used to obtain the column density of the upper state N_{CS_1} via equation (G2). The averaged $\text{C}^{34}\text{S}(1-0)$ spectra detected in some of the studied regions R1,R2,R3 are shown in Fig. C1.

We used the estimated kinetic temperature T_{kin} from our NH_3 analysis (see below) to obtain the total column density N_{CS} using equation (G3). This assumption was only valid if our NH_3 and CS tracers probed the same gas. In all other cases, we assumed $T_{\text{kin}} = 10 \text{ K}$.

In order to obtain the H_2 column density N_{H_2} , we chose the abundance ratio $\chi_{\text{CS}} = 4 \times 10^{-9}$ which was in the range of values $\chi_{\text{CS}} = 10^{-9} \rightarrow 10^{-8}$ indicated by Irvine, Goldsmith & Hjalmarsen (1987) who studied the chemical abundances inside several distinct regions e.g. Orion KL and Sgr B2. Zinchenko et al. (1994) also chose this abundance ratio for the study of several CS cores. The derived H_2 parameters are scaled by the abundance ratio and thus may vary by a factor of 2.

We provided total mass estimates by using the kinematic distance in equation (G11) and considering the molecular gas consisted of 20 per cent Helium. As per our CO analysis, we used a prolate geometry to provide H_2 density n_{H_2} estimates.

4.4 NH_3 analysis

To fit the emission of the $\text{NH}_3(1,1)$ inversion transition, we used five Gaussians separated by known velocities to fit the main peak and the four satellite lines (Wilson, Bieging & Downes 1978). The fit parameters of each regions were listed in Table 3.

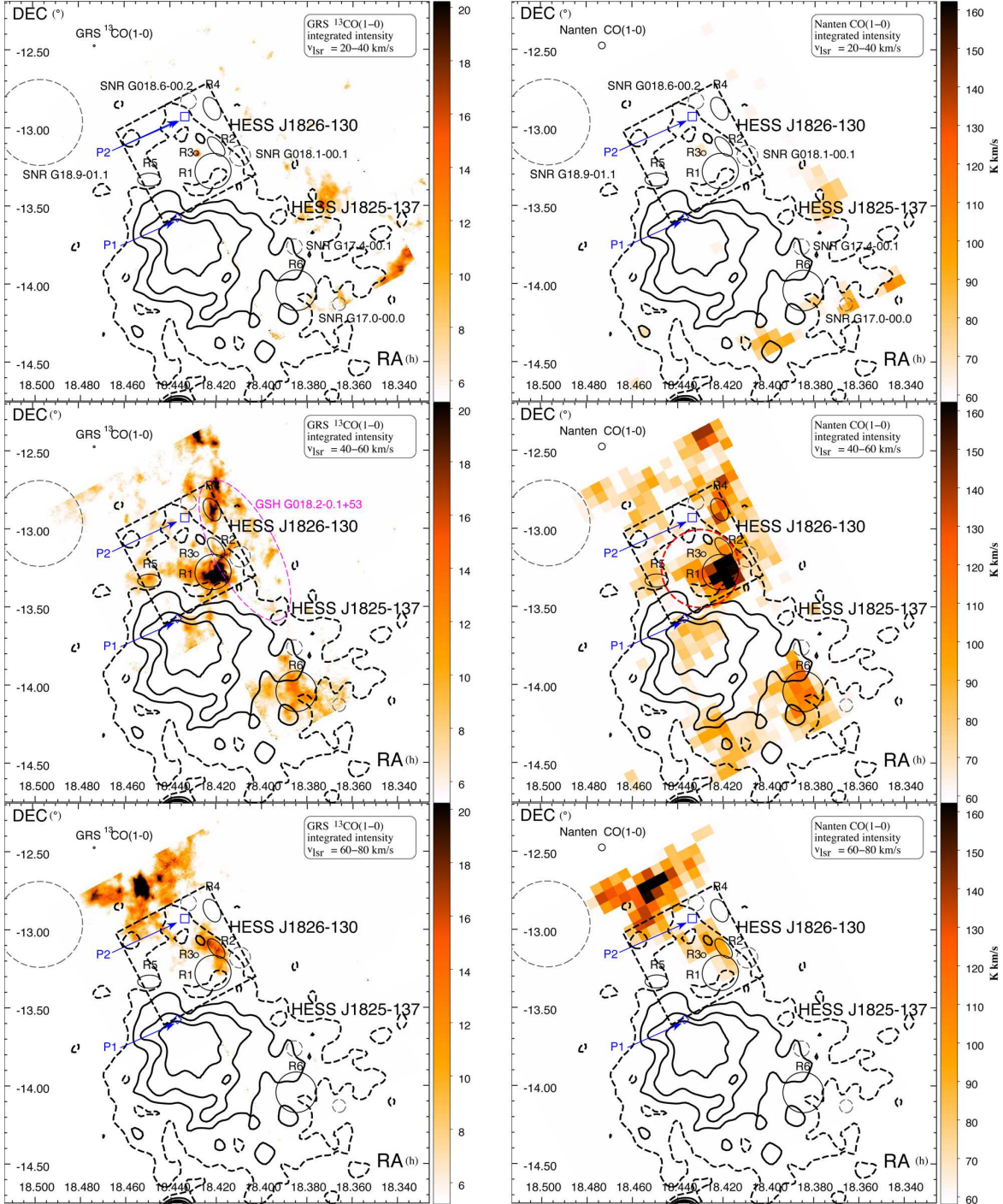


Figure 2. GRS $^{13}\text{CO}(1-0)$ (left) and Nanten $\text{CO}(1-0)$ (right) integrated intensity between $v_{\text{lsr}} = 20\text{--}40\text{ km s}^{-1}$, $v_{\text{lsr}} = 40\text{--}60\text{ km s}^{-1}$ and $v_{\text{lsr}} = 60\text{--}80\text{ km s}^{-1}$. The different black ellipses represent regions for further discussion based on detection of dense gas via the $\text{CS}(1-0)$ and $\text{NH}_3(1,1)$ tracers (see Fig. 3). The HESS TeV emission from HESS J1825–137 and HESS J1826–130 is shown in black contours (dashed and solid) and the surrounding SNRs are displayed in black dashed circles with their label displayed in the first panels. The region covered by our 7 mm survey is shown in black dashed box. The putative molecular shell GSH 18.1–0.2+53 (Paron et al. 2013) is shown in purple dashed ellipse (see online version) in the middle-left panel. Finally, the red dashed circle in the middle-right panel represents the region whose mass and density have been calculated (see Section 4.2).

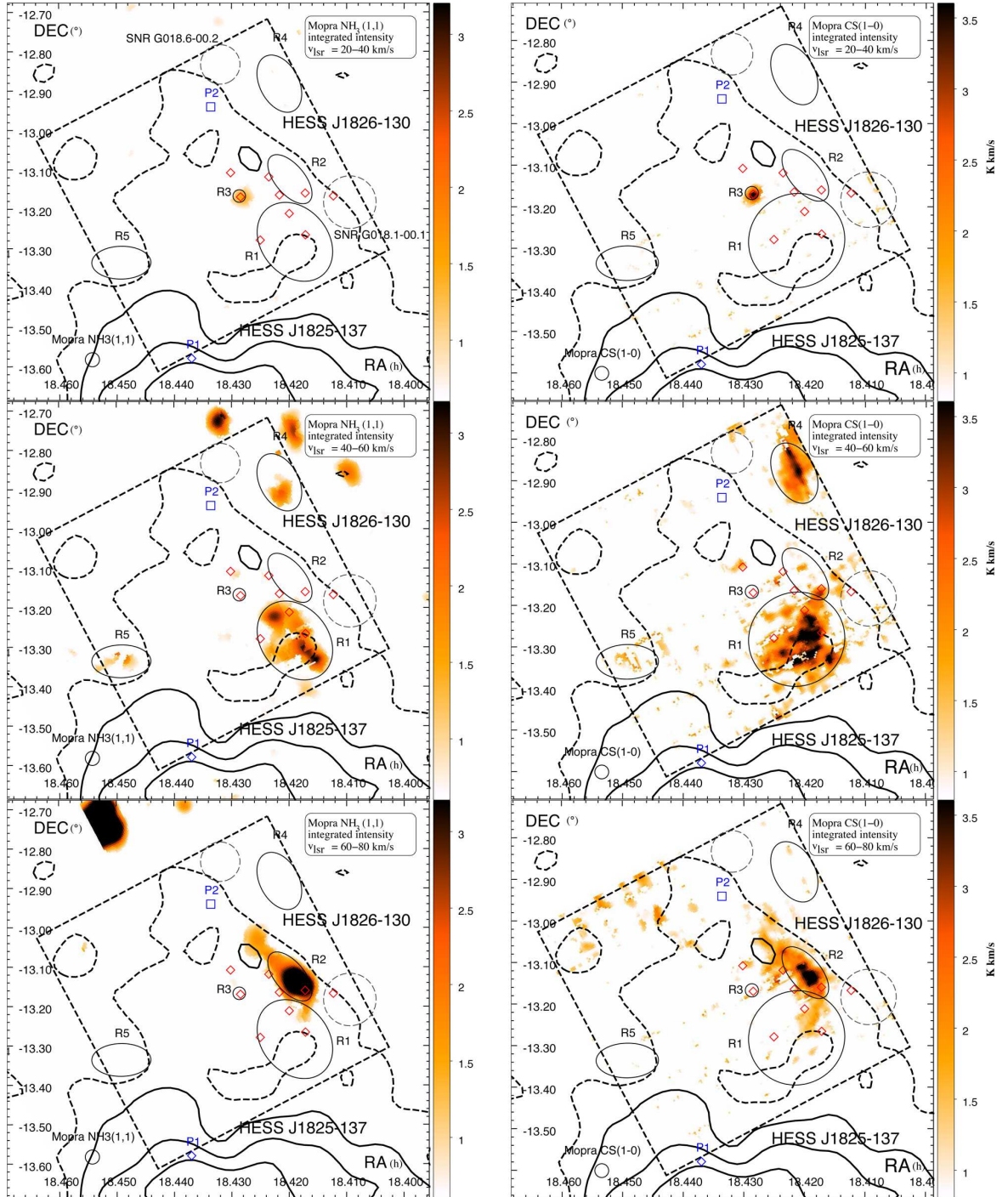


Figure 3. Mopra $\text{NH}_3(1,1)$ and $\text{CS}(1-0)$ integrated intensity between $v_{\text{LSR}} = 20-40 \text{ km s}^{-1}$, $v_{\text{LSR}} = 40-60 \text{ km s}^{-1}$ and $v_{\text{LSR}} = 60-80 \text{ km s}^{-1}$ overlaid by the different regions where $\text{NH}_3(1,1)$ and $\text{CS}(1-0)$ were detected. The region covered by our 7 mm survey is shown in black dashed box. The diamonds (red in colour version) indicate the different H II regions shown in the SIMBAD data base (see Anderson et al. 2014 for latest H II regions catalogue) while the SNRs are shown in black dashed circles with their labels shown in the top panels.

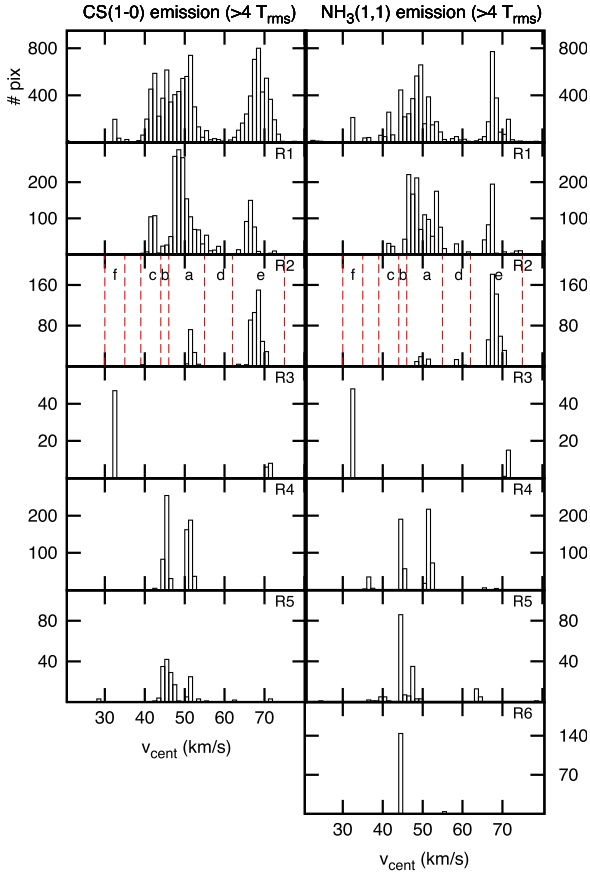


Figure 4. CS(1–0) (left) and NH₃(1,1) (right) binned centroid velocity distribution (1 km s^{−1} intervals) per pixel of the components detected above 4 T_{rms} towards the region covered by our 7 mm survey and more specifically the regions R1 to R6. The sub-components ‘a’ to ‘f’ referring to distinct velocity groups (see text and Tables 2 and 3) are delimited by the dashed-red vertical lines (see online version).

Whenever we detected NH₃(1,1) satellite lines, we used the ratio of the integrated intensity between the main and satellite line and used equation (G4) to determine the averaged main line optical depth. Finally, based on the NH₃(1,1) partition function, we used equation (G5) to estimate the optical depth of the NH₃(1,1) emission $\tau_{\text{NH}_3(1,1)}$.

As per our CS analysis, we approximated our regions to be in LTE and used equation (G7) to obtain the NH₃(1,1) column density. If NH₃(2,2) emission was also detected, we obtained the temperature T_{kin} using equations G8 and G9. This method remains only valid for kinetic temperature below 40 K. We then considered an even chemical abundance between ortho-NH₃ and para-NH₃ to obtain the total column density N_{NH_3} via equation (G10). To convert the NH₃ column density into H₂ column density, we used an abundance ratio $\chi_{\text{NH}_3} = 1 \times 10^{-8}$ which is in the range provided by Irvine et al. (1987). Finally, the same method as per our CS and CO analysis was used to determine the mass and density estimates. From Fig. 3, we find that the morphology of the gas detected by the NH₃(1,1) inversion transition coincides with the CS(1–0) emission towards the region covered by our 7 mm survey.

4.5 H I ANALYSIS

In order to complete the picture of the gas distribution towards HESS J1826–130, we made use of Southern Galactic Plane Survey (SGPS) data with $\Delta v = 0.8$ km s^{−1} and $T_{\text{rms}} = 1.4$ K/channel (McClure-Griffiths et al. 2005) to search for diffuse atomic gas.

Comparing H I and CO(1–0) is an effective method to provide kinematic distance ambiguity resolution of molecular clouds (see Anderson & Bania 2009; Roman-Duval et al. 2010 for further details) provided we know the location of the continuum source appearing in the line of sight. For instance, Fig. 7 shows the association between the CO(1–0) emission (blue lines) and the H I absorption (black lines) in region H1 and H3.

We also use the H I data to probe potential dips associated with energetic sources (e.g. SNRs) in order to provide an estimate of their kinematic distance. Fig. 8 shows the H I integrated intensity towards HESS J1826–130 between $v_{\text{lsr}} = 58$ and 64 km s^{−1}. We noticed a dip in H I emission towards SNR G018.6–0.2 which did not overlap with the ¹³CO(1–0) contour shown in red. From the GRS ¹³CO(1–0) longitude-velocity plot in Fig. E1, we also noted a lack of emission at $v_{\text{lsr}} = 60$ –70 km s^{−1} spatially coincident with this SNR position, with weak emission at $v_{\text{lsr}} \sim 60$ km s^{−1} and ~ 75 km s^{−1}. These weak ¹³CO(1–0) features may provide further evidence of a shell towards this SNR where molecular gas have been accelerated. Thus, we argue a shell has been produced by SNR G018.6–0.2’s progenitor star located at $v_{\text{lsr}} \sim 60$ –64 km s^{−1} inferring a SNR distance $d = 4.5$ kpc (near) or 11.4 kpc (far).

4.6 Discussion of individual regions

4.6.1 Region R1

Region R1 (RA = 18^h421, Dec. = −13^o28) is located 0^o.5 away from the pulsar PSR J1826–1334 and contains the bulk of the ¹³CO(1–0) and CS(1–0) emission. From the CO(1–0) and ¹³CO(1–0) molecular transitions, we detected four components with kinematic velocities $v_{\text{lsr}} = 48$ km s^{−1} (R1a), $v_{\text{lsr}} = 41$ km s^{−1} (R1c), $v_{\text{lsr}} = 58$ km s^{−1} (R1d) and $v_{\text{lsr}} = 67$ km s^{−1} (R1e). CS(1–0) was also found in R1a,b,c. However, only the component R1a and R1b remained visible in NH₃(1,1). The CS(1–0) emission in R1a ($v_{\text{lsr}} = 48$ km s^{−1}, see Table 2) is quite broad ($\Delta v_{\text{FWHM}} \sim 10$ km s^{−1}) compared to the other fainter components along the line of sight.

We also found two 44 GHz CH₃OH masers that we labeled CH1 ($v_{\text{lsr}} = 46$ km s^{−1}) and CH2 ($v_{\text{lsr}} = 56$ km s^{−1}) (see Fig. 6). They are thus associated with the molecular cloud traced by the component R1a and R1d. While the component CH1 seems connected to the IR bubble N22 (labeled by Churchwell et al. 2006), CH2 is likely associated with the H II region HDRS G018.097–0.324 (H2 in Fig. 6). We also found H51 α , H62 α , H65 α and H69 α emission at $v_{\text{lsr}} \sim 50$ –55 km s^{−1} coincident with region H1 at kinematic distances roughly agreeing with the distance $d = 4.3$ kpc proposed by Jackson (2004). From the H I 21 cm SGPS (McClure-Griffiths et al. 2005), we observed several absorptions features towards the region H1 coincident with the CO(1–0) emission in R1a while no H I absorption was associated with R1e (see Fig. 7). Consequently, the cloud is positioned in the near distance $d = 3.9$ kpc.

Fig. 6 also shows the CS(1–0) and NH₃ integrated emission between $v_{\text{lsr}} = 40$ –60 km s^{−1} and the recombination line H62 α between $v_{\text{lsr}} = 45$ and 65 km s^{−1}.

We noted that the NH₃(1,1) appeared less prominent away from the region H1, N21 and N22 as opposed to the CS(1–0). Although the CS(1–0) emission appears uniform across R1 between

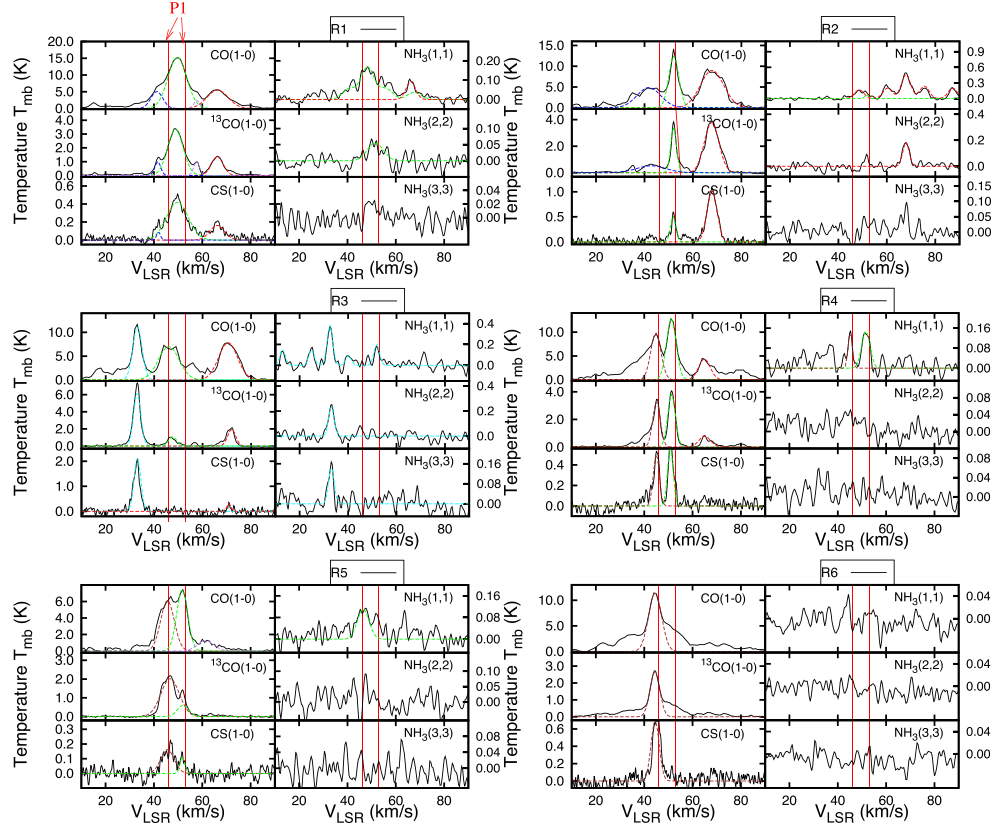


Figure 5. Averaged CO(1–0), $^{13}\text{CO}(1-0)$, CS(1–0) and $\text{NH}_3(1,1)$ to (3,3) spectra for the various regions as labeled in Figs 2 and 3. The vertical lines represent the estimated kinematic velocity range for PSR J1826–1334 (P1 in Fig. 2). Gaussian fits are represented as dashed lines whose colour code indicates the following velocity v_{lsr} ranges in km s^{-1} (30–35, 39–44, 44–46, 46–55, 55–62, 62–75) = (cyan, blue, brown, green, purple, red). We emphasize that the emission located at $v_{\text{lsr}} = 46\text{--}55 \text{ km s}^{-1}$ matches the kinematic distance of pulsar P1.

$v_{\text{lsr}} = 40$ and 60 km s^{-1} , the spectral lines averaged over the grid of boxes as shown in Fig. 9 reveals several contiguous cloud sub-components. For instance, the CS(1–0) emission indicated many line shape variations towards the south of R1, with several peaks with small velocity separations (e.g. boxes 32 to 35), and rapid variations of the peak velocity (e.g. boxes 13–17). Additionally, Fig. 4 also indicates that the $\text{NH}_3(1,1)$ and CS(1–0) emission located at $v_{\text{lsr}} = 45\text{--}60 \text{ km s}^{-1}$ broad velocity structures to the CS and NH_3 compared to the emission in R1e.

The $^{13}\text{CO}(1-0)$ spectral lines illustrated similar features. Interestingly, from the three colour map in Fig. 9 showing the GRS $^{13}\text{CO}(1-0)$ integrated intensity between $v_{\text{lsr}} = 45\text{--}50 \text{ km s}^{-1}$ (red), $v_{\text{lsr}} = 50\text{--}55 \text{ km s}^{-1}$ (green), $v_{\text{lsr}} = 55\text{--}60 \text{ km s}^{-1}$ (blue), we observed that the structure shown in red was distinct from the arch-shaped structure displayed in green. We also noted a spatial overlap between all emission across the aforementioned velocity bands next to the H II region G018.15–0.29 which suggests there is a physical link between the H II region and the these structures. The presence of the double-peaked emission found in boxes 17 and 23 ($v_{\text{lsr}} = 46 \text{ km s}^{-1}$ and $v_{\text{lsr}} = 56 \text{ km s}^{-1}$) which differs from the single-peaked emission found in box 5 ($v_{\text{lsr}} = 51 \text{ km s}^{-1}$) may be caused by the presence of this continuum source. Consequently, it is likely that the component R1a and R1d are physically connected.

The physical parameters listed in Table H1.a in the appendix shows that the molecular gas traced by the R1a component is much

more massive than the gas traced by the other components in the line of sight. From our CS and CO analysis, we found $M_{\text{H}_2}(\text{CS}) = 1.0 \times 10^5 M_{\odot}$ and $M_{\text{H}_2}(\text{CO}) = 1.2 \times 10^5 M_{\odot}$, respectively, which is within the Virial mass range $M_{\text{vir}} = 0.5\text{--}2.1 \times 10^5 M_{\odot}$, and averaged densities $n_{\text{H}_2}(\text{CS}) = 7.5 \times 10^2 \text{ cm}^{-3}$ and $n_{\text{H}_2}(\text{CO}) = 9.6 \times 10^2 \text{ cm}^{-3}$. The similar mass estimation from our CS and CO analysis may suggest the observed molecular gas are concentrated in clumps of density roughly equal to the CS(1–0) critical density $n_c = 2 \times 10^4 \text{ cm}^{-3}$. However, a lower mass and density estimates were attained with our NH_3 analysis with $M_{\text{H}_2} = 1.4 \times 10^4 M_{\odot}$ and $n_{\text{H}_2} = 2.0 \times 10^2 \text{ cm}^{-3}$.

4.6.2 Region R2

Towards region R2 (RA = $18^{\text{h}}420$, Dec = $-13^{\circ}125$), we detected three CO(1–0) components with velocity $v_{\text{lsr}} = 51 \text{ km s}^{-1}$ (R2a), $v_{\text{lsr}} = 43 \text{ km s}^{-1}$ (R2c), $v_{\text{lsr}} = 68 \text{ km s}^{-1}$ (R2e) (see Table 2). However, $^{13}\text{CO}(1-0)$, CS(1–0) and $\text{NH}_3(1,1)$ were solely found in R2a and R2e. We also observed $\text{SiO}_{v=0}(1-0)$ emission, whose centroid velocity coincided with the component R2e revealing the presence of post-shocked gas (see Fig. 6). The combined detection of a 44 GHz maser $\text{CH}_3\text{OH}(7_1-6_0)$ (region CH3), $\text{NH}_3(3,3)$ (see Fig. B1) and cyanopolyne HC_3N (region HC3, see Fig. F1) and

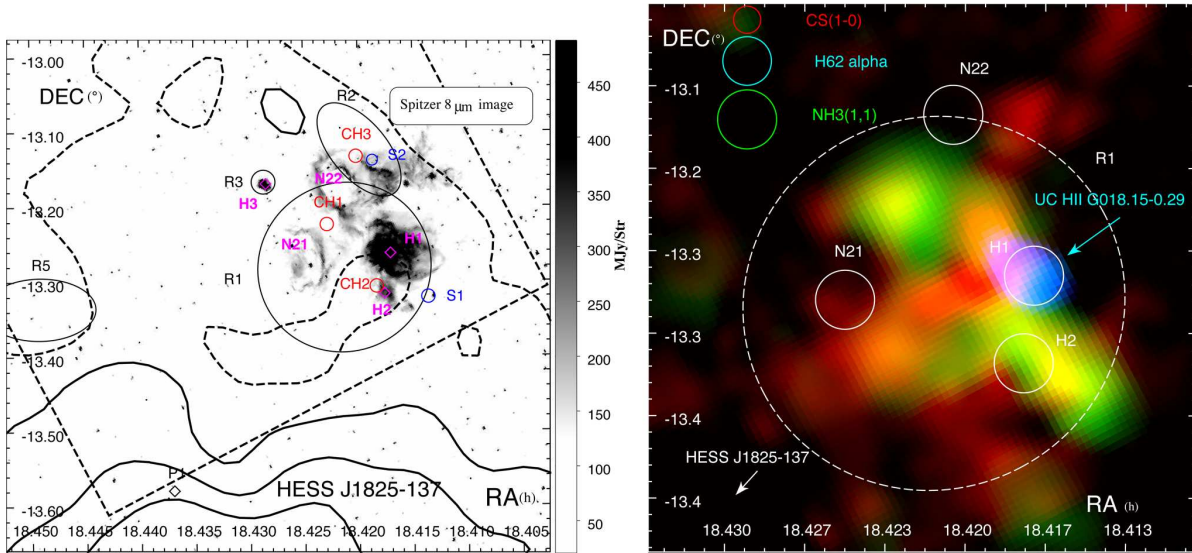


Figure 6. (Left) *Spitzer* 8 μm image towards HESS J1825–130 (black contours). The red circles labeled CH1 to CH3 reveal the location of the 44 GHz $\text{CH}_3\text{OH}(7_1-6_0)$ emission while the blue circles (see online version) S1 and S2 indicate $\text{SiO}(1-0, v=0)$ and $\text{SiO}(1-0, v=2)$ emission. H1 and H2 represent the ultracompact H II region G018.15–0.29 and the H II region G018.142–0.302, respectively, (Anderson et al. 2011) while H3 combines the H II regions G018.303–0.389 and G018.305–0.392 (White, Becker & Helfand 2005). N21 and N22 shown in purple indicate the location of two IR bubbles (Churchwell et al. 2006). The region covered by our 7 mm survey is shown as a black dashed rectangle. (Right) Three colour image showing the CS(1–0) (red) and NH_3 (green) integrated intensity between $v_{\text{lsr}} = 40$ and 60 km s^{-1} and the H62 α integrated intensity (blue) between $v_{\text{lsr}} = 45$ and 65 km s^{-1} towards R1a. The aforementioned H II regions are shown as white circles.

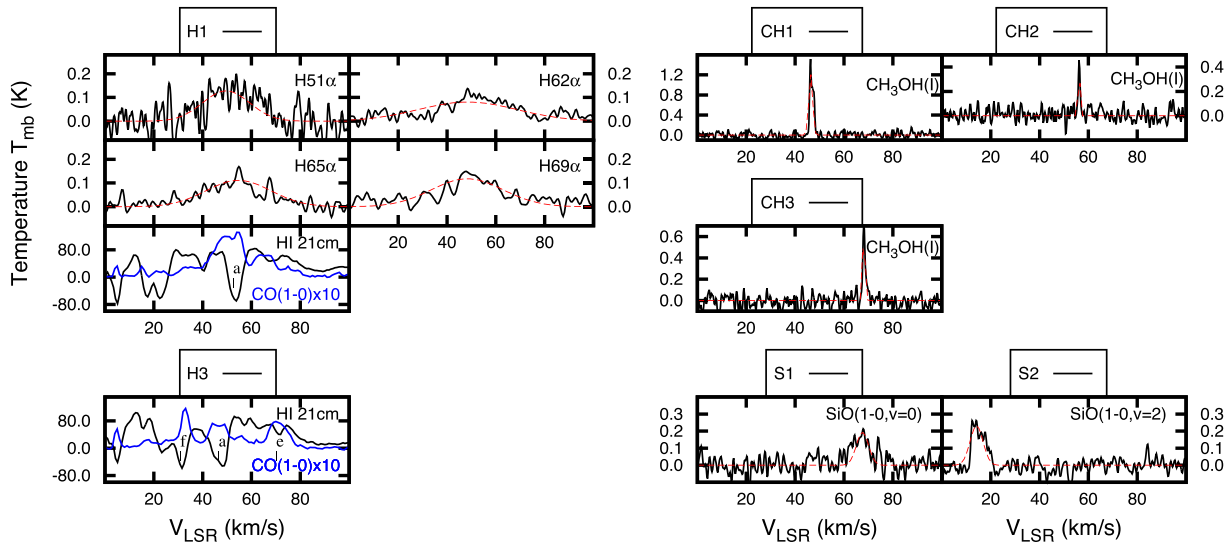


Figure 7. Spectral profile of the 44 GHz maser $\text{CH}_3\text{OH}(\text{I})$, $\text{SiO}(1-0)$, $\text{CO}(1-0)$, H I 21 cm and recombination line detections from the various regions shown in Fig. 6. The dashed line (red in online version) represents the Gaussian fits to the emission. In the $\text{CO}(1-0)$ versus H I plots, the absorptions features are indicated by black vertical lines where the labels ‘a’ to ‘f’ indicate the velocity group (see Tables 2 and 3).

their spatial connection with the IR source (see Fig. 6 left-hand panel) suggested the shock may have been caused by outflows from nearby star-forming regions.

Our CS and NH_3 analysis indicated that this molecular cloud was optically thick ($\tau_{\text{CS}(1-0)} = 1.5$ and $\tau_{\text{NH}_3(1,1)} = 3.5$). Consequently, the $\text{CO}(1-0)$ emission may suffer strong optical depth effects which would cause line width broadening ($\Delta v = 12 \text{ km s}^{-1}$, see Table 2).

Assuming the molecular gas is located at $d = 4.6 \text{ kpc}$ (near distance), we obtained the following masses $M_{\text{H}_2}(\text{CS}) = 3.4 \times 10^4 M_{\odot}$, $M_{\text{H}_2}(\text{NH}_3) = 8.1 \times 10^4 M_{\odot}$ and $M_{\text{H}_2}(\text{CO}) = 2.9 \times 10^4 M_{\odot}$ which were all within the Virial mass limits $M_{\text{vir}} = 0.3-1.1 \times 10^5 M_{\odot}$. We also determined the averaged densities $n_{\text{H}_2}(\text{NH}_3) \sim 4.8 \times 10^3 \text{ cm}^{-3}$, $n_{\text{H}_2}(\text{CS}) \sim 2.0 \times 10^3 \text{ cm}^{-3}$ and $n_{\text{H}_2}(\text{CO}) \sim 1.7 \times 10^3 \text{ cm}^{-3}$.

Table 2. Derived parameters of the Gaussian fits from the selected regions in Fig. 2 (see text). v_{cent} represents the velocity centroid of the Gaussian while Δv indicates the Gaussian FWHM. $W = \int T_{mb} dv$ represents the integrated main beam intensity applying the main beam correction factor η_{mb} (see text for details). The components detected by the different tracers CS(1–0), $^{13}\text{CO}(1-0)$, CO(1–0) are labeled as ‘a,b,c,d,e,f’ according to their velocity range (see footnote below table).

CO(1–0)	R1 (RA,Dec.) = (18 ^h 421, –13 ^o 282) Radii ^a = (405 arcsec × 405 arcsec)				R2 (RA,Dec.) = (18 ^h 420, –13 ^o 125) Radii = (135 arcsec × 270 arcsec)			R3 (RA,Dec.) = (18 ^h 429, –13 ^o 178) Radii = (64 arcsec × 64 arcsec)		
	a	c	d	e	a	c	e	a	e	f
Peak value T_A^* (K)	13.6	4.5	2.7	4.9	11.0	4.3	8.0	6.2	7.0	10.0
v_{cent} (km s ^{–1})	49.6	41.2	57.8	66.2	52.0	41.8	67.9	46.0	70.5	33.1
Δv (km s ^{–1})	9.0	5.7	2.8	10.3	4.8	11.4	11.3	10.0	9.1	4.5
W_{CO} (K km s ^{–1})	148.2	31.0	7.2	60.0	64.4	59.2	108.3	75.6	76.6	53.6
$T_{\text{rms}}/\text{ch}/\sqrt{\text{bins}}$ (K)	–0.07–				–0.18–			–0.30–		
$^{13}\text{CO}(1-0)$	R1				R2			R3		
	a	c	d	e	a	c	e	a	e	f
Peak value T_A^* (K)	1.6	0.5	0.5	0.7	1.7	0.3	1.8	0.5	0.9	3.0
v_{cent} (km s ^{–1})	48.9	41.6	57.7	66.2	52.0	42.8	67.7	47.6	72.0	33.0
Δv (km s ^{–1})	7.5	2.8	2.8	5.6	2.8	13.9	7.1	3.9	3.9	3.4
$W_{^{13}\text{CO}}$ (K km s ^{–1})	27.0	3.1	7.2	8.3	10.1	7.7	28.5	4.6	8.1	23.2
$T_{\text{rms}}/\text{ch}/\sqrt{\text{bins}}$ (K)	–0.01–				–0.01–			–0.03–		
CS(1–0)	R1				R2			R3		
	a	c	d	e	a	c	e	a	e	f
Peak value T_A^* (K)	0.2	<0.1	–	0.1	0.2	–	0.4	–	0.1	0.9
v_{cent} (km s ^{–1})	49.7	41.9	–	66.2	51.8	–	67.9	–	70.8	33.1
Δv (km s ^{–1})	10.7	1.9	–	7.2	2.6	–	4.8	–	1.8	3.2
W_{CS} (K km s ^{–1})	4.7	0.2	–	1.3	1.4	–	5.3	–	0.7	7.5
$T_{\text{rms}}/\text{ch}/\sqrt{\text{bins}}$ (K)	–0.01–				–0.01–			–0.03–		
CO(1–0)	R4 (RA,Dec.) = (18 ^h 422, –12 ^o 832) Radii = (175 arcsec × 280 arcsec)			R5 (RA,Dec.) = (18 ^h 449, –13 ^o 336) Radii = (150 arcsec × 270 arcsec)			R6 (RA,Dec.) = (18 ^h 385, –14 ^o 049) Radii = (460 arcsec × 460 arcsec)			
	a	b	e	a	b	d	b			
Peak value T_A^* (K)	11.5	8.7	3.9	6.6	5.4	1.1	10.2			
v_{cent} (km s ^{–1})	51.2	44.8	64.9	51.7	45.6	61.4	44.5			
Δv (km s ^{–1})	4.6	4.9	5.6	5.4	6.5	7.9	6.3			
W_{CO} (K km s ^{–1})	64.5	51.5	26.3	43.0	43.0	10.6	77.1			
$T_{\text{rms}}/\text{ch}/\sqrt{\text{bins}}$ (K)	–0.23–			–0.24–			–0.10–			
$^{13}\text{CO}(1-0)$	R4			R5			R6			
	a	b	e	a	b	d	b			
Peak value T_A^* (K)	1.8	1.6	0.4	0.3	1.0	–	1.3			
v_{cent} (km s ^{–1})	51.3	45.1	65.0	52.0	46.7	–	44.4			
Δv (km s ^{–1})	3.7	3.6	5.6	5.4	8.9	–4.8				
$W_{^{13}\text{CO}}$ (K km s ^{–1})	15.3	13.0	4.7	3.5	19.2	–	13.6			
$T_{\text{rms}}/\text{ch}/\sqrt{\text{bins}}$ (K)	–0.03–			–0.01–			–0.01–			
CS(1–0)	R4			R5			R6			
	a	b	e	a	b	d	b			
Peak value T_A^* (K)	0.3	0.2	–	0.1	0.1	–	0.3			
v_{cent} (km s ^{–1})	50.8	45.0	–	51.8	46.7	–	44.5			
Δv (km s ^{–1})	2.6	2.8	–	2.2	4.7	–	4.0			
W_{CS} (K km s ^{–1})	1.6	1.6	–	0.3	0.9	–	3.0			
$T_{\text{rms}}/\text{ch}/\sqrt{\text{bins}}$ (K)	–0.01–			–0.01–			–0.01–			

Note. *Radii represents the dimensions of the ellipse (semiminor axis × semimajor axis).

component a: $v_{\text{lsr}} = 46\text{--}55$ km s^{–1}, matching the dispersion measure of P1.

component b: $v_{\text{lsr}} = 44\text{--}46$ km s^{–1}.

component c: $v_{\text{lsr}} = 39\text{--}44$ km s^{–1}.

component d: $v_{\text{lsr}} = 55\text{--}62$ km s^{–1}.

component e: $v_{\text{lsr}} = 62\text{--}75$ km s^{–1}.

component f: $v_{\text{lsr}} = 30\text{--}35$ km s^{–1}.

The component R2a is associated with the component R1a (see Fig. 3) and the masses obtained are: $M_{\text{H}_2}(\text{CS}) > 3.4 \times 10^3 M_{\odot}$, $M_{\text{H}_2}(\text{NH}_3) > 4.5 \times 10^2 M_{\odot}$ and $M_{\text{H}_2}(\text{CO}) = 1.3 \times 10^4 M_{\odot}$, and densities $n_{\text{H}_2}(\text{CS}) > 3.3 \times 10^2 \text{cm}^{-3}$, $n_{\text{H}_2}(\text{NH}_3) > 4.3 \times 10^1 \text{cm}^{-3}$ and $n_{\text{H}_2}(\text{CO}) = 1.2 \times 10^3 \text{cm}^{-3}$ (see Table H1.b). The small fraction of dense gas detected by the

CS and NH₃ tracers at $v_{\text{lsr}} \sim 50$ km s^{–1} explains the large discrepancies between the different masses and densities.

Finally, our CO analysis revealed the H₂ mass traced by the component R2c is $M_{\text{H}_2} = 8.8 \times 10^3 M_{\odot}$ and a density $n_{\text{H}_2}(\text{CO}) = 3.9 \times 10^2 \text{cm}^{-3}$.

Table 3. Derived parameters of the five Gaussian fits used to model NH₃(1,1) emission, and the one Gaussian fit for the NH₃(2,2) emission averaged over the region shown in Fig. 3. T_{Am}^* indicates the peak intensity of the main emission while T_{Ai}^* are the peak intensities of the surrounding satellite lines. v_{cent} represents the velocity centroid of the Gaussian while Δv indicates the Gaussian FWHM. Finally $W = \int T_{mb} dv$ represents the integrated main beam intensity applying the main beam correction factor η_{mb} (see text for details). The different components detected by the different tracers CS(1–0), ¹³CO(1–0), CO(1–0) are labeled as ‘a,b,c,d,e,f’ according to their velocity range (see footnote below table).

NH ₃ (1,1)	R1 (RA,Dec.) = (18 ^h 419 ^m , –13 [°] 284) Radii = (395 arcsec × 305 arcsec)				R2 (RA,Dec.) = (18 ^h 420, –13 [°] 125) Radii = (135 arcsec × 270 arcsec)			R3 (RA,Dec.) = (18 ^h 429, –13 [°] 178) Radii = (64 arcsec × 64 arcsec)		
	a	c	d	e	a	c	e	a	e	f
Peak value T_{Am}^* (K)	0.09	–	–	0.05	0.04	–	0.25	–	–	0.21
Peak value T_{Ai1}^* (K)	0.03	–	–	–	–	–	0.13	–	–	0.05
Peak value T_{Ai2}^* (K)	0.05	–	–	–	–	–	0.11	–	–	0.05
Peak value T_{Ai3}^* (K)	0.02	–	–	–	–	–	0.11	–	–	0.08
Peak value T_{Ai4}^* (K)	–	–	–	–	–	–	0.09	–	–	0.08
v_{cent} (km s ^{–1})	48.3	–	–	66.2	51.7	–	67.9	–	–	33.1
Δv (km s ^{–1})	6.4	–	–	4.5	1.8	–	4.5	–	–	2.7
$W_{NH_3(1,1)}$ (K km s ^{–1})	2.2	–	–	0.8	1.4	–	5.3	–	–	7.5
$T_{rms}/ch/\sqrt{bins}$ (K)	–0.01–	–	–	–	–0.01–	–	–	–0.01–	–	–
NH ₃ (2,2)	R1				R2			R3		
	a	c	d	e	a	c	e	a	e	f
Peak value T_A^* (K)	0.03	–	–	–	–	–	0.10	–	–	0.13
v_{cent} (km s ^{–1})	51.5	–	–	–	–	–	67.9	–	–	33.1
Δv (km s ^{–1})	7.7	–	–	–	–	–	3.1	–	–	2.7
$W_{NH_3(2,2)}$ (K km s ^{–1})	0.5	–	–	–	–	–	0.6	–	–	0.7
$T_{rms}/ch/\sqrt{bins}$ (K)	–0.01–	–	–	–	–0.01–	–	–	–0.02–	–	–
NH ₃ (1,1)	R4 (RA,Dec.) = (18 ^h 422, –12 [°] 832) Radii = (175 arcsec × 280 arcsec)			R5 (RA,Dec.) = (18 ^h 449, –13 [°] 336) Radii = (150 arcsec × 270 arcsec)			R6 (RA,Dec.) = (18 ^h 385, –14 [°] 049) Radii = (460 arcsec × 460 arcsec)			
	a	b	e	a	b	d	b			
Peak value T_{Am}^* (K)	0.08	0.08	–	0.06	–	–	–			
Peak value T_{Ai1}^* (K)	–	–	–	–	–	–	–			
Peak value T_{Ai2}^* (K)	–	–	–	–	–	–	–			
Peak value T_{Ai3}^* (K)	–	–	–	–	–	–	–			
Peak value T_{Ai4}^* (K)	–	–	–	–	–	–	–			
v_{cent} (km s ^{–1})	45.1	51.6	–	46.5	–	–	–			
Δv (km s ^{–1})	2.0	4.0	–	5.6	–	–	–			
$W_{NH_3(1,1)}$ (K km s ^{–1})	0.3	0.6	–	0.7	–	–	–			
$T_{rms}/ch/\sqrt{bins}$ (K)	–0.01–	–	–	–0.01–	–	–	–	–0.01–		
NH ₃ (2,2)	R4			R5			R6			
	a	b	c	a	b	c				
Peak value T_A^* (K)	–	–	–	–	–	–				
v_{cent} (km s ^{–1})	–	–	–	–	–	–				
Δv (km s ^{–1})	–	–	–	–	–	–				
$W_{NH_3(2,2)}$ (K km s ^{–1})	–	–	–	–	–	–				
$T_{rms}/ch/\sqrt{bins}$ (K)	–0.01–	–	–	–0.01–	–	–	–0.02–			

Notes. *Radii represents the dimensions of the ellipse (semiminor axis × semimajor axis).

component a: $v_{lsr} = 46\text{--}55$ km s^{–1}, matching the dispersion measure of P1.

component b: $v_{lsr} = 44\text{--}46$ km s^{–1}.

component c: $v_{lsr} = 39\text{--}44$ km s^{–1}.

component d: $v_{lsr} = 55\text{--}62$ km s^{–1}.

component e: $v_{lsr} = 62\text{--}75$ km s^{–1}.

component f: $v_{lsr} = 30\text{--}35$ km s^{–1}.

4.6.3 Region R3

We detected three spectral components inside R3 (RA,Dec.) = (18^h429^m, –13[°]178). The two components R3a and R3e from CO(1–0) and ¹³CO(1–0) observations appear to be extensions of the molecular gas found in the regions R1 and R2, and their masses listed in Table H1.c indicate small mass contribution. On the other hand, the component R3f ($v_{lsr} = 43$ km s^{–1}) showed prominent NH₃(1,1) and CS(1–0) emission. The additional detection of the cyanopolyne HC₃N(5–4,F = 4–3) suggested the molecular

cloud may be associated with the H II regions G018.303–0.389 and G018.305–0.392 (White et al. 2005). From the H I spectral lines shown in Fig. 7, all CO(1–0) emission found in R3 was associated with an H I absorption feature and consequently puts the molecular cloud in the far distance of $d = 13.4$ kpc. Assuming the gas traced by the component R3f has an angular size equal to the Mopra NH₃(1,1) beam size, we obtained the following H₂ masses M_{H_2} (CS) = $1.5 \times 10^5 M_{\odot}$, M_{H_2} (NH₃) = $1.3 \times 10^4 M_{\odot}$, M_{H_2} (CO) = $1.5 \times 10^4 M_{\odot}$ and Virial mass $M_{vir} = 0.7 - 2.5 \times 10^4 M_{\odot}$ which gives the following H₂ densities

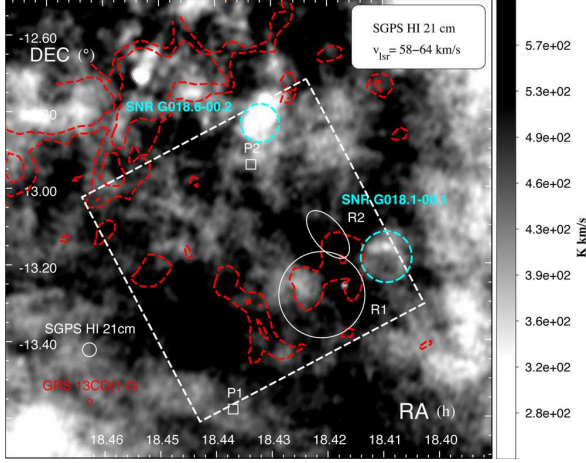


Figure 8. H I 21 cm integrated intensity in grey-scale between $v_{\text{lsr}} = 58$ and 64 km s^{-1} overlaid by the GRS $^{13}\text{CO}(1-0)$ contours in red (2.0 and 3.0 K km s^{-1} , see colour version). The white ellipses indicate the position of R1 and R2, while cyan circles show the two SNRs. The white squares represent the pulsars PSR J1826–1334 (P1) and PSR J1826–1256 (P2). The white dashed box represent our Mopra 7 mm coverage.

$$n_{\text{H}_2}(\text{CS}) = 7.6 \times 10^3 \text{ cm}^{-3}, \quad n_{\text{H}_2}(\text{NH}_3) = 6.2 \times 10^2 \text{ cm}^{-3}, \\ n_{\text{H}_2}(\text{CO}) = 9.3 \times 10^2 \text{ cm}^{-3}.$$

4.6.4 Region R4

Region R4 located north of HESS J1826–130, is nearby the supernova remnant SNR G018.6–0.2. From $\text{NH}_3(1,1)$ and $\text{CS}(1-0)$

observations, we detected two components R4a and R4b with small velocity separation ($v_{\text{cent}} = 45 \text{ km s}^{-1}$ and $v_{\text{cent}} = 51 \text{ km s}^{-1}$).

As shown in Fig. 4, we observed no CS and NH_3 emission connecting the components R4a and R4b. From Fig. 9, we noted that the molecular gas in R4a (shown in green) appeared to be part of the putative molecular shell GSH G018.2–0.1+53 suggested by Paron et al. (2013) whereas the gas in R4b (in red) appeared isolated. However, their similar morphologies as shown by the overlap of the two components (in yellow) the similarities of the $^{13}\text{CO}(1-0)$, CS and NH_3 spectral lines may indicate some association.

Assuming R4a and R4b were situated at the near distance, we derived the total mass lower limit for R4a $M_{\text{H}_2}(\text{CS}) > 7.4 \times 10^3 M_{\odot}$, $M_{\text{H}_2}(\text{NH}_3) > 2.0 \times 10^3 M_{\odot}$, $M_{\text{H}_2}(\text{CO}) = 1.6 \times 10^4 M_{\odot}$ and $M_{\text{H}_2}(\text{CS}) > 5.0 \times 10^3 M_{\odot}$, $M_{\text{H}_2}(\text{NH}_3) > 1.2 \times 10^3 M_{\odot}$ and $M_{\text{H}_2}(\text{CO}) = 1.1 \times 10^4 M_{\odot}$ for R4b agreeing with their Virial mass ranges $M_{\text{vir}} = 0.7\text{--}2.5 \times 10^4 M_{\odot}$ and $M_{\text{vir}} = 0.6\text{--}2.2 \times 10^4 M_{\odot}$, respectively (see Table H1.d). From CO analysis, we obtained the densities $n_{\text{H}_2}(\text{CO}) = 9.3 \times 10^2 \text{ cm}^{-3}$ and $n_{\text{H}_2}(\text{CO}) = 8.2 \times 10^2 \text{ cm}^{-3}$ for R4a and R4b, respectively. In the case where R4a and R4b were associated with the same molecular complex at $d \sim 4 \text{ kpc}$, the total mass obtained would be $M_{\text{H}_2}(\text{CO}) \sim 3.0 \times 10^4 M_{\odot}$.

Therefore, although the region R4 is unlikely to be physically related to HESS J1825–137 and HESS J1826–130, it highlights the complexity of the structure of the molecular gas in the line of sight.

4.6.5 Region R5

The region R5 is located 20 arcmin away from the pulsar PSR J1826–1334. From $\text{CO}(1-0)$ observations, three components in region R5 with centroid velocity $v_{\text{cent}} = 51 \text{ km s}^{-1}$ (R5a), $v_{\text{cent}} = 45 \text{ km s}^{-1}$

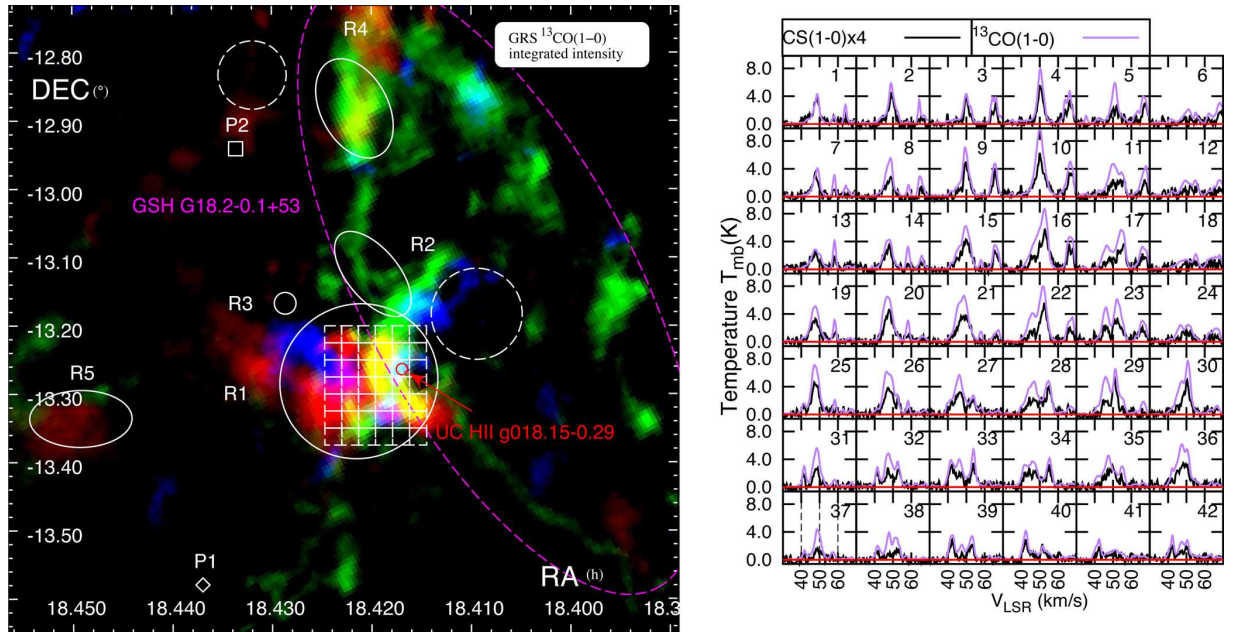


Figure 9. (Left) Three-colour image illustrating the GRS $^{13}\text{CO}(1-0)$ towards HESS J1826–130 integrated intensity at three velocity ranges : $45\text{--}50 \text{ km s}^{-1}$ (red), $50\text{--}55 \text{ km s}^{-1}$ (green), $55\text{--}60 \text{ km s}^{-1}$ (blue). The H II region UC H II G018.15–0.29 is indicated in red. The purple dashed ellipse indicates the position and size of the putative molecular shell GSH 18.1–0.2+53 (Paron et al. 2013). (Right) Spectra of GRS $^{13}\text{CO}(1-0)$ (purple lines in colour version) and Mopra CS(1–0) emission (black lines) averaged over the boxes shown in the left-hand panel.

(R5b), $v_{\text{cent}} = 61 \text{ km s}^{-1}$ (R5d) were detected. However, $^{13}\text{CO}(1-0)$, CS(1-0) were solely observed in R5a and R5b and weak $\text{NH}_3(1,1)$ emission ($< 3T_{\text{rms}}$) was found only in R5a.

From Fig. 4, it appears that most of the emission is located between $v_{\text{lsr}} = 45 \text{ km s}^{-1}$ and $v_{\text{lsr}} = 48 \text{ km s}^{-1}$.

We derived H_2 masses of $M_{\text{H}_2}(\text{NH}_3) > 2.0 \times 10^3 M_{\odot}$, $M_{\text{H}_2}(\text{CS}) > 7.4 \times 10^2 M_{\odot}$, $M_{\text{H}_2}(\text{CO}) = 9.5 \times 10^3 M_{\odot}$ for R5a and $M_{\text{H}_2}(\text{CS}) > 1.8 \times 10^3 M_{\odot}$ and $M_{\text{H}_2}(\text{CO}) = 1.1 \times 10^4 M_{\odot}$ for R5b. Therefore, the molecular gas traced by R5a and R5b appears less clumpy as opposed to R1a. From CO(1-0) analysis, we obtained the densities $n_{\text{H}_2}(\text{CO}) = 6.8 \times 10^2 \text{ cm}^{-3}$ and $n_{\text{H}_2}(\text{CO}) = 6.1 \times 10^2 \text{ cm}^{-3}$ for R5a and R5b, respectively (see Table H1.e). Therefore, the molecular clouds located inside R5 are marginally denser than our other studied regions. If R5a and R5b were to be physically connected and located at $d = 4 \text{ kpc}$, we would obtain the following total mass $M_{\text{H}_2}(\text{CO}) = 2.3 \times 10^4 M_{\odot}$.

4.6.6 Region R6

The region R6 is located in the southern part of HESS J1825-137. It is surrounded by several H II regions and the SNRs G017.4–0.1 and G017.0–0.0. We found CO and $^{13}\text{CO}(1-0)$ emission with a centroid velocity at $v_{\text{lsr}} \sim 44 \text{ km s}^{-1}$. As shown in Fig. 5, we noted that the CO(1-0) emission and its isotopologue $^{13}\text{CO}(1-0)$ revealed a broad positive wing ($v_{\text{lsr}} = 45\text{--}55 \text{ km s}^{-1}$). However, our deep pointing in CS(1-0) revealed no such features.

From our deep pointing measurements, we obtained $N_{\text{H}_2} = 7.5 \times 10^{21} \text{ cm}^{-2}$. If we assumed the molecular clouds have uniform column density across the molecular clouds, we would obtain a total mass $M_{\text{H}_2}(\text{CS}) > 3.6 \times 10^4 M_{\odot}$ (see Table H1.f), which would be a factor of 2 smaller than the mass derived using our Nanten CO(1-0) observations $M_{\text{H}_2}(\text{CO}) = 7.6 \times 10^4 M_{\odot}$.

Region R6 and the surrounding molecular gas reveals a broad spatial distribution of $^{13}\text{CO}(1-0)$ and the molecular cloud may be associated with the TeV source HESS J1825–137. This molecular cloud may therefore influence the morphology of the south region of the TeV PWN.

4.7 Summary

We detected several molecular clouds along the line of sight. Notably, we observed a small molecular cloud located at $v_{\text{lsr}} = 18 \text{ km s}^{-1}$ overlapping with the pulsar PSR J1826-1256 and whose kinematic distance $d = 1.7 \text{ kpc}$ roughly agreed with the pulsar's predicted distance $d = 1.4 \text{ kpc}$ from Wang (2011).

The molecular gas located at $v_{\text{lsr}} = 46\text{--}55 \text{ km s}^{-1}$ and matching the pulsar's distance have a mass $M_{\text{H}_2} = 3.3 \times 10^5 M_{\odot}$ where ~ 30 per cent resides inside the region R1. Moreover, we observed prominent and extended CS(1-0) and $\text{NH}_3(1,1)$ emission in R1a and thus it suggests that the observed molecular gas consists of dense clumps likely to exceed the CS(1-0) critical density $n_c \sim 2 \times 10^4 \text{ cm}^{-3}$ at 10 K.

The molecular gas traced by the component R1a also revealed complex CS and $^{13}\text{CO}(1-0)$ spectral lines surrounding the H II region G018.15–00.29 and towards HESS J1825–137 with several intensity peaks with little velocity separations and rapid variations of the velocity peaks.

We also remarked that the components found at $v_{\text{lsr}} = 44\text{--}46 \text{ km s}^{-1}$ ‘b’ often overlapped and shared similar properties with the component ‘a’ at $v_{\text{lsr}} = 46\text{--}55 \text{ km s}^{-1}$ which may indicate possible physical connection.

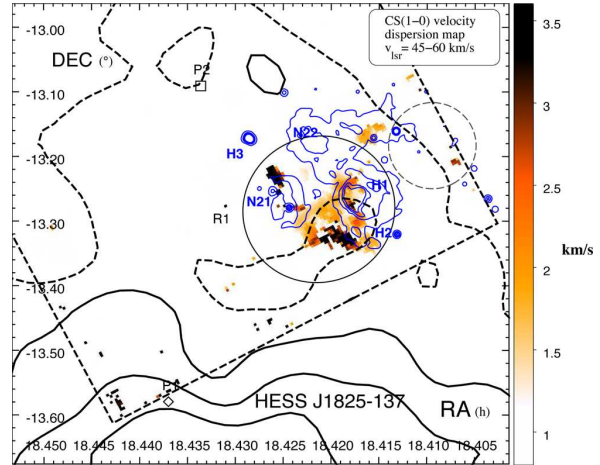


Figure 10. CS(1-0) velocity dispersion v_{disp} map between $v_{\text{lsr}} = 45$ and 60 km s^{-1} with $T_A^* > 4T_{\text{rms}}$, overlaid by the $8 \mu\text{m}$ *Spitzer* GLIMPSE contours (blue in colour version).

Finally the H I and $^{13}\text{CO}(1-0)$ data showed the presence of a plausible void centred at the SNR G018.6–0.2 at $v_{\text{lsr}} \sim 60\text{--}65 \text{ km s}^{-1}$ and associated with the molecular cloud where the dense gas traced by the component R2e resided. This suggests that this SNR may be located at a distance $d = 4.6 \text{ kpc}$ (near distance) or $d = 11.4 \text{ kpc}$ (far distance).

5 DISCUSSION

5.1 Dynamics of the dense molecular gas in region R1a looking for the progenitor SNR

We focus now on the gas dynamics to probe the level of disruption in the observation of this region structure of CS(1-0). Bubbles, core-collapsing clouds and shocks are the common causes of gas disruption. We have shown that the dense molecular cloud traced by the component R1a displays complex morphology and spectral line profiles. The velocity dispersion, or second moment, map of CS(1-0) in Fig. 10 indicates broad dense gas overlapping with the H II region UC H II G018.15–0.28.

Most of the CS(1-0) emission towards the centre of R1a displays a mild velocity dispersion ($v_{\text{disp}} \sim 2 \text{ km s}^{-1}$). There is also no appreciably broad gas overlapping the IR bubbles N21 and N22. However, we observe a $\sim 3.5\text{--}4 \text{ km s}^{-1}$ velocity dispersion to the south of R1a towards HESS J1825–137 which does not seem related to any IR emission as shown in Fig. 10.

We now focus on potential causes of the broad CS(1-0) lines in R1a. Little is known about the progenitor SNR of HESS J1825–137. From hydrodynamical simulation of the PWN, the radius of the SNR is expected to be four times the radius of this middle-aged PWN $r_{\text{SNR}} \sim 4r_{\text{PWN}}$ (van der Swaluw et al. 2001). With the TeV radius of the PWN being $r_{\text{PWN}} \sim 35 \text{ pc}$ (Aharonian et al. 2006), the predicted radius of the SNR thus becomes significantly large at $r_{\text{SNR}} \sim 140 \text{ pc}$.

de Jager & Djannati-Ataï (2009) indicated that the SNR's radius could reach $r_{\text{SNR}} \sim 120 \text{ pc}$ if they assumed a kinetic energy $E_{\text{SN}} = 3 \times 10^{51} \text{ erg}$ from the supernova shock, an ambient density $n_{\text{amb}} = 0.001 \text{ cm}^{-3}$, and an age of the system $t_{\text{age}} \sim 40 \text{ kyr}$. By taking the Nanten CO(1-0) emission over a narrow v_{lsr} range ($52\text{--}56 \text{ km s}^{-1}$) centred on the pulsar PSR J1826–1334 distance and discarding the contribution from the dense region inside the green box in

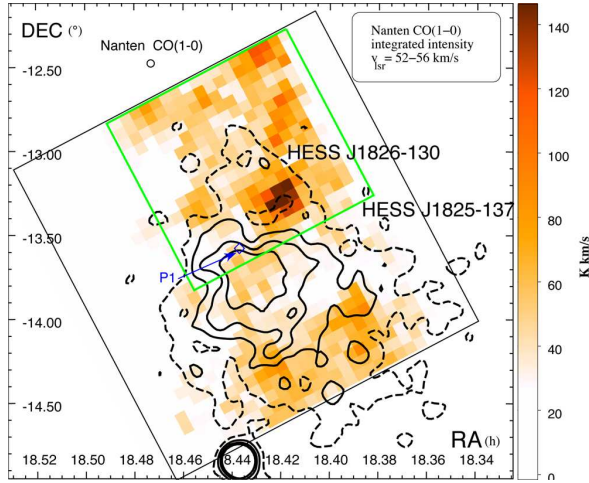


Figure 11. Nanten CO(1–0) integrated intensity between $v_{\text{lsr}} = 52$ and 56 km s^{-1} overlaid by HESS TeV contours. The large black square represents the region where the overall averaged ambient density n_{amb} was estimated (see Section 4.1) with the CO(1–0) emission within the green box (in colour version) being excluded.

Fig. 11, we obtain a density $n_{\text{H}} \sim 4 \text{ cm}^{-3}$. However, the typical noise level $T_{\text{rms}}/\text{ch} \sim 0.4 \text{ K}$ of the Nanten CO(1–0) data (Mizuno & Fukui 2004) greatly affects our density estimation which should then only be used as an upper-limit. Thus, our derived density does not at the moment refute the ambient density predicted by de Jager & Djannati-Ataï (2009). Besides this, due to the contamination of the CO(1–0) emission resulting from local and distant kinematic components, it also becomes difficult to identify the presence of the void caused by the SNR’s progenitor star. The better sensitivity and velocity resolution of the NASCO (Fukui et al. 2006) or Nobeyama⁴ surveys of the CO and ¹³CO emission may provide solutions to this issue. Interestingly though, Stupar et al. (2008) reported a H α rim (see white dashed lines in Fig. 12) located roughly 120 pc away from PSR J1826-1334 (assuming the H α rim is located at $d = 4 \text{ kpc}$) and with a ratio $S_{\text{H}\alpha}/H \sim 1.33$ typical of SNR shock. Moreover, based on the sharp gradient in H α , we might also speculate that the reported H α rim is also seen to the south-east of HESS J1825–137 as shown in white dotted line in Fig. 12. The strong H α emission to the west of HESS J1825–137 (red circles) has been catalogued as H II regions (Anderson et al. 2014). The projected separation of the H α rim roughly matches with the SNR’s expected radius based on $R_{\text{SNR}}/R_{\text{PWN}} \sim 4$ suggested by de Jager & Djannati-Ataï (2009). Furthermore, the lack of H α emission north of HESS J1825–137 may arise due to the blocking effect of dense cloud responsible for the crushed PWN.

The possible association between the H α rim and the TeV source could provide important information about the environment surrounding HESS J1825–137.

We now consider whether this SNR would contribute to the turbulence found inside *R1a*. We do not observe direct evidence of post-shocked gas inside at $v_{\text{lsr}} = 45\text{--}60 \text{ km s}^{-1}$ such as SiO(1–0, $v = 0$) emission or catalogued OH 1720 MHz masers. None the less, if the shock did reach the cloud, we do expect the shock speed v_s to be considerably lowered due to the high averaged density found in

⁴ <http://www.nro.nao.ac.jp/~nro45mrt/html/index-e.html>

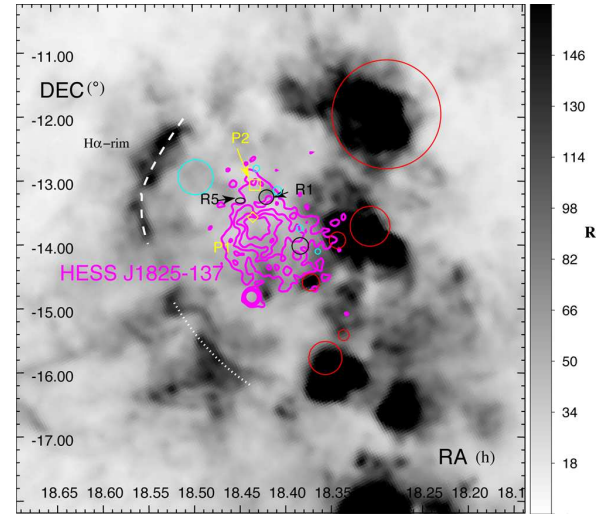


Figure 12. H α image towards HESS J1825–137 in Rayleigh units overlaid by the HESS contours in magenta. The two pulsars labeled P1 and P2 are shown in yellow while the SNRs are displayed in cyan circles (see online version for colours). The white dashed lines represent the SNR H α rim reported by Stupar, Parker & Filipović (2008) while the white dotted lines indicate another putative H α rim which might be associated with the HESS J1825–137’s progenitor SNR. The red circles encompassing the strong H α emission on the right-hand side are catalogued by Anderson et al. (2014) as H II regions.

this region. By applying equation 10 from Uchiyama et al. (2010):

$$v_s \approx 65 \left(\frac{n_{\text{R1a}}}{100 \text{ cm}^{-3}} \right)^{-1/2} \left(\frac{E_{\text{SN}}}{10^{51} \text{ erg}} \right)^{1/2} \left(\frac{R_{\text{R1a}}}{12.5 \text{ pc}} \right)^{-3/2} \text{ km s}^{-1} \quad (1)$$

and assuming the distance to *R1a* boundary $R_{\text{R1a}} = 20 \text{ pc}$, a proton density found from our CO analysis $n_{\text{R1a}} = 2.7 \times 10^3 \text{ cm}^{-3}$, we find that the shock could reduce to a speed $v_s \sim 10 \text{ km s}^{-1}$. Consequently, using the age upper-limit $t = 40 \text{ kyr}$ for the SNR, the shock would have only travelled less than 1 pc (i.e. an angular distance $\theta \sim 0\text{:}01$) inside the dense molecular cloud. Therefore, the SNR might only contribute to the disruptions found south of *R1a* (see Fig. 10) where we see a broader velocity dispersion v_{disp} .

Alternatively, the broad velocity dispersion may also be caused by two distinct but contiguous velocity components as shown in Fig. 9 (red and green components) and thus may not be an indicator of randomly distributed disruption in this region. In fact, we note that this cloud shows similarities with the studied molecular clouds next to the Serpens cluster (Duarte-Cabral et al. 2011) and RCW120 (Torii et al. 2015), whose velocity components are thought to be caused by cloud–cloud collisions. Cloud–cloud collisions, studied using hydrodynamical simulations (Habe & Ohta 1992; Duarte-Cabral et al. 2011; Takahira, Tasker & Habe 2014; Torii et al. 2015), recently renewed popularity to explain the presence of high-mass star formation inside molecular clouds. Notably, such collisions between molecular clouds are thought to generate OB stars, filamentary clouds, dense cores and complex velocity distribution. In our region of study, Paron et al. (2013) in fact detected several O and B stars next to the IR bubble N22, N21 and the UC H II G018.15–00.28 towards the molecular gas *R1a* component.

5.2 TeV emission of HESS J1826–130

An important question is whether or not HESS J1826–130 can be associated with HESS J1825–137. Now, we will discuss potential origins of this northern TeV emission. For HESS J1826–130, Deil et al. (2015) reported its location at (18.434, –13°02), and a TeV flux above 1 TeV $F(>1\text{ TeV}) = 7.4 \times 10^{-13} \text{ ph cm}^{-2} \text{ s}^{-1}$.

5.2.1 CRs from the progenitor SNR of PSR J1826–1334

The general spatial match between the molecular cloud and the TeV emission of HESS J1826–130 may suggest a hadronic origin. Here, the progenitor SNR of HESS J1825–137 is an obvious candidate source for CRs in the region. A key question is whether the observed emission can be explained by the *sea* (Galactic plane averaged CR energy density $w_{\text{CR}} \sim 1 \text{ eV cm}^{-3}$) of cosmic rays or require the presence of a nearby CR source. Using equation 10 from Aharonian (1991) and the mass of the molecular cloud $M_{\text{H}_2} = 3.3 \times 10^5 M_{\odot}$ calculated earlier, we obtain $F(>1\text{ TeV}) = 5.8 \times 10^{-14} \text{ ph cm}^{-2} \text{ s}^{-1}$ produced by the sea of cosmic rays towards HESS J1826–130. This predicted flux is ~ 15 times below the observed flux estimated above. Therefore, a nearby accelerator providing CRs at an energy density 15 times the Earth-like value is required. The required CR density enhancement to produce the observed TeV flux towards HESS J1826–130 can easily be reached by SNRs (e.g. W28; see Aharonian et al. 2008). Therefore, the progenitor SNR of PSR J1826–1334 may contribute to the HESS J1826–130 TeV emission.

5.2.2 Other potential particle accelerators

Paron et al. (2013) argued the distance of SNR G018.2–0.1 to be $d = 4 \text{ kpc}$ based on its possible association with the nearby H II regions. Its small projected radius $r \sim 4 \text{ pc}$ would imply a very young SNR with age $< 1000 \text{ yr}$. By comparing our CO(1–0) column density the those derived from X-ray measurements $N_{\text{H}} = 7.2 \times 10^{22} \text{ cm}^{-2}$ (Sugizaki et al. 2001) and $N_{\text{H}} = 5.7 \times 10^{22} \text{ cm}^{-2}$ (Leahy, Green & Tian 2014), we would argue an SNR distance greater than 4 kpc, consistent with the distance estimate from Leahy et al. (2014). Additionally, Pavlovic et al. (2014) suggest a much further distance $d > 8.8 \text{ kpc}$ based on their updated Σ – D relation. In the case where the SNR is located at $d = 4 \text{ kpc}$, CRs would probably remain confined inside the SNR shock and would not be responsible of the TeV γ -ray emission found in HESS J1826–130. We did not find molecular gas overlapping the HESS J1826–130 emission in the case where $d > 4 \text{ kpc}$. Therefore, we suggest that the TeV γ -ray emission towards HESS J1826–130 cannot be produced by CRs accelerated by the SNR G018.2–0.1.

The radio-quiet pulsar PSR J1826–1256 (P2), which powers the diffuse X-ray nebula PWN G018.5–0.4 (Roberts, Romani & Kawai 2001; Roberts, Gotthelf, Halpern, Brogan & Ransom 2007), may also be a candidate for the origin of HESS J1826–130. The distance $d = 1.2$ – 1.4 kpc suggested by Wang (2011) infers a TeV γ -ray efficiency $\eta_{\gamma} \sim 2 \times 10^{-4}$ which is at the lower end of typical η_{γ} values for $\dot{E}_{\text{SD}} \sim 10^{36-37} \text{ erg s}^{-1}$ (Kargaltsev, Rangelov & Pavlov 2013). We find that the Nanten CO(1–0) emission located at this distance ($v_{\text{lsr}} = 10$ – 25 km s^{-1} , see Fig. D1) overlaps the pulsar and makes the PWN scenario at this distance unlikely. However, the adjacent position of the molecular gas at $v_{\text{lsr}} = 60$ – 80 km s^{-1} (with near/far distance $d = 4.6/11.4 \text{ kpc}$) appears spatially consistent with the PWN scenario. The molecular cloud north of P2 indeed support the offset position of the pulsar (coincident with AX J1826.1–1257;

see Ray et al. 2011) with respect to the X-ray (Roberts et al. 2007) and TeV emission. At these distances, η_{γ} would then rise to 1.5×10^{-3} ($d = 4.6 \text{ kpc}$) and 1.0×10^{-2} ($d = 11.4 \text{ kpc}$), more consistent with the canonical η_{γ} values.

The plausible shell at $v_{\text{lsr}} = 60$ – 65 km s^{-1} spatially coincident with the SNR G018.6–0.4 puts this SNR at the same distance to the pulsar P2 and may suggest an association between the two objects. To reconcile the small size of SNR G018.6–0.2 and the characteristic age of P2 ($\tau_c = 13 \text{ kyr}$), they need to be placed at a far distance $\sim 11.4 \text{ kpc}$. Finally, the lack of an overlap in the 60– 80 km s^{-1} gas and HESS J1826–130 would tend to rule out any direct association with SNR G018.6–0.2.

6 CONCLUSIONS

In this paper, we presented a detailed picture of the ISM surrounding HESS J1825–137, powered by the pulsar PSR J1826–1334 (here labeled P1) and discussed morphological and spectral properties of the TeV source.

Following Lemièrè et al. (2005)’s detection of a molecular cloud overlapping HESS J1826–130, we carried out a study of the diffuse and the dense molecular gas across the region using the Nanten CO(1–0) Galactic survey, the GRS $^{13}\text{CO}(1–0)$ data, and our 7 and 12 mm Mopra observations tracing CS(1–0) and $\text{NH}_3(1,1)$.

We observed that the bulk of the molecular gas towards HESS J1826–130 was located at $v_{\text{lsr}} = 45$ – 60 km s^{-1} which appeared consistent with the dispersion measure distance of P1. We also noted a dense region at (RA, Dec.) = (18^h421, –13°282) with mass $M_{\text{H}_2} \sim 1 \times 10^5 M_{\odot}$ and H_2 density $n_{\text{H}_2} \sim 7 \times 10^2 \text{ cm}^{-3}$ which showed enhanced turbulence. We indicated that its CS(1–0) and $^{13}\text{CO}(1–0)$ velocity structure, the presence of a Ultra-Compact (UC) H II region and several OB stars and high-mass star-forming regions, can be signatures of turbulent clouds caused by cloud–cloud collisions (e.g. RCW 120; Torii et al. 2015). We also suggested that its possible interaction with P1’s progenitor SNR was unlikely to cause such disruptions.

The H α rim discovered by Stupar et al. (2008) may be associated with P1’s progenitor SNR, as the distance between the H α rim and P1 appears consistent with an SNR radius $R_{\text{SNR}} \sim 120 \text{ pc}$ suggested by de Jager & Djannati-Ataï (2009) based on their suggestion that radius of the SNR being ~ 4 times that of the corresponding PWN.

We found that CRs produced by the P1’s progenitor SNR could explain to the TeV γ -ray emission found in HESS J1826–130. The origin of HESS J1826–130 might also be leptonic if associated with the PWN G018.5–0.4. If this PWN produces the HESS J1826–130 emission, the adjacent molecular gas at $v_{\text{lsr}} = 60$ – 80 km s^{-1} may explain the TeV morphology and would suggest a PWN distance $d = 4.6 \text{ kpc}$ (near) or $d = 11.4 \text{ kpc}$ (far). SNR G018.2–0.1 and SNR G018.6–0.2 (see Brogan et al. 2006 and Green 2014) are also positioned close to HESS J1826–130. Their small angular diameters however and their offset position makes the two SNRs unlikely to be associated with HESS J1826–130.

Further Very High Energy (VHE) observations with H.E.S.S. would provide more refined spatial resolution with advanced analysis (e.g. Parsons & Hinton 2014). This will enable a detail comparison between the TeV emission and the molecular gas and consequently add key information about the hadronic and/or leptonic nature of HESS J1826–130, and probe the diffusion of CRs into the gas (e.g. see Gabici, Aharonian & Blasi 2007).

ACKNOWLEDGEMENTS

The Mopra radio telescope is part of the Australia Telescope National Facility which is funded by the Australian Government for operation as a National Facility managed by CSIRO. Operations support was provided by the University of New South Wales and the University of Adelaide. The University of New South Wales Digital Filter Bank used for the observations with the Mopra Telescope (the UNSW–MOPS) was provided with support from the Australian Research Council (ARC). This research has made use of the SIMBAD data base, operated at CDS, Strasbourg, France.

REFERENCES

- Aharonian F. A., 1991, *Ap&SS*, 180, 305
 Aharonian F. et al., 2006, *A&A*, 460, 365
 Aharonian F. et al., 2008, *A&A*, 481, 401
 Anderson L. D., Bania T. M., 2009, *ApJ*, 690, 706
 Anderson L. D., Bania T. M., Balsler D. S., Rood R. T., 2011, *ApJS*, 194, 32
 Anderson L. D., Bania T. M., Balsler D. S., Cunningham V., Wenger T. V., Johnstone B. M., Armentrout W. P., 2014, *ApJS*, 212, 1
 Blondin J. M., Chevalier R. A., Frierson D. M., 2001, *ApJ*, 563, 806
 Brogan C. L., Gelfand J. D., Gaensler B. M., Kassim N. E., Lazio T. J. W., 2006, *ApJ*, 639, L25
 Churchwell E. et al., 2006, *ApJ*, 649, 759
 Churchwell E. et al., 2009, *PASP*, 121, 213
 Dame T. M., Hartmann D., Thaddeus P., 2001, *ApJ*, 547, 792
 de Jager O. C., Djannati-Ataï A., 2009, in Becker W., ed., *Astrophysics and Space Science Library*, Vol. 357, Neutron Stars and Pulsars. Springer-Verlag, Heidelberg, p. 451
 Deil C., Brun F., Carrigan S., Chaves R., Donath A., Gast H., Marandon V., Terrier R., 2015, 34th International Cosmic Ray Conference (ICRC 2015), PoS, announcement of new H.E.S.S galactic plane sources.
 Duarte-Cabral A., Dobbs C. L., Peretto N., Fuller G. A., 2011, *A&A*, 528, A50
 Frerking M. A., Wilson R. W., Linke R. A., Wannier P. G., 1980, *ApJ*, 240, 65
 Fukui Y. et al., 2006, *Proc. IAU Symp. 1, Astronomical Facilities of the Next Decade*, p. 21
 Gabici S., Aharonian F. A., Blasi P., 2007, *Ap&SS*, 309, 365
 Green D. A., 2014, *Bull. Astron. Soc. India*, 42, 47
 Gusdorf A., Cabrit S., Flower D. R., Pineau Des Forêts G., 2008, *A&A*, 482, 809
 Habe A., Ohta K., 1992, *PASJ*, 44, 203
 Ho P. T. P., Townes C. H., 1983, *ARA&A*, 21, 239
 Irvine W. M., Goldsmith P. F., Hjalmarsen A., 1987, in Hollenbach D. J., Thronson H. A., Jr, eds, *Astrophysics and Space Science Library*, Vol. 134, Interstellar Processes. Kluwer, Dordrecht, p. 561
 Jackson J. M., 2004, in Lamers H. J. G. L. M., Smith L. J., Nota A., eds, *ASP Conf. Ser. Vol. 322, The Formation and Evolution of Massive Young Star Clusters*. Astron. Soc. Pac., San Francisco, p. 227
 Kargaltsev O., Rangelov B., Pavlov G. G., 2013, in Strakovsky I., Blokhintsev L., eds, *Nova Science, The Universe Evolution: Astrophysical and Nuclear Aspects*, p. 359
 Leahy D., Green K., Tian W., 2014, *MNRAS*, 438, 1813
 Lemièrre A., Terrier R., Djannati-Ataï A., 2005, in 29th Int. Cosmic Ray Conf., Vol. 4, p. 105
 McClure-Griffiths N. M., Dickey J. M., Gaensler B. M., Green A. J., Haverkorn M., Strasser S., 2005, *ApJS*, 158, 178
 Mizuno A., Fukui Y., 2004, in Clemens D., Shah R., Brainerd T., eds, *ASP Conf. Ser. Vol. 317, Milky Way Surveys: The Structure and Evolution of our Galaxy*. Astron. Soc. Pac., San Francisco, p. 59
 Morris M., Turner B. E., Palmer P., Zuckerman B., 1976, *ApJ*, 205, 82
 Paron S., Weidmann W., Ortega M. E., Albacete Colombo J. F., Pichel A., 2013, *MNRAS*, 433, 1619
 Parsons R. D., Hinton J. A., 2014, *Astropart. Phys.*, 56, 26
 Pavlovic M. Z., Dobardzic A., Vukotic B., Urosecvic D., 2014, *Serb. Astron. J.*, 189, 25
 Protheroe R. J., Ott J., Ekers R. D., Jones D. I., Crocker R. M., 2008, *MNRAS*, 390, 683
 Ray P. S. et al., 2011, *ApJS*, 194, 17
 Roberts M. S. E., Romani R. W., Kawai N., 2001, *ApJS*, 133, 451
 Roberts M. S. E., Gotthelf E. V., Halpern J. P., Brogan C. L., Ransom S. M., 2007, in Becker W., Huang H. H., eds, *WE-Heraeus Seminar on Neutron Stars and Pulsars 40 years after the Discovery*. Max-Planck Institute für extraterrestrische Physik, Garching, p. 24
 Roman-Duval J., Jackson J. M., Heyer M., Rathborne J., Simon R., 2010, *ApJ*, 723, 492
 Schilke P., Walmsley C. M., Pineau des Forets G., Flower D. R., 1997, *A&A*, 321, 293
 Strong A. W., Moskalenko I. V., Reimer O., Digel S., Diehl R., 2004, *A&A*, 422, L47
 Stupar M., Parker Q. A., Filipović M. D., 2008, *MNRAS*, 390, 1037
 Sugizaki M., Mitsuda K., Kaneda H., Matsuzaki K., Yamauchi S., Koyama K., 2001, *ApJS*, 134, 77
 Takahira K., Tasker E. J., Habe A., 2014, *ApJ*, 792, 63
 Torii K. et al., 2015, *ApJ*, 806, 7
 Uchiyama Y., Blandford R. D., Funk S., Tajima H., Tanaka T., 2010, *ApJ*, 723, L122
 Urquhart J. S. et al., 2010, *PASA*, 27, 321
 van der Swaluw E., Achterberg A., Gallant Y. A., Tóth G., 2001, *A&A*, 380, 309
 Voronkov M. A., Caswell J. L., Ellingsen S. P., Green J. A., Breen S. L., 2014, *MNRAS*, 439, 2584
 Walsh A. J. et al., 2011, *MNRAS*, 416, 1764
 Wang W., 2011, *Res. Astron. Astrophys.*, 11, 824
 White R. L., Becker R. H., Helfand D. J., 2005, *AJ*, 130, 586
 Wilson T. L., Bieging J., Downes D., 1978, *A&A*, 63, 1
 Zinchenko I., Forsstroem V., Lapinov A., Mattila K., 1994, *A&A*, 288, 601

APPENDIX A: BEAM EFFICIENCY AND COUPLING FACTOR

The Mopra main beam only receives only a fraction of the true emission, the rest being taken by the side lobes. Urquhart et al. (2010) obtained the main beam efficiencies, η_{mb} , at different frequencies by calibrating the Antenna flux while observing Jupiter. The following coefficient will be useful to get the real antenna temperature of the source:

$$T_{mb} = \frac{T_A^*}{\eta_{mb}} \quad (A1)$$

The coupling factor fK brings the true brightness temperature for core sizes smaller than the beam size. Indeed, the beam will average the signal from the core with the noise coming from the rest of the beam, minimizing its strength.

$$fK = \left(1 - \exp\left(-\frac{4R^2}{\theta_{mb}^2} \ln 2\right)\right)^{-1} \quad (A2)$$

$$\frac{\Delta\Omega_A}{\Delta\Omega_S} = \frac{1}{fK} \quad (A3)$$

APPENDIX B: NH₃(2,2) AND NH₃(3,3)

Fig. B1 presents the NH₃(2,2) and NH₃(3,3) integrated intensities map for emissions located in the different kinematic velocity spans: 20–40 km s⁻¹, 40–60 km s⁻¹ and 60–80 km s⁻¹.

It appears that R1, R2 and R3 shows significant emission of NH₃(2,2). However NH₃(3,3) are mostly found inside R2 and R3.

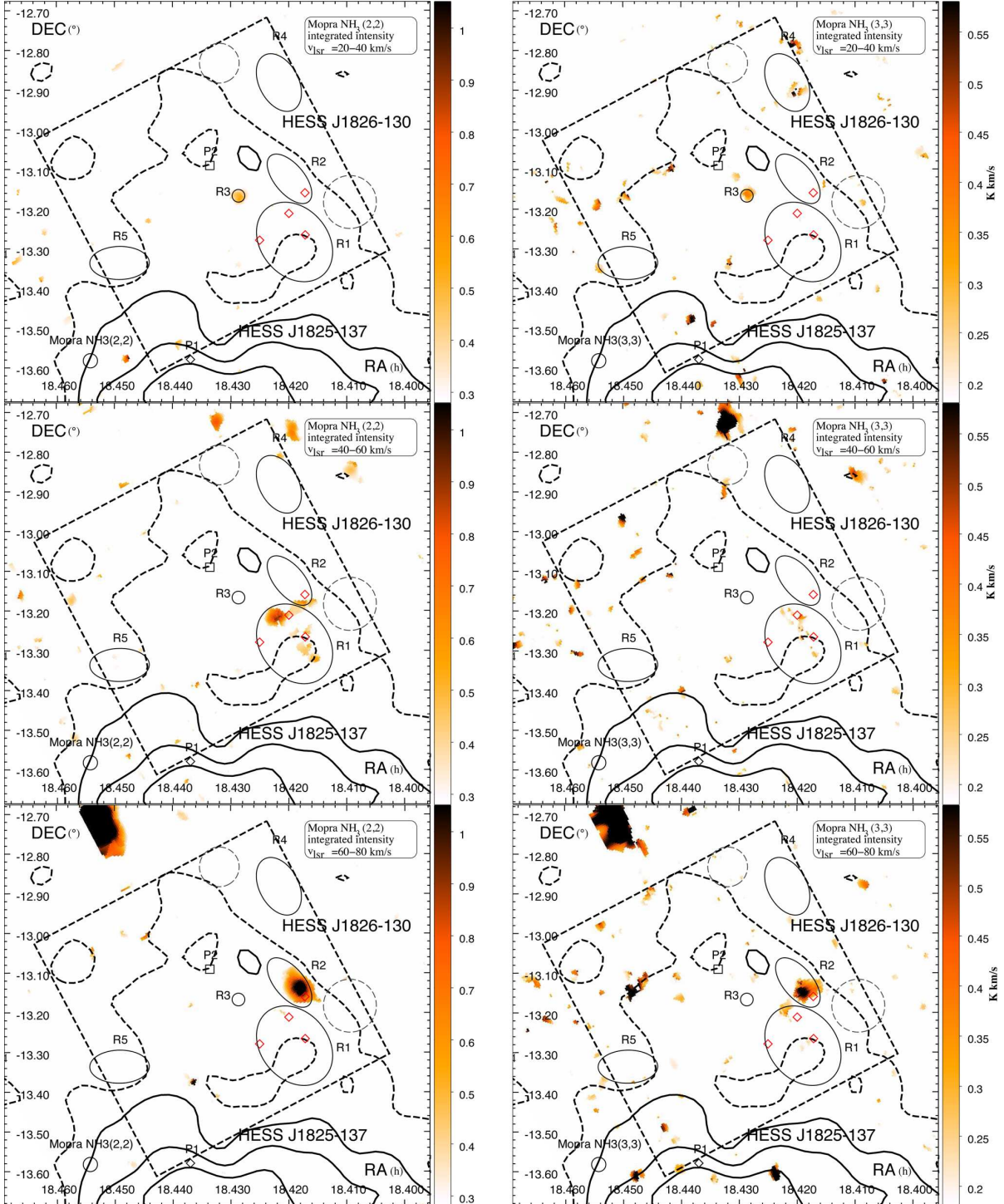


Figure B1. $\text{NH}_3(2,2)$ and $\text{NH}_3(3,3)$ integrated velocity over the different kinematic velocity spans: $v_{\text{lsr}} = 20\text{--}40$ km s^{-1} , $v_{\text{lsr}} = 40\text{--}60$ km s^{-1} , $v_{\text{lsr}} = 60\text{--}80$ km s^{-1} . The diamonds represent the different H II regions next to R1. The black circles represent the size of the catalogued SNRs. The region covered by our 7 mm survey is shown as a black dashed rectangle.

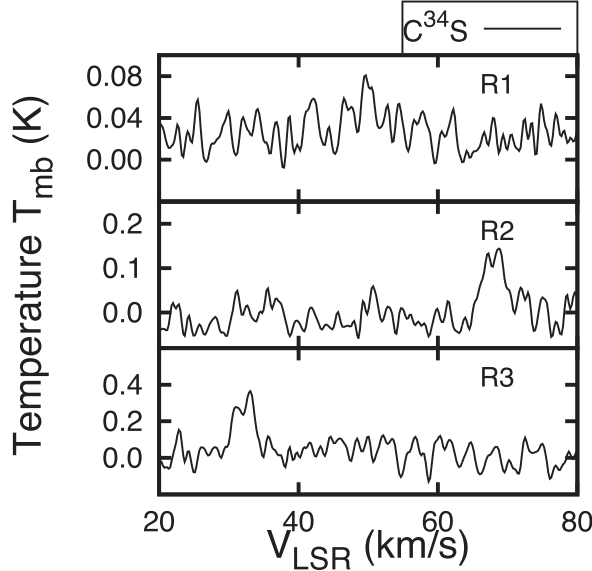


Figure C1. Averaged $C^{34}S(1-0)$ emission over the three regions of interest $R1$, $R2$, $R3$.

APPENDIX C: $C^{34}S(1-0)$

Fig. C1 displays the averaged $C^{34}S(1-0)$ emission profiles found in $R1$, $R2$ and $R3$.

APPENDIX D: $CO(1-0)$ EMISSION AT $v_{lsr} = 10-25 \text{ KM S}^{-1}$

Fig. D1 shows the Nanten $CO(1-0)$ integrated intensity between $v_{lsr} = 10$ and 25 km s^{-1} matching the pulsar PSR J1826–1256 ($P2$) kinematic distance. The presence of a molecular cloud (red

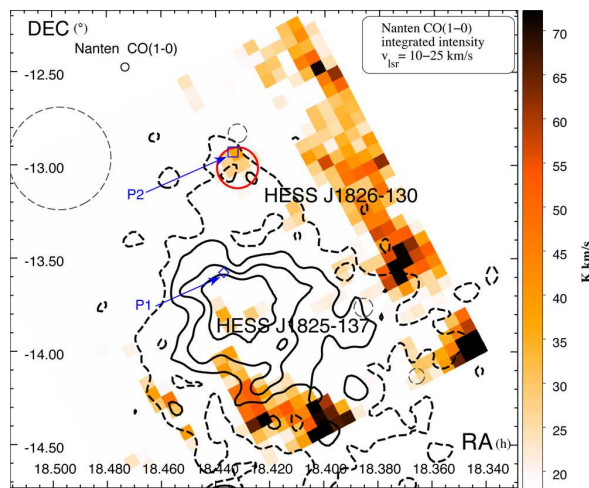


Figure D1. Nanten $CO(1-0)$ integrated intensity between $v_{lsr} = 10$ and 25 km s^{-1} overlaid by the HESS TeV contours in black (dashed and solid). The pulsars are displayed in blue while the SNRs are represented in grey dashed circles. The red circle highlights the molecular gas close to the pulsar PSR J1826–1256 ($P2$) highlighted in the text. The black dashed rectangle represents the region covered by our 7 mm survey (see online version).

circle) spatially overlapping the pulsar is observed. Provided the TeV emission originated from the PWN powered by $P2$, the association with the molecular cloud would have significantly affected the morphology of the TeV emission.

APPENDIX E: $^{13}CO(1-0)$ EMISSION POSITION-VELOCITY PLOTS TOWARDS SNR G018.6–0.2

Fig. E1 shows the $^{13}CO(1-0)$ position-velocity (in Galactic coordinates) map towards the SNR G018.6–0.2. We observe from the Galactic longitude-velocity plot a drop of ^{13}CO at $v_{lsr} = 60-70 \text{ km s}^{-1}$ towards the SNR (whose boundaries are shown as red dashed lines). However, weak emission appears at $v_{lsr} \sim 60$ and 75 km s^{-1} (appearing in both maps) suggesting that gas may have been accelerated. Its spatial coincidence with the SNR position support the scenario of a putative shell produced by the SNR progenitor star.

APPENDIX F: $HC_3N(5-4, F = 4-3)$

Fig. F1 shows the position of the observed $HC_3N(5-4, F = 4-3)$ position, and their respective spectra.

APPENDIX G: PHYSICAL PARAMETERS DERIVATION

G1 CS parameters

$CS(1-0)$ optical depth:

$$\frac{W_{CS(1-0)}}{W_{C^{34}S(1-0)}} = \frac{1 - e^{-\tau_{CS(1-0)}}}{1 - e^{-\alpha\tau_{CS(1-0)}}}, \quad (G1)$$

where α represents the relative abundance ratio $C^{34}S/CS = 0.04$ (see section 4).

Column density of energy state 1:

$$N_{CS_1} = \frac{8k\pi\nu_{10}^2}{A_{10}hc^3} \left(\frac{\Delta\Omega_A}{\Delta\Omega_S} \right) \left(\frac{\tau_{CS(1-0)}}{1 - e^{-\tau_{CS(1-0)}}} \right) \int T_{mb}(v) dv, \quad (G2)$$

where ν_{10} and A_{10} is the rest frequency and Einstein's coefficient of the $CS(1-0)$ emission, respectively. $\Delta\Omega_A$ and $\Delta\Omega_S$ are the antenna and source solid angle, respectively. In the case where $\Delta\Omega_A > \Delta\Omega_S$, we use equations A2 and A3.

CS column density:

$$N_{CS} = N_{CS_1} \left(1 + \frac{1}{3} e^{2.35/T_{kin}} + \frac{5}{3} e^{-4.7/T_{kin}} + \dots \right) \quad (G3)$$

G2 NH_3 parameters

$NH_3(1,1)$ optical depth:

$$\frac{T_{Am}^*}{T_{As}^*} = \frac{1 - e^{-\tau_m}}{1 - e^{-\alpha\tau_m}} \text{ for } NH_3 \quad (G4)$$

$$\tau_{NH_3(1,1)} = \frac{\tau_m}{0.5}. \quad (G5)$$

Now, τ_m is the optical depth of the main emission and α represents the relative strength of the satellite line compared to the main line.

$NH_3(1,1)$ and $NH_3(2,2)$ column densities:

$$N_{1,1} = \frac{8k\pi\nu_{11}^2}{A_{11}hc^3} \left(\frac{\Delta\Omega_A}{\Delta\Omega_S} \right) \left(\frac{\tau_{NH_3(1,1)}}{1 - e^{-\tau_{NH_3(1,1)}}} \right) \int T_{mb}(v) dv \quad (G6)$$

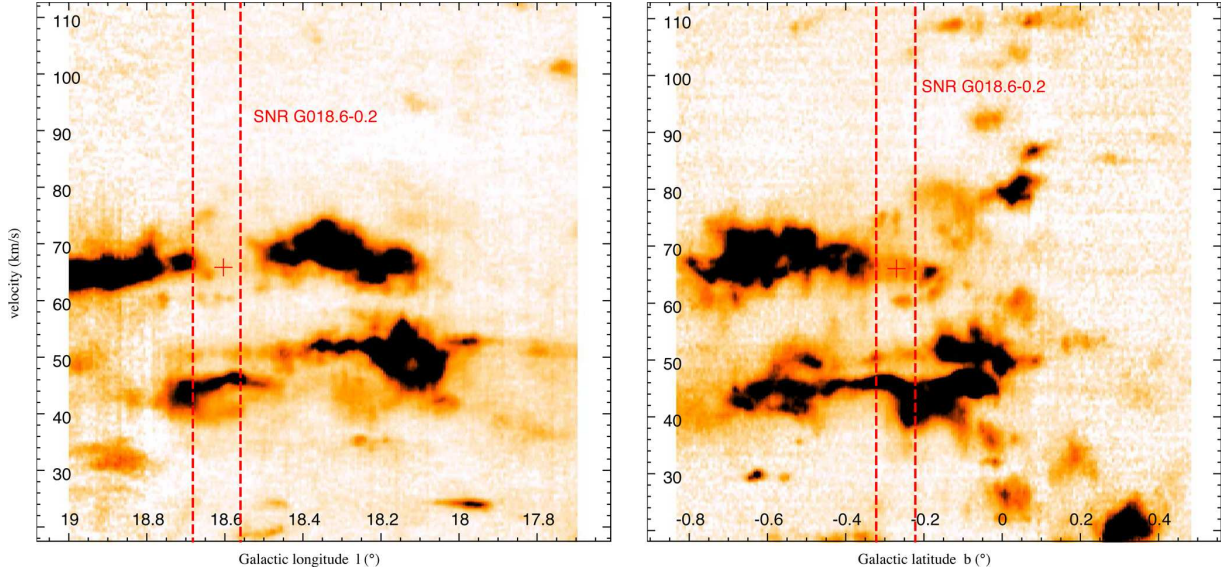


Figure E1. GRS $^{13}\text{CO}(1-0)$ Galactic longitude-velocity (l,v) (left) and Galactic latitude-velocity (b,v) (right) maps integrated between $b = [-0.227: -0.338]$ and $l = [18.554: 18.687]$. The red cross indicates the plausible location of a weak shell spatially coincident with the SNR G018.6–0.2 whose position is delimited by the two red dashed lines (see online version for colours).

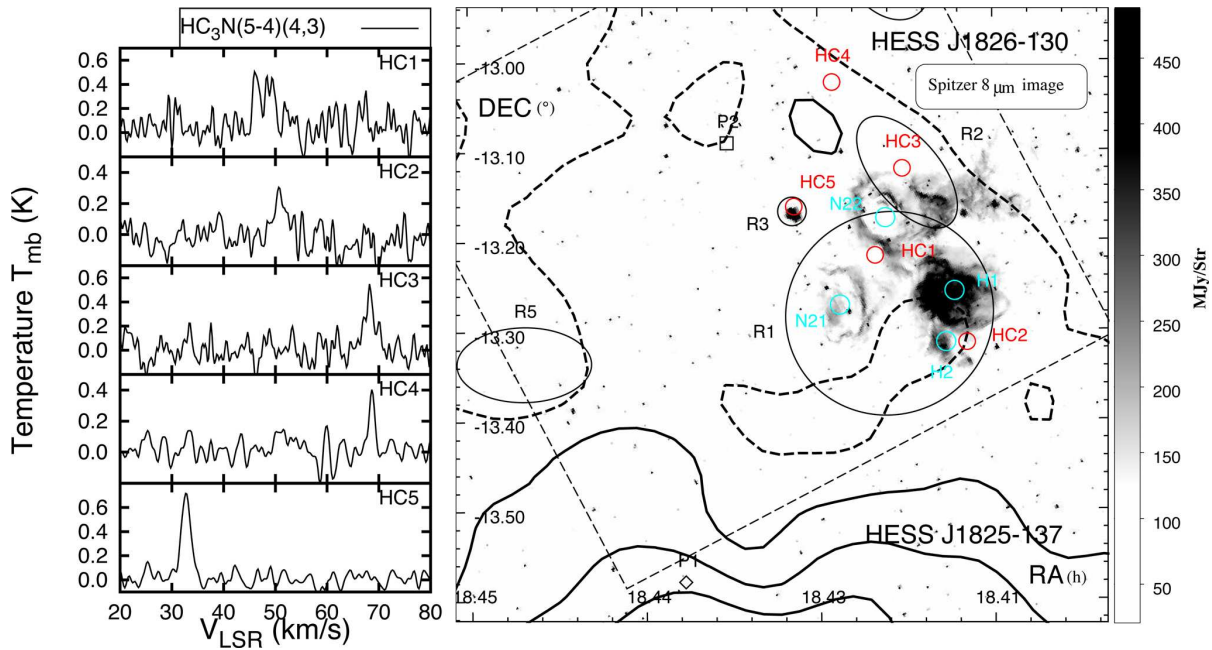


Figure F1. *Spitzer* 8 μm map towards HESS J1826–130. The red circles indicate the regions where $\text{HC}_3\text{N}(5-4, F=4-3)$ emission are found. Their respective spectra are shown in the left-hand side. The aforementioned H II regions are displayed as cyan circles (see online version for colours).

$$N_{2,2} = \frac{8k\pi\nu_{22}^2}{A_{22}hc^3} \left(\frac{\Delta\Omega_A}{\Delta\Omega_S} \right) \left(\frac{\tau_{\text{NH}_3(2,2)}}{1 - e^{-\tau_{\text{NH}_3(2,2)}}} \right) \int T_{\text{mb}}(v) dv, \quad (\text{G7})$$

where ν_{11} and ν_{22} are the rest frequencies of the $\text{NH}_3(1,1)$ and $\text{NH}_3(2,2)$ emission, respectively. $\Delta\Omega_A$ and $\Delta\Omega_S$ are the antenna and source solid angle, respectively. In the case where $\Delta\Omega_A > \Delta\Omega_S$, we use equations A2 and A3.

Rotational and kinetic temperature

$$T_{\text{rot}} = -\frac{41}{\ln(3N_{2,2}/(5N_{1,1}))} \quad (\text{G8})$$

$$T_{\text{kin}} = T_{\text{rot}} \left(1 - \frac{T_{\text{rot}}}{42} \log(1 + 1.1 \exp(-16/T_{\text{rot}})) \right)^{-1}. \quad (\text{G9})$$

2832 *F. Voisin et al.*

NH₃ column density

$$N_{\text{tot}} = N_{1,1} \left(1 + \frac{1}{3} e^{23.26/T_{\text{kin}}} + \frac{14}{3} e^{-100.25/T_{\text{kin}}} + \dots \right) \quad (\text{G10})$$

where $\mu = 2.8$ represents the weight factor assuming the molecular cloud consisted of 20 per cent of He, X was either NH₃ or CS and a , b was the semiminor and semimajor axis, respectively. ab^2 assumes the cloud also extends at distance b in the z -direction.

G3 Mass and density

$$M_{\text{H}_2}(X) = \mu m_{\text{H}} \pi a b N_{\text{H}_2} \quad (\text{G11})$$

$$n_{\text{H}_2}(X) = \frac{M}{4/3 (\mu m_{\text{H}}) \pi a b^2}, \quad (\text{G12})$$

APPENDIX H: GAS PARAMETERS DERIVED FOR REGIONS R1 TO R6

Table H1a. Parameters derived towards region R1 using the molecular transition CS(1–0), CO(1–0), ¹³CO(1–0), NH₃(1,1), NH₃(2,2) and C³⁴S(1–0) when emission are found. The labels a, b, c, d denote a distinct emission. Lower limits have been derived when we assumed $\tau = 0$.

CS	R1	distance (kpc)	$\frac{W_{\text{CS}(1-0)}}{W_{\text{C}^{34}\text{S}(1-0)}}$	$\tau_{\text{CS}(1-0)}$	$N_{\text{CS}} [10^{12}]^a$ (cm ⁻²)	$N_{\text{H}_2} [10^{20}]^{ab}$ (cm ⁻²)	$M_{\text{H}_2}^{abc}$ (M _⊙)	$n_{\text{H}_2}^{abc}$ (cm ⁻³)
	R1a	near : 3.9 far : 12.2	23.5	0.1	80	200	1.0×10^5 1.0×10^6	7.5×10^2 3.8×10^2
	R1c	near : 3.5 far : 12.6	–	–	>2	>5	$>1.8 \times 10^3$ $>2.4 \times 10^4$	$>1.4 \times 10^1$ >4
	R1e	near : 4.7 far : 11.4	–	–	>13	>31	$>2.4 \times 10^4$ $>1.4 \times 10^5$	$>7.4 \times 10^1$ $>3.0 \times 10^1$
NH ₃	R1	distance (kpc)	$\tau_{\text{NH}_3(1,1)}$	T_{kin} (K)	$N_{\text{NH}_3} [10^{12}]$ (cm ⁻²)	$N_{\text{H}_2} [10^{20}]^{ab}$ (cm ⁻²)	$M_{\text{H}_2}^{abc}$ (M _⊙)	$n_{\text{H}_2}^{abc}$ (cm ⁻³)
	R1a	near : 3.9 far : 12.2	0.43	18	46	46	1.4×10^4 9.7×10^4	2.0×10^2 6.3×10^1
	R1e	near : 4.7 far : 11.4	–	–	>14	>14	$>6.1 \times 10^3$ $>3.6 \times 10^4$	$>4.8 \times 10^1$ $>2.0 \times 10^1$
CO	R1	distance (kpc)	$M_{\text{H}_2}^d$ (M _⊙)	$M_{\text{vir}}(^{13}\text{CO})^e$ (M _⊙)	$n_{\text{H}_2}^e$ (cm ⁻³)			
	R1a	near : 3.9 far : 12.2	1.2×10^5 1.1×10^6	$4.8 \times 10^4 - 2.1 \times 10^5$ $1.5 \times 10^5 - 5.3 \times 10^5$	9.6×10^2 3.0×10^2			
	R1c	near : 3.5 far : 12.6	2.0×10^4 2.6×10^5	$6 \times 10^3 - 2.1 \times 10^4$ $2.1 \times 10^4 - 7.6 \times 10^4$	2.2×10^2 6.0×10^1			
	R1d	near : 4.3 far : 11.8	6.8×10^3 5.2×10^4	$7.0 \times 10^3 - 2.6 \times 10^4$ $2.0 \times 10^4 - 7.1 \times 10^4$	4.3×10^1 1.5×10^1			
	R1e	near : 4.7 far : 12.2	6.8×10^4 4.2×10^5	$1.5 \times 10^5 - 5.3 \times 10^5$ $7.8 \times 10^4 - 2.8 \times 10^5$	3.2×10^2 1.3×10^2			

Notes. ^aParameters have been derived using the LTE assumption.

^bThe H₂ physical parameters derived using a NH₃ abundance ratio $\chi_{\text{NH}_3} = 1 \times 10^{-8}$ and using a CS abundance ratio $\chi_{\text{CS}} = 4 \times 10^{-9}$.

^cH₂ mass and density from CS and NH₃ have been computed assuming the observed region is spherical or ellipsoid and whose size are given in Tables 2 and 3.

^dH₂ mass are derived using a $X_{\text{CO}} = 2.0 \times 10^{20} \text{ cm}^{-2} (\text{K km s}^{-1})^{-1}$ and assuming a spherical region.

^eVirial mass is computed using CO(1–0) and ¹³CO(1–0) emission FWHM and assuming a spherical region. The left value represents the Virial mass for a $1/r^2$ density distribution whereas the right value indicate the value for a Gaussian distribution.

Table H1b. Parameters derived towards region R2 using the molecular transition CS(1–0), CO(1–0), ¹³CO(1–0), NH₃(1,1), NH₃(2,2) and C³⁴S(1–0) when emission are found. The labels *a,b,c,d* denote a distinct emission. Lower limits have been derived when we assumed $\tau = 0$.

CS	R2	distance (kpc)	$\frac{W_{\text{CS}(1-0)}}{W_{\text{C}^{34}\text{S}(1-0)}}$	$\tau_{\text{CS}(1-0)}$	$N_{\text{CS}} [10^{12}]^a$ (cm ⁻²)	$N_{\text{H}_2} [10^{20}]^{ab}$ (cm ⁻²)	$M_{\text{H}_2}^{abc}$ (M _⊙)	$n_{\text{H}_2}^{abc}$ (cm ⁻³)
	R2a	near : 4.0 far : 12.1	–	–	>14	>36	>3.4 × 10 ³ >3.2 × 10 ⁴	>3.3 × 10 ² >1.1 × 10 ²
	R2e	near : 4.7 far : 11.4	13.3	1.5	100	250	3.4 × 10 ⁴ 2.0 × 10 ⁵	2.0 × 10 ³ 8.5 × 10 ²
NH ₃	R2	distance (kpc)	$\tau_{\text{NH}_3(1,1)}$	T_{kin} (K)	$N_{\text{NH}_3} [10^{12}]$ (cm ⁻²)	$N_{\text{H}_2} [10^{20}]^{ab}$ (cm ⁻²)	$M_{\text{H}_2}^{abc}$ (M _⊙)	$n_{\text{H}_2}^{abc}$ (cm ⁻³)
	R2a	near : 4.0 far : 12.1	–	–	>5	>5	>4.5 × 10 ² >4.0 × 10 ³	>4.3 × 10 ¹ >1.4 × 10 ¹
	R2e	near : 4.7 far : 11.4	3.5	11	600	600	8.1 × 10 ⁴ 4.8 × 10 ⁵	4.8 × 10 ³ 2.0 × 10 ³
CO	R2	distance (kpc)	$M_{\text{H}_2}^d$ (M _⊙)	$M_{\text{vir}}(^{13}\text{CO})^e$ (M _⊙)	$n_{\text{H}_2}^e$ (cm ⁻³)			
	R2a	near : 4.0 far : 12.1	1.3 × 10 ⁴ 1.1 × 10 ⁵	4.2 × 10 ³ – 2.5 × 10 ⁴ 1.3 × 10 ⁴ – 4.4 × 10 ⁴	1.2 × 10 ³ 8.9 × 10 ²			
	R2c	near : 3.5 far : 12.6	8.8 × 10 ³ 1.1 × 10 ⁵	8.9 × 10 ⁴ – 3.1 × 10 ⁵ 3.2 × 10 ⁵ – 1.1 × 10 ⁶	3.9 × 10 ² 2.5 × 10 ²			
	R2e	near : 4.7 far : 11.4	2.9 × 10 ⁴ 2.0 × 10 ⁵	3.1 × 10 ⁴ – 1.1 × 10 ⁵ 7.5 × 10 ⁴ – 2.7 × 10 ⁵	1.7 × 10 ³ 6.4 × 10 ²			

Notes. ^aParameters have been derived using the LTE assumption.

^bThe H₂ physical parameters derived using a NH₃ abundance ratio $\chi_{\text{NH}_3} = 1 \times 10^{-8}$ and using a CS abundance ratio $\chi_{\text{CS}} = 4 \times 10^{-9}$.

^cH₂ mass and density from CS and NH₃ have been computed assuming the observed region is spherical or ellipsoid and whose size are given in Tables 2 and 3.

^dH₂ mass are derived using a $X_{\text{CO}} = 2.0 \times 10^{20} \text{ cm}^{-2} (\text{K km s}^{-1})^{-1}$ and assuming a spherical region.

^eVirial mass is computed using CO(1–0) and ¹³CO(1–0) emission FWHM and assuming a spherical region. The left value represents the Virial mass for a $1/r^2$ density distribution whereas the right value indicate the value for a Gaussian distribution.

Table H1c. Parameters derived towards region R3 using the molecular transition CS(1–0), CO(1–0), ¹³CO(1–0), NH₃(1,1), NH₃(2,2) and C³⁴S(1–0) when emission are found. The labels *a,b,c* denote a distinct emission. Lower limits have been derived when we assumed $\tau = 0$.

CS	R3	distance (kpc)	$\frac{W_{\text{CS}(1-0)}}{W_{\text{C}^{34}\text{S}(1-0)}}$	$\tau_{\text{CS}(1-0)}$	$N_{\text{CS}} [10^{12}]^a$ (cm ⁻²)	$N_{\text{H}_2} [10^{20}]^{ab}$ (cm ⁻²)	$M_{\text{H}_2}^{abc}$ (M _⊙)	$n_{\text{H}_2}^{abc}$ (cm ⁻³)
	R3e	near : 4.8 far : 11.3	–	–	>7	>16	>2.5 × 10 ² >1.7 × 10 ³	>2.0 × 10 ² >1.1 × 10 ²
	R3f	near : 2.9 far : 13.3	8.3	3.0	520	1300	7.4 × 10 ³ 1.5 × 10 ⁵	3.5 × 10 ⁴ 7.6 × 10 ³
NH ₃	R3	distance (kpc)	$\tau_{\text{NH}_3(1,1)}$	T_{kin} (K)	$N_{\text{NH}_3} [10^{12}]$ (cm ⁻²)	$N_{\text{H}_2} [10^{20}]^{ab}$ (cm ⁻²)	$M_{\text{H}_2}^{abc}$ (M _⊙)	$n_{\text{H}_2}^{abc}$ (cm ⁻³)
	R3f	near : 2.9 far : 13.3	2.0	20	165	165	9.5 × 10 ² 1.3 × 10 ⁴	4.4 × 10 ³ 6.2 × 10 ²
CO	R3	distance (kpc)	$M_{\text{H}_2}^d$ (M _⊙)	$M_{\text{vir}}(^{13}\text{CO})^e$ (M _⊙)	$n_{\text{H}_2}^e$ (cm ⁻³)			
	R3a	near : 2.9 far : 13.3	3.3 × 10 ³ 7.2 × 10 ⁴	1.2 × 10 ³ – 4.4 × 10 ³ 5.7 × 10 ³ – 2.0 × 10 ⁴	1.6 × 10 ⁴ 4.3 × 10 ³			
	R3e	near : 4.8 far : 11.3	2.3 × 10 ³ 1.3 × 10 ⁴	2.7 × 10 ³ – 9.6 × 10 ³ 6.4 × 10 ⁴ – 2.3 × 10 ⁵	2.5 × 10 ³ 1.1 × 10 ³			
	R3f	near : 3.8 far : 12.3	1.4 × 10 ³ 1.5 × 10 ⁴	2.1 × 10 ³ – 7.6 × 10 ³ 6.9 × 10 ³ – 2.5 × 10 ⁴	3.1 × 10 ³ 9.3 × 10 ²			

Notes. ^aParameters have been derived using the LTE assumption.

^bThe H₂ physical parameters derived using a NH₃ abundance ratio $\chi_{\text{NH}_3} = 1 \times 10^{-8}$ and using a CS abundance ratio $\chi_{\text{CS}} = 4 \times 10^{-9}$.

^cH₂ mass and density from CS and NH₃ have been computed assuming the observed region is spherical or ellipsoid and whose size are given in Tables 2 and 3.

^dH₂ mass are derived using a $X_{\text{CO}} = 2.0 \times 10^{20} \text{ cm}^{-2} (\text{K km s}^{-1})^{-1}$ and assuming a spherical region.

^eVirial mass is computed using CO(1–0) and ¹³CO(1–0) emission FWHM and assuming a spherical region. The left value represents the Virial mass for a $1/r^2$ density distribution whereas the right value indicate the value for a Gaussian distribution.

2834 *F. Voisin et al.***Table H1d.** Parameters derived towards region R4 using the molecular transition CS(1–0), CO(1–0), ¹³CO(1–0), NH₃(1,1), NH₃(2,2) and C³⁴S(1–0) when emission are found. The labels *a,b,c* denote a distinct emission. Lower limits have been derived when we assumed $\tau = 0$.

CS	R4	distance (kpc)	$\frac{W_{\text{CS}(1-0)}}{W_{\text{C}^{34}\text{S}(1-0)}}$	$\tau_{\text{CS}(1-0)}$	$N_{\text{CS}} [10^{12}]^a$ (cm ⁻²)	$N_{\text{H}_2} [10^{20}]^{ab}$ (cm ⁻²)	$M_{\text{H}_2}^{abc}$ (M _⊙)	$n_{\text{H}_2}^{abc}$ (cm ⁻³)
	R4a	near : 4.0 far : 12.2	–	–	>23	>58	>7.4 × 10 ³ >7.0 × 10 ⁴	>4.1 × 10 ² >1.4 × 10 ²
	R4b	near : 3.6 far : 12.5	–	–	>15	>38	>5.0 × 10 ³ >4.9 × 10 ⁴	>2.7 × 10 ² >9.0 × 10 ¹
NH ₃	R4	distance (kpc)	$\tau_{\text{NH}_3(1,1)}$	T_{kin} (K)	$N_{\text{NH}_3} [10^{12}]$ (cm ⁻²)	$N_{\text{H}_2} [10^{20}]^{ab}$ (cm ⁻²)	$M_{\text{H}_2}^{abc}$ (M _⊙)	$n_{\text{H}_2}^{abc}$ (cm ⁻³)
	R4a	near : 4.0 far : 12.2	–	–	>19	>19	>2.0 × 10 ³ >2.4 × 10 ⁴	>1.5 × 10 ² >4.4 × 10 ¹
	R4b	near : 3.6 far : 12.5	–	–	>10	>10	>1.2 × 10 ³ >1.1 × 10 ⁴	>7.0 × 10 ¹ >2.3 × 10 ¹
CO	R4	distance (kpc)		$M_{\text{H}_2}^d$ (M _⊙)	$M_{\text{vir}}(^{13}\text{CO})^e$ (M _⊙)	$n_{\text{H}_2}^e$ (cm ⁻³)		
	R4a	near : 4.0 far : 12.2		1.6 × 10 ⁴ 1.5 × 10 ⁵	7.2 × 10 ³ – 2.5 × 10 ⁴ 2.2 × 10 ⁴ – 7.8 × 10 ⁴	9.3 × 10 ² 3.0 × 10 ²		
	R4b	near : 3.6 far : 12.5		1.1 × 10 ⁴ 1.3 × 10 ⁵	6.1 × 10 ³ – 2.2 × 10 ⁴ 2.1 × 10 ⁴ – 7.5 × 10 ⁴	8.2 × 10 ² 2.5 × 10 ²		
	R4e	near : 4.6 far : 11.5		9.0 × 10 ³ 5.6 × 10 ⁴	1.9 × 10 ⁴ – 6.7 × 10 ⁴ 4.7 × 10 ⁴ – 1.7 × 10 ⁵	3.6 × 10 ² 1.1 × 10 ²		

Notes. ^aParameters have been derived using the LTE assumption.

^bThe H₂ physical parameters derived using a NH₃ abundance ratio $\chi_{\text{NH}_3} = 1 \times 10^{-8}$ and using a CS abundance ratio $\chi_{\text{CS}} = 4 \times 10^{-9}$.

^cH₂ mass and density from CS and NH₃ have been computed assuming the observed region is spherical or ellipsoid and whose size are given in Tables 2 and 3.

^dH₂ mass are derived using a $X_{\text{CO}} = 2.0 \times 10^{20} \text{ cm}^{-2} (\text{K km s}^{-1})^{-1}$ and assuming a spherical region.

^eVirial mass is computed using CO(1–0) and ¹³CO(1–0) emission FWHM and assuming a spherical region. The left value represents the Virial mass for a $1/r^2$ density distribution whereas the right value indicate the value for a Gaussian distribution.

Table H1e. Parameters derived towards region R5 using the molecular transition CS(1–0), CO(1–0), ¹³CO(1–0), NH₃(1,1), NH₃(2,2) and C³⁴S(1–0) when emission are found. The labels *a,b,c* denote a distinct emission. Lower limits have been derived when we assumed $\tau = 0$.

CS	R5	distance (kpc)	$\frac{W_{\text{CS}(1-0)}}{W_{\text{C}^{34}\text{S}(1-0)}}$	$\tau_{\text{CS}(1-0)}$	$N_{\text{CS}} [10^{12}]^a$ (cm ⁻²)	$N_{\text{H}_2} [10^{20}]^{ab}$ (cm ⁻²)	$M_{\text{H}_2}^{abc}$ (M _⊙)	$n_{\text{H}_2}^{abc}$ (cm ⁻³)
	R5a	near : 4.0 far : 12.1	–	–	>3	>7	>7.4 × 10 ² >6.7 × 10 ³	>5.7 × 10 ¹ >1.9 × 10 ¹
	R5b	near : 3.7 far : 12.4	–	–	>8	>21	>1.8 × 10 ³ >2.1 × 10 ⁴	>1.9 × 10 ² >5.5 × 10 ¹
NH ₃	R5	distance (kpc)	$\tau_{\text{NH}_3(1,1)}$	T_{kin} (K)	$N_{\text{NH}_3} [10^{12}]$ (cm ⁻²)	$N_{\text{H}_2} [10^{20}]^{ab}$ (cm ⁻²)	$M_{\text{H}_2}^{abc}$ (M _⊙)	$n_{\text{H}_2}^{abc}$ (cm ⁻³)
	R5b	near : 3.7 far : 12.4	–	–	>21	>21	>2.0 × 10 ³ >2.1 × 10 ⁴	>1.9 × 10 ² >5.6 × 10 ¹
CO	R5	distance (kpc)		$M_{\text{H}_2}^d$ (M _⊙)	$M_{\text{vir}}(^{13}\text{CO})^e$ (M _⊙)	$n_{\text{H}_2}^e$ (cm ⁻³)		
	R5a	near : 3.7 far : 12.4		9.5 × 10 ³ 1.1 × 10 ⁴	3.8 × 10 ⁴ – 1.4 × 10 ⁵ 1.3 × 10 ⁵ – 4.6 × 10 ⁵	6.8 × 10 ² 2.0 × 10 ²		
	R5b	near : 4.0 far : 12.1		1.1 × 10 ⁴ 1.0 × 10 ⁵	1.5 × 10 ⁴ – 5.4 × 10 ⁴ 4.6 × 10 ⁴ – 1.6 × 10 ⁵	6.1 × 10 ² 1.9 × 10 ²		
	R5c	near : 4.5 far : 11.6		3.4 × 10 ³ 2.3 × 10 ⁴	3.7 × 10 ⁴ – 1.3 × 10 ⁵ 8.0 × 10 ⁴ – 2.9 × 10 ⁵	1.4 × 10 ² 5.0 × 10 ¹		

Notes. ^aParameters have been derived using the LTE assumption.

^bThe H₂ physical parameters derived using a NH₃ abundance ratio $\chi_{\text{NH}_3} = 1 \times 10^{-8}$ and using a CS abundance ratio $\chi_{\text{CS}} = 4 \times 10^{-9}$.

^cH₂ mass and density from CS and NH₃ have been computed assuming the observed region is spherical or ellipsoid and whose size are given in Tables 2 and 3.

^dH₂ mass are derived using a $X_{\text{CO}} = 2.0 \times 10^{20} \text{ cm}^{-2} (\text{K km s}^{-1})^{-1}$ and assuming a spherical region.

^eVirial mass is computed using CO(1–0) and ¹³CO(1–0) emission FWHM and assuming a spherical region. The left value represents the Virial mass for a $1/r^2$ density distribution whereas the right value indicate the value for a Gaussian distribution.

ISM studies towards HESS J1825–137 2835

Table H1f. Parameters derived towards region R5 using the molecular transition CS(1–0), CO(1–0), ¹³CO(1–0), NH₃(1,1), NH₃(2,2) and C³⁴S(1–0) when emission are found. Lower limits have been derived when we assumed $\tau = 0$.

CS	R6	distance (kpc)	$\frac{W_{\text{CS}(1-0)}}{W_{\text{C}^{34}\text{S}(1-0)}}$	$\tau_{\text{CS}(1-0)}$	$N_{\text{CS}} [10^{12}]^a$ (cm ⁻²)	$N_{\text{H}_2} [10^{20}]^{ab}$ (cm ⁻²)	$M_{\text{H}_2}^{abc}$ (M _⊙)	$n_{\text{H}_2}^{abc}$ (cm ⁻³)
	R6	near : 3.7 far : 12.5	–	–	>30	>75	>3.6 × 10 ⁴ >4.2 × 10 ⁵	>2.2 × 10 ² >6.5 × 10 ¹
	CO	R6	distance (kpc)	$M_{\text{H}_2}^d$ (M _⊙)	$M_{\text{vir}}(^{13}\text{CO})^e$ (M _⊙)	$n_{\text{H}_2}^e$ (cm ³)		
		R6b	near : 3.7 far : 12.5	7.6 × 10 ⁴ 8.7 × 10 ⁵	2.2 × 10 ⁴ – 7.9 × 10 ⁴ 7.6 × 10 ⁴ – 2.7 × 10 ⁵	4.3 × 10 ² 1.7 × 10 ²		

Notes. ^aParameters have been derived using the LTE assumption.

^bThe H₂ physical parameters derived using a NH₃ abundance ratio $\chi_{\text{NH}_3} = 1 \times 10^{-8}$ and using a CS abundance ratio $\chi_{\text{CS}} = 4 \times 10^{-9}$.

^cH₂ mass and density from CS and NH₃ have been computed assuming the observed region is spherical or ellipsoid and whose size are given in Tables 2 and 3.

^dH₂ mass are derived using a $X_{\text{CO}} = 2.0 \times 10^{20} \text{ cm}^{-2} (\text{K km s}^{-1})^{-1}$ and assuming a spherical region.

^eVirial mass is computed using CO(1–0) and ¹³CO(1–0) emission FWHM and assuming a spherical region. The left value represents the Virial mass for a $1/r^2$ density distribution whereas the right value indicate the value for a Gaussian distribution.

This paper has been typeset from a T_EX/L^AT_EX file prepared by the author.

Chapter 6

Gamma-ray contribution of HESS J1825–137 towards HESS J1826–130

HESS J1825–137 is a pulsar wind nebulae (PWN) (Aharonian et al., 2006b) powered by the pulsar PSR J1826–1334 (P1 in Fig. 6.1), with current spin down energy $\dot{E}_{\text{SD}} = 2.6 \times 10^{36}$ erg/s, a rotation period $P = 109$ ms and a dispersion measure distance $d \sim 4.0$ kpc. The TeV emission appears very extended ($\sim 1^\circ$, see black contours in Fig. 6.1). The offset position of the pulsar PSR J1826–1334 with respect to the TeV emission peak position also suggests a crushed PWN scenario from the SNR reverse shock, result of the interaction of the progenitor SNR with a denser region (e.g. molecular cloud, Blondin et al. 2001).

The detection of HESS J1826–130, located north of HESS J1825–137, have been announced by Deil et al. (2015). Notably, using a 0.22° integration radius (red circle in Fig. 6.1), the flux above 1 TeV reaches 3% of the Crab flux $F_{\text{obs}}^{\text{J1826}} (> 1 \text{ TeV}) = 2.4 \times 10^{-13}$ ph cm $^{-2}$ s $^{-1}$. The observed TeV gamma-ray spectrum has been fitted with a power-law distribution with hard spectral index $\Gamma = 1.6 \pm 0.2$ and an energy cutoff $E_0 = 12$ TeV. The PWN G18.5–0.4, observed in X-rays with ASCA (Roberts et al., 2007), is powered by the radio quiet gamma-ray pulsar PSR J1826–1256 (P2 in Fig. 6.1), and appears to be a viable candidate to explain the origin of this TeV emission. However, the distance of the gamma-ray pulsar still remain unconstrained. From our ISM analysis in chapter 5, I argued that the pulsar is located at $d = 11.4$ kpc, as it would reconcile the characteristic age $\tau_c = 11$ kyr with the small angular diameter ($4'$) of the nearest detected SNR G018.6–0.2. I have also argued that the SNRs G018.1–0.1 and G018.6–0.2 are unlikely to contribute to the TeV emission towards HESS J1826–130 as no significant amount of gas were found overlapping the TeV emission at the assumed distances $d > 4$ kpc and $d = 11.4$ kpc respectively. However, I also confirmed of an extended molecular complex at $d \sim 4$ kpc (previously detected by Lemi re et al. 2006, see green circle in Fig. 6.1) which overlaps the TeV emission in black contours. CS and NH $_3$ observations showed two embedded dense molecular regions ‘R1’ and ‘R5’ (see cyan ellipses) appearing quite close to P1 ($20'$). From our density estimates of this molecular complex ($n_{\text{H}} \sim 700$ cm $^{-3}$), the energy density required for CRs to produce the TeV emission towards HESS J1826–130 could, in fact, be attained by CRs escaping by the middle aged progenitor SNR of PSR J1826–1334. Consequently, understanding how the PWN HESS J1825–137 and its progenitor SNR could contribute to the TeV emission towards HESS J1826–130 is the first step to understand its origin. Additionally, HESS J1825–137 and

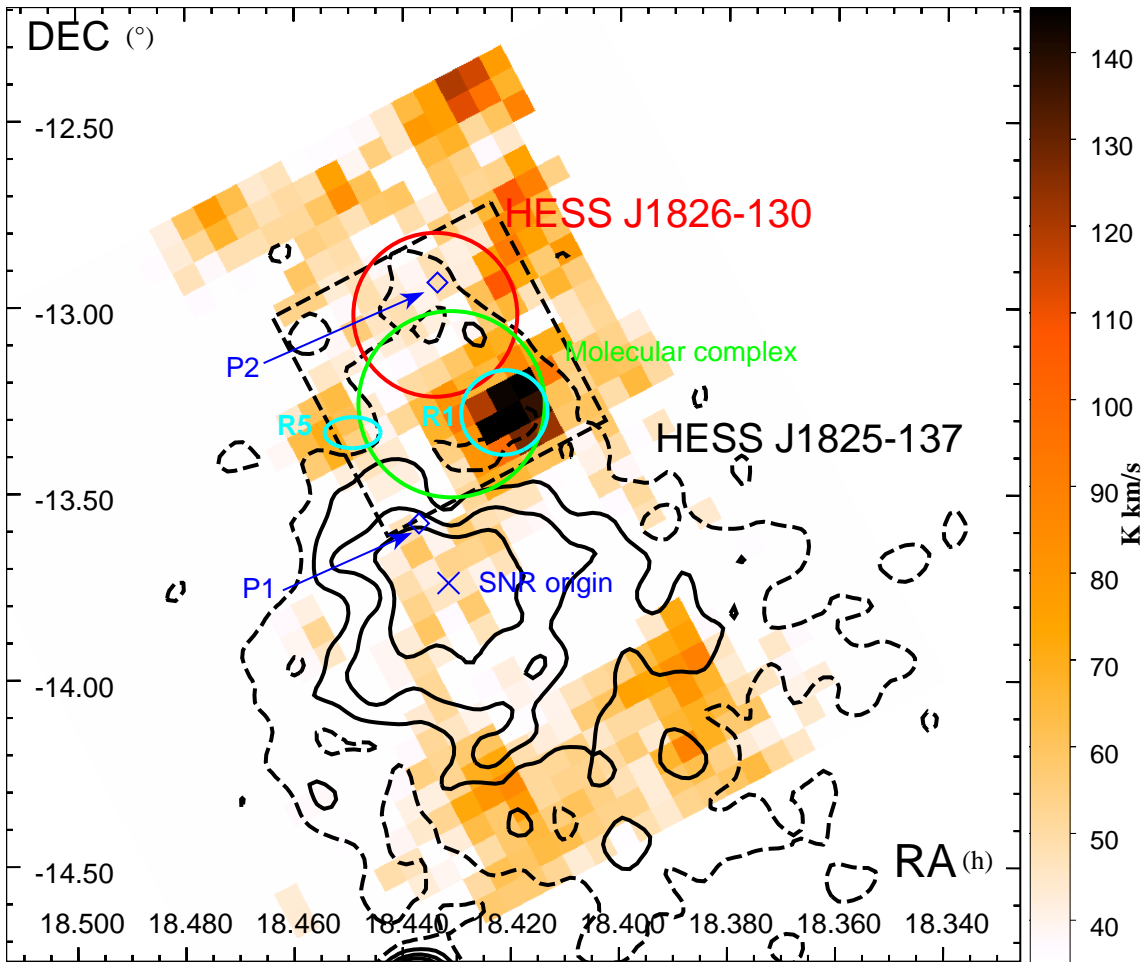


Figure 6.1: Nanten CO(1–0) integrated intensity map between $v_{\text{lsr}} = 45 - 60 \text{ km/s}$ ($d \sim 4 \text{ kpc}$) towards HESS J1825–137 and HESS J1826–130. The position and size of the molecular complex are shown as a green circle whereas the positions and sizes of the dense molecular regions ‘R1’ and ‘R5’ (see Voisin et al. 2016) are shown as cyan ellipses. The assumed position of the origin of the progenitor SNR of HESS J1825–137 is indicated by the blue cross. The locations of the pulsar PSR J1826–1337 (P1) and PSR J1826–1256 (P2) are shown as blue diamonds. Finally, the $0^\circ.22$ radius region indicate the region used to obtain the photon flux towards HESS J1826–130 (see text).

the northern TeV source HESS J1826–130 appear to be a good laboratory to study the propagation of CRs inside molecular clouds. In this chapter, I thus aim to use an isotropic diffusion model accounting energy losses to model the contribution of CRs/high energy electrons escaping the PWN HESS J1825–137 and its progenitor SNR to the TeV emission towards HESS J1826–130.

6.1 Progenitor SNR

In this section, I discuss the energy required for the SNR to produce the TeV flux towards HESS J1826–130. I also discuss, using an isotropic diffusion, whether high energy electrons could reach and contribute to HESS J1826–130. In both cases, I assume the origin of the SNR to be positioned at the HESS J1826–130 TeV peak (see blue cross in Fig. 6.1).

6.1.1 Contribution from CRs

The first step is to obtain the total proton energy W_p required to produce the TeV flux from $F_{\text{obs}}^{\text{J1826}} (> 1 \text{ TeV}) = 7.4 \times 10^{-13} \text{ ph cm}^{-2} \text{ s}^{-1}$ towards HESS J1826–130. In Chapter 5 I noted that, assuming a hadronic sce-

nario, the *sea* of CRs could not produce such flux and a nearby CR source was required to match with the observed flux. I thus check whether the progenitor SNR of PSR J1826–1334 could attain the energy required for the CRs to produce the observed TeV flux. Here, I first assume that a fraction $\eta_{pp} = 0.1$ of the SNR kinetic energy E_{SNR} is transferred into CRs (Aharonian et al., 1994) with total energy $W_p = \eta_{pp} E_{\text{SNR}}$. As per Voisin et al. (2016) (Chapter 5), I approximate the northern molecular cloud as a spherical cloud with radius $R_{\text{MC}} = 15 \text{ pc}$ and averaged proton density (including regions ‘R1’ and ‘R5’) $n_{\text{H}} \sim 700 \text{ cm}^{-3}$. The centre of the molecular cloud is located at a distance $d_{\text{MC}} \sim 40 \text{ pc}$ from the assumed position of the SNR origin (Fig. 6.1 blue cross). Assuming the distribution of CRs to be isotropic, I obtain the filling factor $A = \pi R_{\text{MC}}^2 / 4\pi d_{\text{MC}}^2 = 0.035$ which, as a first order, indicates the fraction of energy deposited inside the molecular cloud. From Fig. 6.1, I assume that $\sim 25\%$ of the molecular complex spatially overlaps HESS J1826–130. Accounting for this and a differential CR spectral index $\alpha = 2.2$ from SNR shock acceleration, I use the following equation to obtain the E_{SNR} required to produce such TeV flux :

$$\frac{E_{\text{SNR}}}{1 \times 10^{51} \text{ erg}} = \frac{1}{\eta_{pp} A} F(\geq 1 \text{ TeV}) \left(\frac{d}{1 \text{ kpc}} \right)^2 \left(\frac{n}{1 \text{ cm}^{-3}} \right) \quad (6.1)$$

As a first order approximation, I thus find that the required SNR energy to produce the observed TeV emission towards HESS J1826–130 must exceed $E_{\text{SNR}} \sim 4 \times 10^{50} \text{ erg}$ (i.e $W_p = 4 \times 10^{49} \text{ erg}$) which is significantly smaller than the $E_{\text{SNR}} = 3 \times 10^{51} \text{ erg}$ argued by de Jager & Djannati-Ataï (2009) to explain the large PWN size. This first simple calculation has however not accounted for energy losses nor the confinement and escape of CRs from the molecular cloud.

Accounting for CR Energy losses due to p-p interaction

If I approximate the progenitor SNR as an impulsive source of cosmic-rays and account for energy losses due to p-p collisions, the total CR energy budget W_p at time t evolves as follow :

$$\frac{W_p(t)}{W_p(t=0)} = \exp\left(\frac{-\alpha + 1}{\tau_{pp}}\right) \quad (6.2)$$

with $\tau_{pp} \sim 6 \times 10^7 / n_{\text{H}} \text{ yr}$ being the proton-proton interaction cooling time. Using the age $t = 40 \text{ kyr}$ as suggested by de Jager & Djannati-Ataï (2009), the current CR total energy budget represents $\sim 55\%$ of its initial total energy budget. Consequently, the required E_{SNR} must increase by a factor of 2 reaching $E_{\text{SNR}} \sim 8 \times 10^{50} \text{ erg}$ to produce the observed flux.

Accounting for CR confinement inside the SNR shock and their escape from the molecular complex.

Due to the enhanced turbulence surrounding the SNR shock, CRs and high energy electrons are not released spontaneously at $t = 0$, and the confinement of CRs/high energy electrons is energy dependent. It is thought that once the SNR gets past the Sedov phase (see Chapter 1 for explanation), CRs and high energy electrons start to escape the SNR shock and diffuse into the ISM. I here aim to quantify the total energy loss from escaping CRs. Gabici et al. (2009) modelled the CR escape time as a function of the SNR transition time to Sedov phase t_{SED} , and the CRs maximum energy E_0 accelerated inside the SNR. Let $t_i(E_p)$ represent the epoch when CRs with energy E_p escape the SNR. I also assume that the evolution of the maximum energy attained by CRs follows a power-law distribution $E_p = E_0 (t/t_{\text{SED}})^{-\xi}$ with spectral index ξ (see Gabici et al. 2009). Consequently, the escaped time is modelled as follow :

$$t_i(E_p) = t_{\text{SED}} \left(\frac{E_p}{E_0} \right)^{-1/\xi} \quad (6.3)$$

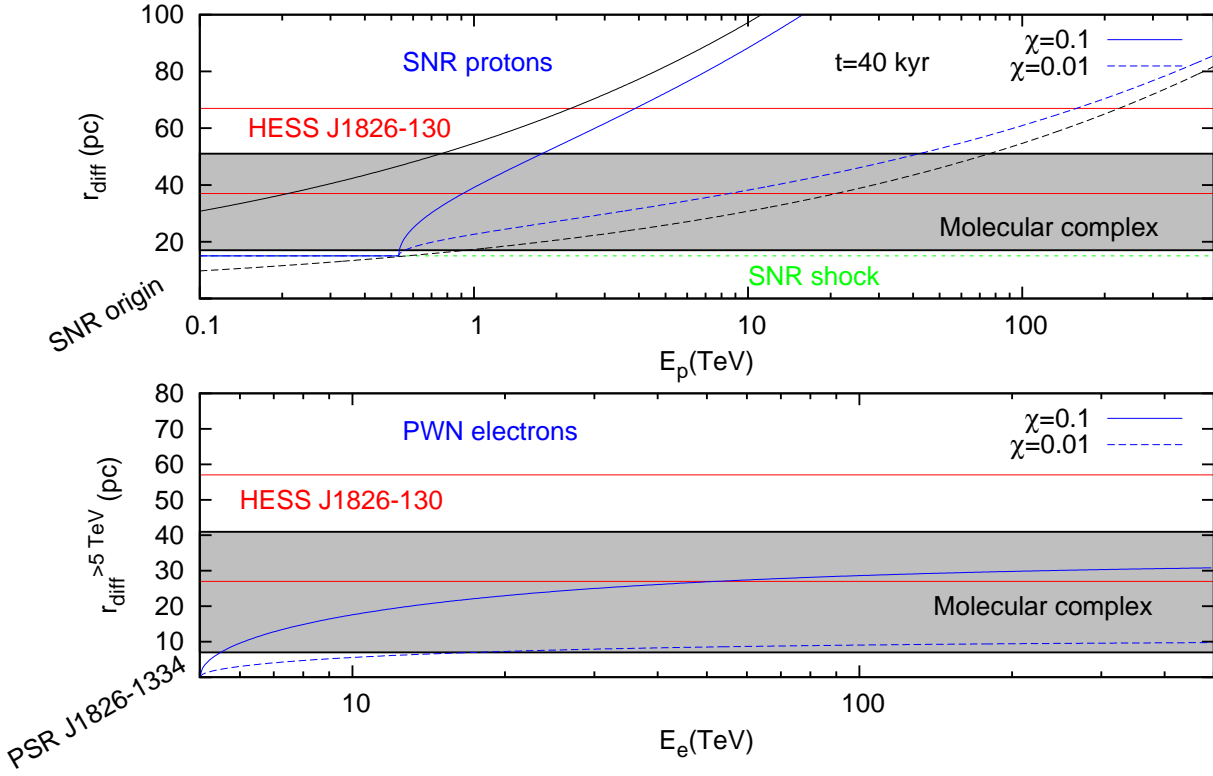


Figure 6.2: (*Top*) Diffusion radius (see Eq. 6.6) of CRs as a function of the CR energy E_p , accounting for p-p radiation losses for a SNR age $t_{\text{age}} = 40$ kyr. The grey region shows the boundaries of the molecular complex (see green circle in Fig. 6.1) and its position with respect to the SNR origin. The region delimited by the two red horizontal lines represent the 0.22° radius region used to obtain the TeV flux above 1 TeV towards HESS J1826–130 (see red circle in Fig. 6.1). The black lines indicate the diffusion of CRs as they all escaped the SNR at $t = 0$ while the blue lines show the case where the CRs have gradually escaped the SNR front shock (see text). The dashed and solid lines represent the case of a particle diffusion with a suppression factor $\chi = 0.01$ and $\chi = 0.1$ respectively. (*Bottom*) Propagation radius for electrons escaping the PSR J1826–1334 (P1 in Fig. 6.1) as a function of their initial energy E_e as they lose energy from synchrotron radiation and reach 5 TeV (see text). The dashed and solid blue lines indicate an electron diffusion coefficient suppression factor $\chi = 0.01$ and $\chi = 0.1$ respectively.

I also use the Crutcher et al. (2010) phenomenological relation, obtained from population study of various molecular clouds, to obtain the magnetic field strength inside a molecular cloud from its particle density :

$$B = \begin{cases} 10 \left(\frac{n_H}{300 \text{ cm}^{-3}} \right)^{0.6} \mu\text{G} & \text{for } n_H \geq 300 \text{ cm}^{-3} \\ 10 \mu\text{G} & \text{for } n_H < 300 \text{ cm}^{-3} \end{cases} \quad (6.4)$$

I thus combine Eqs. 4.29 and 6.4 in order to obtain the diffusion coefficient of CRs while propagating inside the molecular clouds :

$$D(E) = \chi D_0 \left(\frac{E}{1 \text{ GeV}} \right)^{1/2} \left(\frac{100}{3} \left(\frac{n_{\text{H}_2}}{300 \text{ cm}^{-3}} \right)^{0.6} \right)^{-1/2} \text{ cm}^2 \text{ s}^{-1} \text{ for } n_H \geq 300 \text{ cm}^{-3} \quad (6.5)$$

Fig. 6.2 sums up the above discussion and illustrates the diffusion radius

$$r_{\text{diff}}(E_p) = \sqrt{6D(E_p)(t - t_i(E_p))} \quad (6.6)$$

as a function of the proton energy E_p at $t_{\text{age}} = 40$ kyr. Here, I assume a SNR Sedov transition age $t_{\text{sed}} \sim 1000$ yr, $E_0 = 5$ PeV (consistent with the position of the knee in the CR spectrum) and $\xi = 2.48$ as per Gabici et al. (2009). I also assume that the SNR front shock has stopped expanding while crossing

the boundary of the molecular cloud at ~ 15 pc from the SNR origin. I observed that, for the case where $\chi = 0.01$ (see dashed blue lines in Fig. 6.2), CRs with energy $E_p = 20 - 70$ TeV both reside inside the molecular clouds and overlap with HESS J1826–130. From the p-p inelastic interaction, $\sim 10\%$ of the proton energy is usually transferred to the produced gamma-rays (Kelner et al., 2006). Consequently, CRs escaping the progenitor SNR would mostly produce photons with energies between $E_\gamma = 2$ to 7 TeV towards HESS J1826–130. Assuming an injected proton spectral index $\alpha = 2.2$, the gamma-ray flux between 2–7 TeV would then represent $\sim 33\%$ of the total flux above 1 TeV. Consequently, the new proton energy required to produce the TeV emission towards HESS J1826–130 becomes $E_{\text{SNR}} = 2.4 \times 10^{51}$ erg, similar to the SNR kinetic energy indicated by de Jager & Djannati-Ataï (2009). In this case ($\chi = 0.01$), it thus appears that the contribution of the CRs from the progenitor SNR of PSR J1826–1334 could then significantly contribute to the TeV emission towards HESS J1826–130.

In the case where $\chi = 0.1$ (see solid blue lines in Fig. 6.2), I note however that most of the CRs would have escaped the molecular complex. Consequently, the contribution from CRs originating from the progenitor SNR of HESS J1825–137 towards HESS J1826–130 would be significantly reduced. As a conclusion, based on this analysis on energetics, a slow diffusion of CRs is required to contribute to the TeV emission above 1 TeV towards HESS J1826–130

6.1.2 High energy electrons

I now check whether high energy electrons, also accelerated inside SNR shocks, could also produce significant TeV emission via inverse-Compton. Severe synchrotron losses due to enhanced magnetic fields near the SNR shocks prevent electrons from reaching energies $E_{\text{CR}}^{\text{max}} \sim 5$ PeV (Reynolds & Keohane, 1999). The maximum electron energy produced by SNRs may in fact only attain $E_e^{\text{max}} \sim 50$ TeV (see Ohira et al. 2012 and references therein). Also, the required energy to produce gamma-ray emission via inverse-Compton at energies observable by HESS is $E_e \sim 5$ TeV. Past the Sedov age of the SNR, I also assume that the SNR is no longer an efficient accelerator and that electrons continuously lose energy from Synchrotron radiation. Consequently, assuming that the highest energy electrons have been produced at the very early stage (free expansion stage), I rearrange Eq. 4.15 and derive the averaged magnetic field required for electrons with initial energy $E_e^{\text{max}} = 50$ TeV to end up with $E_e > 5$ TeV (minimal energy required to produce IC gamma-ray emission in the energy range of HESS) after $t_{\text{age}} = 40$ kyr :

$$\langle B^{\text{max}} \rangle = 1.12 \times 10^2 \left[\left(\frac{t_{\text{age}}}{1 \text{ kyr}} \right)^{-1} \left(\frac{1}{E_e^{\text{f}}} - \frac{1}{E_e^{\text{max}}} \right) \right]^{1/2} \mu\text{G} \quad (6.7)$$

From Eq. 6.7 I obtain $\langle B^{\text{max}} \rangle = 7.5 \mu\text{G}$, much smaller than $B \sim 20 \mu\text{G}$ obtained from Eq. 6.4 for a molecular cloud with averaged proton density $n_{\text{H}} \sim 700 \text{ cm}^{-3}$. I also note that the strength of the magnetic field inside the molecular clouds may be enhanced due to the possible SNR-MC interaction. Therefore, I argue that it is unlikely that high energy electrons escaping the SNR can contribute to the TeV emission towards HESS J1826–130

6.2 Contribution from the PWN?

Here, I consider whether high energy particles from the PWN HESS J1825–137 itself could also contribute to the TeV emission towards HESS J1826–130.

6.2.1 High energy electrons

As explained in section 6.1.2, it requires high energy electrons reaching energies $E_e \sim 5$ TeV to produce gamma-rays with energy $E_\gamma \sim 0.2$ TeV, which are in the HESS energy range. Fig. 6.2 (bottom panel) shows the propagation radius of electrons with *initial* energy E_e as they lose energy and reach 5 TeV.

In the case where $\chi = 0.01$ (dashed blue line), I note that the electrons do not reach HESS J1826–130 (delimited by the red horizontal lines) with sufficient energy to produce VHE gamma-rays. In the case where $\chi = 0.1$ (solid blue line), I observe that only electrons with initial energy $E_e > 100$ TeV may reach HESS J1826–130.

However, this analysis does not account for effects such as the possibility that high energy electrons may diffuse in front and behind the molecular complex. Numerical methods (see later sections) are thus required to quantify the contribution of these PWN electrons towards the unidentified TeV source. Nonetheless I expect spectral steepening effects in the leptonic gamma-ray emission as I move away from the pulsar location (see Chapter 4) and consequently it is unlikely the PWN electrons thus contribute to the TeV emission towards HESS J1826–130 $E_\gamma > 1$ TeV.

6.2.2 Contribution from CRs?

As already covered in Chapter 1, I should also take into account the contribution of potential CRs escaping the PWN as they may account for a small fraction of the pulsar spin down power. Assuming the pulsar has a braking index $n = 2$ (consistent with $t_{\text{age}} = 40$ kyr claimed by de Jager & Djannati-Atai 2009), it is possible to estimate the total energy budget of the PWN.

$$W_{\text{PWN}} = \frac{\dot{E}_{\text{SD}}^0 P^0}{2\dot{P}} \left(1 - \frac{1}{(1 + \dot{P}t/P^0)^2} \right) \quad (6.8)$$

with $\dot{E}_{\text{SD}}^0 = E_{\text{SD}}(t) (P(t)/P^0)^3 = 6.9 \times 10^{39} \text{ erg s}^{-1}$ being the initial spin down power, $P^0 = P - \dot{P}t = 7.5$ ms being the initial period, and $\dot{P} = 7.4 \times 10^{-14} \text{ s s}^{-1}$ is the period derivative (which remains constant for the case where the braking index $n = 2$). For a pulsar age $t = 40$ kyr, I thus obtain a total energy budget $W_{\text{PWN}} = 3.4 \times 10^{50} \text{ erg}$. As I compare to the required proton energy $W_p = E_{\text{SNR}}/\eta_{\text{pp}} = 2.6 \times 10^{50} \text{ erg}$ to produce the TeV emission towards HESS J1826–130 (see section 6.1.1), the minimal amount of energy transferred to CRs should be very close to the total PWN energy budget. Besides, as the CRs are here injected continuously, CRs which have recently been injected into the PWN may have not reached HESS J1826–130 yet. As the contribution from PWN CRs is sensitive to their diffusion properties, a more detailed study (see later sections) is thus required to quantify their contribution to the TeV flux towards HESS J1826–130. Recent PWN studies suggested that the maximum energy available for PWN CRs is $\eta_{\text{pp}} \sim 0.2$ of the PWN energy budget (Bucciantini et al., 2011). Consequently, it is unlikely that CRs from the PWN HESS J1825–137 could contribute to the TeV emission towards HESS J1826–130. Nonetheless, as discussed in section 4.2.4, CRs continuously injected inside the PWN produce a relatively harder gamma-ray spectra and might therefore contribute at high energies compared to (CR spectrum from impulsive source, see Chapter 4). A more detailed study is thus required to quantify their contribution.

6.3 Modelling particle diffusion from HESS J1825–137 and its progenitor SNR

6.3.1 Motivation

From the previous section, it is evident that the molecular regions north of HESS J1826–130 could provide information about the contribution of HESS J1825–137 and its progenitor SNR to the TeV emission of HESS J1826–130. Consequently, a 3D numerical computation of the diffusion of CRs/high energy electrons over a template distribution of the molecular gas north of HESS J1825–137 could reveal features and provide insight into the observed spectral properties of the TeV emission towards HESS J1826–130.

I also aim to provide predictions which could be observed by the upcoming gamma-ray ground-based observatory CTA (Acharya et al., 2013), based on the diffusion of CRs/high energy electrons released by the progenitor SNR, or the PWN and accounting for radiation losses. I will explore the parameter space (e.g. diffusion suppression χ and time t) and look at their effect on the morphology of the gamma-ray emission.

6.3.2 Solving the diffusion equation

To solve Eq. 4.25, I divide our regions into $120 \times 120 \times 120$ grids cube of length Δx (see Fig. 6.3 for an illustration of the region of interest). As shown in Fig. 6.3 (top right panel), the energy density of CRs/high energy electrons is stored at each grid and, after a time duration Δt , a net fraction of the energy density at a discrete location x_i, y_j, z_k is transferred to its neighbour grids via the following equation :

$$n \left| \begin{array}{c} \gamma \\ t \\ x, y, z \end{array} \right. = \sum_{i=x,y,z} \left[\frac{\dot{\gamma}_0}{\dot{\gamma}} \mathbf{D} \left| \begin{array}{c} \gamma_0 \\ t - \Delta t \\ i + \Delta i/2 \end{array} \right. \left(n \left| \begin{array}{c} \gamma_0 \\ t - \Delta t \\ i + \Delta i \end{array} \right. - n \left| \begin{array}{c} \gamma_0 \\ t - \Delta t \\ i \end{array} \right. \right) \right. \\ \left. + \frac{\dot{\gamma}'_0}{\dot{\gamma}} \mathbf{D} \left| \begin{array}{c} \gamma'_0 \\ t - \Delta t \\ i - \Delta i/2 \end{array} \right. \left(n \left| \begin{array}{c} \gamma'_0 \\ t - \Delta t \\ i - \Delta i \end{array} \right. - n \left| \begin{array}{c} \gamma'_0 \\ t - \Delta t \\ i \end{array} \right. \right) \right] \quad (6.9)$$

where $\mathbf{D} = D(E) \Delta t / \Delta x^2$ is thus a dimensionless variable which indicates the fraction of the energy density $n(\gamma_0, t - \Delta t, x, y, z)$ transferred from one grid to its neighbour grid. As shown in Fig. 6.3 (top right panel), Eq. 6.9 illustrates the net energy density transfer of particles (CRs/high energy electrons) with Lorentz factor γ_0 found at $t - \Delta t$ from one grid to its neighbours.

In order not to hold the diffusion equation solution mathematical properties (e.g. $n(\gamma, r, t) \geq 0$, and the energy distribution peak position remaining constant with time), I find that the value \mathbf{D} must not exceed $1/7$ (see Appendix C for further details). In our model, I choose the time step so that the maximum value \mathbf{D}_{\max} does not exceed 0.1. In order to use computational time more effectively, the grid size has also been increased by a factor of 2 for particles with energies $E \geq 10$ TeV and by a factor of 4 for the diffusion of particles at energy $E \geq 200$ TeV (see Fig. 6.3 for the evolution of the grid size for various energy threshold). Further details about the method used in our program can be found in Appendix C.

For a slow diffusion of particles (diffusion coefficient suppression factor $\chi = 0.01$). I set the length of each grid to be 1 pc wide. On the other hand, in order to reduce computational time, each grid is set to be 2 pc wide for the case $\chi = 0.1$.

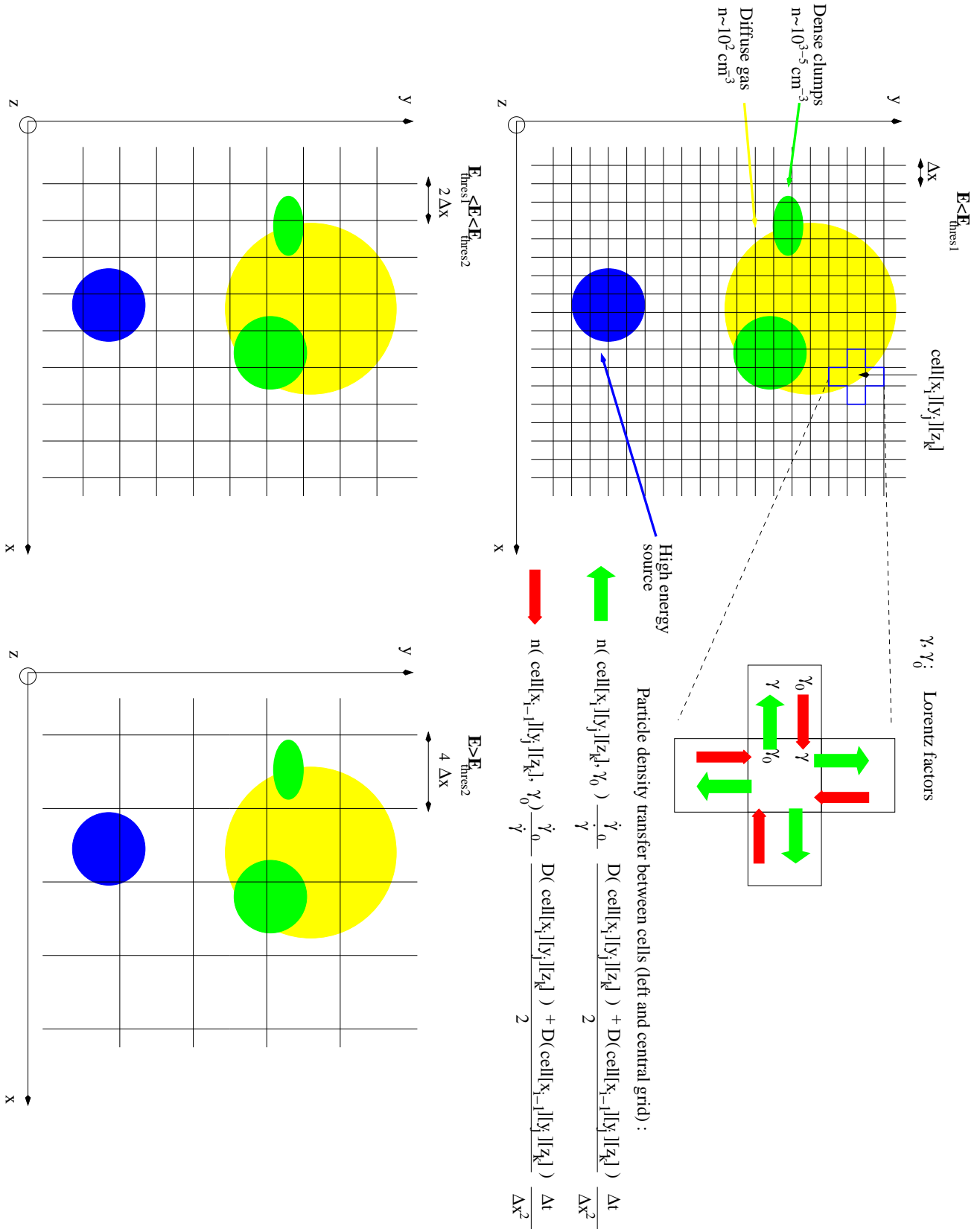


Figure 6.3: Sketch illustrating the grid set-up to numerically solve the energy density of CRs/high energy electrons at a given grid. The equation and diagram in the top right panel indicate how the energy density is transferred from one grid to another. Finally, in order to reduce the computational time, the bottom panel illustrates that the spatial resolution decreases by a factor of 2 and 4 for particles with energies past E_{thres1} and E_{thres2} respectively.

6.3.3 Modelling scenarios and assumptions

Several scenarios have been chosen to explore the effects of various parameters on the morphological and spectral properties of the TeV emission. In the following, hadronic scenarios are labelled ‘P’ while leptonic scenarios are labelled ‘E’. Here is a short description of the scenarios used in this chapter :

- P1 : *Slow* diffusion ($\chi = 0.01$) of *CRs* escaping the SNR at time $t = 0$ for 40 kyr (estimated age of the PWN). The clouds are located at the same distance as the SNR.
- P2 : Same as P1 except for the *clouds now located offset* along the line of sight.
- P3 : Same as P1 but I use the *characteristic age* of the pulsar $\tau_c = 20$ kyr for the system age.
- P4 : *Faster* diffusion ($\chi = 0.1$) of CRs escaping the SNR at time $t = 0$ for 40 kyr.
- P5 : Slow diffusion ($\chi = 0.01$) of CRs released from the *pulsar* PSR J1826–1334 with $t = 40$ kyr (estimated age of the PWN).
- P6 : Same as P5 but with a *faster* diffusion of CRs ($\chi = 0.1$).
- E1 : Slow diffusion ($\chi = 0.01$) of high energy electrons escaping the *SNR* at time $t = 0$ for 40 kyr.
- E2 : Slow diffusion ($\chi = 0.01$) of high energy electrons released from the *pulsar* PSR J1826–1334 for 40 kyr.
- E3 : Same as E2 except for the *clouds now located offset* along the line of sight.
- E4 : Same as E2 but I use the *characteristic age* of the pulsar $\tau_c = 20$ kyr for the system age.
- E5 : *Faster* diffusion ($\chi = 0.1$) of high energy electrons released from the *pulsar* PSR J1826–1334 for 40 kyr.

Tables 6.1 and 6.2 list the different parameters chosen for different modelling scenarios. The SNR origin is positioned at the center of the grid, while the pulsar PSR J1826–1334 is located slightly offset. From Figs. 6.6, 6.8, 6.10 and 6.9, the value of each grid represents the energy flux within the CTA beam size which depends on energy (e.g. $\theta_{\text{CTA}}(E = 0.1 \text{ TeV}) \sim 3.6'$, $\theta_{\text{CTA}}(E = 1 \text{ TeV}) \sim 1.4'$, $\theta_{\text{CTA}}(E = 5 \text{ TeV}) \sim 1.2'$ Acharya et al. 2013). I now describe the various assumptions used to model the injection of CRs/high energy electrons escaping the PWN and its progenitor SNR.

Progenitor SNR

I first assumed that $\eta_{\text{pp}}=0.1$ of the total SNR energy $E_{\text{SNR}} = 3 \times 10^{51}$ erg (de Jager & Djannati-Ataï, 2009) has been converted in CRs, while $\eta_{\text{ee}}=0.001$ of the total SNR energy has been transferred to high energy electrons (Dermer & Powale, 2013). I also approximate the SNR as an impulsive source located at a distance $d = 4 \text{ kpc}$ ($z = 0$ in the grid position) where all CRs/high energy electrons escape the source at $t = 0$. Although these particles are in fact likely to be released once the SNR expansion reaches the Sedov phase (as already discussed in section 6), I observe in Fig. 6.2 (black lines in Fig. 6.2) that our assumption should yield similar results to the one using a time dependent release of CRs (see blue lines in Fig. 6.2). Due to computational limits, the maximum CR energy injected is $E_{\text{p}}^{\text{max}} = 2 \text{ PeV}$ which is below the knee of the CR distribution. However, I already discussed in the section 6 that CRs with energies above $\sim 70 \text{ TeV}$ have likely escaped the molecular clouds. As discussed in section 6.1.2, for the case of high energy electrons, I used a power-law with spectral index $\alpha = 2.2$ and energy cut-off $E_{\text{cutoff}} = 50 \text{ TeV}$ (Ohira et al., 2012). Finally, a diffusion coefficient suppression factor $\chi = 0.01$ and $\chi = 0.1$ was used (see section 6).

Hadron modelling scenario		P1	P2	P3	P4	P5	P6
Source		SNR	SNR	SNR	SNR	PWN	PWN
ratio η_{pp}		0.1	0.1	0.1	0.1	1	1
Suppression χ		0.01	0.01	0.01	0.1	0.01	0.1
t_{age}	[kyr]	40	40	40	20	40	40
molecular complex	$\begin{pmatrix} x \\ y \\ z \end{pmatrix}$	$\begin{pmatrix} 0 \\ 30 \\ 0 \end{pmatrix}$	$\begin{pmatrix} 0 \\ 30 \\ 25 \end{pmatrix}$	$\begin{pmatrix} 0 \\ 30 \\ 0 \end{pmatrix}$	$\begin{pmatrix} 0 \\ 30 \\ 0 \end{pmatrix}$	$\begin{pmatrix} 0 \\ 30 \\ 0 \end{pmatrix}$	$\begin{pmatrix} 0 \\ 30 \\ 0 \end{pmatrix}$
	Region R1	$\begin{pmatrix} 5 \\ 23 \\ 0 \end{pmatrix}$	$\begin{pmatrix} 5 \\ 23 \\ 20 \end{pmatrix}$	$\begin{pmatrix} 5 \\ 23 \\ 0 \end{pmatrix}$	$\begin{pmatrix} 5 \\ 23 \\ 0 \end{pmatrix}$	$\begin{pmatrix} 5 \\ 23 \\ 0 \end{pmatrix}$	$\begin{pmatrix} 5 \\ 23 \\ 0 \end{pmatrix}$
	Region R5	$\begin{pmatrix} -17 \\ 25 \\ 0 \end{pmatrix}$	$\begin{pmatrix} -17 \\ 25 \\ 30 \end{pmatrix}$	$\begin{pmatrix} -17 \\ 25 \\ 0 \end{pmatrix}$	$\begin{pmatrix} -17 \\ 25 \\ 0 \end{pmatrix}$	$\begin{pmatrix} -17 \\ 25 \\ 0 \end{pmatrix}$	$\begin{pmatrix} -17 \\ 25 \\ 0 \end{pmatrix}$

Table 6.1: Hadronic input parameters used for the different scenarios labeled ‘P1’ to ‘P6’ to model the hadronic gamma-ray emission towards HESS J1826–130 and HESS J1825–137. The different scenarios either used the progenitor SNR of PSR J1826–1334 (impulsive source) with total kinetic energy $E_{SNR} = 3 \times 10^{51}$ erg or the pulsar itself with spin down power $\dot{E}_{SD} = 2.6 \times 10^{36}$ erg/s, as source high energy CRs. I assume for the injected CRs a power-law distribution $N(E) \propto E^{-2.2}$ with a sharp cut-off at $E_{cutoff} = 2$ PeV (see text). The energy transferred to high energy CRs relative to the total energy available is given by the ratio η_{pp} (SNR). Finally χ represents the diffusion coefficient suppression factor (see text).

Lepton modelling scenario		E1	E2	E3	E4	E5
Source		SNR	PWN	PWN	PWN	PWN
t_{age}	[kyr]	40	40	40	20	40
Injection type		PL	BPLC	BPLC	BPLC	BPLC
Spectral index α_1		2.2	1.6	1.6	1.6	1.6
Spectral index α_2		-	2.2	2.2	2.2	2.2
Energy cut-off E_{cutoff}	[TeV]	50	300	300	300	300
Energy break E_{break}	[TeV]	-	0.1	0.1	0.1	0.1
Ratio η_{ee}		0.001	1	1	1	1
Suppression χ		0.01	0.01	0.01	0.01	0.1
molecular complex	$\begin{pmatrix} x \\ y \\ z \end{pmatrix}$	$\begin{pmatrix} 0 \\ 30 \\ 0 \end{pmatrix}$	$\begin{pmatrix} 0 \\ 30 \\ 0 \end{pmatrix}$	$\begin{pmatrix} 0 \\ 30 \\ 25 \end{pmatrix}$	$\begin{pmatrix} 0 \\ 30 \\ 0 \end{pmatrix}$	$\begin{pmatrix} 0 \\ 30 \\ 0 \end{pmatrix}$
	Region R1	$\begin{pmatrix} 5 \\ 23 \\ 0 \end{pmatrix}$	$\begin{pmatrix} 5 \\ 23 \\ 0 \end{pmatrix}$	$\begin{pmatrix} 5 \\ 23 \\ 20 \end{pmatrix}$	$\begin{pmatrix} 5 \\ 23 \\ 0 \end{pmatrix}$	$\begin{pmatrix} 5 \\ 23 \\ 0 \end{pmatrix}$
	Region R5	$\begin{pmatrix} -17 \\ 25 \\ 0 \end{pmatrix}$	$\begin{pmatrix} -17 \\ 25 \\ 0 \end{pmatrix}$	$\begin{pmatrix} -17 \\ 25 \\ 30 \end{pmatrix}$	$\begin{pmatrix} -17 \\ 25 \\ 0 \end{pmatrix}$	$\begin{pmatrix} -17 \\ 25 \\ 0 \end{pmatrix}$

Table 6.2: Leptonic input parameters used for the different scenarios labeled ‘E1’ to ‘E5’ to model the leptonic gamma-ray emission towards HESS J1826–130 and HESS J1825–137. The different scenarios either used the progenitor SNR of PSR J1826–1334 (impulsive source) with total kinetic energy $E_{SNR} = 3 \times 10^{51}$ erg or the pulsar itself with spin down power $\dot{E}_{SD} = 2.6 \times 10^{36}$ erg/s as source high energy electrons. For the injection type, PL indicates a power-law spectrum $N(E) = N_0 E^{-\alpha_1}$ and BPLC a broken-power law with energy cutoff spectrum $N(E) = N_0 (E/E_{break})^{-\alpha} \exp(-E/E_{cutoff})$ ($\alpha = \alpha_1$ for $E < E_{break}$ and $\alpha = \alpha_2$ for $E \geq E_{break}$) with α_1 and α_2 being the electron distribution spectral indices, E_{cutoff} being the energy cutoff and E_{break} being the energy where the spectral index changes. The energy transferred to high energy electrons relative to the total energy available is given by the ratio η_{ee} . Finally χ represents the diffusion coefficient suppression factor (see text).

PWN

I used the pulsar PSR J1826–1334 current spin down energy $\dot{E}_{\text{SD}}(t_{\text{age}}) = 2.6 \times 10^{36}$ erg/s, its rotational period $P = 109$ ms and period derivative $\dot{P} = 7.4 \times 10^{-14}$ s s⁻¹ to model the evolution of its spin down energy $\dot{E}_{\text{SD}}(t)$ with time :

$$\dot{E}_{\text{SD}}(t) = \dot{E}_{\text{SD}}(t_{\text{age}}) \left(1 + \frac{(n-1)\dot{P}}{P(t_{\text{age}})}(t - t_{\text{age}}) \right)^{-(n+1)/(n-1)} \quad \text{for } n > 2 \quad (6.10)$$

$$\dot{E}_{\text{SD}}(t) = \dot{E}_{\text{SD}}(t_{\text{age}}) \left(1 - \frac{\dot{P}}{P(t_{\text{age}})}(t - t_{\text{age}}) \right) \quad \text{for } n = 2 \quad (6.11)$$

I assume that the spin down energy is fully transferred into CRs ($\eta_{\text{pp}}=1$) or high energy electrons ($\eta_{\text{ee}}=1$), and therefore the results that will be shown in the next sections are upper-limits and can be scaled down appropriately. In reality, it is generally accepted that the gamma-ray emission towards PWNe can be explained if a portion of the spin down energy \dot{E}_{SD} is transferred to high energy electrons (Gelfand et al., 2009; Bucciantini et al., 2011). I also fixed the magnetic field outside the molecular regions to $3 \mu\text{G}$. While this assumption would roughly match the magnetic field strength inside middle-aged PWNe (see Torres et al. 2014), it clearly underestimates the ones inside young PWNe (e.g Crab nebula). Consequently, high energy electrons injected in the very early time ($t \sim 1$ kyr) would be likely to lose a large amount of energy from synchrotron radiation and may not propagate as far as what may be predicted in the following sections. Although I use a single power-law to model the injection of CRs, I use a broken power-law spectrum with energy cut-off to describe the injected distribution of electrons generally required to account for various acceleration mechanisms in the pulsar environment (briefly reviewed in Chapter 1) :

$$N(E_e) \propto \left(\frac{E}{E_{\text{break}}} \right)^{-\alpha_1} \exp\left(-\frac{E_e}{E_{\text{cut}}}\right) \quad \text{for } E_e < E_{\text{break}} \quad (6.12)$$

$$N(E_e) \propto \left(\frac{E}{E_{\text{break}}} \right)^{-\alpha_2} \exp\left(-\frac{E_e}{E_{\text{cut}}}\right) \quad \text{for } E_e \geq E_{\text{break}} \quad (6.13)$$

$$(6.14)$$

I notably assumed the spectral indices to be $\alpha_1 = 1.6$ and $\alpha_2 = 2.2$, which are similar to the Crab spectral parameters given by Meyer et al. (2010). I put the spectral break at $E_{\text{break}} = 0.1$ TeV and a energy cutoff $E_{\text{cut}} = 100$ TeV, well within the range indicated by Torres et al. (2014)

Molecular clouds

Fig. 6.4 illustrates the arrangement of molecular regions used in this study. I used the molecular complex and the two molecular regions ‘R1’ and ‘R5’, with averaged proton densities $n_{\text{H}} = 2.7 \times 10^3 \text{ cm}^{-3}$ and $n_{\text{H}} = 1.8 \times 10^3 \text{ cm}^{-3}$ and mean radii $R_{\text{R1}} = 8$ pc are assumed to be embedded inside the molecular complex with radius $R = 15$ pc and averaged proton density (excluding the regions ‘R1’ and ‘R5’) $n_{\text{H}} = 5 \times 10^2 \text{ cm}^{-3}$ (see Chapter 5). The total mass then matches with the observed total mass $M \sim 3 \times 10^5 M_{\odot}$. I use Crutcher et al. (2010) phenomenological relation (Eq. 6.4) to obtain the magnetic field strength B at each position coincident with the molecular gas. Finally, although the position of each molecular cloud is here fixed in its (x,y) position, I can shift their position in the line of sight to see the effect of the position of molecular clouds on the modelled gamma-ray morphology (see scenario P2 and E3).

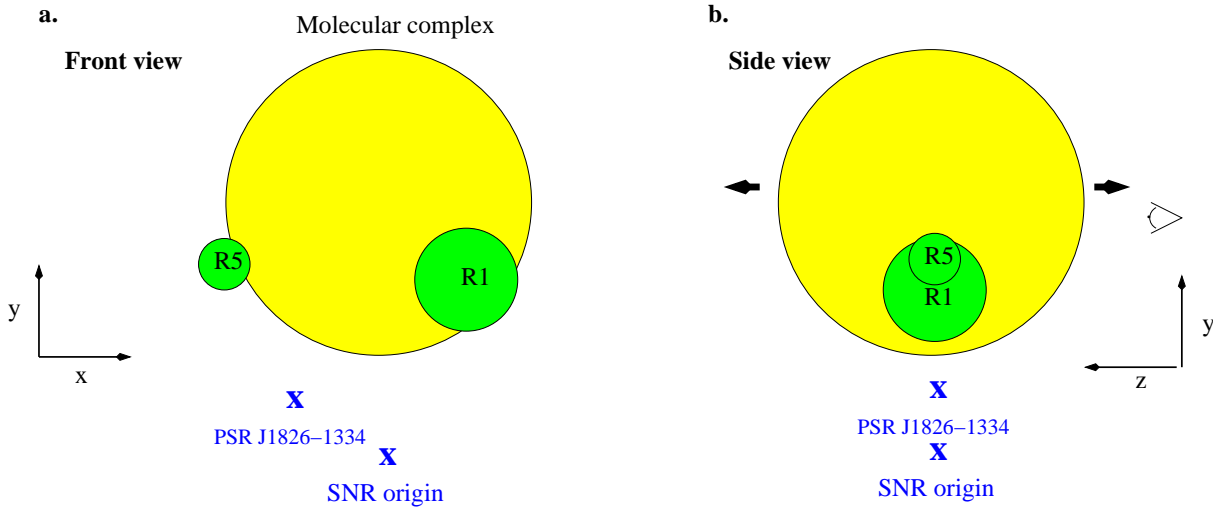


Figure 6.4: Sketch illustrating the position of the SNR origin and the pulsar PSR J1826–1334 (in blue crosses) and the various molecular clouds in front view (left panel) and side view (right panel). The position of the molecular clouds may vary in the line of sight (z axis) as shown by the black arrows.

6.3.4 Contribution from the progenitor SNR

In this section, I look at various scenarios where CRs and high energy electrons, escaping the progenitor SNR of PSR J1826–1334 (see Fig. 6.4), propagate into and across the molecular complex. I remind that hadronic and leptonic scenarios are labeled ‘P’ and ‘E’ respectively. I will look at key morphological features of the gamma-ray emission and their contribution towards HESS J1826–130. In Tables 6.3 and 6.4, I provide the ratio between the photon flux $F_{\text{model}}^{\text{J1826}} (> 1 \text{ TeV})$ predicted by our models and that observed $F_{\text{obs}}^{\text{J1826}} (> 1 \text{ TeV})$ towards HESS J1826–130, to quantify how CRs and high energy electrons escaping the progenitor SNR would contribute to the unidentified TeV source. I also model our modelled differential photon flux as a power-law distribution $dN_{\gamma}/dE_{\gamma} = N_0 E^{-\Gamma} \exp(-E/E_0)$. In Tables 6.3 and 6.4, I provide the parameters N_0 , Γ and E_0 which best describe the predicted spectra in each scenarios. Notably, the predicted gamma-ray spectrum spectral index Γ can be compared to $\Gamma = 1.6$ derived by Anguner et al (2016) which will help constrain which scenarios are likely to contribute to the observed spectrum. I remind that the aim of these modelled SED is not to find parameters which could reproduce the observed spectrum but define conditions in which HESS J1825–137 and its progenitor SNR could contribute (or not) to the photon SED observed HESS J1826–130.

I also aim to monitor the relevance of our results by comparing the modelled integrated fluxes with observational ones. The observed TeV emission of HESS J1825–137 between 0.25-10 TeV peaks towards PSR J1826–1334 with an observed energy between 0.25 and 210 TeV $\mathcal{F}_{\text{obs}}^{\text{P1}} (0.25 - 10 \text{ TeV}) = 2.9 \times 10^{-12} \text{ erg cm}^{-2} \text{ s}^{-1}$ (Aharonian et al., 2006b). I thus use the ratio between our modelled energy flux $\mathcal{F} (0.25 - 10 \text{ TeV})$ towards PSR J1826–1334 (P1) to monitor our leptonic scenarios. The region R1 (see Fig. 6.4 for details about the size and position of this region) has the highest density $n_{\text{H}} = 2700 \text{ cm}^{-3}$ and it is consequently a good region to monitor both hadronic and leptonic scenarios. Using the total integrated flux of HESS J1825–137 $\mathcal{F}^{\text{J1825}} (0.25 - 10 \text{ TeV}) \sim 1.1 \times 10^{-10} \text{ erg cm}^{-2} \text{ s}^{-1}$ and the size ratio between HESS J1825–137 and the region R1, I construct the upper limit of the energy flux towards the region R1 $\mathcal{F}_{\text{lim}}^{\text{R1}} (0.25 - 10 \text{ TeV}) \sim 2.3 \times 10^{-10} \text{ erg cm}^{-2} \text{ s}^{-1}$. The predicted hadronic and leptonic photon spectra, contributed by the CRs escaping the SNR towards HESS J1826–130, are shown in Fig. 6.5

Fig. 6.6 shows the modelled integrated energy flux per beam size (i.e. convolved with the point spread function of CTA at $E = 0.1 \text{ TeV}$, $E = 1 \text{ TeV}$ and $E = 5 \text{ TeV}$) in the gamma-ray energy bands

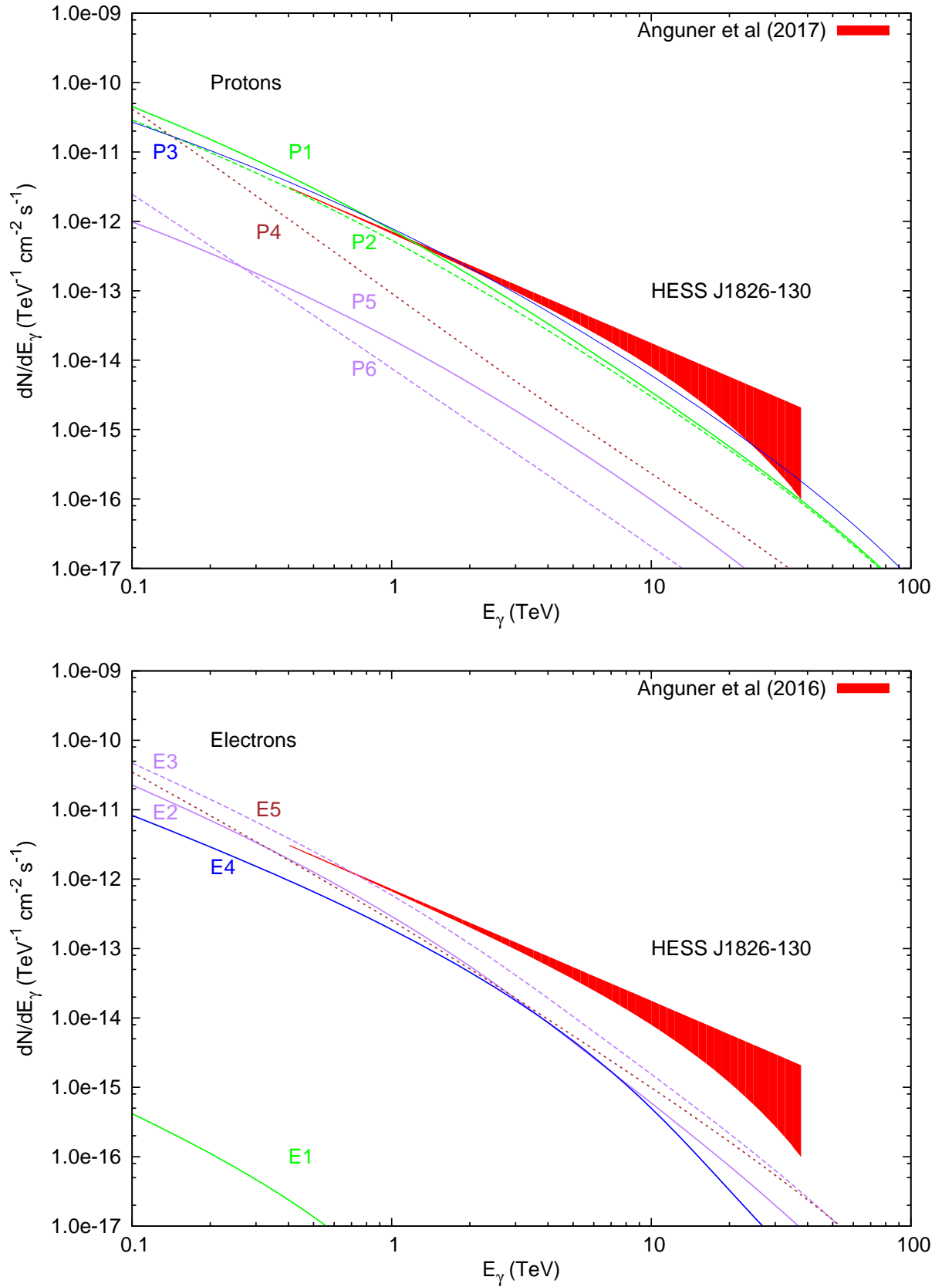


Figure 6.5: Photon SED modelled from various hadronic (top panel) and leptonic scenario (bottom panel) towards HESS J1826–130. The red region indicates the observed photon SED from HESS (Angüner et al., 2017).

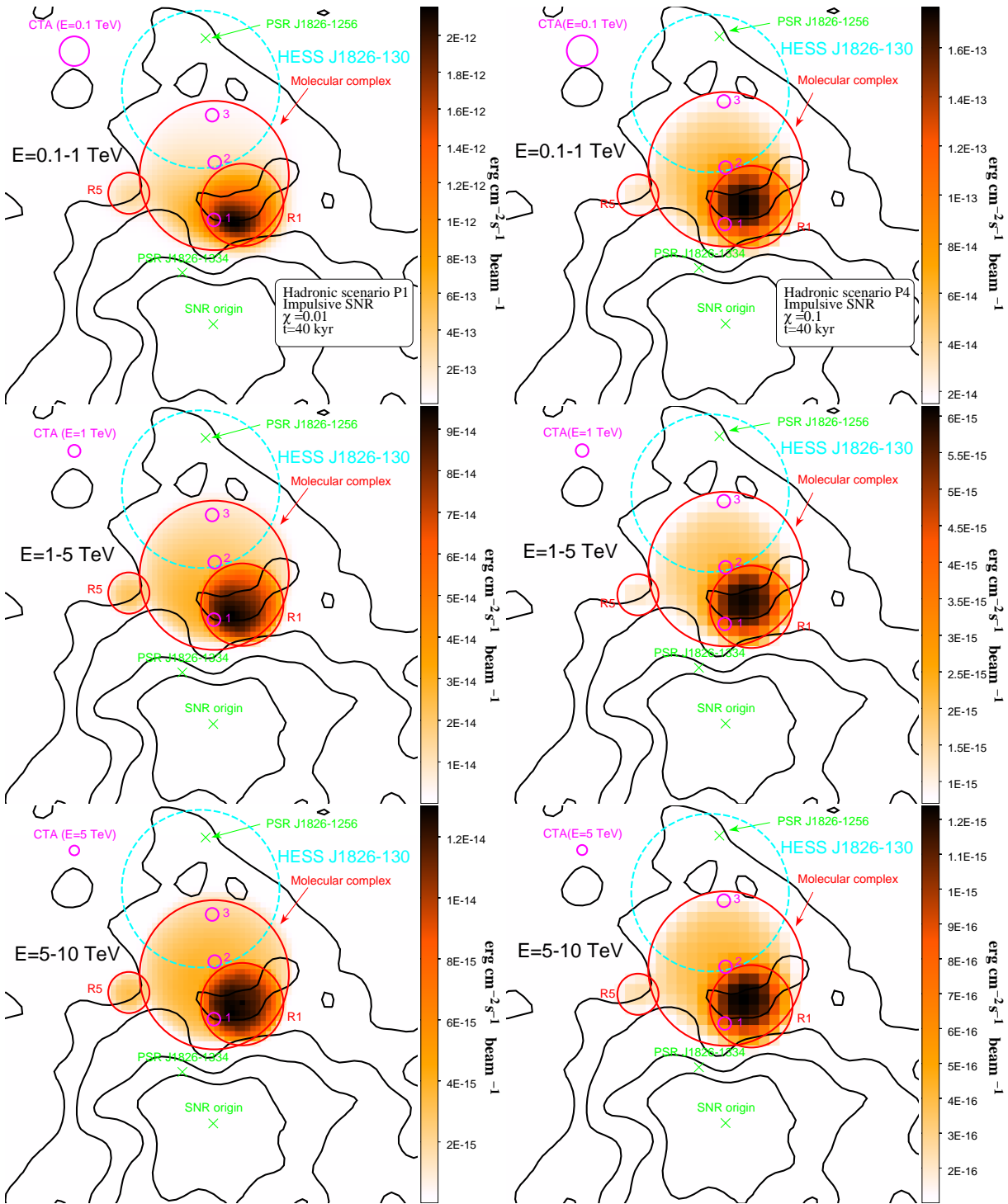


Figure 6.6: Integrated energy flux of gamma-rays between the energy ranges $E_\gamma = 0.1 - 1$ TeV (top), $1 - 5$ TeV (middle), $5 - 10$ TeV (bottom) produced by cosmic rays from the progenitor SNR of PSR J1826–1334 using a diffusion coefficient suppression factor $\chi=0.01$ (left, scenario P1) and $\chi = 0.1$ (right, scenario P4) overlaid by the observed TeV emission in black contours. The assumed origin of the SNR is shown in green cross. The position, sizes and densities of the three molecular clouds shown as red circles are displayed in Table 6.1. The thick cyan circle represents the area used to obtain the flux towards HESS J1826–130.

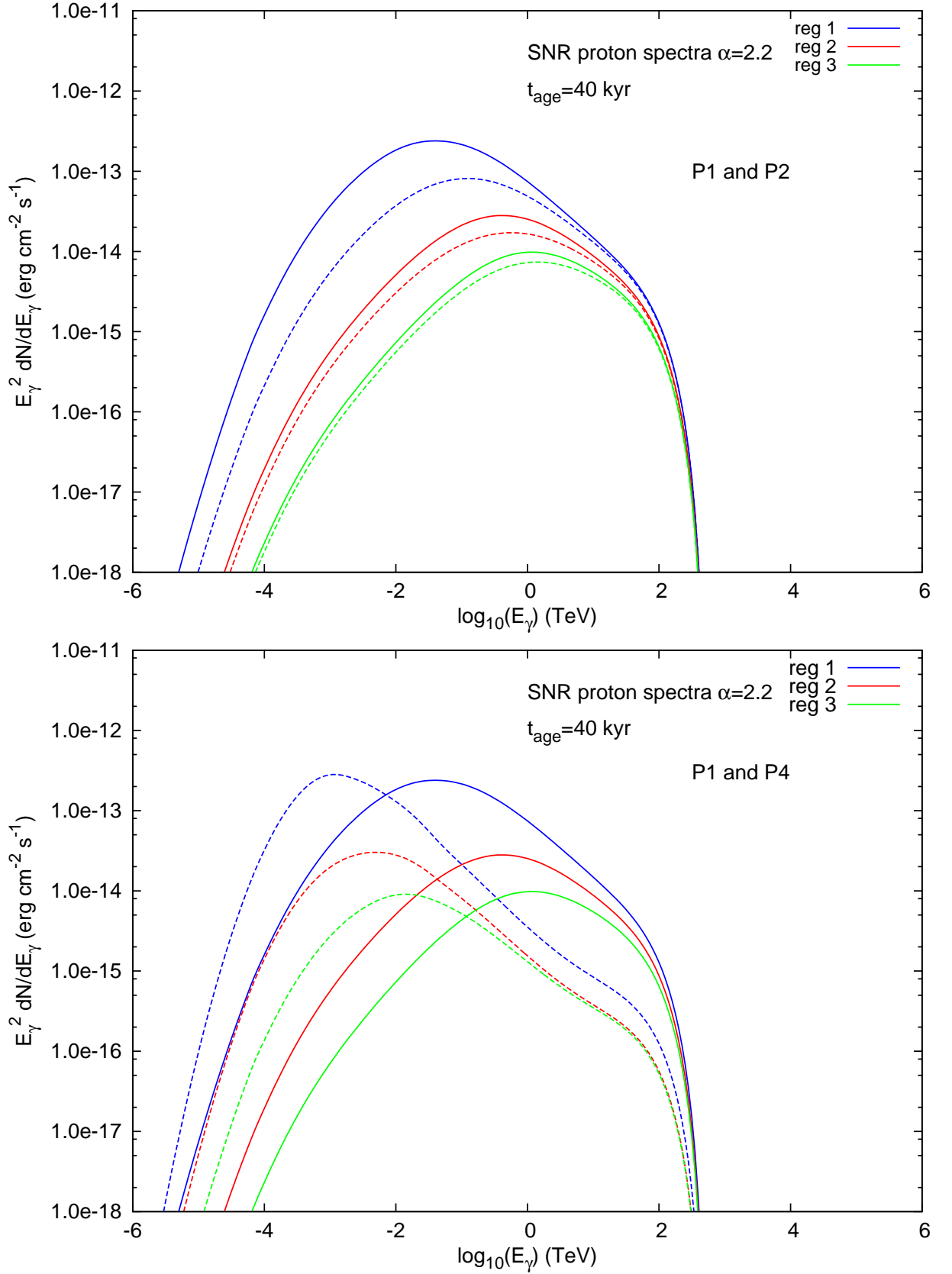


Figure 6.7: (Top) Spectral energy distribution of gamma-rays produced via p-p interaction in region ‘1’ (blue), ‘2’ (red) and ‘3’ (green) (see Fig. 6.6). The results from scenario P1 (left panels in Fig. 6.6) and P2 are shown in solid and dashed lines respectively. (Bottom) Comparison of the different SED in the aforementioned regions between models P1 (solid lines) and P4 (dashed lines, see Fig. 6.6 for gamma-ray morphology).

$E_\gamma = 0.1 - 1$ TeV (top panel), $1 - 5$ TeV (middle panel), and $5 - 10$ TeV (bottom panel) for scenario P1 ($\chi = 0.01$, left panels) and P4 ($\chi = 0.1$, right panels).

Case $\chi=0.01$, Impulsive source (scenario P1, P2, P3)

In scenario P1, I observe in Fig. 6.6 (left panel) that the gamma-rays produced coincide with the northern molecular complex. In Fig. 6.6 (left panel), I observe that the CRs responsible for gamma-rays with energy $E \sim 0.1$ TeV have however not entirely crossed the molecular complex. As shown by the solid lines in Fig. 6.7 (top panel), I thus observe a shift of the spectral peak (~ 50 GeV for region 1 up to ~ 1 TeV for region 3) associated with the energy dependent diffusion of particles.

In Table 6.3, the gamma-ray photon flux predicted in this scenario roughly equals the total observed photon flux in HESS J1826–130 and is thus consistent with our analytical predictions found in section 6.1 regarding the required SNR energy to produce the required HESS J1826–130 flux above 1 TeV. The photon flux spectral index predicted by this scenario is however ~ 2.1 , softer than the spectral index recently indicated by Angüner et al. (2017) (see green solid line in Fig. 6.5). From this scenario, I can not explain the TeV spectrum of HESS J1826–130 using the progenitor SNR of PSR J1826–1334 as sole contributor, which is relevant since some contribution from the pulsar PSR J1826–1256 should be expected. I also observe that between the energy flux $\mathcal{F}_{\text{model}}^{\text{R1}}$ (0.25 – 10 TeV) towards the region R1 is a factor of 6 higher than our upper limit $\mathcal{F}_{\text{lim}}^{\text{R1}}$.

A possible cause could be the position of the molecular gas in the line of sight (z direction, see Fig. 6.4) not being very accurate. In scenario P1, I indeed positioned the molecular clouds at the same position $z = 0$ as the source of CRs but it is possible that they are slightly shifted in the foreground or background. van der Swaluw et al. (2001) indicated that the time required for the reverse shock to crush the PWN is roughly four times the Sedov time t_{sed} . Given the expected fast expansion of the SNR (de Jager & Djannati-Ataï, 2009), the PWN would still be crushed at $t \sim 40$ kyr even if the molecular clouds were located a few tens of parsecs away from the pulsar. In scenario P2 (see Fig. D.1 left panels for modelled gamma-ray morphologies), I thus shifted the molecular complex and the dense regions R1 and R5, by 25, 20 and 30 pc respectively along the line of sight. I observe that the SED towards the region 1 to 3 (see dashed lines in Fig. 6.7) did not change shape and was only slightly reduced, mostly in the GeV band, and consequently that the modelled flux towards R1 remained considerably higher than the upper-limit.

Consequently, the distance of the molecular clouds along the line of sight does not here appear to significantly change the hadronic gamma-ray morphology towards the northern source. However, an overestimation of the column density towards R1 may be the cause of this gamma-ray energy flux overestimation. The distribution of the molecular gas towards the region R1 may indeed be more complex than assumed in these scenarios and a more vigorous description of the gas in our model may be necessary to reproduce most of the (non) features from HESS observations. Alternatively, I discussed in Chapter 5 that the molecular gas towards the region R1 appeared disrupted. The enhanced turbulence towards this dense region could then also further suppress the diffusion of CRs towards the dense molecular clouds, and could result in a lower gamma-ray energy flux.

In scenario P3 (see Fig. D.1 right panels for modelled gamma-ray morphologies), I instead use the characteristic age of the pulsar $\tau_c = 20$ kyr, and I observe in Fig. 6.5 (solid blue line) that the modelled gamma-ray spectral shape, with spectral index $\Gamma = 1.8$ roughly matches with the observed TeV spectrum towards HESS J1826–130. In this case, a large fraction of the observed TeV emission could be explained using CRs from the progenitor SNR of PSR J1826–1334. However, the molecular complex does not entirely overlap the TeV emission (shown in black contours in Fig. 6.6) and I thus do expect

Scenario	SNR				PWN	
	P1	P2	P3	P4	P5	P6
HESS J1826–130 $F_{\text{model}}^{\text{J1826}} (> 1 \text{ TeV}) / F_{\text{obs}}^{\text{J1826}} (> 1 \text{ TeV})$	(see Fig. 6.6 cyan dashed)					
N_0	1.1	0.8	1.6	0.03	0.03	0.01
Γ	7.5	5.0	8.0	1.0	0.2	< 0.1
E_0	2.1	2.1	1.8	2.5	2.1	2.5
	30	30	20	40	25	40
Region R1 $\mathcal{F}_{\text{model}}^{\text{R1}} (0.25 - 10 \text{ TeV}) / \mathcal{F}_{\text{lim}}^{\text{R1}} (0.25 - 10 \text{ TeV})$	6.3	4.4	1.6	5.7	0.3	< 0.1

Table 6.3: Predicted hadronic photon flux ratio between our predicted photon flux $F (> 1 \text{ TeV})$ from our various scenarios (see Table 6.1) and the observed one $F_{\text{obs}} (> 1 \text{ TeV})$ towards HESS J1826–130 (using a 0.22° integration radius). N_0 and Γ represent the parameters of the power-law with energy cut-off $dN/dE_\gamma = N_0 E^{-\Gamma} \exp(-E/E_0)$ used to fit the spectra towards HESS J1826–130 from the various scenarios. PSR J1826–1334 (see text). I also illustrate the ratio between our predicted energy flux between 0.25 and 10 TeV $\mathcal{F} (0.25 - 10 \text{ TeV})$ and an upper-limit value $\mathcal{F}_{\text{obs}} (0.25 - 10 \text{ TeV})$ towards the region R1 which here corresponds to the observed energy flux towards PSR J1826–1334 (see text).

some contribution from the PWN powered by the PSR J1826–1256. Reducing the SNR total energy E_{SNR} could help circumvent this problem. Another issue is that the characteristic age is thought not to explain the large PWN size (de Jager & Djannati-Ataï, 2009).

Case $\chi = 0.1$, scenario P4

In the scenario P4, I observe in Fig. 6.6 that the gamma-ray emission perfectly coincide with the modelled gas distribution in all the aforementioned energy bands. The contribution of HESS J1825–137 towards HESS J1826–130 has been considerably reduced (see Table 6.3). In fact, the high energy CRs responsible for the production of gamma-rays above 1 TeV have escaped the molecular complex and therefore could not contribute to the observed flux. Compared to scenario P1, I observe that the SEDs in Fig. 6.7 (right panel) in region 1 to 3 are all much softer. The photon spectral index $\Gamma \sim 2.5$ towards HESS J1826–130, is also much softer than the observed one (see black dotted lines in Fig. 6.5). Consequently, CRs escaping the progenitor SNR of HESS J1826–137 would not be able to contribute to the TeV emission. I finally remark that the predicted energy flux towards the region R1 is still much higher than what it is observed. Thus, it confirms that, in the case of hadronic scenarios, I either have overestimated the total column density towards the region R1 or underestimated the suppression of the diffusion coefficient in this region due to the observed turbulence.

High energy electrons case $\chi = 0.01$, scenario E1

As shown in Table 6.4 and Fig. 6.5, I confirm that the TeV emission produced by high energy electrons escaping the SNRs towards HESS J1826–130 is orders of magnitude below the observed flux towards HESS J1826–130¹. As already discussed in section 6.1 and Chapter 4, the enhanced magnetic fields in the molecular clouds lead to considerable energy losses for high energy electrons.

6.3.5 Association with the PWN HESS J1825–137?

As per the SNR case, all the results from the PWN scenarios, whose setups are shown in Tables 6.1 and 6.2, are shown in Tables 6.3 and 6.4. All the modelled spectra are also shown in Fig. 6.5.

¹See Fig. D.2 (left panels) for modelled gamma-ray morphologies for this scenario

Scenario	SNR		PWN		
	E1	E2	E3	E4	E5
HESS J1826–130					
$F_{\text{model}}^{\text{J1826}}(> 1 \text{ TeV}) / F_{\text{obs}}^{\text{J1826}}(> 1 \text{ TeV})$	10^{-4}	0.32	0.68	0.24	0.30
N_0 $[10^{-13} \text{ ph cm}^{-2} \text{ s}^{-1}]$	< 0.01	2.5	3.6	6.0	2.0
Γ	2.5	2.3	2.3	1.9	2.3
E_0 [TeV]	12	15	20	7	40
PSR J1826–1334					
$\mathcal{F}_{\text{model}}^{\text{P1}}(0.25 - 10 \text{ TeV}) / \mathcal{F}_{\text{obs}}^{\text{P1}}(0.25 - 10 \text{ TeV})$	< 0.1	1.3	1.5	1.5	0.2
Region R1					
$\mathcal{F}_{\text{model}}^{\text{R1}}(0.25 - 10 \text{ TeV}) / \mathcal{F}_{\text{lim}}^{\text{R1}}(0.25 - 10 \text{ TeV})$	< 0.1	0.4	0.6	0.6	0.4

Table 6.4: Leptonic photon flux towards HESS J1826–130 (using a 0.22° integration radius) originating from HESS J1825–137 in the different scenarios. N_0 , Γ and E_{cut} represent the parameters of the power-law with energy cutoff fit $dN/dE_\gamma = N_0 E^{-\Gamma} \exp(-E/E_0)$. In order to monitor possible overestimation or underestimation of the TeV flux at key regions the ratio between our predicted TeV energy flux $\mathcal{F}(0.25 - 10 \text{ TeV})$ and the observed TeV energy flux towards PSR J1826–1334 $\mathcal{F}_{\text{obs}}(0.25 - 10 \text{ TeV})$ (cyan circle in Fig. 6.6), here used as an upper-limit, towards this region and region R1 (see text).

Cosmic-ray from the PWN? scenarios P5 and P6

Here, I focus on the gamma-ray morphology produced by the CRs originating from the PWN powered by PSR J1826–1334.

Case $\chi = 0.01$, scenario P5

Unsurprisingly, as shown as Fig. 6.8 (left panels), the gamma-ray morphology is similar to the one from scenarios P1 and P2 (see Fig. 6.6). I also note in Fig. 6.9 (top panel) that the energy flux shown in coloured solid lines towards the regions 1 to 3 is significantly less than the one found in scenario P1 (black solid line). Therefore, in the case of a slow diffusion of CRs, the gamma-ray contribution of CRs escaping the PWN would be shadowed by the larger contribution from CRs escaping the SNR. Also, even by using total PWN energy budget of the pulsar PSR J1826–1334, I observe from Table 6.3 and Fig. 6.5 (purple solid line) that the CRs originating from the PWN would provide little contribution towards HESS J1826–130. The predicted gamma-ray spectral shape towards HESS J1826–130 (see purple solid line in Fig. 6.5) is similar to the one scenario P1. From Fig. 6.8 (left panels), the energy flux above 1 TeV using the CTA beam size barely reaches $10^{-14} \text{ erg cm}^{-2} \text{ s}^{-1}$. Consequently, the CTA sensitivity might not be enough to detect gamma-rays produced by the CRs from this PWN with high spatial resolution. Thus, at the current age of the PWN, the CRs escaping the SNRs would still produce a higher γ -ray flux inside the molecular clouds.

Case $\chi = 0.1$, scenario P6

As per the scenario P3, the gamma-ray morphology perfectly coincides with the gas distribution. It should be noted that the energy flux above 1 TeV shown in Fig. 6.8 (right panels) appears below the CTA sensitivity ($< 10^{-14} \text{ erg cm}^{-2} \text{ s}^{-1}$), it would be therefore quite difficult to probe the gamma-rays from PWN from a fast diffusion of CRs ($\chi > 0.1$). I note that the SEDs towards the region ‘1’ to ‘3’ are overall reduced compared to the case $\chi = 0.01$. Indeed, in the case of a somewhat continuous source, the number of CRs inside the molecular cloud gradually converges to a steady-state value. In the case $\chi = 0.1$, this steady-state is reached at earlier times compared to the case $\chi = 0.01$, and the maximum number of CRs inside the molecular complex is also reduced due to the larger diffusion rate of CRs. Although the

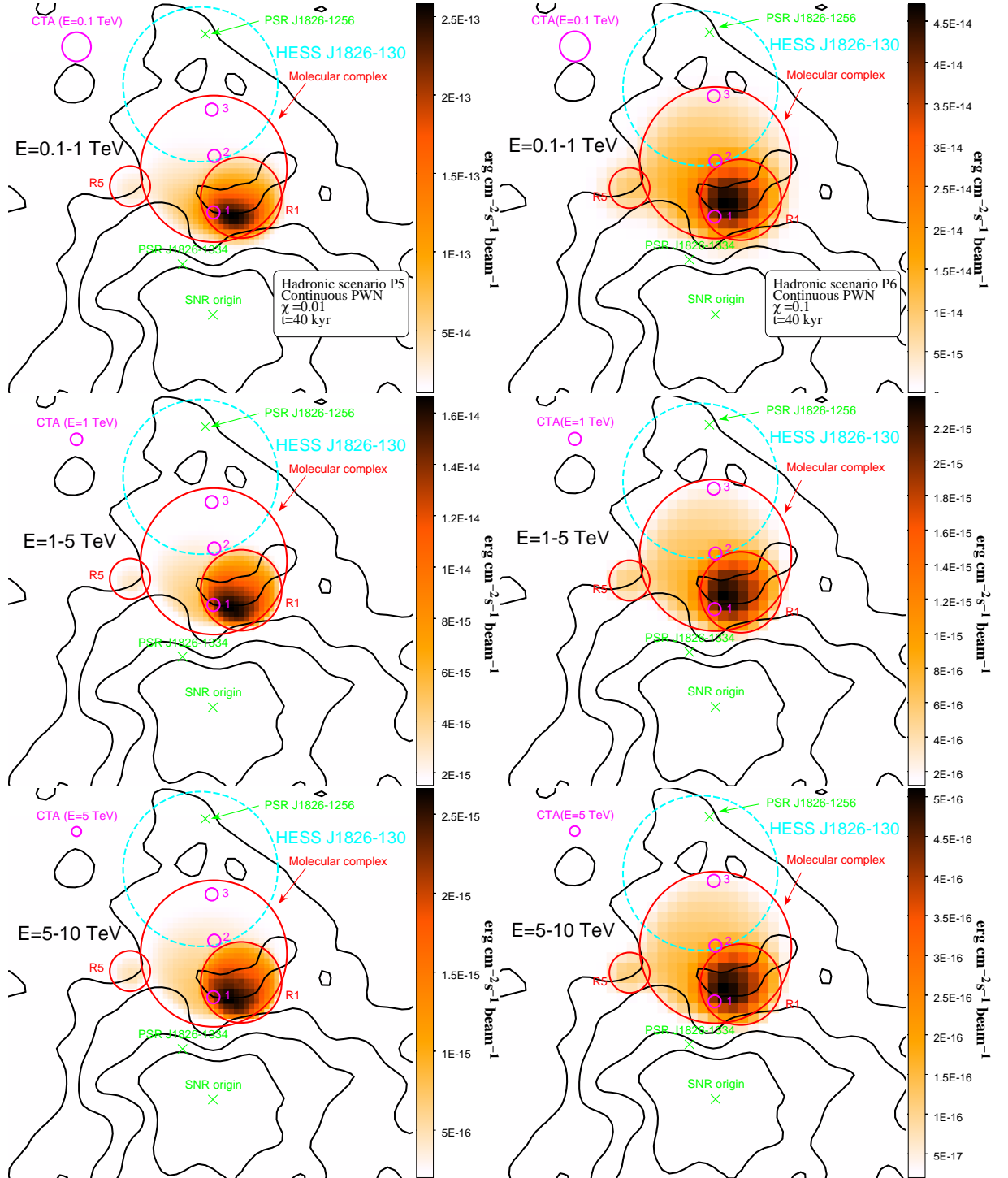


Figure 6.8: Integrated energy flux of gamma-rays between the energy ranges $E_\gamma = 0.1 - 1$ TeV (top), $1 - 5$ TeV (middle), $5 - 10$ TeV (bottom) produced by cosmic-rays escaping the PWN powered by the pulsar PSR J1826–1334 (shown in green cross) using a diffusion coefficient suppression factor $\chi=0.01$ (left, scenario P5) and $\chi = 0.1$ (right, scenario P6). The position, sizes and densities of the three molecular clouds shown as red circles are displayed in Table 1. The thick cyan dashed circle represents the area used to obtain the flux towards HESS J1826–130.

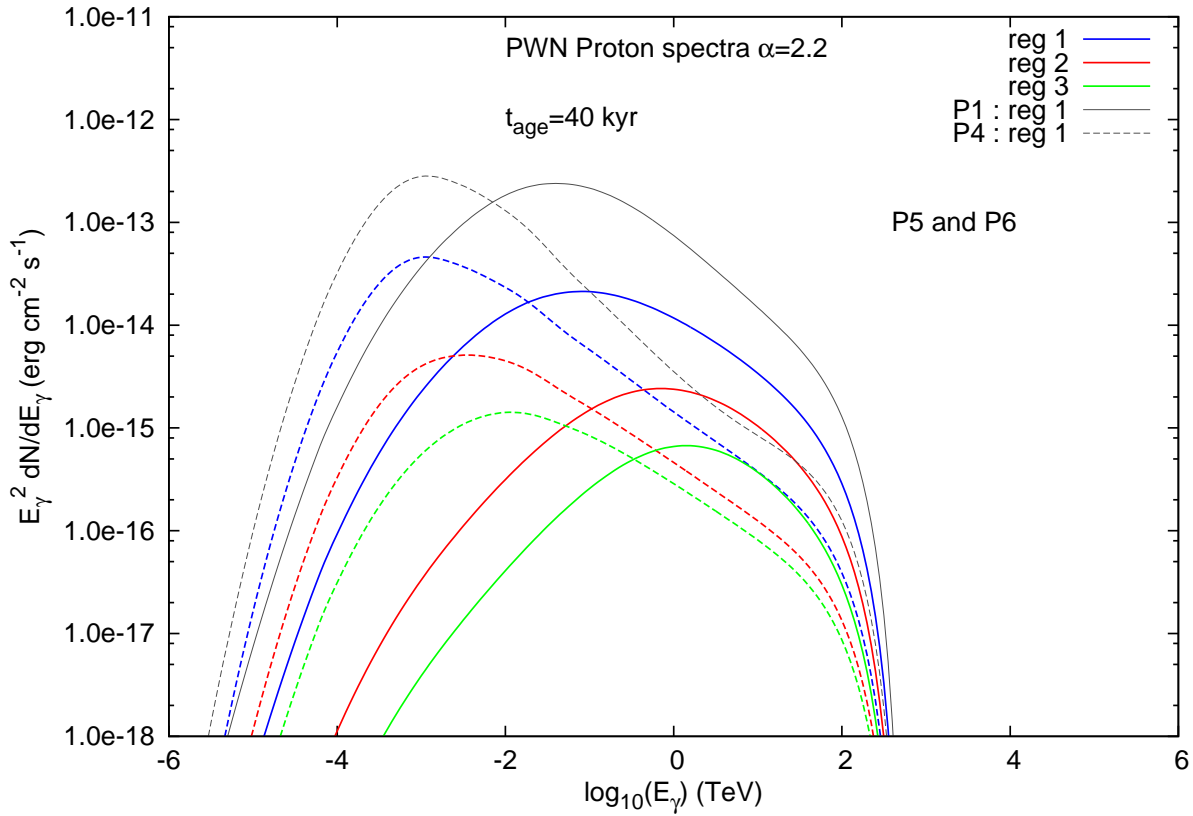


Figure 6.9: Spectral energy distribution of gamma-rays in regions ‘1’ to ‘3’ produced by cosmic-rays originating from the pulsar PSR J1826–1334 (scenario P5 and P6), see Table 6.1 for parameters details) via p-p interaction.

gamma-ray spectrum towards the region ‘1’ in scenario in scenario P6 compared to scenario P4, I still observe that the gamma-ray contribution of CRs escaping the PWN would be less than the contribution from CRs escaping the SNR.

Finally, from Table 6.3, I remark that the photon flux towards HESS J1826–130 contributed by the PWN CRs barely reaches a few percent of the total observed photon flux above 1 TeV. Therefore, in this scenario, it is unlikely that the CR would produce significant contribution towards HESS J1826–130 as opposed to the CRs from the progenitor SNR.

Contribution from the high energy electrons.

Electrons escaping the PWN produce gamma-ray emission via inverse-Compton and bremsstrahlung in dense molecular regions. However, due to the significant energy losses due to synchrotron radiation, the gamma-ray morphology is expected to be very sensitive to the position and morphology of dense molecular clouds (e.g R1 and R5) and their increased magnetic field strength.

Case $\chi = 0.01$, scenario E2, E3, E4

Fig. 6.10 shows the integrated energy flux between the energy range $E = 0.1–1$ TeV (top panels), $1–5$ TeV (middle panels), $5–10$ TeV (top panels) for the scenario E2 (left panels), and E3 (right panels). I here remark a striking contribution of bremsstrahlung (shown in green) radiation between $0.1–1$ TeV in scenario E2, at the southern edge of the molecular complex and region R1 while inverse Compton radiation

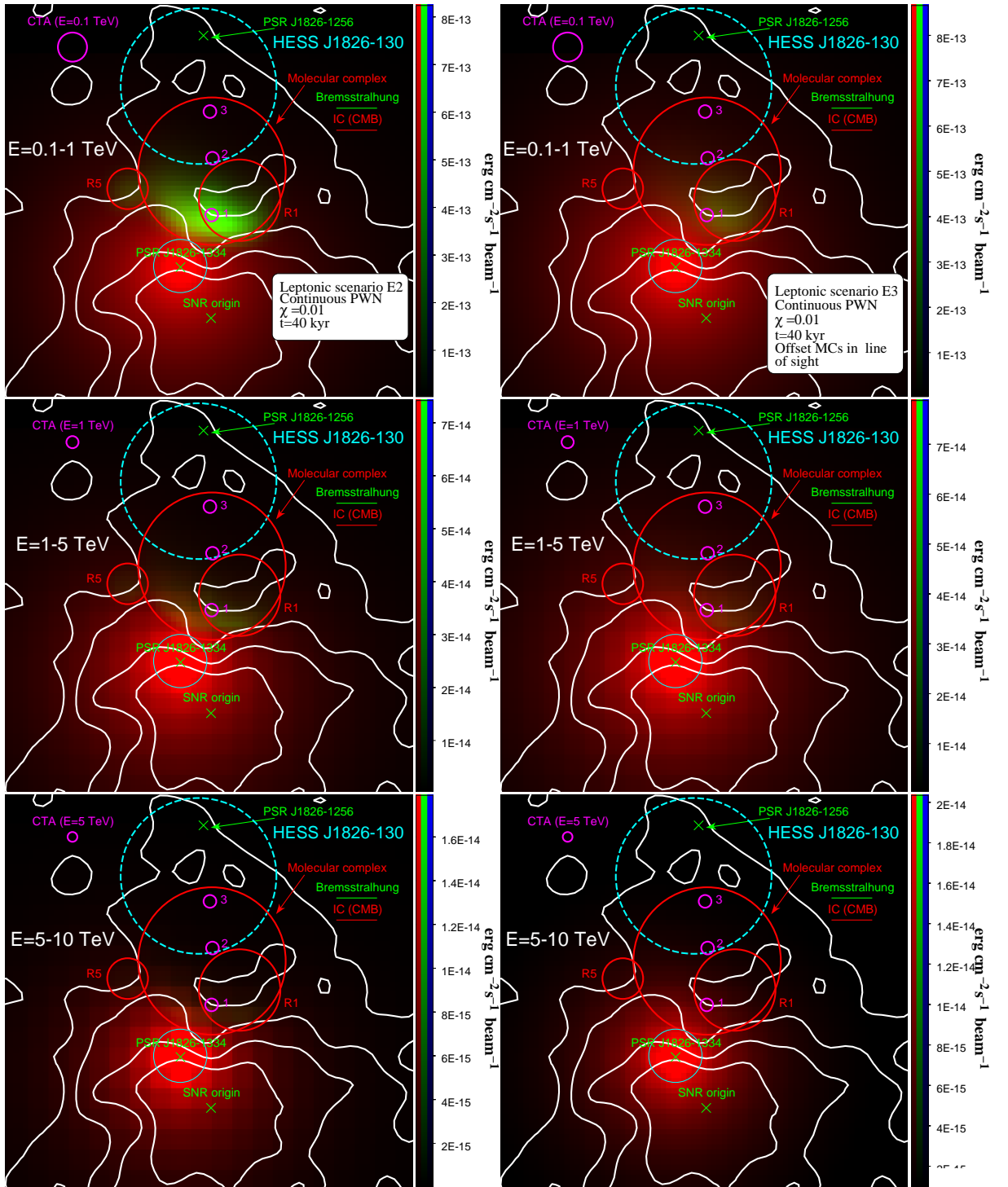


Figure 6.10: Two colour maps showing the energy flux of gamma-rays between the energy ranges $E_\gamma = 0.1-1$ TeV (top), $1-5$ TeV (middle), $5-10$ TeV (bottom) produced by the high energy electrons escaping the PWN powered by the pulsar PSR J1826–1334 (shown in green cross) from scenario P5 (left) and P6 (right). Inverse Compton emission from the up-scattering of CMB soft photons is here shown in red while the bremsstrahlung contribution is shown in green. The position, sizes and densities of the three molecular clouds shown as red circles are displayed in Table 1. The thick cyan dashed circle represents the area used to obtain the flux towards HESS J1826–130 while the thin circle represents the HESS beam-size area used to obtain the modelled flux towards PSR J1826–1334.

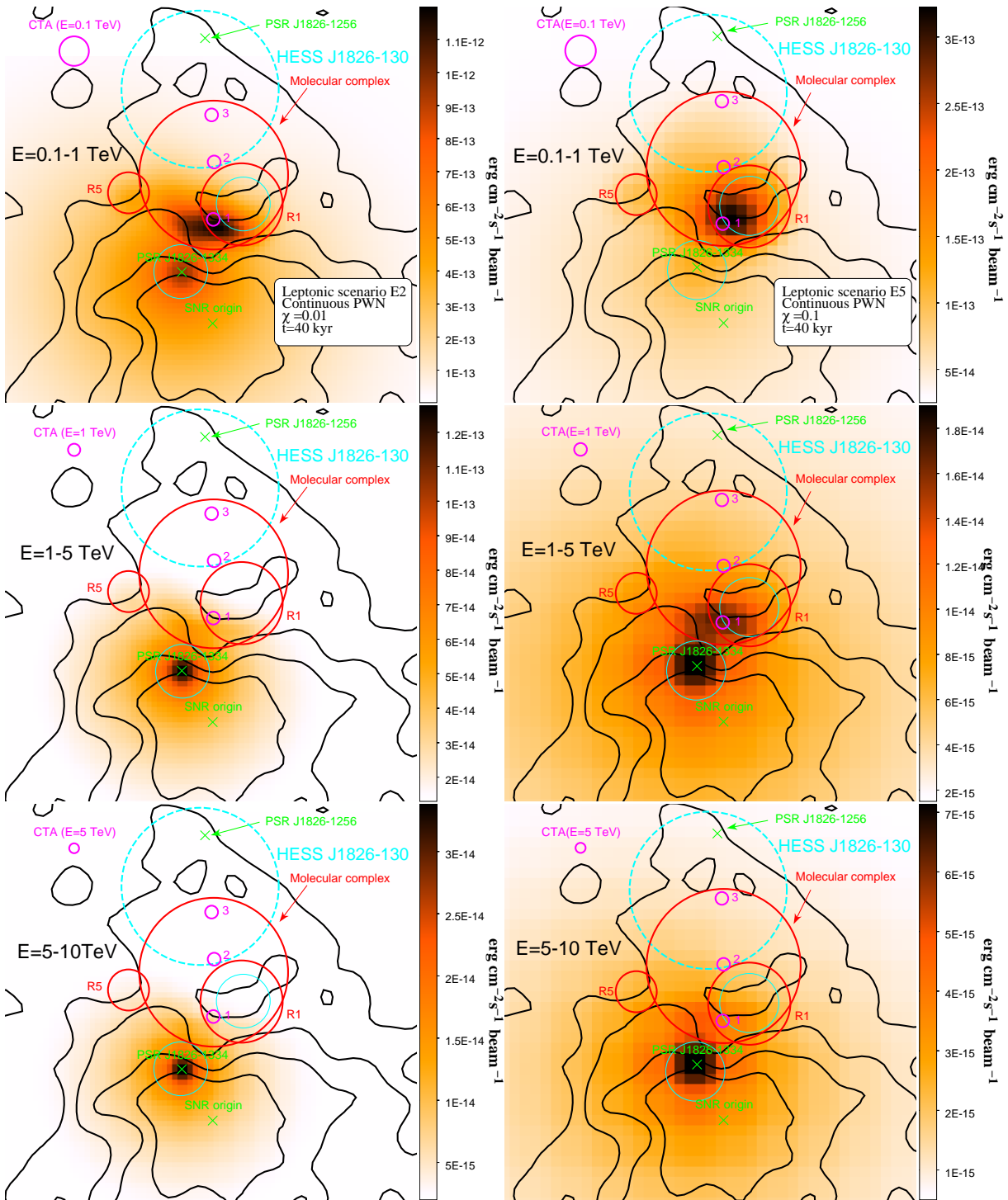


Figure 6.11: Integrated energy flux of gamma-rays between the energy ranges $E_\gamma = 0.1 - 1$ TeV (top), $1 - 5$ TeV (middle), $5 - 10$ TeV (bottom) produced by high energy electrons escaping the PWN powered by the pulsar PSR J1826–1334 (shown in green cross) using a diffusion coefficient suppression factor $\chi=0.01$ (left, scenario E2) and $\chi = 0.1$ (right, scenario E5). The position, sizes and densities of the three molecular clouds shown as red circles are displayed in Table 1. The thick cyan circle represents the area used to obtain the flux towards HESS J1826–130 while the thin circle represents the HESS beam-size area used to obtain the modelled flux towards PSR J1826–1334.

dominates at $E_\gamma > 1$ TeV. The large amount of target density combined with the reduction of the propagation speed of high energy electrons (due to synchrotron losses) result in to a pile-up of bremsstrahlung radiation. This gamma-ray flux enhancement has however not been observed by H.E.S.S. I also remark on the lack of significant gamma-ray emission overlapping the molecular complex. From Fig. 6.12, the SEDs of the regions ‘1 to ‘3’ for scenario E2 (in solid lines) indeed illustrate the spectral steepening, characteristic of synchrotron radiation losses. In scenario E3, where the molecular clouds are located further away, I note two major differences compared to scenario E2. First, as shown in Fig. 6.10 (right panels), the bremsstrahlung emission is much more reduced (except towards region R1). Secondly, the radiation appears more isotropic, indicating that high energy electrons have in fact not interacted much with the dense molecular gas. The inverse-Compton radiation coincident with the molecular complex in fact originates from electrons located in the foreground. This isotropic morphology in fact differs from the striking anisotropic morphology of the TeV emission towards HESS J1825–137 in the north-south direction (Aharonian et al., 2006b). As a consequence, the discrepancy between these leptonic scenarios and the observed morphology of HESS J1825–137 suggests that a more complex propagation model (e.g. diffusion + advection + adiabatic losses) may be required to model the energy distribution of high energy electrons.

In Fig. 6.12, for scenario E2, the SEDs in regions 1 to 3 also appear somewhat harder compared to the one from scenario E3. As I assumed the magnetic field strength outside molecular clouds to be fixed at $3 \mu\text{G}$, electrons did not lose as much energy while propagating into the ISM and consequently, the spectral steepening has become less apparent. From Table 6.3, I note that in both scenarios, the contribution from the electrons escaping the PWN would contribute 32% and 68% to the total photon flux above 1 TeV towards HESS J1826–130 respectively. As shown in Fig. 6.5, the modelled gamma-ray photon spectrum are much softer than the observed one towards HESS J1826–130 with spectral index $\Gamma = 2.3$ for both scenarios E2 (purple solid line) and E3 (purple dashed line) respectively. Finally, if I use assume that the PWN is $\tau_c = 20$ kyr old (scenario E4, see Fig. D.2 for modelled gamma-ray morphologies), I notice from Fig. 6.4 (solid blue line) that the predicted gamma-ray emission remains significantly lower than the observed spectrum. As the shown predicted spectra are upper-limits, it is thus unlikely that high energy electrons escaping the PWN would significantly contribute to the TeV emission towards HESS J1826–130.

Case $\chi = 0.1$, scenario E5

For the case of a faster diffusion, the electrons cross the molecular clouds much faster and significant bremsstrahlung radiation becomes prominent towards the region R1, where the column density is high (see Fig. 6.11). From Fig. 6.13, the spectra in region 1 to 3 (in dashed lines) are, in this scenario, harder compared to the one from scenario E2 (in solid lines) . From Table 6.4, I also remark that, assuming an isotropic diffusion, the electrons would reach HESS J1826–130 and could contribute up to 30% to the observed photon flux above 1 TeV. However, from the spectral index $\Gamma \sim 2.3$, electrons would only contribute to the lower energy gamma-ray, and thus I would need an additional source to explain most of the TeV flux towards HESS J1826–130.

6.4 Summary, discussion what next?

In this chapter, I made predictions about the possible contribution of CRs/high energy electrons HESS J1825–137 and its progenitor SNR to the observed TeV emission towards HESS J1826–130. I notably revealed in each scenarios, morphological features which could be resolved by the next gamma-ray observatory CTA (Acharya et al., 2013).

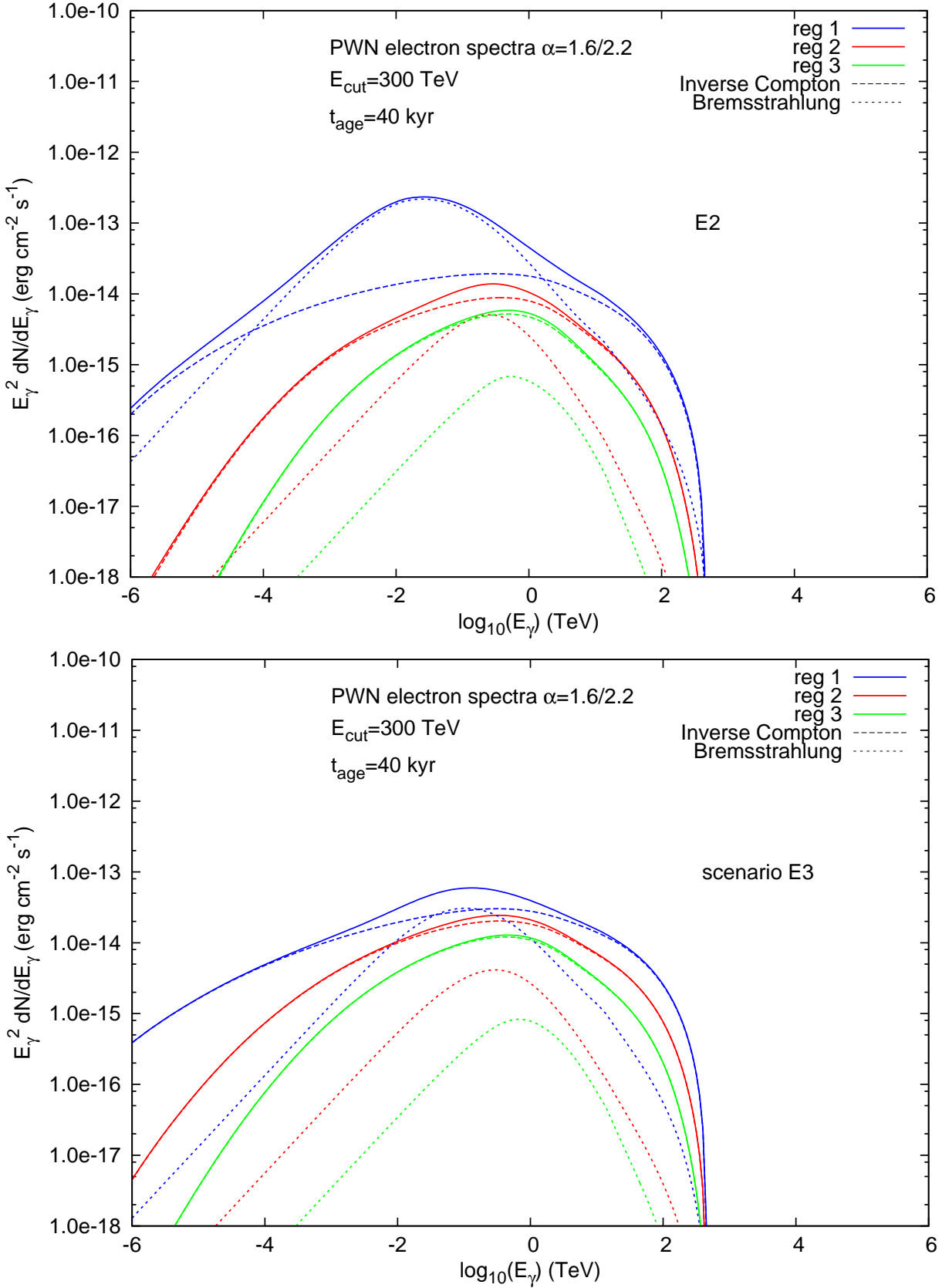


Figure 6.12: Spectral energy distribution of gamma-rays in regions ‘1’ to ‘3’ produced by the high energy electrons escaping the pulsar PSR J1826–1334 from the scenario E2 (top panel) and E3 (bottom panel) (see Fig. 6.10). While the total SED spectral flux are shown in solid lines, the contribution from the IC CMB emission and bremsstrahlung emission are also shown in dashed and dotted lines respectively.

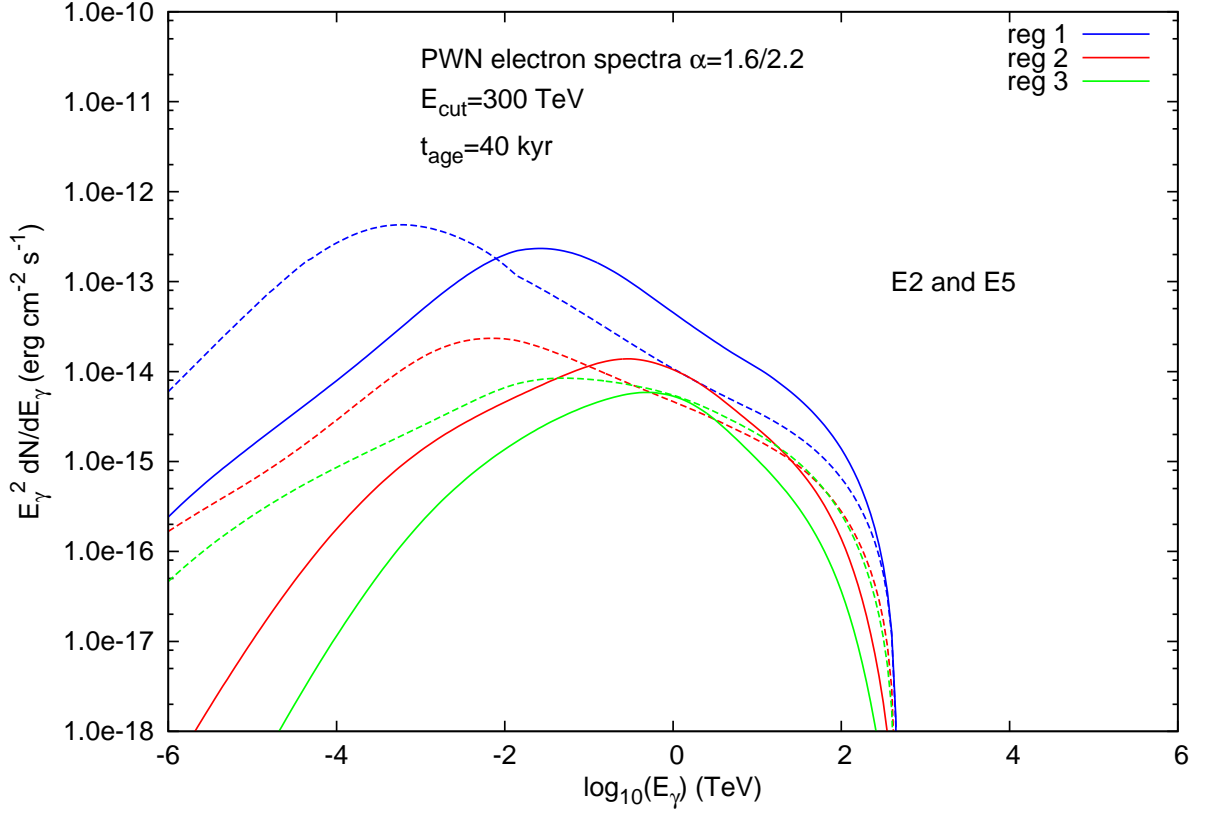


Figure 6.13: Spectral energy distributions of gamma-rays in the aforementioned regions produced by the high energy electrons escaping the pulsar PSR J1826–1334 (scenario E2 and E5) via inverse Compton up-scattering of CMB soft photons and bremsstrahlung. The solid and dashed lines represent the SED flux from SNR protons with a diffusion suppression factor $\chi = 0.01$ (scenario E2) and $\chi = 0.1$ (scenario E5) respectively.

In this detailed analysis, I found that only a slow diffusion of CRs ($\chi = 0.01$) escaping from the progenitor SNR would significantly contribute to the observed gamma-ray flux towards HESS J1826–130 (Angüner et al., 2017). Notably, in the case where I assume a slow diffusion of CRs escaping the progenitor of PSR J1826–1334 and a pulsar age $t_{\text{age}} = 20$ kyr (characteristic age of the pulsar), the modelled photon SED, with spectral index $\Gamma \sim 1.8$, would appear to explain most of the observed TeV emission. In this case, the gamma-ray contribution from the PWN G018.5–0.4 powered by the pulsar PSR J1826–1256 (P2 in Fig. 6.1), may not be dominant in any energy ranges. HESS J1826–130 would then be a combination of both the PWN G18.5–0.4 and the progenitor SNR of HESS J1825–137. However, this age disagrees with the estimated age $t = 40$ kyr argued by de Jager & Djannati-Ataï (2009) to explain the large PWN size. In the case where $t = 40$ kyr, the predicted softer spectral index $\Gamma \sim 2.2$ indicates that, although the contribution of CRs may be non negligible, the contribution of PWN G018.5–0.4 is likely to dominate at energies $E_\gamma >$ a few TeV (see Fig. 6.5). The next step would be to quantify the contribution of the PWN G018.5–0.4 and test whether its contribution combined with one of the above mentioned scenario could explain the spectral properties of HESS J1826–130

I found that CRs from the PWN are not likely to contribute to the flux towards HESS J1826–130 as the modelled gamma-ray emission is significantly less than the gamma-rays produced by the CRs from the progenitor SNR. For this reason, it is, in this case, unlikely to directly detect CRs escaping the PWN. I should perhaps look for older PWN surrounded by denser gas to isolate gamma-rays from the PWN CRs, as the gamma-ray flux from CRs escaping the SNR would decrease, while the contribution from PWN CRs would remain somewhat constant.

I confirmed that the modelled the leptonic emission is sensitive to the gas distribution surrounding

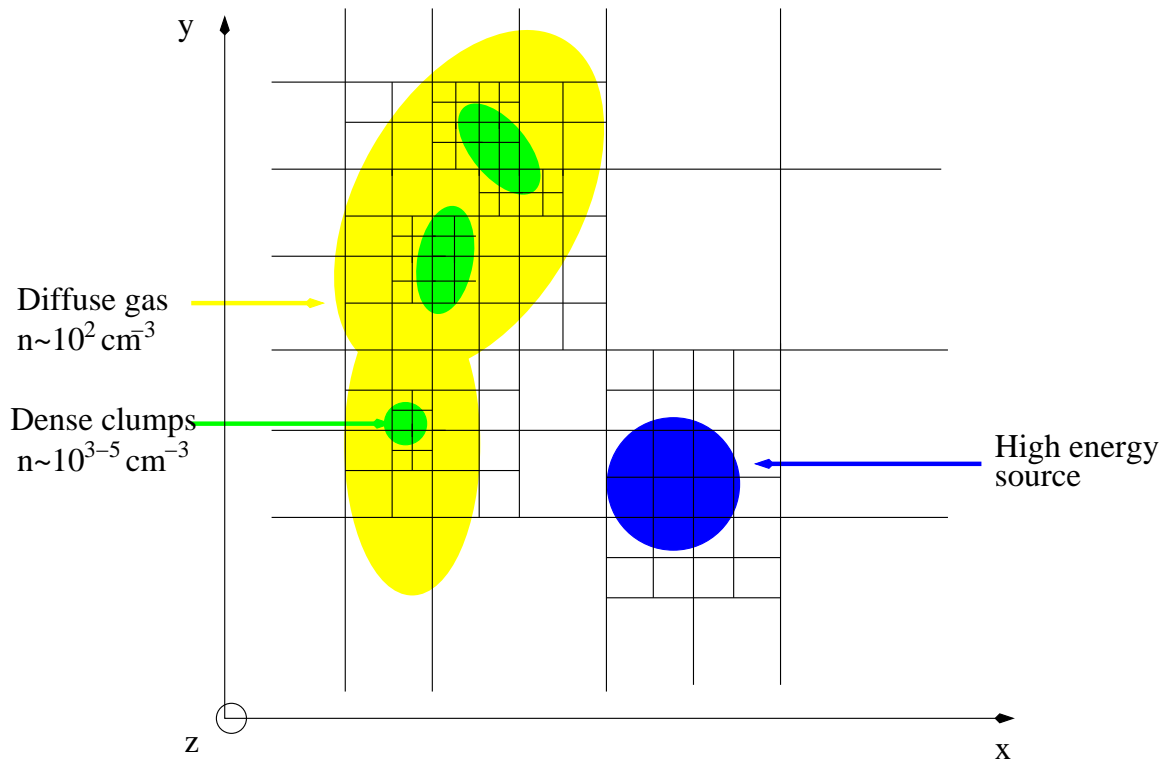


Figure 6.14: Sketch illustrating the Octree algorithm which will be used to derive the diffusion equation. The size of each cells will become smaller in order to accurately probe the diffusion towards dense clumps and next to high energy sources.

the PWN. Notably, the lack of observed bremsstrahlung emission in the 0.1 – 1 TeV band (as opposed to scenario E2) may provide an additional constraint about the morphology of the interface PWN-molecular clouds. Consequently, a more accurate description of the gas distribution (constraining the column density pixels by pixels) may be required to accurately reproduce the gamma-ray features. Alternatively, a more accurate modelling of the propagation of PWN electrons (accounting for advection and adiabatic losses) may be required to model the propagation of PWN electrons.

Another issue to overcome is the quite significant overestimation (up to a factor of 6 higher) of the gamma-ray emission towards the region R1 from hadronic scenarios. Although an overestimation of the column density could be the cause, I argue that the large disruption found in the region R1 (see Chapter 5) may result in a further suppression of the propagation of CRs/high energy electrons in this region. Consequently, in order to account for the effect of localised enhanced turbulence in the ISM, I may be required to model the distribution of the diffusion suppression factor as a function position, time and energy $\chi = \chi(\mathbf{r}, \gamma, t)$. These discrepancies may also be caused by the anisotropic diffusion CRs along magnetic field lines (e.g. see Nava & Gabici 2013; Prosekin et al. 2015 and Chapter 4 for further details). Thus, implementing a non isotropic diffusion of the CRs/high energy electrons escaping the SNRs might be eventually required to obtain accurate descriptions of the gamma-ray emission from HESS J1825–137 towards HESS J1826–130.

Currently, the numerical computation has been limited due to the large number of grids, and consequently the computational time, required to perform the task. In order to circumvent this problem, I aim to use the octree algorithm, in which a parent grid keeps splitting into eight sub-grids towards important regions (e.g. dense molecular clouds, see Fig. 6.14 for basic illustration). The dynamic gridding will help to achieve detailed predictions nearby dense molecular clouds without considerably increase the computational time.

Chapter 7

ISM Studies Towards Seven PWNe and PWNe Candidates (PAPER II)

Statement of Authorship

Title of Paper	The ISM study towards seven PWNe candidates
Publication Status	Draft: Unpublished and Unsubmitted work written in Manuscript style.
Publication Details	To be Published in PASA

Principal Author

Name of Principal Author (Candidate)	Fabien Voisin
Contribution to the Paper	Mopra observations - data reduction - molecular line analysis- ISM and high energy interpretation- writing
Overall percentage (%)	52 %
Certification:	This paper reports on original research I conducted during the period of my Higher Degree by Research candidature and is not subject to any obligations or contractual agreements with a third party that would constrain its inclusion in this thesis. I am the primary author of this paper.
Signature	Date
	01/02/2017

Co-Author Contributions

By signing the Statement of Authorship, each author certifies that:

- i. the candidate's stated contribution to the publication is accurate (as detailed above);
- ii. permission is granted for the candidate to include the publication in the thesis; and
- iii. the sum of all co-author contributions is equal to 100% less the candidate's stated contribution.

Name of Co-Author	Gavin Rowell
Contribution to the Paper	Mopra observations - ISM interpretation / High energy interpretation – review (15%)
Signature	Date
	1/2/17

Name of Co-Author	Michael Burton
Contribution to the Paper	Mopra observations – ISM interpretation – review (10%)
Signature	Date
	20/01/2017

Please cut and paste additional co-author panels here as required.


Name of Co-Author	Yasuo Fukui		
Contribution to the Paper	Nanten CO(1-0) data – ISM interpretation (7%)		
Signature		Date	January 20, 2017


Name of Co-Author	Hidetoshi Sano		
Contribution to the Paper	Nanten CO(1-0) data- ISM interpretation (7%)		
Signature		Date	17 Oct. 2016

Name of Co-Author	Felix Aharonian		
Contribution to the Paper	High energy interpretation (5%)		
Signature		Date	24/11/2016

Name of Co-Author	Nigel Maxted		
Contribution to the Paper	Mopra observations (1%)		
Signature		Date	19/10/2016

Name of Co-Author	Catherine Braiding		
Contribution to the Paper	Mopra observations (1%)		
Signature		Date	24/11/2016

Name of Co-Author	Rebecca Blackwell		
Contribution to the Paper	Mopra observations (1%)		
Signature		Date	01/02/2017

Name of Co-Author	James Lau		
Contribution to the Paper	Mopra observations (1%)		
Signature		Date	1/2/2017

The ISM study towards seven TeV gamma-ray PWNe and PWNe candidates

F. J. Voisin^{1*}; G. P. Rowell¹; M. G. Burton^{2,3}; Y. Fukui⁴; H. Sano⁴; F. Aharonian^{5,6}; N. Maxted²; C. Braiding²; R. Blackwell¹; J. Lau¹;

¹ School of Physical Sciences, University of Adelaide, South Australia, Australia

² School of Physics, University of New South Wales, New South Wales, Australia

³ Armagh Observatory and Planetarium, College Hill, Armagh BT61 9DG, Northern Ireland

⁴ Department of Physics, Nagoya University, Furo-cho, Chikusa-ku, Nagoya, 464-8601, Japan

⁵ Dublin Institute for Advanced Studies, Dublin 2, Ireland

⁶ Max-Planck-Institut für Kernphysik, Heidelberg, Germany

Abstract

We investigate the ISM morphology towards seven TeV gamma-ray pulsar wind nebulae (PWNe) and PWNe candidates using Mopra molecular line observations at 7mm [CS(1–0), SiO(1–0,v=0)], Nanten CO(1–0) data and the SGPS/GASS HI survey. We found extended CS(1–0) emission towards HESS J1809–193, HESS J1026–583 and HESS J1418–609 while point-like features were only detected towards the other sources.

We have found SiO(1–0) detections in dense molecular clouds at the pulsar PSR J1809–1917 distance $d \sim 3.7$ kpc with no apparent infra-red counterparts, which may suggest a plausible SNR-MC interaction south of HESS J1809–193. Our 7mm molecular line observations have also showed several dense clumps towards the TeV source HESS J1026–582 at $d \sim 5.0$ kpc that might provide enough target material to produce significant hadronic gamma-ray emission. We also revealed a possible molecular shell at $d \sim 2.8$ kpc spatially coincident with the newly found SNR towards HESS J1303–631 from the Nanten CO(1–0) data. From the mass and density estimates, we also provide first order predictions on how the adjacent molecular clouds could affect the morphology of the TeV emission, which would provide further information regarding the distance to the TeV sources.

We also studied the contribution from hadronic components, by comparing the required cosmic-ray enhancement found towards molecular clouds overlapping the various TeV sources with that expected from nearby high energy accelerators. Interestingly, we found that the pulsar PSR J1809–1917 might provide enough CRs to produce significant TeV gamma-ray emission towards adjacent molecular clouds. Thus this becomes a suitable laboratory to investigate whether CRs could be produced inside PWNe.

Keywords:

1 Introduction

Pulsar wind nebulae (PWNe) represent the majority of the identified TeV gamma-ray sources in the Galactic plane (Deil et al. 2015). The TeV emission is generally believed to be of leptonic origin, where high energy electrons are accelerated after crossing the pulsar termination shock, and scatter soft photons to produce inverse-

Compton (IC) radiation at TeV gamma-ray energies. The interstellar medium (ISM) greatly affects the morphology of the PWN observed from radio up to gamma-ray energies. For instance, the interaction between the progenitor SNR and a nearby molecular cloud (MC) leads to an offset position of the pulsar with respect to the TeV peak along the pulsar-MC axis (Blondin et al. 2001).

In this paper, we investigate the ISM towards seven TeV PWNe and PWNe candidates (Acero et al. 2013). We make use of the Nanten CO(1–0) survey (Mizuno & Fukui 2004) to illustrate the wide-field morphology of the diffuse molecular gas towards the PWNe

*E-mail: fabien.voisin@student.adelaide.edu.au (RCB)

and 7mm Mopra spectral line observations to probe the dense molecular, and possibly shocked, gas along with star forming regions. An accurate description of the ISM can help explain the morphology of the PWN. Linking the TeV source to its local ISM can also provide additional constraints on its distance. We can identify target material for hadronic components (i.e. cosmic-rays) escaping the TeV source, for example from a progenitor supernova remnant (e.g. Voisin et al. 2016), or for high energy electrons as they produce Bremsstrahlung radiation. Lastly, by combining ISM mapping with the improved sensitivity and angular resolution of the next generation Cerenkov Telescope Array (Parsons & Hinton 2014), we will be able to study the diffusion process of high energy particles towards and inside the ISM clouds.

In section 2, we briefly outline the technical properties of the Mopra and Nanten telescopes as well as the analyses used for our 7mm Mopra data reduction. We also review the different analysis used in this paper in section 3. We provide the results towards the different individual sources in section 4 and discuss the distance and/or the nature of the TeV source in section 5.

2 ISM Data and Analysis Procedure

2.1 7mm Mopra data and Analysis

We conducted the observation of the ISM towards several HESS TeV sources as part of our ‘MopraGam’ survey¹. Table 1 indicates the position and size of the different observations towards the seven regions which were mapped.

We used the Mopra spectrometer MOPS in ‘zoom’ mode, which records 16 sub-bands, each consisting of 4096 channels over a 137.5 MHz bandwidth. The ‘on the fly mapping’ (OTF) Nyquist sampled these regions with a 1’ beam size and a velocity resolution of ~ 0.2 km/s.

We used Livedata² to produce the spectra of each observation, calibrated by an OFF position, and subtracted the baseline using a linear fit. Then, we used Gridzilla³ to obtain a 3D cube showing the variation of the antenna temperature T_A^* as a function of position and line of sight velocity v_{lsr} . The data cubes were then smoothed via a Gaussian of 1.25’ Full Width Half Maximum (FWHM) in order to smooth out fluctuations. Finally, we iteratively performed a linear and sinusoidal fit across the datasets to mitigate systematic effects such as ripples and other baselining issues.

We used the 7mm CS(1–0) transition to probe the denser gas which provides a complementary view of the molecular clouds. Each CS(1–0) components was fitted using Gaussian functions.

Table 1 The position in (RA, Dec)^a and the area covered by the 7mm Mopra line survey taken in Galactic coordinates.

TeV sources	position (α° , δ°) (J2000.0)	Area $\Delta l \times \Delta b$
HESS J1018–589B	(154.7°, -58.9°)	20’ × 20’
HESS J1026–582	(156.4°, -58.1°)	20’ × 60’
	(155.9°, -58.0°)	10’ × 10’
HESS J1119–614	(169.7°, -61.4°)	20’ × 20’
HESS J1303–631	(195.4°, -63.1°)	20’ × 20’
HESS J1418–609	(215.1°, -60.8°)	20’ × 20’
HESS J1420–607	(214.4°, -60.9°)	20’ × 20’
HESS J1809–193	(272.5°, -19.5°)	40’ × 40’

In J2000.0 coordinate system

We then used the Galactic rotation curve model from Brand & Blitz (1993) to obtain near/far kinematic distance estimates based on the detections peak velocity. In the case where the isotopologue C³⁴S(1–0) is detected, we use Eq. B.1 to derive the averaged optical depth $\tau_{\text{CS}(1-0)}$ using the isotopologue ratio $\alpha = {}^{32}\text{S}/{}^{34}\text{S} \sim 24$ based on terrestrial measurements. Otherwise, an optically thin scenario $\tau_{\text{CS}(1-0)} = 0$ was adopted. We obtained the column density of the upper state N_{CS_1} using Eq. B.2. Assuming the gas to be in local thermal equilibrium, we thus obtained the total CS column density N_{CS} using Eq. B.3, assuming a kinetic temperature $T_{\text{kin}} = 10$ K typical of cold dense molecular clouds. The CS to H₂ abundance ratio X_{CS} inside dense molecular clumps varies between 10^{-9} and 10^{-8} as suggested by Irvine et al (1987). In this work we chose $X_{\text{CS}} = 4 \times 10^{-9}$ as per Zinchenko et al. (1994) which studied molecular clouds associated with star-forming regions. Thus, we expect our H₂ column density estimates to systematically vary by a factor of 2. Finally, we use Eqs. B.4 and B.5 as in the CO(1–0) analysis to determine the total mass M and H₂ density. The Gaussian fits for the CS(1–0) components towards the regions of the individual TeV sources can be found in Tables A.1 to A.6 and their derived physical properties in Tables B.1 to B.6.

2.2 CO(1–0) Data and Analysis

We used data of the 4-metre Nanten telescope CO(1–0) survey (Mizuno & Fukui 2004) which covered the Galactic plane with a 4’ sampling grid, a velocity resolution $\Delta v = 0.625$ km/s and an averaged noise temperature per channel of ~ 0.4 K.

The CO(1–0) emission provides a probe of the more diffuse molecular gas surrounding the PWN. As PWNe generally expand inside a low density medium, we mostly focus on regions where the CO(1–0) emission

¹<http://www.physics.adelaide.edu.au/astrophysics/MopraGam/>

²<http://www.atnf.csiro.au/computing/software/Livedata/>

³<http://www.atnf.csiro.au/computing/software/Gridzilla/>

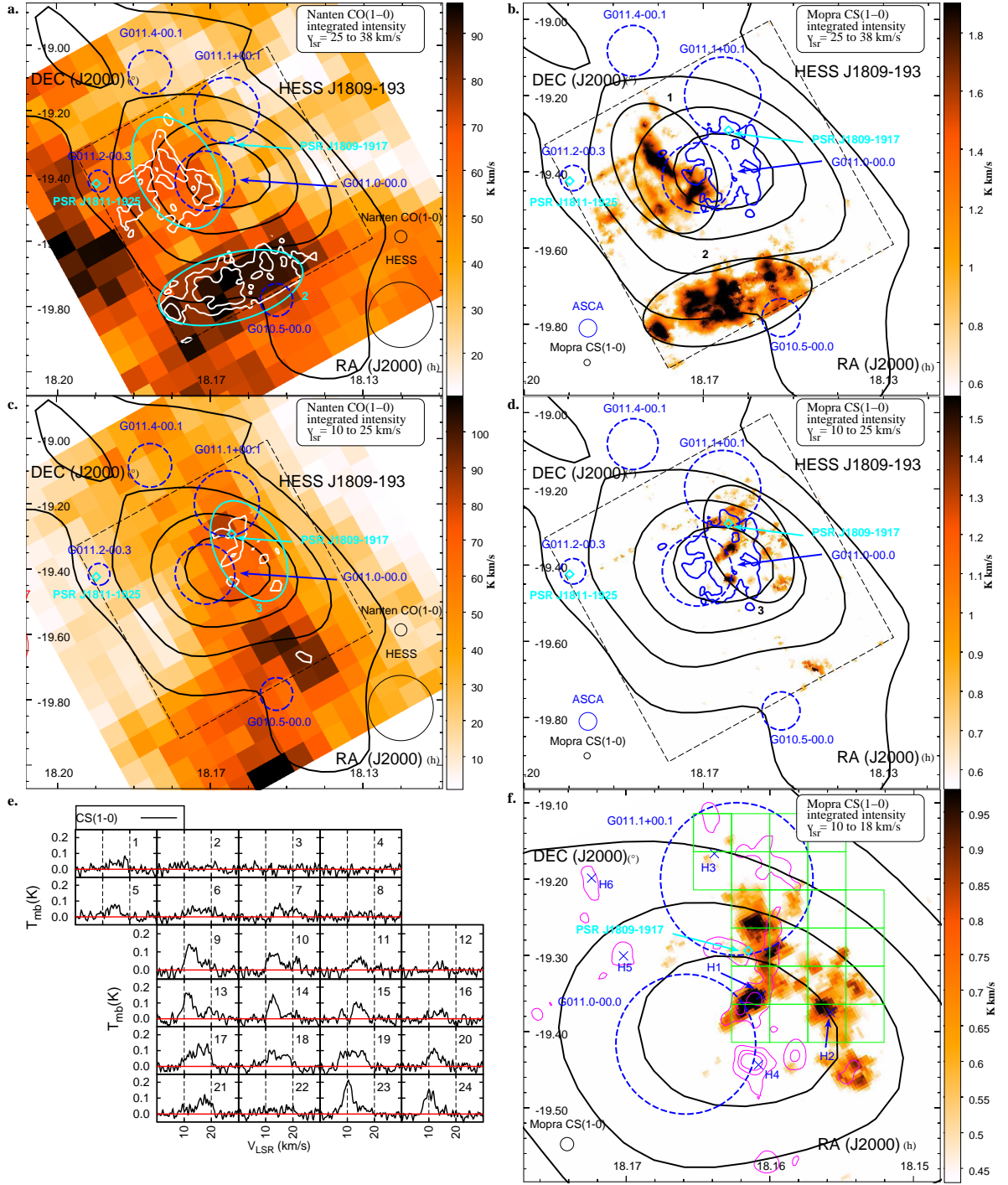


Figure 1. Nanten CO(1-0) and Mopra CS(1-0) integrated intensity maps across two velocity bands $v_{\text{LSR}} = 25$ to 38 km/s (panels a. b.) and $v_{\text{LSR}} = 10$ to 25 km/s (panels c. d.) towards HESS J1809-193 overlaid by the TeV gamma-ray counts in black contours (Aharonian et al. 2007b). The dashed black box represents the area covered during our 7mm survey. The regions selected for the CO and CS analysis are shown in cyan and black respectively. The SNRs are shown as dashed blue circles while the pulsars are illustrated as cyan diamonds. The ASCA hard X-ray (2 to 10 keV) contours are displayed on the right panels in blue while the CS contours overlays the CO(1-0) integrated intensity map on the left panels are displayed in white contours. A zoomed image of the CS(1-0) integrated intensity emission at $v_{\text{LSR}} = 10$ to 18 km/s is shown in panel f. overlaid by the CS(1-0) integrated intensity at $v_{\text{LSR}} = 18$ to 22 km/s contours in magenta. The position of HII regions ‘H1→H5’ are shown in blue crosses. The averaged CS(1-0) emission over the green grid of boxes in panel f. is displayed in panel e.

anti-correlates with the PWN TeV emission. As molecular gas may provide sufficient target material to produce TeV emission, probing extended CO(1–0) emission overlapping the TeV emission is also a powerful means to test the hadronic scenario in the vicinity of a cosmic-ray (CR) accelerator or for electron to produce significant Bremsstrahlung radiation. Several prominent and extended features were highlighted, and their CO(1–0) spectral components fitted with Gaussians. We then used the X-factor $X_{\text{CO}} = 2 \times 10^{20} \text{ cm}^{-2}/(\text{K km/s})$ to convert the CO integrated intensity into H_2 column density. Bolatto et al. (2013) have argued that this value is correct to $\sim 30\%$ across the Galactic plane.

We then used Eq. B.4 to obtain the total mass of the cloud, accounting for a 20% contribution from Helium. We finally assumed a prolate geometry to obtain the H_2 volume occupied by the molecular gas, and the averaged particle density n_{H_2} using Eq. B.5 (see Appendix A1 below). The Gaussian fits for the CO(1–0) components towards the regions of the individual TeV source can be found in Tables A.1 to A.6 and their derived physical properties in Tables B.1 to B.6.

2.3 HI analysis with SGPS/GASS surveys

From the Southern Galactic Plane Survey (SGPS) and GASS HI surveys (McClure-Griffiths et al. 2005, 2009), we also obtained the atomic HI column density N_{HI} assuming the (optically thin) conversion factor $X_{\text{HI}} = 1.8 \times 10^{18} \text{ cm}^{-2}/(\text{K km/s})$ (Dickey & Lockman 1990). Comparing the total column density $N_{\text{H}} = N_{\text{HI}} + 2N_{\text{H}_2}$ to the absorbed X-ray column density from X-ray counterparts can provide further constraints on the distance to the TeV source.

3 TeV sources-ISM analysis

We list here various detections from our 7mm observations. For each source (see Figure 1 to 14) we labeled the regions with CS(1–0) detections in numerical order (e.g. ‘1’) while the regions with SiO(1–0, $v=0$), $\text{HC}_3\text{N}(5-4, F=4-3)$, $\text{CH}_3\text{OH}(I)$ detections are labeled ‘S’, ‘HC’ and ‘CH’ respectively. In this section, we however focus on combining our CS(1–0) detections with the Nanten CO(1–0) and primarily focus on the morphology of the various molecular regions surrounding our TeV PWNe and PWNe candidates, useful to understand their nature and morphology.

3.1 HESS J1809-193

HESS J1809–193 is a bright and extended TeV source whose position is coincident with several potential cosmic-ray (CR) accelerators (Aharonian et al. 2007b). ASCA (Bamba et al. 2003) and Suzaku observations (Anada et al. 2010) revealed non-thermal X-rays likely

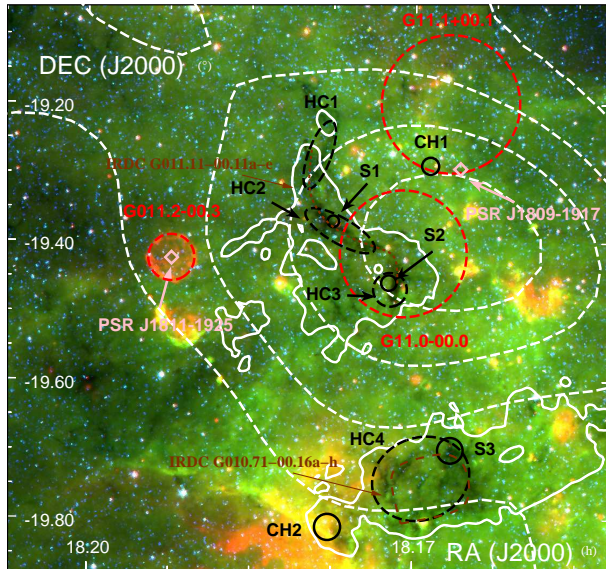


Figure 2. Three colour image showing the MIPS GAL 24 μm and GLIMPSE 8 μm and 4.6 μm in red, green and blue respectively towards HESS J1809–193 overlaid by the HESS TeV gamma-ray counts in dashed white contours and CS(1–0) integrated intensity between $v_{\text{lsr}} = 25$ to 38 km/s contours (0.6 K) in solid white. The SNRs are shown in red dashed circles while the pulsars position are indicated in pink diamonds. The black dashed ellipses labeled ‘HC’ indicates the positions of $\text{HC}_3\text{N}(5-4, F=4-3)$ detections, while the black solid circles labeled ‘CH’ and ‘S’ respectively indicate CH_3OH and SiO(1–0, $v=0$) detections. The spectra of these regions can be found in Figure 3

associated with the pulsar PSR J1809–1917 (shown as a cyan diamond in Figure 1), with spin down energy $\dot{E}_{\text{SD}} = 1.8 \times 10^{36} \text{ erg s}^{-1}$, a characteristic age $\tau_c = 51 \text{ kyr}$ and a dispersion measure distance $d \sim 3.7 \text{ kpc}$ (Cordes et al. 2002). It is consequently likely that the observed PWN contributes to the observed TeV γ -ray emission. However the presence of two SNR shells G011.0–0.0 and G011.1+0.1 (shown as blue circles in Figure 1) both observed at 330 MHz and 1465 MHz (Brogan et al. 2004; Castelletti et al. 2016) adds more complexity in the picture. Additionally, the $\sim 2 \text{ kyr}$ old millisecond pulsar PSR J1809–1925 with spin down energy $\dot{E}_{\text{SD}} = 6.4 \times 10^{36} \text{ erg s}^{-1}$ (Torii et al. 1999) and its progenitor SNR G011.2–0.3, located at $d \sim 4.4$ to 7 kpc, are also positioned adjacent to HESS J1809–193 (see Figure 1) and thus might also contribute to the TeV emission. It should be also noted that this SNR has also been revealed from 24 μm continuum observations (see Figure 2), indicative of collisionally heated warm dust and Fe rich ejecta (Pinheiro Gonçalves et al. 2011), and is also thought to be expanding in a quite dense environment based on the detection of shocked H_2 gas spatially coincident with the SNR. We provide additional observational in-

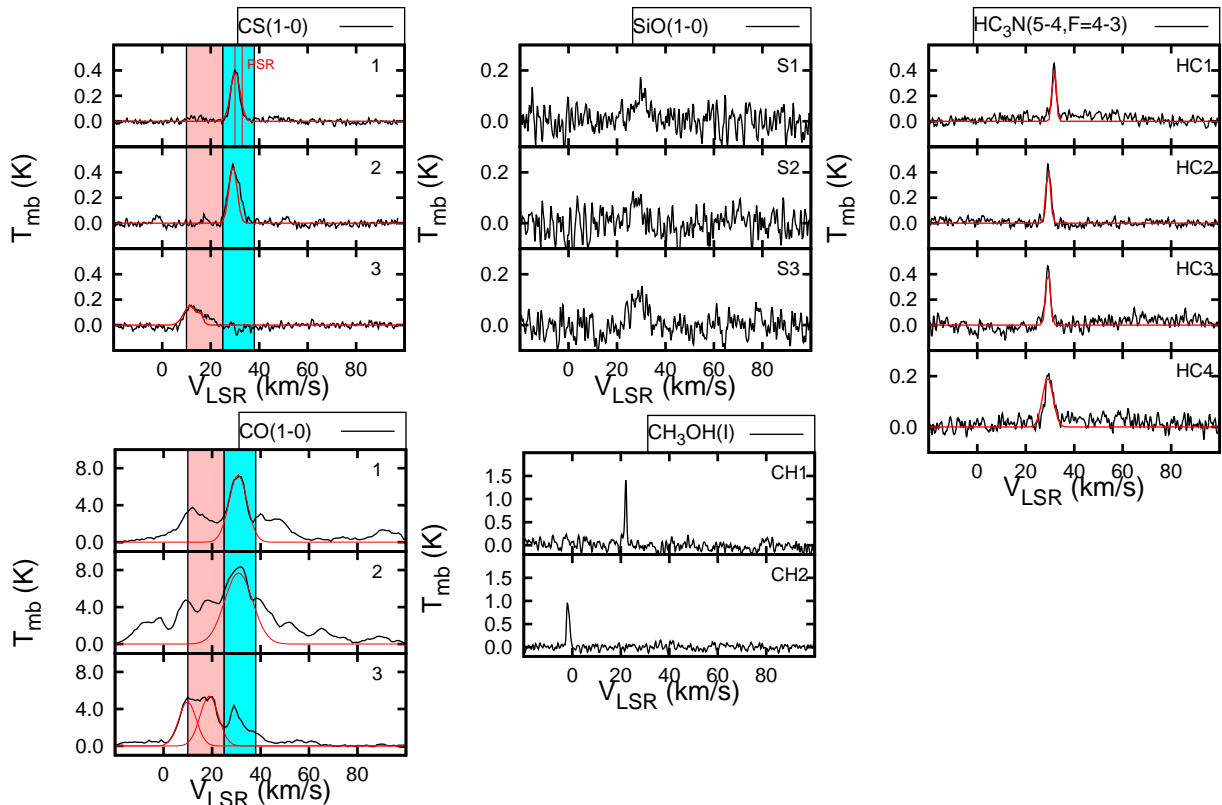


Figure 3. Averaged CS(1–0), CO(1–0), HC₃N(5–4, F=4–3), SiO(1–0, v=0) and CH₃OH(l) spectra towards the emission from the selected regions in Figs. 1 and 2 towards HESS J1809–193. The solid red lines represent the Gaussian fit of the emission whose parameters are shown in Table A.1. The two red vertical lines indicate the pulsar PSR J1809–1917 dispersion measure distance converted to kinematic range. The pink and cyan regions represent the velocity range for the CS(1–0) and CO(1–0) integrated intensity maps displayed in Figure 1.

formation about this intriguing SNR in Appendix D.1. Based on the kinematic distance of PSR J1809–1917 ($d \sim 3.7$ kpc), we here focus on components at $v_{\text{lsr}} = 10$ to 38 km/s (see blue and pink regions in Figure 3), although our Nanten CO(1–0) data have revealed several components in the line of sight (see CO(1–0) emission in Figure D.1).

At this velocity range, we remark that the molecular gas overlaps with the TeV emission shown in black contours. Notably, at $v_{\text{lsr}} = 25$ to 38 km/s ($d \sim 3.6$ kpc), prominent CO emission is found south and east of the TeV emission while the prominent CO emission spatially overlaps the TeV emission at $v_{\text{lsr}} = 10$ to 25 km/s ($d \sim 2.5$ kpc) although the small velocity separation between these features lead to uncertainties regarding the morphology of the ISM diffuse molecular gas at these velocities. Our Mopra CS(1–0) integrated intensity (see Figure 1 panels b., d., f.) however provides a much clearer view of the dense gas.

At $v_{\text{lsr}} = 25 - 38$ km/s (Figure 1, panels a., b.), the molecular clouds in the regions labeled ‘1’ and ‘2’ and

located east and south of SNR G011.0+00.0 respectively appear very extended. From our CO and CS analyses, the masses derived in region ‘1’ reach M_{H_2} (CO) = $8.1 \times 10^4 M_{\odot}$ and M_{H_2} (CS) = $3.2 \times 10^4 M_{\odot}$ while we obtain M_{H_2} (CO) = $2.3 \times 10^5 M_{\odot}$ and M_{H_2} (CS) = $1.2 \times 10^4 M_{\odot}$ in region ‘2’. It thus reveals that a large fraction of the molecular gas in region ‘1’ and ‘2’ respectively are concentrated in clumps. Interestingly, we have found embedded dense filaments in region ‘1’ from C³⁴S(1–0) and HC₃N(5–4, F=4–3) detections (see Figure D.2 in Appendix D.1). In fact, the positions of the HC₃N detections labeled ‘HC1 to HC3’ in Figure 2 coincide with the Spitzer infra-red (IR) dark cloud IRDC G011.11–00.11a–e (Parsons et al. 2009, see Figure 2), confirming the position of the molecular gas in the foreground. We have also identified two weak but broad SiO(1–0) features in region ‘1’ (see Figure 2), labeled ‘S1’ and ‘S2’. The absence of IR continuum emission indicates the lack of active star-forming region and thus suggests the possible interaction between the molecular cloud and a non star-

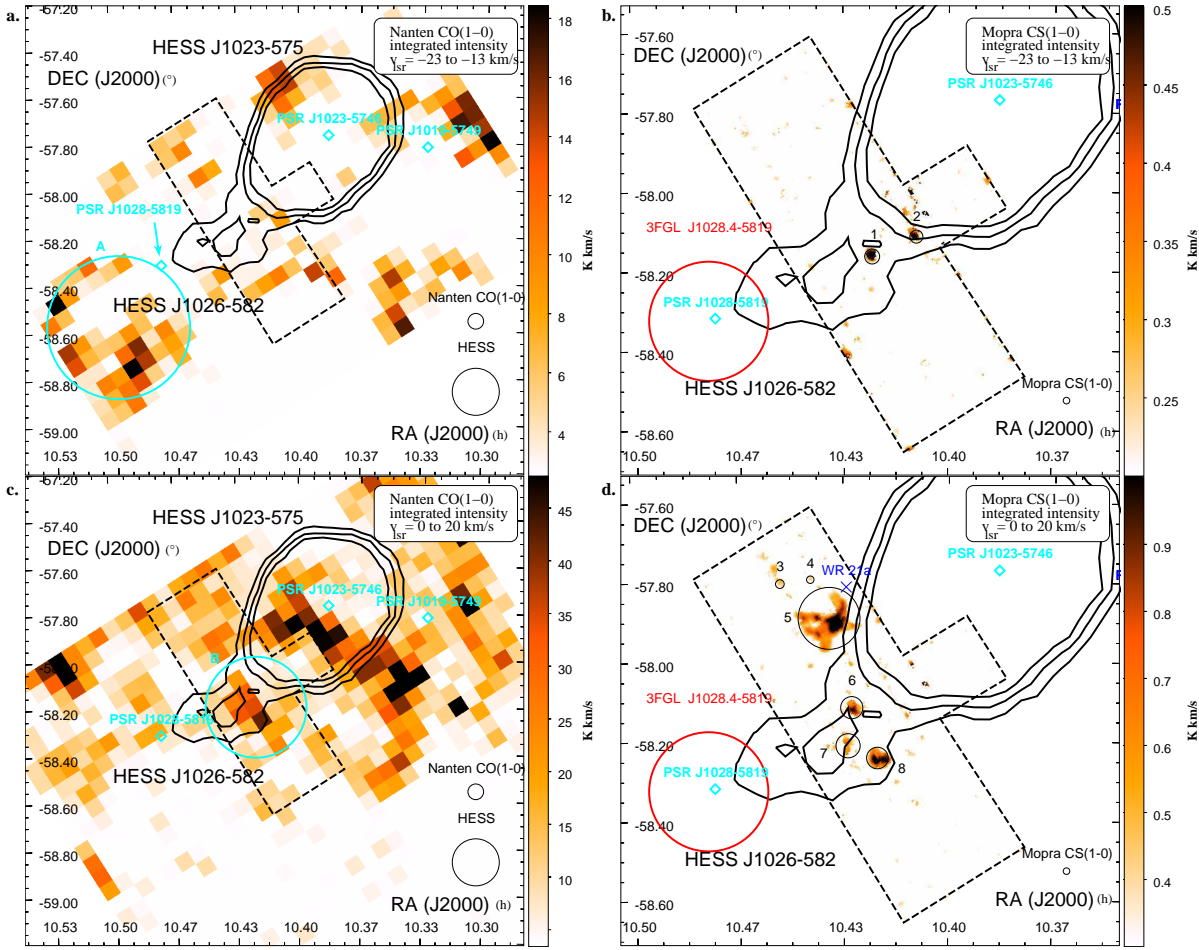


Figure 4. Nanten CO(1–0) and Mopra CS(1–0) emission between $v_{\text{lsr}} = -23$ to 13 km/s and $v_{\text{lsr}} = 0$ to 20 km/s towards HESS J1026–582 and HESS J1023–575 whose TeV gamma-ray counts are shown in black contours. The position of the pulsars PSR J1028–5819, PSR J1023–5746 and PSR J1019–5749 are indicated as cyan diamonds. The GeV emission 3FGL J1018–5819 associated to PSR J1028–5819 is shown as a red circle. The cyan ellipses show the selected regions (labelled A and B) from our CO analysis. The black circles (labelled 1 to 8 in panels c. and d.) denote the position of the dense molecular regions traced by the CS(1–0) molecular transition. The location of WR 21a is shown as a blue cross in panel d.

forming shock (Schilke et al. 1997; Gusdorf et al. 2008), which could here be the adjacent SNR G011.0–0.0. This molecular gas also appears to anti-correspond with the ASCA X-ray diffuse emission shown in blue, supposedly produced by high energy electrons from the pulsar PSR J1809–1317 (see Anada et al. 2010).

In region ‘2’, we have also detected extended $\text{HC}_3\text{N}(5-4, F=4-3)$ emission and $\text{C}^{34}\text{S}(1-0)$ emission overlapping the infra-red dark cloud IRDC G010.71–00.16a–h (Parsons et al. 2009), highlighting another dense region. A prominent $\text{SiO}(1-0)$ detection (see region ‘S3’ Figure 2) was also found inside this dark cloud.

At $v_{\text{lsr}} = 10 - 25$ km/s (Figure 1 panel d.), we observe several CS(1–0) components inside the region

here labeled ‘3’, containing the sub-regions identified by Castelletti et al. (2016). From our CO and CS analyses, we obtain a total mass $M_{\text{H}_2}(\text{CS}) = 6.5 \times 10^3 M_{\odot}$ and $M_{\text{H}_2}(\text{CO}) = 4.3 \times 10^4 M_{\odot}$, which are much higher than the mass derived by Castelletti et al. (2016). Our ~ 2 times larger selected region can explain this discrepancy. Also, they used the X_{CO} and the CO(2–1) molecular transition to provide column density and mass estimates. Using the LTE approximation, their method requires an equal distribution of CO molecules at $J = 2$ and $J = 0$, only achievable if the traced molecular gas has a kinetic temperature $T_{\text{kin}} \sim 20$ K. Consequently, their column densities and masses may be underestimated if the temperature is below this value. We also observe that the CS(1–0) emission averaged over

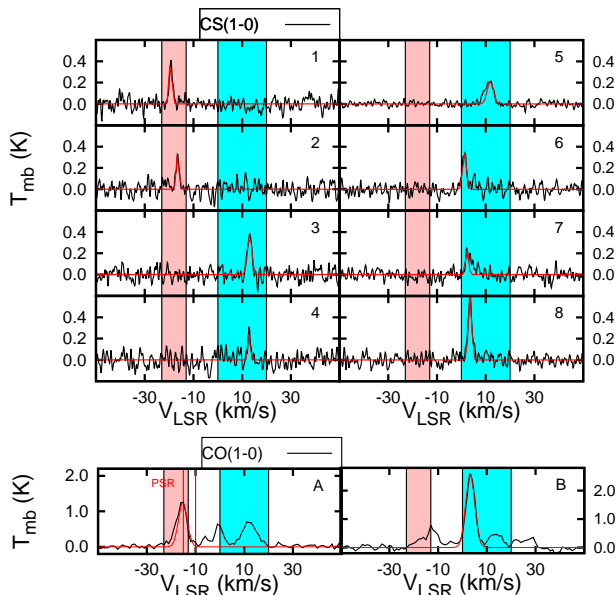


Figure 5. Averaged CO(1–0) and CS(1–0) emission from the regions from the selected regions in Figure 4 towards HESS J1026–582. The red lines indicate the fit used to parametrise the emission. The fit parameters are displayed in Table A.2. The two red vertical lines show the dispersion measure distance of the pulsar PSR J1018–5819. The blue and pink regions indicate the velocity range shown in Figure 4.

the grid regions (Figure 1 panels e-f.) exhibit considerable variation of the peak velocity ranging between $v_{\text{lsr}} = 10 - 22$ km/s. Indeed, the two peaks at $v_{\text{lsr}} \sim 12$ and 18 km/s inside ‘boxes 9 and 10’ merge to a single peaked emission with $v_{\text{lsr}} \sim 15$ km/s in ‘box 15’. Most double peaks notably appear located near most of the identified HII regions. Consequently, the two spectral components may actually probe the same molecular gas, disrupted by the driving motion forces from various HII regions.

3.2 HESS J1026–583

The TeV source HESS J1026–583 was discovered from energy dependent morphology studies towards HESS J1023–591 (Abramowski et al. 2011). The latter source is thought to be powered by the colliding winds from Wolf-Rayet stars within the massive stellar cluster Westerlund 2 at $d = 5.4^{+1.1}_{-1.4}$ kpc (Furukawa et al. 2009). Acero et al. (2013) catalogued HESS J1026–583 as a PWN candidate based on the detection of a nearby radio quiet gamma-ray pulsar PSR J1028–5810 (Ray et al. 2011) responsible for the GeV emission towards 3FGL J1028.4–5819 (shown as a red circle in Figure 4). PSR J1028–5819 has a spin down power $\dot{E}_{\text{SD}} = 8.3 \times 10^{35}$ erg s $^{-1}$, characteristic age $\tau = 89$ kyr,

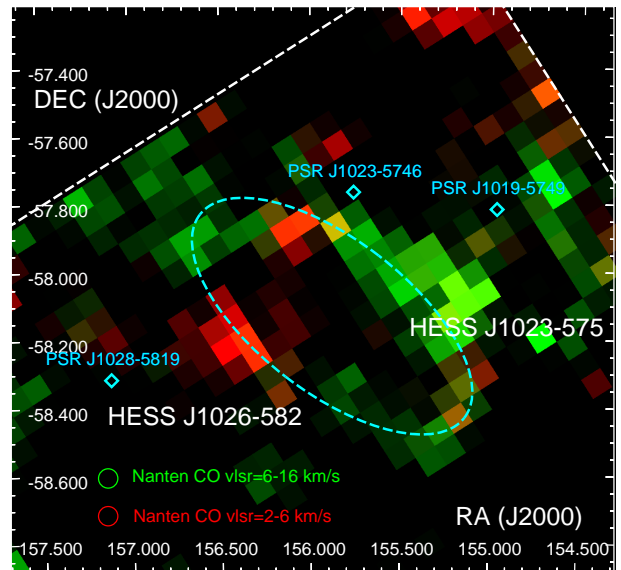


Figure 6. Two-colour image showing the Nanten CO(1–0) integrated intensity at $v_{\text{lsr}} = 2$ to 6 km/s (red) and $v_{\text{lsr}} = 6$ to 16 km/s (green) overlaid by the HESS TeV contours in white towards HESS J1026–582. The cyan dashed ellipse represent the possible molecular ring structure (see Section 3.2).

and a dispersion measure distance $d = 2.3 \pm 0.7$ kpc. However, HESS J1026–583 shows a hard VHE spectral index $\Gamma_{\gamma} = 1.94$ and exhibits neither any X-rays nor GeV emission that is spatially coincident with the TeV source. Consequently, a clear identification remains to be seen. Because of its proximity to HESS J1023–575, several ISM features have already extensively been studied (Dame 2007; Fukui et al. 2009; Furukawa et al. 2009, 2014; Hawkes et al. 2014).

Figure 4 shows the Nanten CO(1–0) integrated intensity at $v_{\text{lsr}} = -23$ to -13 km/s (panel a.) and 0 to 20 km/s (panel c.), inferring a distance $d \sim 2.5$ kpc and $d \sim 5$ kpc respectively. At $v_{\text{lsr}} = -23$ to -13 km/s, we observe that the CO emission does not overlap the TeV emission, nor the pulsar’s position. In fact, the molecular region with prominent CO emission, that we labeled ‘A’, is located next to the pulsar position, and could support the crushed PWN scenario. Assuming a kinematic distance $d \sim 2.1$ kpc, we obtain a total mass $M_{\text{H}_2}(\text{CO}) = 9.7 \times 10^3 M_{\odot}$. Lastly, from our CS survey, we have also identified two narrow and point-like CS(1–0) features labeled ‘1’ and ‘2’ in Figure 4b.

At $v_{\text{lsr}} = 0$ to 20 km/s (see Figure 4 panel c.), we observe prominent CO emission at $v_{\text{lsr}} \sim 4$ km/s, labeled ‘B’, with total mass which has a spatial coincidence with the HESS J1026–582 TeV peak. The molecular cloud in region ‘B’, with total mass $M_{\text{H}_2}(\text{CO}) = 4.9 \times 10^4 M_{\odot}$ appears next to a shell like structure which overlaps the HESS J1023–575 TeV emission. From Fig-

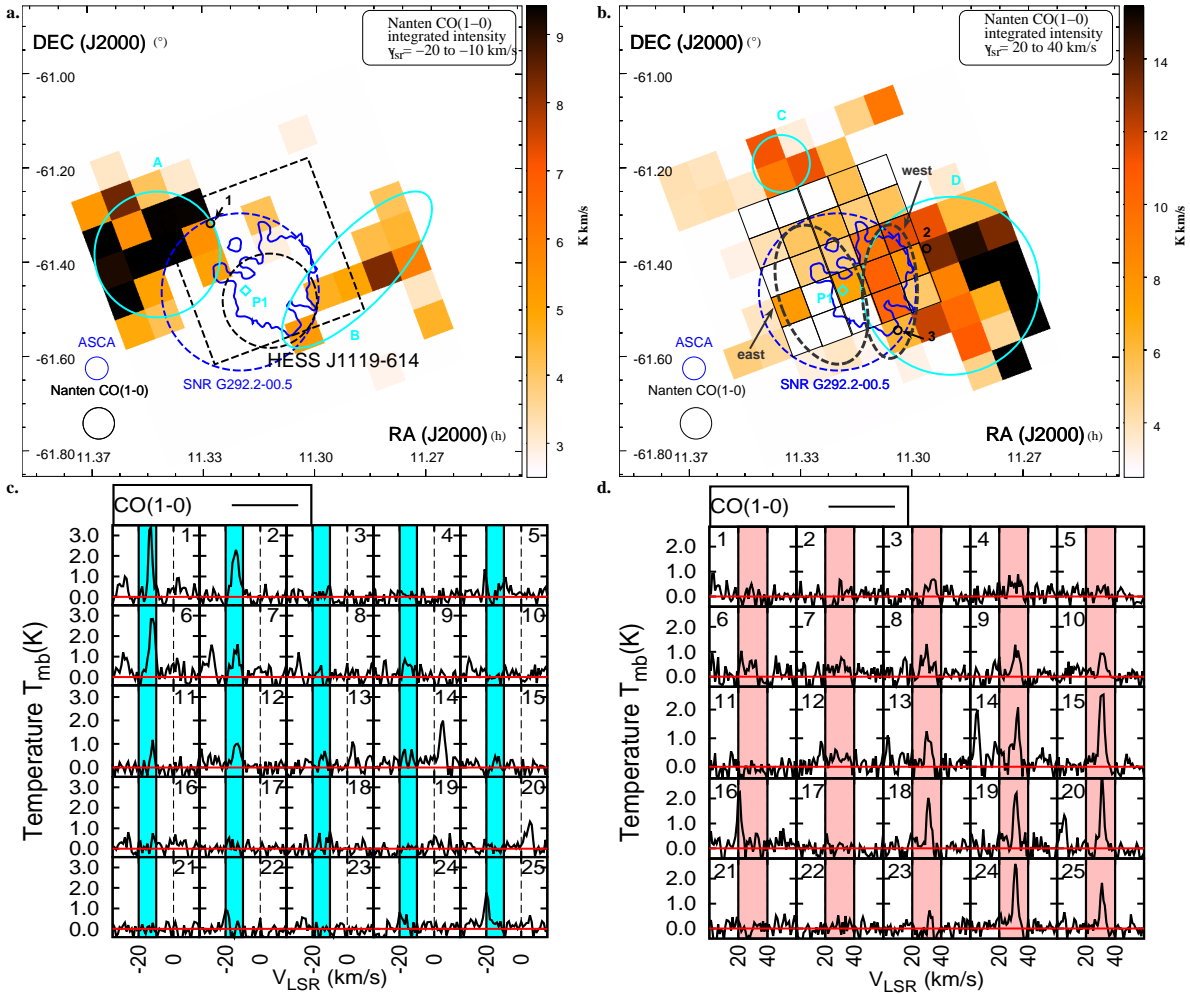


Figure 7. Nanten CO(1-0) and Mopra CS(1-0) emission between $v_{\text{LSR}} = -20$ to 0 km/s and $v_{\text{LSR}} = 20$ to 40 km/s towards HESS J1119-614 whose position and extension is shown as a thin black dashed circle. The progenitor SNR G292.2-0.5 is delimited by the blue dashed circle. The ASCA hard X-ray (2 to 10 keV) emission are also shown in blue contours. The pulsar PSR J1119-6127 position is indicated as a cyan diamond. The cyan ellipses show the selected regions (labelled A to D) for our CO analysis while the black circles (labelled 1 to 3) denote the position of the dense molecular clumps traced by the CS(1-0) molecular line. The thick black dashed ellipses indicate the region used for our column density study (see Figure C.1). Panels c. and d. show the variation of the averaged CO(1-0) spectra over the black grid of boxes shown in panel b. The cyan and pink regions indicate the velocity ranges mapped in panels a. and b.

ure 6, it appears that the CO(1-0) emission at $v_{\text{LSR}} = 2$ to 6 km/s “fills the gap” of the shell-like structure and might form a ‘ring’ (indicated as a dashed-cyan ellipse) structure whose centre is located south-west of HESS J1026-582 observed at $v_{\text{LSR}} = 6$ to 16 km/s. Consequently, the molecular gas in region ‘B’ may be physically connected to this structure.

Among the CS(1-0) features found at $v_{\text{LSR}} = 0$ to 20 km/s, the dense clumps labelled ‘6 to 8’ (Figure 4, panel d.), with masses $M_{\text{H}_2}(\text{CS}) = 0.8$ to $2.0 \times 10^3 M_{\odot}$ (see Table B.2), appear physically associated with the molecular gas in region ‘B’ and also spatially

overlap the TeV source. Finally, we remark that the CS(1-0) emission in region ‘5’ is quite spatially extended. Although its line emission seems narrow (see Figure 5), we notice that the emission line is asymmetric, with a non-Gaussian extension on the blue-shifted side, possibly indicating disrupted gas. We note that WR21a (shown as a blue cross in Figure 4 panel d.), thought to be located at a maximum distance $d \sim 3$ kpc appears next to the molecular cloud, and could be the cause of such disruptions. However, WR21a is also thought to be at a maximum distance $d \sim 3$ kpc (see Benaglia et al. 2005 and reference therein), which dis-

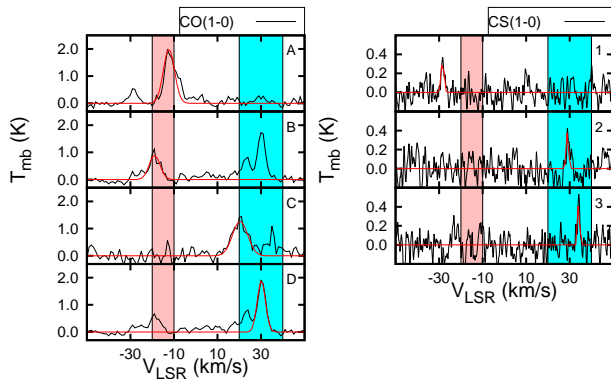


Figure 8. Averaged CO(1–0) and CS(1–0) emission from the selected regions from Figure 7 towards HESS J1119–164. The red lines indicate the fit used to parametrise the emission. The fit parameters are displayed in Table A.5. The pink and cyan regions show the velocity range used for the integrated intensity maps in Figure 7.

agrees with the kinematic distance of the molecular cloud.

3.3 HESS J1119–164

The detection of HESS J1119–614 (see black dashed circle in Figure 7) was first announced by Djannati-Ataï (2009). Its GeV counterpart was identified as a PWN powered by the young pulsar PSR J1119–617 (Acero et al. 2013) with characteristic age $\tau_c = 1900$ yr and a large rotation period $P = 400$ ms. The progenitor SNR of this pulsar has also been identified in the radio band with ATCA (Crawford et al. 2001), and in X-rays with ASCA between 0.4–10 keV (Pivovarov et al. 2001). Although no radio counterpart for the PWN has been detected, the $3'' \times 3''$ PWN has also been seen in X-rays with Chandra (Safi-Harb & Kumar 2008). We note that the distance to the source remains somewhat unconstrained. Indeed, Caswell et al. (2004) estimated the pulsar to be located at $d > 8.6$ kpc from HI absorption and magnetic field studies towards the SNR. Gonzalez & Safi-Harb (2005) however used the absorbed X-ray column density obtained from a non equilibrium ionization (NEI) thermal model to fit the X-ray spectrum towards the SNR interior and then used the relation between the column density, the extinction and distance and obtain $d = 3.6 - 6.3$ kpc. Thus, an ISM study of the gas surrounding the TeV source may shed more light about the PWN distance.

From our Nanten CO(1–0) data, several components have been detected along the line of sight at $v_{\text{lsr}} \sim -30$ km/s, $v_{\text{lsr}} \sim -10$ km/s (near/far distance $d \sim 2.6/4.5$ kpc), $v_{\text{lsr}} = 20$ km/s ($d \sim 8$ kpc) and $v_{\text{lsr}} = 30$ km/s ($d \sim 9.6$ kpc).

Notably, the Nanten CO(1–0) integrated intensity emission for $v_{\text{lsr}} = -20$ to -10 km/s shows two molecular clouds in the regions we label ‘A’ and ‘B’, with masses $M_{\text{H}_2}(\text{CO}) = 2.3 \times 10^4 M_\odot$ and $M_{\text{H}_2}(\text{CO}) = 7.1 \times 10^4 M_\odot$ respectively, positioned adjacent to the SNR. From the averaged CO(1–0) emission grid in Figure 7, we also found detections at $v_{\text{lsr}} = -30$ km/s (boxes 1,6,7,8 in Figure 8 panel c.) and a point-like CS(1–0) emission (see region ‘1’ in Figure 7 panel a.) spatially coincident with region ‘A’. As shown in Figure C.1, we in fact observe that the radial velocity distribution at this Galactic position does not go below $v_{\text{lsr}} \sim -20$ km/s. Thus, it may highlight the presence of disrupted gas.

At $v_{\text{lsr}} = 20$ to 40 km/s, we observe that the bulk of the molecular gas is found in two regions that we label ‘C’ and ‘D’, with masses reaching $M_{\text{H}_2}(\text{CO}) = 1.3 \times 10^4 M_\odot$ and $M_{\text{H}_2}(\text{CO}) = 1.3 \times 10^5 M_\odot$. The morphology of the molecular gas in region ‘D’ not only spatially overlaps the western side of the SNR but also appears spatially coincident with the ASCA hard X-ray contours (2 to 10 keV) in blue. The clumps, labelled ‘2’ and ‘3’ were also identified inside the region ‘D’ with our CS(1–0) tracer at this velocity range (see Figure 7 and Table A.3).

3.4 Kookaburra and Rabbit

The two TeV sources HESS J1418–609 and HESS J1420–607 have been classified as PWNe based on their spatial coincidence with the X-ray (Roberts & Romani 1998) and GeV gamma-ray counterparts (Acero et al. 2013). Ng et al. (2005) indicated that two diffuse non-thermal X-ray sources were associated with the pulsar PSR J1420–6048 (labelled P1 in Figure 9), a 68.2 ms period pulsar with spin down power $\dot{E}_{\text{SD}} = 1.0 \times 10^{37}$ erg s $^{-1}$, characteristic age $\tau_c = 13$ kyr and dispersion measure distance $d \sim 5.6$ kpc; and the 108 ms radio-quiet gamma-ray pulsar PSR J1418–6058 (labelled P2), with a characteristic age $\tau_c = 1.6$ kyr. It has also been noted that P2’s location is offset ($\sim 8.4'$) from the HESS J1418–609 TeV peak. The distance to P2 has not yet been constrained. Thus, by looking at the gas distribution in various velocity ranges, we could then highlight the distance which would support the PWN scenario.

From our CO(1–0) observations (see Figure 9), several molecular complexes have been detected at $v_{\text{lsr}} = -65$ to -55 km/s, ($d \sim 5.5$ kpc), ~ 50 km/s (near/far distance $d \sim 4.0/9.0$ kpc), ~ 0 km/s ($d \sim 11.5$ kpc) respectively. At $v_{\text{lsr}} = -65$ to -55 km/s (see Figure 9a.), we note the bulk of the CO(1–0) emission is located towards the west and north side of HESS J1418–609. We also remark that the molecular emission shows little overlap with any of the TeV sources at this velocity range. From our CS(1–0) observations (Figure 9 panel

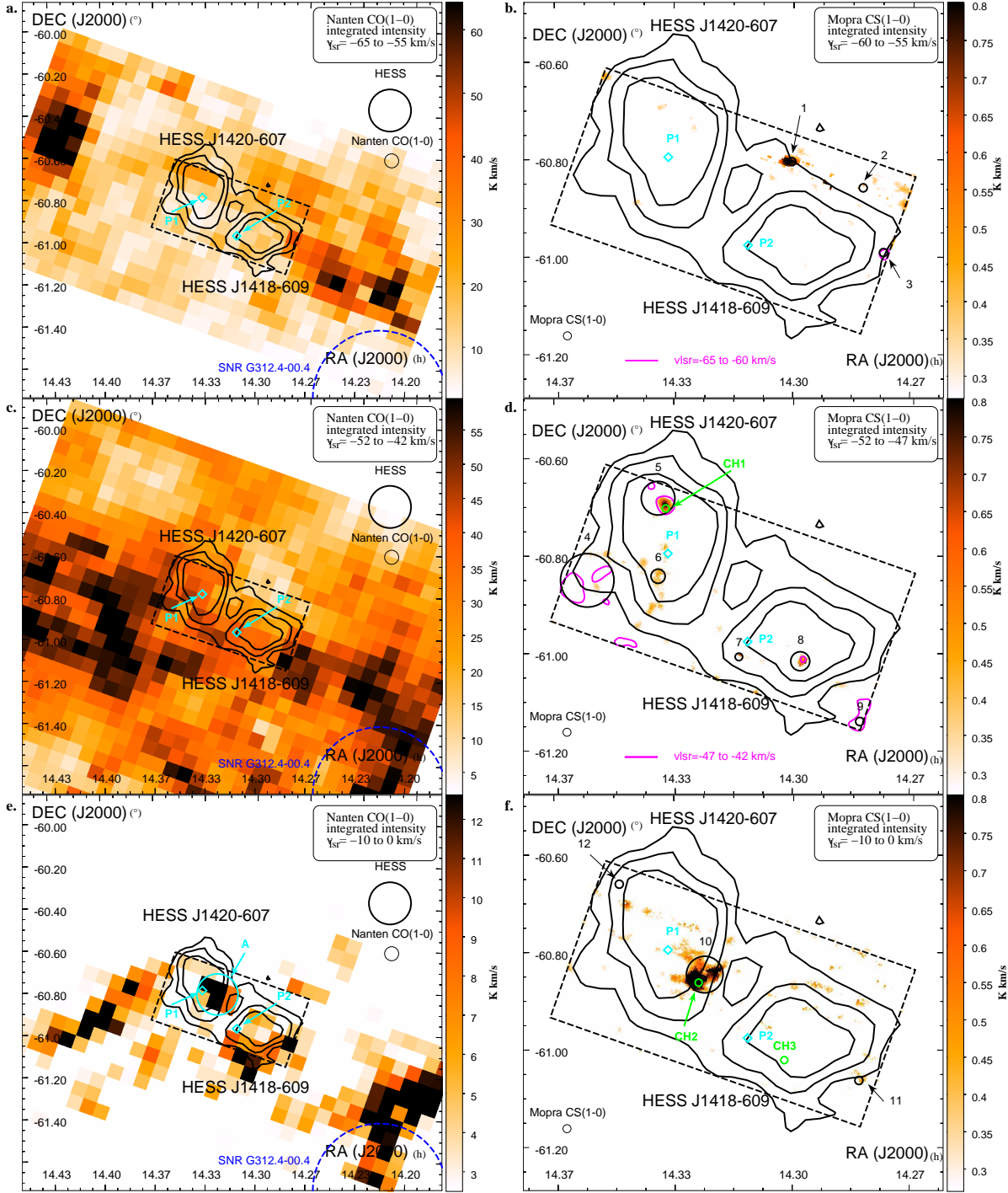


Figure 9. Nanten CO(1-0) and Mopra CS(1-0) emission between $v_{lsr} = -65$ to -55 km/s, -52 to -42 km/s and -10 to 0 km/s towards HESS J1420-607 and HESS J1418-609 shown in black contours. In panel b. and d., the map shows the velocity range at $v_{lsr} = -60$ to -55 km/s and -52 to -47 km/s overlaid by the CS(1-0) at the velocity ranges $v_{lsr} = -65$ to -50 km/s and -47 to -42 km/s in magenta respectively. The black dashed box indicate our Mopra 7mm coverage. The position of the pulsars PSR J1420-6048 and PSR J1418-6058 (labelled P1 and P2 here) are shown as cyan diamonds while the nearest SNR G312.4-0.04 are indicated as a blue dashed circle. The region A for our CO analysis is shown in cyan while the black circles (labelled 1 to 12) denote the position of the dense molecular regions traced by the CS(1-0) transition. The position of the CH₃OH(I) detections labelled ‘CH1’ to ‘CH3’ are shown in green circles.

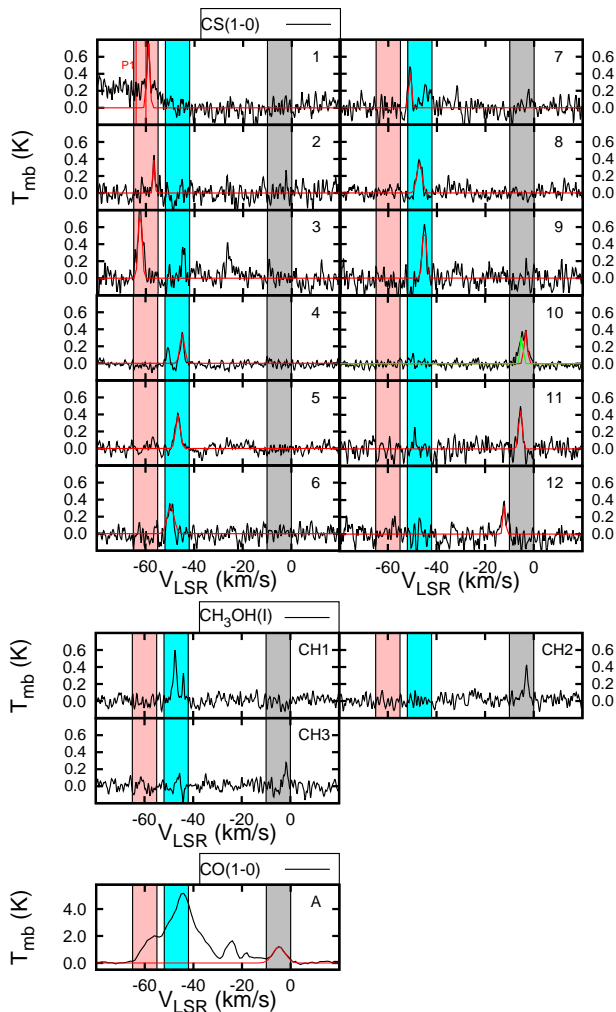


Figure 10. Averaged CS(1–0) emission from the regions towards HESS J1418–609 and HESS J1420–607 shown in Figure 9. The red lines indicate the fit used to parametrise the emission at the velocity ranges where the regions are shown in Figure 9. The fit parameters are displayed in Table A.4. The red vertical lines show the dispersion measure distance of the pulsar PSR J1420–6048 (P1 in Figure 9). The pink, cyan and grey regions show the velocity ranges for the integrated intensity maps in Figure 9.

b.), three small molecular clumps labeled ‘1 to 3’ have also been detected. Their narrow line spectra shown in Figure 10 do not however indicate any enhanced disruption.

At $v_{\text{lsr}} = -52$ to -42 km/s, we note that the CO(1–0) emission overlaps the two TeV sources, and is peaked west of HESS J1018–609 and south east of HESS J1420–607. However, due to the small velocity separation between the components and the components at $v_{\text{lsr}} = -65$ to -55 km/s, it is somewhat difficult to accurately describe the morphology of the dif-

fuse molecular gas at these velocities. Several dense regions traced by our CS(1–0) observation have also been detected, with peak velocities ranging from $v_{\text{lsr}} = -51$ to -44 km/s.

Finally, at $v_{\text{lsr}} = -10$ to 0 km/s (bottom panels), we found prominent CO emission south of HESS J1418–609, east of HESS J1420–607, and between the two pulsars. Notably, the latter molecular region (labeled ‘A’) with mass $M_{\text{H}_2}(\text{CO}) = 6 \times 10^3 M_{\odot}$ nests an extended dense clumps (see region ‘10’) with averaged density reaching $n_{\text{H}_2}(\text{CS}) = 10^2 \text{ cm}^{-3}$.

3.5 HESS J1303-631

HESS J1303–631 was first classified as a ‘dark source’ due to its lack of any counterparts at other wavelengths (Aharonian et al. 2005; Acero et al. 2013). However, energy dependent morphology of the TeV source (see Abramowski et al. 2012b) unambiguously highlighted its association with the pulsar PSR J1301–6305 (P1 in Figure 11) with spin down energy $\dot{E}_{\text{SD}} = 2.6 \times 10^{36} \text{ erg s}^{-1}$, a rotation period $P = 184$ ms, and a characteristic age $\tau_c = 11$ kyr. PSR J1301–6305 located off-set to the TeV source position. Follow-up observations with XMM-Newton revealed diffuse X-ray emission towards the pulsar with spectral index $\Gamma_X = 2.0^{+0.6}_{-0.7}$ (Abramowski et al. 2012b). Acero et al. (2013) detected a GeV counterpart with a gamma-ray spectral index $\Gamma_{\gamma} = 1.7$. Finally, from the 1.384 GHz ATCA observations, Sushch et al. (2015) recently announced the presence of a plausible SNR radio shell with radius $\sim 12'$ next to the pulsar PSR J1301–6305, although its association with the aforementioned pulsar remained unclear.

Based on the dispersion measure of this pulsar, Cordes et al. (2002) suggested a distance $d \sim 6.6$ kpc, much closer than the previous distance $d \sim 12.6$ kpc (Taylor & Cordes 1993). From the Nanten CO(1–0) components identified (see Figure 12), we focus on several molecular complexes in the line of sight at $v_{\text{lsr}} = -35$ to -25 km/s (near/far distance $d \sim 3.5/6.7$ kpc), $v_{\text{lsr}} = -25$ to -15 km/s (near/far distance $d \sim 1.5/8$ kpc), $v_{\text{lsr}} = -5$ to 5 km/s ($d \sim 9.6$ kpc) and $v_{\text{lsr}} = 25$ to 35 km/s (near/far distance $d \sim 12$ kpc) shown in Figure 11. From our 7mm CS observations, which cover the north-west part of the SNR towards the TeV source, we have identified several molecular clumps, that we have labeled ‘1 to 10’ (see Tables A.5 and B.4 for fitting and physical parameters respectively).

The angular radii of these clumps do not exceed $100''$ and consequently indicate that the molecular complex does not seem clumpy. At all the aforementioned velocity ranges, it appears that the CO(1–0) emission always overlaps the TeV emission in black contours. We note however the morphology of the components at $v_{\text{lsr}} = -25$ to -15 km/s is contaminated by

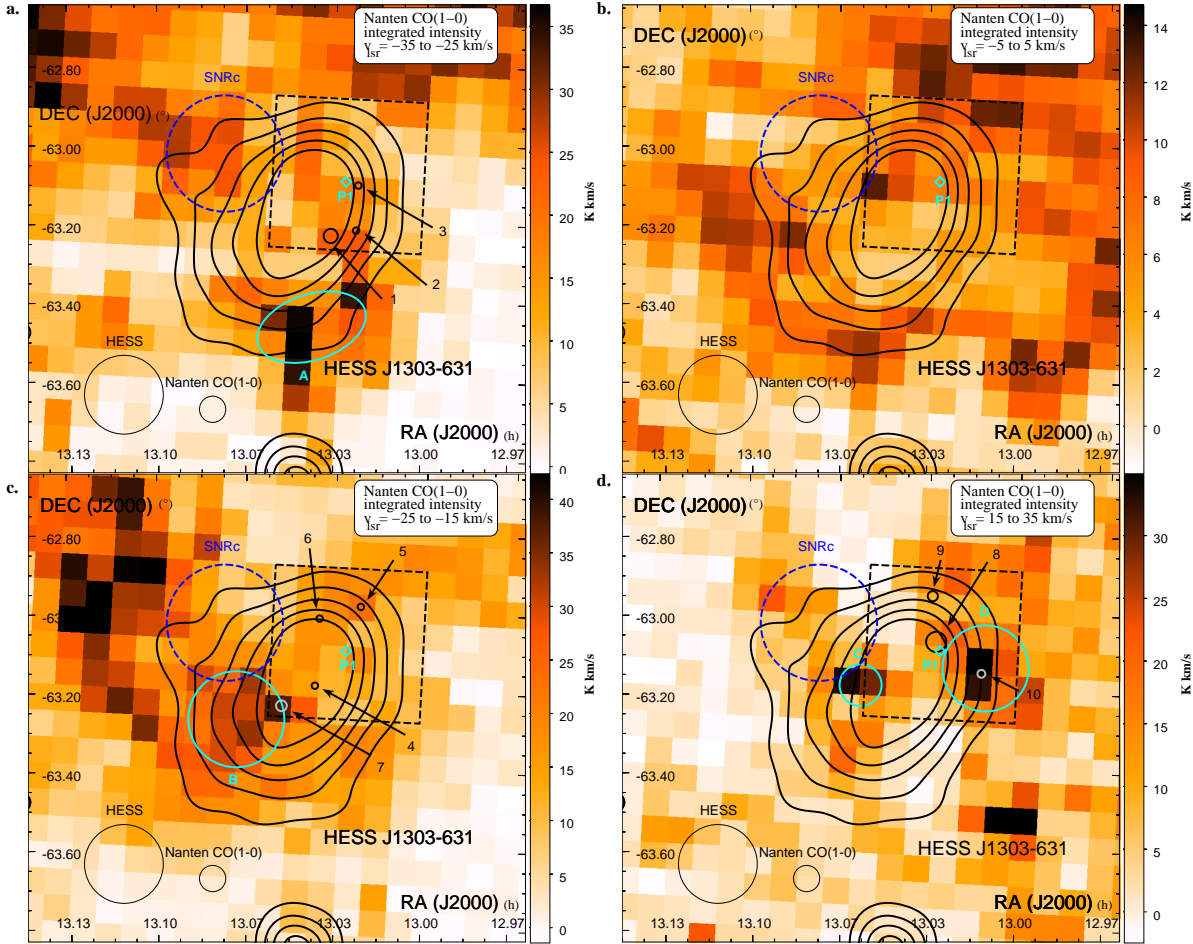


Figure 11. Nanten CO(1-0) integrated intensity map towards HESS J1303-631 (shown in black contours) between $v_{\text{LSR}} = -35$ to -25 km/s, -25 to -15 km/s, -5 to $+5$ km/s and 15 to 35 km/s overlaid by integrated intensity contours in green. The position of the pulsar PSR J1301-6305 (P1), are shown in blue diamonds. The regions labelled 1 to 10 where CS(1-0) were detected are shown in black circles. The positions of prominent CO detections slightly overlapping the TeV emission are shown in cyan circles

the components at $v_{\text{LSR}} = -35$ to -25 km/s. Nonetheless, it should be noted that the CO emission peaks south of HESS J1303-631 inside region ‘A’ at $v_{\text{LSR}} = -35$ to -25 km/s, while at $v_{\text{LSR}} = -5$ to 5 km/s is distributed north east of the TeV source and at $v_{\text{LSR}} = 15$ to 35 km/s, prominent CO emission are found towards HESS J1303-631 (see regions ‘C’ and ‘D’). We also notice that the CO(1-0) emission does overlap the position of the SNR candidate represented in blue circle in Figure 11 at $v_{\text{LSR}} = -35$ to -25 km/s and 15 to 35 km/s.

Interestingly, we have found a CO(1-0) emission dip at $v_{\text{LSR}} = -25$ to -15 km/s localised towards the SNR candidate. From the position-velocity plots shown in Figure 13, we notably observe prominent CO emission which in fact appears to surround the SNR position

(whose boundaries are shown in red dashed lines in Figure 13 bottom panels) between $v_{\text{LSR}} = 22$ to -15 km/s. From the CO(1-0) integrated intensity region at these velocity range, we also observe little spatial overlap between the molecular gas and the SNR candidate. Consequently, it may highlight the presence of a putative molecular shell at $d \sim 8$ kpc coincident with the recently observed SNR candidate. The green cross and circle in Fig. 13 here indicates the position and area of the expansion speed of the putative molecular shell surrounding the SNR candidate.

3.6 HESS J1018-589

HESS J1018-589 has been reported by Abramowski et al. (2012a) and actually consists

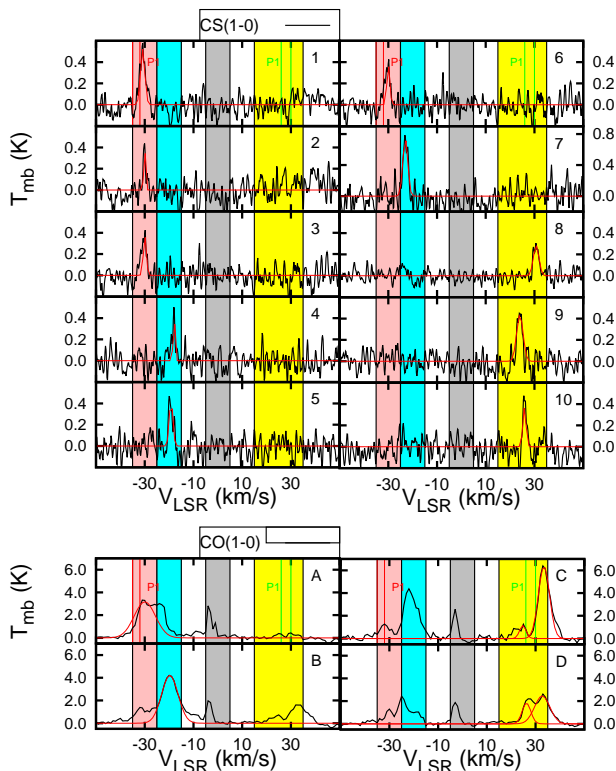


Figure 12. The averaged CS(1–0) emission from the different regions shown in Figure 11 towards HESS J1303–631. The red lines indicate the fit used to parametrise the emission. The fit parameters are displayed in Table A.5. Finally, the red and green vertical lines represent the dispersion measure distance of the pulsar P1 as predicted by Cordes et al. (2002) and Taylor & Cordes (1993) respectively. The pink, cyan, grey and yellow regions indicate the velocity range of the integrated intensity maps shown in Figure 11.

of two distinct sources. The gamma-ray binary 1FGL J1018.6–5856 appears to be responsible for the HESS J1018–589A TeV emission (Abramowski et al. 2012a) while HESS J1018–589B (shown in black in Figure 14) is thought to be a PWN powered by the pulsar PSR J1016–587 (shown by a cyan diamond), with a rotation period $P = 107$ ms, a spin down energy $\dot{E}_{\text{SD}} = 2.6 \times 10^{36}$ erg, and a characteristic age $\tau_c = 21$ kyr (Camilo et al. 2001). It has been suggested that the pulsar, with dispersion measure distance $d = 8$ kpc, is not associated with the nearby SNR G292–1.8 located at $d \sim 2.9$ kpc (Ruiz & May 1986).

From the Nanten CO(1–0) observations shown in Figure 14, we have identified CO emission at $v_{\text{lsr}} = -23$ to -10 km/s, inferring a near distance $d \sim 2.8$ kpc, matching the SNR distance. The CO(1–0) emission appears filamentary north of HESS J1018–589B, and partially overlaps the northern rim of SNR G292–1.8. The molecular gas in

region ‘A’ shows quite broad emission ($\Delta v \sim 12$ km/s, see Table A.6 and Figure 14) and its mass reaches $M_{\text{H}_2}(\text{CO}) = 2.9 \times 10^3 M_{\odot}$.

We also report three marginal point-like CS(1–0) emission in the region labeled ‘1 to 3’ located towards the western side of the SNR and matching the pulsar estimated distance. Although no CO emission were revealed at this distance, we note from Figure C.4 significant HI, which may suggest that the ISM surrounding HESS J1018–589B mostly consists of atomic gas.

4 Discussion

In this section, we use results from our ISM studies to provide input into the various potential origins of the TeV sources. We will notably discuss whether the CRs and/or high energy electrons interacting with ISM molecular regions can contribute to the TeV emission or at least affect their morphology. In this section, we first introduce the method used to check whether nearby high energy sources could produce TeV emission. Then, we will briefly indicate how leptonic emission can be affected by nearby dense molecular clouds.

4.1 Contribution from hadronic components

Based on the mass estimates towards molecular regions overlapping the TeV sources, we use eq. 10 from Aharonian (1991) to derive the cosmic-ray enhancement factor $k_{\text{CR}} = w_{\text{CR}}/w_{\text{M}_{\odot}} \text{ eV cm}^{-3}$ which represents the ratio between w_{CR} the energy density of CRs towards a molecular cloud next to a TeV source, and $w_{\text{M}_{\odot}} \sim 1.0 \text{ eV cm}^{-3}$ the energy density found in the solar neighbourhood. Table 2 indicates the k_{CR} values required for each molecular regions (partially) overlapping the TeV sources to account for the observed TeV fluxes. Nearby SNRs are the most likely viable candidates to produce high CRs energy densities (see Reynolds 2008 and references therein).

CRs propagate along the magnetic field lines and they scatter from their interaction with magnetic field perturbations (provided the scale of the perturbation roughly equals the CR gyroradius). As in molecular clouds, the magnetic field turbulences are thought to be enhanced, we here assume an isotropic diffusion of CRs and electrons as zeroth order approximation. Thus, we can estimate the density of cosmic-rays with energies between E and $E + \Delta E$, located at a given distance R from the SNR which is assumed as an impulsive source by assuming a purely diffusive and isotropic propagation of CRs and neglecting energy losses, (see

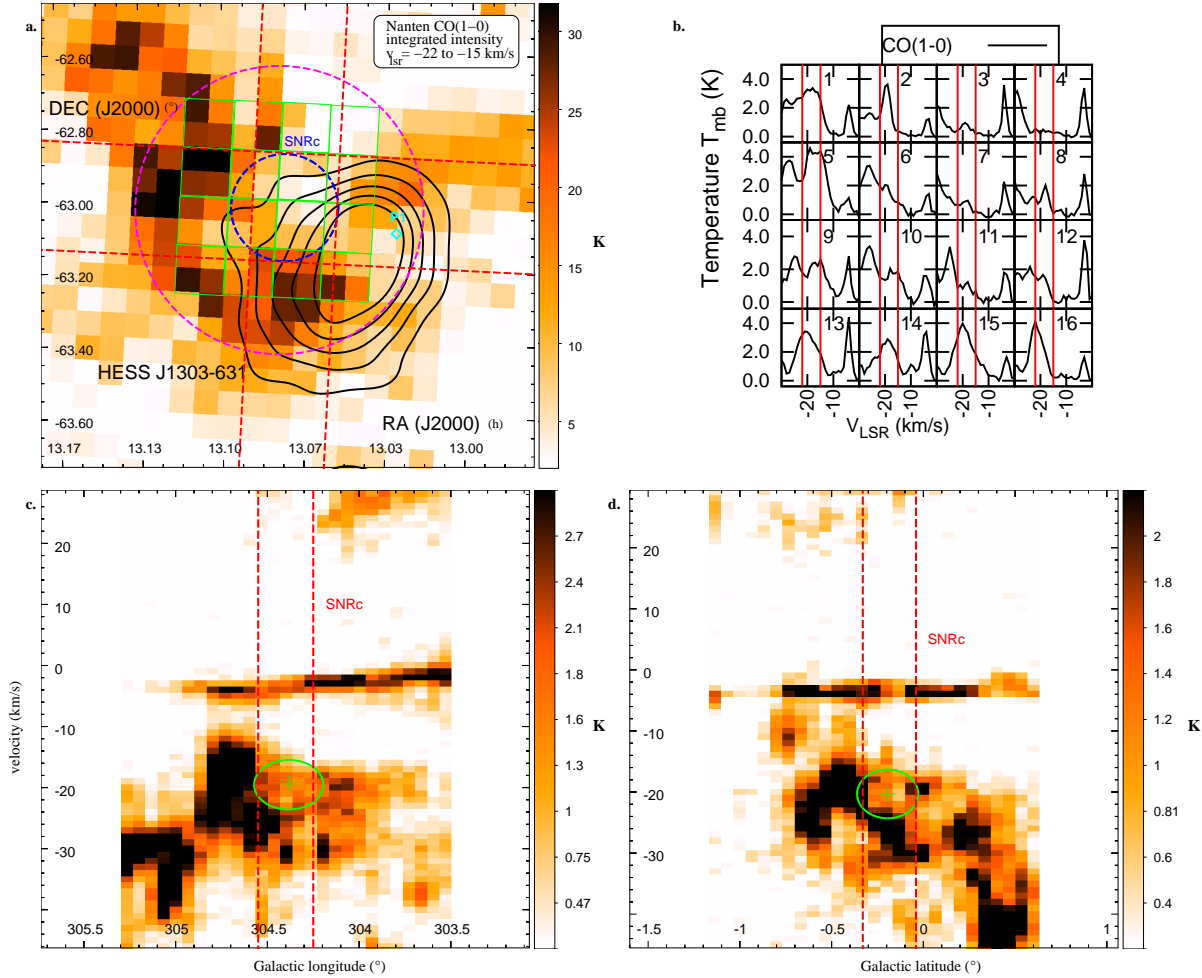


Figure 13. (panel a.) Nanten CO(1-0) integrated intensity between $v_{\text{LSR}} = -22$ to -15 km/s overlaid by the HESS TeV contours in black. The blue circle indicates the size of the candidate SNR (Sushch et al. 2015). The blue diamonds show the position of the pulsars PSR J1301–6305 (P1) PSR J1303–6305 (P2), PSR J1301–6310 (P3) and PSR J1302–6319 (P4). The purple circle indicates the region used to compute the mass of the putative molecular shell (see discussion in section 5) The green grid of boxes indicates the position of the displayed CO(1-0) spectral lines (panel b.). (panels c. and d.) Galactic longitude-velocity (l, v) and latitude-velocity (b, v) image integrated between $b = [304.25^\circ : 304.55^\circ]$ and $b = [-0.34^\circ : -0.04^\circ]$ respectively (shown as red dashed lines in top left panel). The green cross-hairs shown the location of a putative expanding molecular shell while the red dashed lines indicate the boundaries of the candidate SNR.

Aharonian & Atoyan 1996) :

$$n(E, R, t) = \frac{\eta_{\text{pp}} E_{\text{SNR}}}{(m_p c^2)^{2-\alpha}} \frac{E^{-\alpha}}{\pi^{3/2} R_d^3} \exp\left(-\left(\frac{R}{R_d}\right)^2\right) \quad (1)$$

$$R_d = 2 \left(\chi D_{10} t_{\text{age}} \sqrt{E/10 \text{ GeV}} \right)^{1/2} \quad (2)$$

with m_p being the proton mass, $D_{10} = 10^{28} \text{ cm}^2 \text{ s}^{-1}$ being the diffusion coefficient of 10 GeV CRs, α the spectral index of the proton distribution, η_{pp} the ratio of the total SNR energy E_{SNR} transferred to CRs. $R_d(t)$ represents the diffusion radius travelled by CRs at time t . Finally the diffusion suppression factor χ accounts

for slower diffusion of particles which can be caused, for instance, by streaming instabilities or perturbations caused by shocks (Nava et al. 2016 and references therein). Here we use, $\chi = 0.01$ to 1 which matches the slow and fast diffusion coefficient regime defined by Aharonian & Atoyan (1996). Notably, in the case where $\chi = 0.01$, the diffusion coefficient of high energy proton would be close to the Bohm diffusion limit. However, the value of χ remains poorly constrained. From Eq. 1, we can then obtain the total energy density of

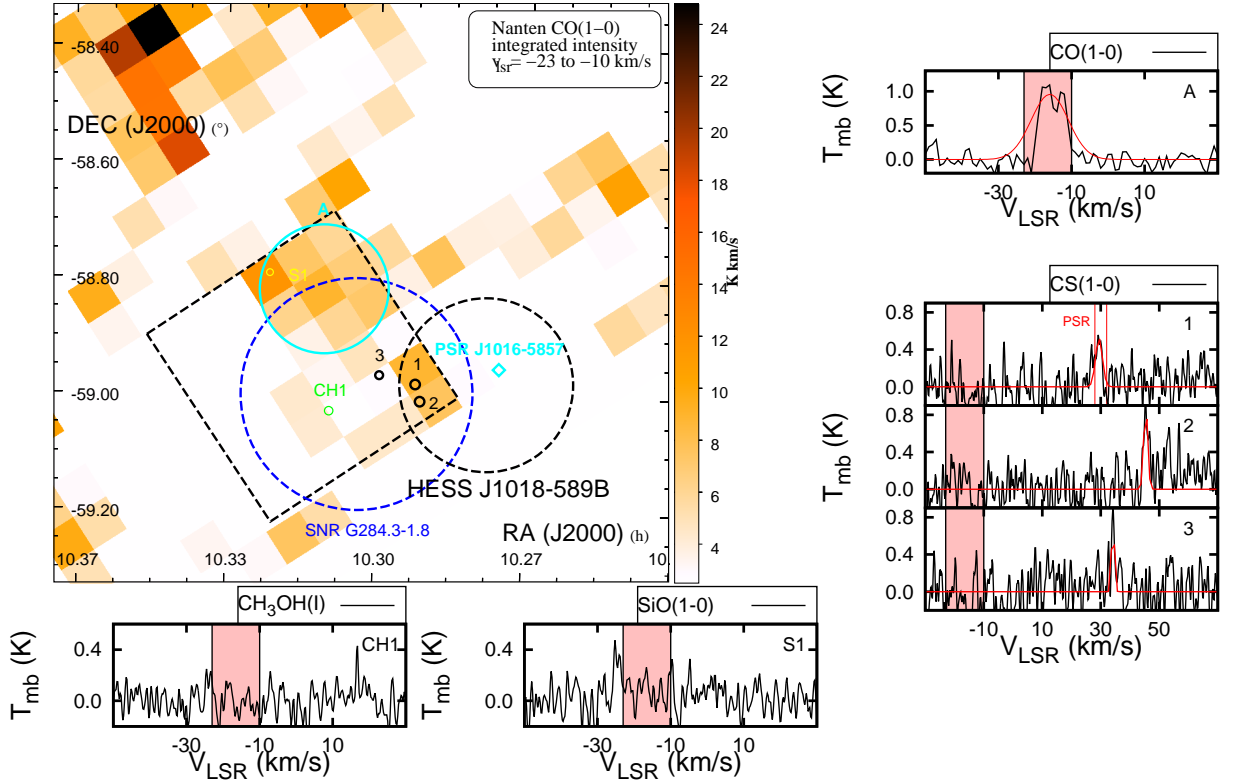


Figure 14. Nanten CO(1–0) integrated intensity map towards HESS J1018–589 between $v_{\text{lsr}} = -23$ to 10 km/s with green contours overlays. The black circle indicates the size of the TeV emission HESS J1018–589B. The SNR G284.3–01.8 is shown as a blue dashed circle while the pulsar PSR J1019–5857 is shown as a cyan diamond. The extended CO region labelled ‘A’ is shown in cyan, the position of the SiO(1–0, $v=0$) ‘S1’ are displayed in yellow and the CH₃OH maser found in the region ‘CH1’ is shown in green. Their respective spectral lines are displayed on the right-hand side. The region within the red vertical lines represents the kinematic position of the pulsar PSR J1016–5857 while the pink region illustrates the aforementioned velocity range.

CRs $w_{\text{CR}}(R, t)$ using the following equation:

$$w_{\text{CR}}(R, t) = \int_{m_p c^2} n(E, R, t) E dE \quad (3)$$

Figure 15 illustrates the range of k_{CR} produced by SNRs with initial energy $E_{\text{SNR}} = 10^{51}$ erg as a function of the SNR age, using a proton spectral index $\alpha = 2.2$ and $\eta_{\text{pp}} = 0.1$. From the distance between the SNRs and the surrounding molecular regions (see Table 2), and the age of the SNRs, we can then check whether the required enhancement factor falls within the predicted range from nearby SNRs.

Additionally, a few authors (see Amato 2014 and references therein) have also argued that high energy hadrons could also be produced from the pulsar environment, and be responsible for several features inside the PWN (e.g wisps in the Crab PWN Gallant & Arons 1994). In the quest for a direct observation of PWN hadronic components, Ivanov et al. (2016) recently argued that the CRs from middle-aged PWN might create degree-scale gamma-ray halos that may be observed by

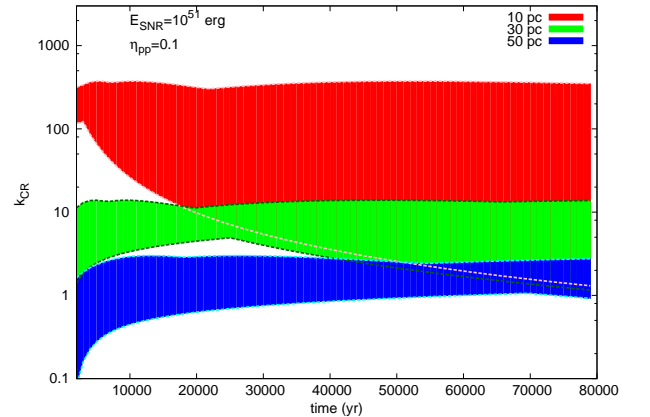


Figure 15. Evolution of the cosmic-ray enhancement factor k_{CR} range as a function of time at a distance $d = 10$ pc (red), $d = 30$ pc (green), and $d = 50$ pc (blue) away from an impulsive source with initial energy $E_0 = 10^{51}$ erg and initial CR spectral index $\alpha = 2.2$. A energy dependent diffusion of CRs (see Section 4) has been applied with a diffusion coefficient at 10 GeV bounded between $D_{10} = 10^{26}$ to 10^{28} cm² s⁻¹.

Fermi-LAT in the 1-10 GeV band. Here, providing high energy CRs has indeed been produced inside PWNe and not suffered heavy adiabatic losses, we will thus discuss whether the pulsars considered in this work could also generate the required cosmic-ray enhancement factors shown in Table 2. In order to model the high cosmic-ray energy density potentially produced by those pulsars, we account for the evolution of the spin down power \dot{E}_{SD} as a function of time t , which can be described as :

$$\dot{E}_{\text{SD}}(t) = \dot{E}_{\text{SD}}(t_{\text{age}}) \left(1 + (n_b - 1) \frac{\dot{P}(t - t_{\text{age}})}{P} \right)^{-\Gamma} \quad (4)$$

$$\Gamma = \frac{n_b + 1}{n_b - 1} \quad (5)$$

with t_{age} being the current age of the PWN, $P(t)$ and $\dot{P}(t)$ being the current period and period derivative of a pulsar respectively at time t , $\dot{E}_{\text{SD}}(t)$ being the pulsar spin down power at time t , and n_b being the pulsar braking index (here assumed to be $n_b = 3$). In order to obtain the density of CRs at a given radius R from the pulsar, we rewrite Eq. 1 with the source term $S(t) = \dot{\eta}_{\text{pp}} \dot{E}_{\text{SD}}(t) / (m_p c^2)^{2-\alpha}$, with $\dot{\eta}_{\text{pp}}$ here being the fraction of the spin down power transferred to CRs. We thus numerically solve the following equation :

$$n(E, R, t) = \frac{E^{-\alpha}}{\pi^{3/2}} \int_{t_{\text{age}}}^0 -\frac{S(\xi - t_{\text{age}})}{R_d^3(\xi)} \exp\left(-\frac{R^2}{R_d^2(\xi)}\right) d\xi \quad (6)$$

with $\xi = t_{\text{age}} - t$. As per the SNR scenario, we finally obtain the CR energy density at a given distance R from pulsar using Eq. 3.

Figure 16 illustrates the CR energy density produced by the various pulsars as a function of the diffusion coefficient suppression factor χ . Here, we assumed $n_b = 3$ for all pulsars except for PSR J1119–6127 where we used $n_b = 2.92$ derived by Djannati-Ataï (2009). Spectral modelling towards several PWNe shows that the energy rate transferred to protons must be at most $\dot{\eta}_{\text{pp}} = 0.20$ of the total spin down power (Bucciantini et al. 2011). We have used here $\eta_{\text{pp}} = 0.20$ and thus the k_{CR} values shown in Figure 16 are upper-limits. In the later sections, we compare these results with the various required k_{CR} (see Table 2) derived inside the molecular regions.

4.2 TeV emission from high energy electrons

As opposed to CRs, the high energy electrons suffer heavy radiation losses as they diffuse inside the molecular clouds because of their potentially enhanced magnetic field strength (see Crutcher et al. 2010). In the lack of intense radiation fields, synchrotron losses, with time-scale $\tau_{\text{sync}} = (4.07 \times 10^{-8} B_{\text{mg}}^2 E / m_e c^2)^{-1}$ yr is likely to dominate over inverse Compton in-

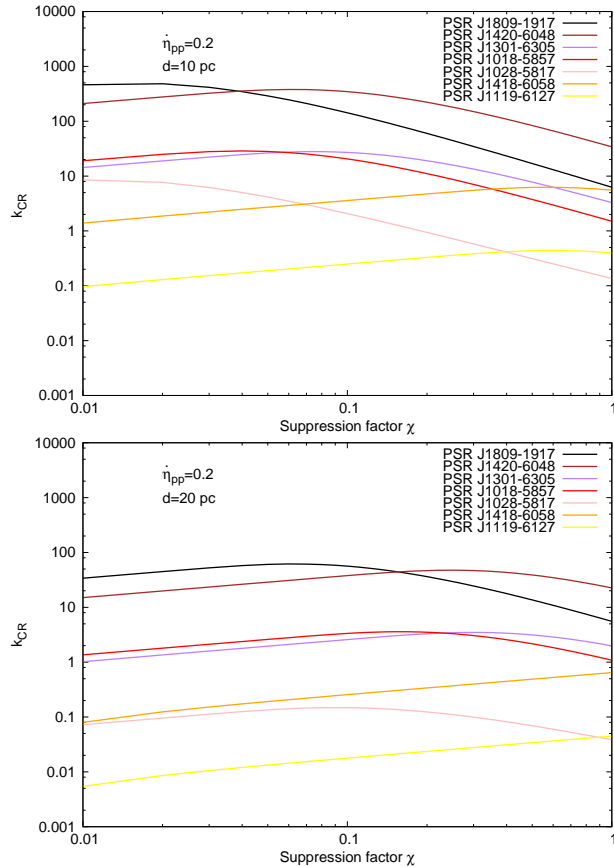


Figure 16. Energy density k_{CR} at 10 pc (top panel) and at 20 pc (bottom panel) distance from the listed pulsars as a function of the diffusion coefficient suppression factor χ .

side molecular clouds. However, we note that inside molecular clouds with densities $n_{\text{H}} > \text{a few } 10^3 \text{ cm}^{-3}$, Bremsstrahlung losses, with time-scale $\tau_{\text{brem}} \sim 4.6 \times 10^7 (n/1 \text{ cm}^{-3})^{-1}$ yr, may become significant for electrons with energies up to $E_e \sim 1$ TeV. Consequently, we could potentially observe leptonic TeV emission overlapping these dense molecular regions in the 0.1 to 1 TeV band. Nonetheless, we expect the leptonic gamma-ray emission above 1 TeV to anti-correlate with the molecular gas. Table 3 indicates the synchrotron energy loss time-scale τ_{sync} for electrons with energy $E = 10$ TeV, required to produce photons with energy $E_\gamma \sim 1$ TeV. To obtain B values inside molecular clouds, we use the Crutcher et al. (2010) relation from :

$$B = 10 \mu\text{G} \quad \text{for } n_{\text{H}} < 300 \text{ cm}^{-3} \quad (7)$$

$$B = 10 \left(\frac{n_{\text{H}}}{300 \text{ cm}^{-3}} \right)^{0.6} \mu\text{G} \quad \text{for } n_{\text{H}} \geq 300 \text{ cm}^{-3} \quad (8)$$

We compare these time-scales with the age of nearby high energy sources and the diffusion time-scale τ_{diff} required for the particles with energy above 10 TeV

to fully cross a molecular region. We here define $\tau_{\text{diff}} = (\langle r \rangle + d_{\text{source}})^2 / 6D(E, B, \chi)$ with $\langle r \rangle$ being the mean radius of the molecular region, d_{source} the distance separating the centre of the high energy source to the centre of the molecular region. By comparing these different time-scales, we will discuss whether the molecular clouds could affect morphology of the TeV emission.

4.3 Discussion of Individual Sources

HESS J1809–193

Combining the most recent JVLA observations with HI absorption and CO(3–2) morphology studies, [Castelletti et al. \(2016\)](#) recently argued for the TeV source distance to be $d \sim 3$ kpc. They also discussed the possible hadronic origin of the HESS J1809–193 TeV emission based its spatial coincidence with the molecular gas.

From our 7mm analysis at $v_{\text{lsr}} = 10 - 25$ km/s, we have revealed dense molecular clumps, which appeared disrupted based on the broad CS emission, and host several HII regions (see Figure 1 panels e-f). Aside from the nearby SNR G011.0–0.0, the stellar winds coming from these HII regions can also provide an additional source of heat and ISM disruption. Consequently, it may be difficult to claim an association between the molecular gas and the SNR G011.0–0.0 solely based on the presence of adjacent CO(3–2) detections.

From our SiO(1–0, v=0) detections, we have more importantly revealed a possible interaction between the molecular clouds in region ‘1’ and ‘2’ at $v_{\text{lsr}} \sim 30$ km/s with external shocks. If SNR G011.0–0.0 interacted with these molecular clouds at $d \sim 3.7$ kpc, it would then be located at the pulsar PSR J1809–1917 distance and quite likely be its progenitor SNR. Reconciling the small projected SNR radius $r_{\text{SNR}} \sim 5$ pc with the pulsar characteristic age $\tau_c = 51$ kyr, however requires the SNR to expand in a very dense environment. Although we find that the averaged density $n_{\text{H}_2}(\text{CO}) = 440 \text{ cm}^{-3}$ and $n_{\text{H}_2}(\text{CS}) = 170 \text{ cm}^{-3}$ towards the region ‘1’ appears consistent with the previous statement, further evidence may be required to claim their physical association.

We now discuss the various leptonic/hadronic contribution towards HESS J1809–193. Regarding the TeV emission from the PWN high energy electrons, we also remark that the synchrotron energy loss time-scale τ_{sync} for electrons above 10 TeV is significantly smaller than the diffusion time-scale through the various ISM regions. Consequently, most electrons producing gamma-rays above 1 TeV would not penetrate the dense molecular regions.

We also check whether the CRs in molecular clouds may produce significant TeV emission. To match

the observed ISM regions, the TeV flux was scaled simplistically by area ratio, that is 16%, 16% and 12% towards region ‘1’, ‘2’ and ‘3’ respectively. We derive that a cosmic-ray enhancement factor $k_{\text{CR}} = 35, 23, 20$ (see Table 2) is required to attain the TeV flux towards the region 1, 2 and 3 respectively. The distances between these SNRs and the molecular regions ranging between 10 and 20 pc (see Table 3), we find from Figure 15 that, at $t_{\text{age}} = 51$ kyr, the predicted k_{CR} ranges between $k_{\text{CR}} \sim 1$ and 300. Consequently, the SNRs G011.0–0.0 and G011.1+0.1 may be able to produce the required cosmic-ray enhancement and produce significant hadronic TeV emission. Interestingly, from Figure 16, we find that the PWN could also significantly increase the cosmic-ray density towards nearby molecular clouds with k_{CR} values reaching ~ 270 (for diffusion suppression $\chi = 0.02$) and thus generally exceeds the aforementioned k_{CR} towards the molecular regions ‘1’ and ‘2’. Although these CR energy densities are upper-limits, the PWN powered by the PSR J1809–5158 may consequently be a viable laboratory to probe possible hadronic components originating from the PWN.

HESS J1026–583

It has already been stated that, based on energetics alone, the spin down energy of the pulsar PSR J1028–5819 could produce the HESS J1026–583 TeV emission ([Abramowski et al. 2011](#)). From our Nanten CO(1–0) data, we have found that the morphology of the molecular gas at $v_{\text{lsr}} = -23$ to -13 km/s ($d \sim 2.1$ kpc) supports the PWN scenario. The molecular gas in region ‘A’ may have interacted with the progenitor SNR and provoked the offset TeV emission with respect to the aforementioned pulsar. From Table 3, we notice that, for the molecular region ‘A’, τ_{sync} is much larger than t_{diff} for $\chi = 0.1$. Consequently, the high energy electrons escaping the PWN is likely able to cross the molecular regions without significant energy losses.

From our CO(1–0) and CS(1–0) data, we have however identified a dense molecular region spatially coincident with the TeV emission. If the TeV emission is indeed of hadronic origin, we also require a proton spectrum $J(E) \propto E^{-1.94}$ to generate the photon spectrum towards HESS J1026–583 (see [Abramowski et al. 2011](#)). Energy dependent diffusion of CRs could reproduce such features ([Aharonian & Atayan 1996](#)) provided only the very high energy CRs have reached the molecular gas in region ‘B’.

Taking into account this hard gamma-ray spectra, the eq. 10 from [Aharonian \(1991\)](#) must be scaled up by a factor of $1.6/0.94 = 1.7$. We thus derived a cosmic-ray enhancement factor $k_{\text{cr}} = 96$. It should also be noted that the averaged densities $n_{\text{H}_2} = 1.0$ to $3.0 \times 10^2 \text{ cm}^{-3}$ of the clumps found in region ‘6 to 8’ (see Table B.2) would also lower the required k_{CR} to produce the ob-

served TeV flux. From Figure 15, we find that this value can only be attained if there is a SNR located very close to the molecular region ‘B’ ($d \sim 10$ pc). However, the key issue in this scenario is the lack of TeV emission observed towards the nearby structure at $v_{\text{lsr}} \sim 10$ km/s that appears connected to our molecular cloud. This could be avoided by arguing for an anisotropic diffusion of CRs following magnetic field lines (Nava & Gabici 2013).

Finally, claiming a hadronic TeV emission at $d \sim 5$ kpc might endorse a possible association with the nearby TeV source HESS J1023–591, thought to be produced by the colliding winds from the stellar cluster Westerlund 2 (Aharonian et al. 2007a).

HESS J1119–164

We first discuss the potential distance of this TeV source based on our ISM study. As shown in Figure C.1, we first note that atomic and molecular emission equally contribute to the column density N_{H} . We considered the region ‘east’ and ‘west’ regions (shown as grey ellipses in Figure 7b.), and compared the column densities from our ISM analysis with their derived column densities from X-ray measurements (Pivovarov et al. 2001).

Towards the ‘east’ region, we reach the absorbed X-ray column density $N_{\text{H}} = 1.1$ to $1.8 \times 10^{22} \text{ cm}^{-2}$ (see table 3 from Pivovarov et al. 2001) at a distance $d \sim 9$ kpc. Towards the western region, the smaller column density $N_{\text{H}} = 0.1$ to $0.3 \times 10^{22} \text{ cm}^{-2}$ derived from X-ray measurements leads to a distance $d \sim 3 - 4$ kpc. However, it is likely that the nearby strong continuum may lead to large systematic uncertainties in the HI signal. We nonetheless notice that the column density towards the western region roughly equals that towards the eastern region at a distance $d > 10$ kpc (as shown by the blue dashed line in Figure C.1), and sets an upper limit to the SNR distance.

If the system is indeed located at 9.6 kpc and provided the molecular cloud is located behind the SNR (to avoid significant X-ray absorption), the hard X-ray components correlating with the CO emission towards the western side of the SNR could be non thermal X-ray synchrotron emission produced by high energy electrons from the ~ 1.6 kyr old SNR while interacting with the potentially enhanced magnetic field in region ‘D’.

We now check whether the TeV emission towards HESS J1119–164 could be of hadronic origin. Only the molecular regions ‘A’ and ‘D’ partially overlaps the TeV emission. To produce the observed TeV emission towards HESS J1119–164 via p-p interaction, we require a cosmic-ray enhancement factor $k_{\text{cr}} \sim 100$ and 63 (see Table 2) for region ‘A’ and ‘D’ respectively. As both molecular regions are at least located at $R \geq 20$ pc from the SNR centre, we note from Figure 15 and Figure 16 that the maximum k_{CR} value predicted at this distance is $\sim 20 \text{ eV cm}^{-3}$. Thus, if we were to assume an isotropic

Table 2 Cosmic-ray enhancement factors k_{cr} derived using eq. 10 from Aharonian (1991), required to reproduce the observed TeV emission above 1 TeV $F(> 1 \text{ TeV}) = \int N_0 E_{\gamma}^{-1} dE_{\gamma}$ via CR-ISM interaction.

	Molecular Regions	k_{cr}	$F(> 1 \text{ TeV})$ [ph $\text{cm}^{-2} \text{ s}^{-1}$]
HESS J1809–193	1 ^a	35	$6.2 \times 10^{-13*}$
	2 ^a	23	$4.7 \times 10^{-13*}$
	3 ^a	20	$6.2 \times 10^{-13*}$
HESS J1026–582	B	96	$1.1 \times 10^{-12\dagger}$
HESS J1119–193	A	100	$2.5 \times 10^{-13\dagger}$
	D	63	$2.5 \times 10^{-13\dagger}$
HESS J1303–631 ^c	A ^b	296	$1.8 \times 10^{-12\pm}$
	C ^b	235	$2.9 \times 10^{-13\pm}$
	D ^b	320	$1.3 \times 10^{-12\pm}$
HESS J1018–589A	A	115	$2.40 \times 10^{-13*}$

*Aharonian et al. (2007b), [†]Abramowski et al. (2011),
[‡]Djannati-Ataï (2009), [±]Abramowski et al. (2012b),
^{*}Abramowski et al. (2015)

^a: Due to the extended nature of HESS J1809–193, the derived photon flux has been scaled down by 16%, 16% and 12% for regions 1, 2, 3 respectively, corresponding to the ratio between the molecular regions and the TeV emission sizes.

^b: We scaled down the HESS J1303–631 photon flux by 44%, 7% and 31% for region ‘A’, ‘B’ and ‘C’ respectively based on the area ratio between the molecular regions and the TeV emission.

diffusion, the CRs would not be produce the observed TeV emission towards these molecular regions. However, the ~ 1.6 kyr old SNR may still confine these CRs. Consequently, significant TeV emission might still be expected if the SNR has interacted with the molecular gas in region ‘D’.

From Figure 16, we also find that the pulsar is unlikely to have produced enough CRs to produce the TeV emission towards HESS J1119–164.

HESS J1418–609

The pulsar PSR J1418–6058 being radio-quiet, the distance of HESS J1418–609 has yet been constrained. A first approach to constrain the distance is by comparing our column density from CO and HI measurements with the column density $N_{\text{H}} = 2.7 \pm 0.2 \times 10^{22} \text{ cm}^{-2}$ towards the pulsar PSR J1418–6058 derived from X-ray measurements (Kishishita et al. 2012). Using the extreme cases where all the emission is at the near (dashed lines) and far (solid lines) distance, we observe in Figure C.1 that the column density value from X-ray measurements is matched at $v_{\text{lsr}} \leq -50$ km/s, which infers a distance range $d = 3 - 8$ kpc. We can also comment on the distance of this TeV source based on the molecular gas morphology. The anti-correlation between the molecular gas and the TeV source at $v_{\text{lsr}} =$

Table 3 Table showing the diffusion time-scale $t_{\text{diff}} = (\langle r \rangle + d_{\text{source}})^2 / 6D(E, B)$ for a particle with energy $E = 10$ TeV to cross the listed molecular regions with mean radius $\langle r \rangle$ and positioned at d_{source} from the centre of the listed sources. The age of the source t_{age} , the CR-ISM interaction time-scale τ_{pp} for protons, and the synchrotron time scale τ_{sync} for electrons with energy $E = 10$ TeV are also displayed as means of comparison.

	Molecular region properties					Source particle properties			
	Reg.	$\langle r \rangle$ [pc]	B^a [μG]	τ_{pp}^b [kyr]	τ_{sync}^c [kyr]	Source	t_{age} [kyr]	d_{source} [pc]	$t_{\text{diff}}(10 \text{ TeV})^d$ [kyr/ $\chi_{0.1}$]
HESS J1809–193	1	9	29	69	1.4	{ SNR G011.0–0.0 PSR J1809–5158	51	8	2
	2	10	41	35	0.6		{ SNR G011.0–0.0 PSR J1809–5158	51	20
HESS J1026–582	A	11	10	1200	12	PSR J1028–5819	89	5	1
HESS J1119–164	A	11	14	300	6	SNR 292.2–0.5	2	22	4
	D	30	10	1100	13	SNR 292.2–0.5	2	33	13
HESS J1303–631	A	5	31	64	1	PSR J1301–6305	11	17	3
	B	17	14	300	6	SNRc ^e	11 ^e	44	13
	C	11	19	167	3	PSR J1301–6305	11	31	7
	D	24	10	555	11	PSR J1301–6305	11	11	1
HESS J1418–609	A	20	10	1100	12	PSR J1418–6058	2	42	12
HESS J1018–589	A	4	26	85	2	SNR G284.3–1.8	10	8	1

^a: Obtained from eq. 21 from Crutcher et al (2010) (see Section 4.2).

^b $\tau_{\text{pp}} = 6 \times 10^7 / 2n_{\text{H}_2}$ where n_{H_2} can be found in Tables B.1 to B.6

^c: $\tau_{\text{sync}} = (1.292 \times 10^{-15} B_{\text{mG}}^2 E / m_e)^{-1}$ (Ginzburg & Syrovatskii 1964).

^d: See eqs. 2 and 3 from Gabici et al. (2007) to obtain the diffusion time-scale. The results shown assume a diffusion coefficient suppression factor $\chi = 0.1$

^e SNR candidate, see text and Sushch et al. (2015) for further details and Figure 11 for location. We used standards SNR expansion parameter to provide an age estimate of the SNRc if located at this distance (see text).

–65 to –55 km/s, is consistent with a PWN scenario at $d \sim 5.6$ kpc, but it does not explain the offset position of PSR J1418–6058 with the TeV peak. However, if this pulsar has a high space velocity, Roberts et al. (2005) argues that the expected cometary shape of the PWN would explain the offset position of the TeV emission with respect to the pulsar.

Alternatively, based on the ISM morphology, we also consider the possibility that HESS J1418–609 is located at $d \sim 11.5$ kpc, as the molecular cloud in region ‘A’ could here explain the offset position of the pulsar with respect to the TeV source. However the γ -ray luminosity $L_\gamma = 2.4 \times 10^{35} \text{ erg s}^{-1}$ would infer a γ -ray efficiency $\epsilon_\gamma \sim 0.9 - 8\%$, which is higher than the typical γ -ray efficiency for young PWN (Kargaltsev et al. 2013). At this distance, we find that the molecular gas in region ‘A’ partially overlaps the TeV emission. As a result, hadronic TeV emission should also be investigated. If associated with this PWN, the region ‘A’ would then be located at $d_{\text{source}} \sim 42$ pc from this pulsar. We note from Figures 15 and 16 that the required k_{CR} would barely exceed unity. However, as per HESS J1119–164, CRs may have remained confined inside the SNR front

shock. Thus, if the SNR has indeed interacted with the molecular cloud in region ‘D’, the CRs could in fact provide some contribution to the observed TeV emission.

HESS J1303–631

HESS J1303–631 has clearly been identified as a PWN based on energy dependent morphology at TeV energies (Abramowski et al. 2012b). From our ISM analysis, we could not constrain the distance to the PWN as the CO emission appears to overlap with the TeV source at all velocity ranges. We have however found several prominent CO detections in region ‘A’ to ‘D’ located west and south of the TeV peak (see Figure 11). We thus check whether these molecular regions could lead to significant radiation losses for crossing high energy electrons and consequently affect the morphology of the TeV emission.

From Table 3, we find that, assuming a suppression factor $\chi = 0.1$, high energy electrons would only reach the molecular regions ‘A’ (located at $d \sim 6$ kpc) and ‘C’, ‘D’ (both located at $d \sim 13.6$ kpc). In all cases, the shorter synchrotron time-scale indicate that any high

energy electrons would lose most of their energy while diffusing into these molecular regions. Consequently, if associated with the PWN, no TeV emission spatially that overlaps with these molecular regions should be expected.

Now, we discuss whether the selected molecular regions can also affect the morphology of the TeV emission from CR-ISM interactions. As per the case of HESS J1809–193, we scaled down the photon flux of HESS J1303–631 to 44%, 7% and 31% for regions ‘A’, ‘C’ and ‘D’ respectively, based on the size ratio between the molecular regions and the TeV emission and we obtain $k_{\text{CR}}=296$, 233 and 320 (see Table 2). Based on the distances between the molecular clouds to the pulsar or SNR candidate (see Table 3), we find from Figures 15 and 16 that neither the pulsar nor the SNR candidate can provide sufficient CR energy density to produce significant hadronic TeV emission.

Another interesting issue to discuss is the SNR candidate could be associated with the pulsar PSR J1303–6305, supposedly located at $d \sim 6.6$ kpc. We first discuss the energy required to create the putative molecular shell observed at $v_{\text{lsr}} \sim -20$ km/s. From the dashed magenta circular region in Figure 13 centred towards the SNR candidate position, the maximum mass swept reaches $M_{\text{H}_2} = 1.9 \times 10^6 M_{\odot}$. From the position-velocity plot (see Fig. 13 bottom panels), and assuming the mass is pushed outwards at an expansion speed $v_{\text{exp}} \sim 4$ km/s, we obtain as a upper limit a required kinetic energy $E_{\text{kin}} = 3.0 \times 10^{50}$ erg which represents less than 10% of the total kinetic energy from powerful O stars stellar winds over 1 Myr time-scale (see Weaver et al. 1977 for detailed study on interstellar bubbles). Consequently, the molecular shell may have been produced by the SNR progenitor star. Thus, if the SNR were to be located at a distance $d \sim 8$ kpc, the projected distance between the pulsar and the SNR would reach $d \sim 25$ pc. Assuming a typical density $n_{\text{amb}} \sim 0.1$ surrounding the SNR, a kinetic energy $E_{\text{kin}} = 10^{51}$ erg, The Sedov-Taylor time needed for the SNR to reach a radius $R_{\text{SNR}} \sim 25$ pc would be $t \sim 10$ kyr, similar to the pulsar characteristic age. However, at this age, the velocity required for the pulsar to travel such distance is $v \geq 2200$ km/s, which is much higher than typical values. The characteristic age however underestimate the true age of the pulsar if its braking index $n_b < 3$. The pulsar age must be increased by a factor of 4 in order to attain more reasonable speeds and thus claim a possible association between the pulsar and the SNR.

HESS J1018–589

Towards this TeV source, we solely discuss the possible contribution from CRs originating from the SNR G284.3–1.8. From our mass estimate in region ‘A’, we find that the cosmic-ray enhancement factor

$k_{\text{CR}} = 115$ is required for the CRs to produce the observed TeV flux. As the SNR is thought to be 11 kyr old and appear quite close to this molecular region ($d \sim 8$ pc), we find that this value can be attained by CRs originating from this SNR. Consequently, if associated with the molecular region ‘A’, the CRs from the SNR might contribute to the HESS J1028–589A TeV emission.

5 Conclusion

In this paper, we have thoroughly studied the ISM towards pulsar wind nebulae (PWNe) and PWNe candidates, combining our new 7mm Mopra survey with the Nanten CO(1–0) data and the SGPS/G.A.S.S. HI survey.

Towards HESS J1809–193, we have found several dense molecular regions at $v_{\text{lsr}} = 10$ to 22 km/s and $v_{\text{lsr}} = 25$ to 38 km/s adjacent to the pulsar PSR J1809–1918 and the SNRs G011.0–0.0 and G011.1+0.1. Notably, we have detected SiO(1–0) emission towards the dense molecular cloud south of HESS J1809–193 with no infra-red counterparts, suggesting a possible SNR-MC interaction at the pulsar distance $d \sim 3.7$ kpc. It remains however difficult to associate the SNR G011.0–0.0 with the aforementioned pulsar. We argue that the PWN high energy electrons could lose most of their energies while propagating inside the nearby molecular clouds. Although Bremsstrahlung radiation may be expected due to the high density inside the molecular cloud, we also note that the CRs that have escaped the progenitor SNR may produce significant TeV emission towards these molecular clouds. Additionally, we have found that the pulsar PSR J1809–1917 may be a viable laboratory for the study of CRs originating from the PWN itself as it may provide the required CR energy density to produce significant TeV emission inside the nearby molecular cloud.

Towards HESS J1026–582, the molecular clouds east to the pulsar PSR J1028–5819 may explain its offset position with respect to the peak of the TeV emission at $d \sim 2.7$ kpc. However, we have also found several dense clumps spatially coincident with the TeV emission at $d \sim 5$ kpc. Thus, a hadronic scenario remains to be investigated.

The molecular clouds found at the kinematic distances $d \sim 5.0$ kpc and $d \sim 9.6$ kpc both appear consistent with the hard X-ray morphology towards HESS J1119–164. However, by comparing the column density estimates with the column density derived from X-ray measurements, the distance $d \sim 9$ kpc seems favoured.

Morphological studies and column density studies towards the X-rays towards HESS J1418–609 seem to agree with the estimated distance $d \sim 5.6$ kpc.

Our ISM analysis could not constraint the distance of the PWN HESS J1303–631 as the CO(1–0) morphologies at all velocity range do not appear to support the PWN scenario. We however found at $v_{\text{lsr}} = -22$ to -15 km/s a CO dip spatially coincident with the SNR candidate found by [Sushch et al. \(2015\)](#), inferring a distance $d \sim 8$ kpc. Several molecular clouds coincident with HESS J1303–631, notably a possible molecular shell at $d \sim 5.0$ kpc spatially coincident with the newly found SNR.

Although CO(1–0) emission north of the SNR G284.3–1.8 towards HESS J1018–589 has been found at $d \sim 2.8$ kpc, only a few CS clumps have been found at the pulsar PSR J1019–5857 dispersion measure distance, suggesting a atomic dominated ISM surrounding HESS J1018–589B. An extension of high resolution HI survey would shed more light concerning this TeV source.

Acknowledgments

The Mopra radio telescope is part of the Australia Telescope National Facility which is funded by the Australian Government for operation as a National Facility managed by CSIRO. Operations support was provided by the University of New South Wales and the University of Adelaide. The University of New South Wales Digital Filter Bank used for the observations with the Mopra Telescope (the UNSWMOPS) was provided with support from the Australian Research Council (ARC).

REFERENCES

- Abramowski A., et al., 2011, *A&A*, **525**, [A46](#)
 Abramowski A., et al., 2012a, *A&A*, **541**, [A5](#)
 Abramowski A., et al., 2012b, *A&A*, **548**, [A46](#)
 Abramowski A., et al., 2015, *A&A*, **577**, [A131](#)
 Acero F., et al., 2013, *ApJ*, **773**, [77](#)
 Aharonian F. A., 1991, *Ap&SS*, **180**, [305](#)
 Aharonian F. A., Atayan A. M., 1996, *A&A*, **309**, [917](#)
 Aharonian F., et al., 2005, *A&A*, **439**, [1013](#)
 Aharonian F., et al., 2007a, *A&A*, **467**, [1075](#)
 Aharonian F., et al., 2007b, *A&A*, **472**, [489](#)
 Amato E., 2014, *IJMPS*, **28**, [60160](#)
 Anada T., Bamba A., Ebisawa K., Dotani T., 2010, *PASJ*, **62**, [179](#)
 Bamba A., Ueno M., Koyama K., Yamauchi S., 2003, *ApJ*, **589**, [253](#)
 Benaglia P., Romero G. E., Koribalski B., Pollock A. M. T., 2005, *A&A*, **440**, [743](#)
 Blondin J. M., Chevalier R. A., Frierson D. M., 2001, *ApJ*, **563**, [806](#)
 Bolatto A. D., Wolfire M., Leroy A. K., 2013, *ARA&A*, **51**, [207](#)
 Borkowski K. J., Reynolds S. P., Roberts M. S. E., 2016, *ApJ*, **819**, [160](#)
 Brand J., Blitz L., 1993, *A&A*, **275**, [67](#)
 Brogan C. L., Devine K. E., Lazio T. J., Kassim N. E., Tam C. R., Brisken W. F., Dyer K. K., Roberts M. S. E., 2004, *AJ*, **127**, [355](#)
 Bucciantini N., Arons J., Amato E., 2011, *MNRAS*, **410**, [381](#)
 Camilo F., et al., 2001, *ApJ*, **557**, [L51](#)
 Castelletti G., Giacani E., Petriella A., 2016, preprint, ([arXiv:1601.04962](#))
 Caswell J. L., McClure-Griffiths N. M., Cheung M. C. M., 2004, *MNRAS*, **352**, [1405](#)
 Cordes J., Lazio T., Chatterjee S., Arzoumanian Z., Chernoff D., 2002, in 34th COSPAR Scientific Assembly.
 Crawford F., Gaensler B. M., Kaspi V. M., Manchester R. N., Camilo F., Lyne A. G., Pivovarov M. J., 2001, *ApJ*, **554**, [152](#)
 Crutcher R. M., Wandelt B., Heiles C., Falgarone E., Troland T. H., 2010, *ApJ*, **725**, [466](#)
 Dame T. M., 2007, *ApJ*, **665**, [L163](#)
 Deil C., Brun F., Carrigan S., Chaves R., Donath A., Gast H., Marandon V., Terrier R., 2015, in 34th International Cosmic Ray Conference (ICRC 2015). PoS
 Dickey J. M., Lockman F. J., 1990, *ARA&A*, **28**, [215](#)
 Djannati-Ataï A., 2009, HESS discovery of VHE gamma-ray emission from a remarkable young composite SNR, <http://cxc.harvard.edu/cdo/snr09/pres/Djannati>
 Fukui Y., et al., 2009, *PASJ*, **61**, [L23](#)
 Furukawa N., Dawson J. R., Ohama A., Kawamura A., Mizuno N., Onishi T., Fukui Y., 2009, *ApJ*, **696**, [L115](#)
 Furukawa N., et al., 2014, *ApJ*, **781**, [70](#)
 Gabici S., Aharonian F. A., Blasi P., 2007, *Ap&SS*, **309**, [365](#)
 Gallant Y. A., Arons J., 1994, *ApJ*, **435**, [230](#)
 Ginzburg V. L., Syrovatskii S. I., 1964, The Origin of Cosmic Rays
 Gonzalez M., Safi-Harb S., 2005, *ApJ*, **619**, [856](#)
 GUSDORF A., Cabrit S., Flower D. R., Pineau Des Forêts G., 2008, *A&A*, **482**, [809](#)
 Hawkes J., et al., 2014, *IJMPS*, **28**, [1460198](#)
 Ivanov M. M., Pshirkov M. S., Rubtsov G. I., 2016, preprint, ([arXiv:1606.01480](#))
 Kargaltsev O., Rangelov B., Pavlov G. G., 2013, preprint, ([arXiv:1305.2552](#))
 Kishishita T., Bamba A., Uchiyama Y., Tanaka Y., Takahashi T., 2012, *ApJ*, **750**, [162](#)
 McClure-Griffiths N. M., Dickey J. M., Gaensler B. M., Green A. J., Haverkorn M., Strasser S., 2005, *ApJS*, **158**, [178](#)
 McClure-Griffiths N. M., et al., 2009, *ApJS*, **181**, [398](#)

Mizuno A., Fukui Y., 2004, in Clemens D., Shah R., Brainerd T., eds, *Astronomical Society of the Pacific Conference Series* Vol. 317, *Milky Way Surveys: The Structure and Evolution of our Galaxy*. p. 59

Nava L., Gabici S., 2013, *MNRAS*, **429**, 1643

Nava L., Gabici S., Marcowith A., Morlino G., Ptuskin V. S., 2016, *MNRAS*, **461**, 3552

Ng C.-Y., Roberts M. S. E., Romani R. W., 2005, *ApJ*, **627**, 904

Parsons R. D., Hinton J. A., 2014, *Astroparticle Physics*, **56**, 26

Parsons H., Thompson M. A., Chrysostomou A., 2009, *MNRAS*, **399**, 1506

Pinheiro Gonçalves D., Noriega-Crespo A., Paladini R., Martin P. G., Carey S. J., 2011, *AJ*, **142**, 47

Pivovarov M. J., Kaspi V. M., Camilo F., Gaensler B. M., Crawford F., 2001, *ApJ*, **554**, 161

Ray P. S., et al., 2011, *ApJS*, **194**, 17

Reynolds S. P., 2008, *ARA&A*, **46**, 89

Roberts M. S. E., Romani R. W., 1998, *ApJ*, **496**, 827

Roberts M. S. E., Brogan C. L., Gaensler B. M., Hessler J. W. T., Ng C.-Y., Romani R. W., 2005, *Ap&SS*, **297**, 93

Ruiz M. T., May J., 1986, *ApJ*, **309**, 667

Safi-Harb S., Kumar H. S., 2008, *ApJ*, **684**, 532

Schilke P., Walmsley C. M., Pineau des Forets G., Flower D. R., 1997, *A&A*, **321**, 293

Sushch I., Oya I., Schwanke U., Johnston S., Dalton M., 2015, preprint, ([arXiv:1509.01427](https://arxiv.org/abs/1509.01427))

Taylor J. H., Cordes J. M., 1993, *ApJ*, **411**, 674

Torii K., Tsunemi H., Dotani T., Mitsuda K., Kawai N., Kinugasa K., Saito Y., Shibata S., 1999, *ApJ*, **523**, L69

Urquhart J. S., et al., 2010, *PASA*, **27**, 321

Voisin F., Rowell G., Burton M. G., Walsh A., Fukui Y., Aharonian F., 2016, *MNRAS*, **458**, 2813

Weaver R., McCray R., Castor J., Shapiro P., Moore R., 1977, *ApJ*, **218**, 377

Zinchenko I., Forsstroem V., Lapinov A., Mattila K., 1994, *A&A*, **288**, 601

A Fit parameters

B Physical parameters

B.1 CS(1-0)

The averaged optical depth $\tau_{CS(1-0)}$ can be derived using the integrated intensity ratio $W_{CS(1-0)}$ and $W_{C^{34}S(1-0)}$ via :

$$\frac{W_{CS(1-0)}}{W_{C^{34}S(1-0)}} = \frac{1 - e^{-\tau_{CS(1-0)}}}{1 - e^{-\alpha\tau_{CS(1-0)}}} \quad (\text{B.1})$$

where $\alpha = [^{32}\text{S}]/[^{34}\text{S}] = 22$ represent the abundance ratio between the two isotopologues based on terrestrial measurements. We obtain the column density of the upper state

N_{CS_1} .

$$N_{CS_1} = \frac{8k\pi\nu_{10}^2}{A_{10}hc^3} \left(\frac{\Delta\Omega_A}{\Delta\Omega_S} \right) \left(\frac{\tau_{CS(1-0)}}{1 - e^{-\tau_{CS(1-0)}}} \right) \int T_{mb}(v) dv \quad (\text{B.2})$$

Assuming the gas to be in local thermal equilibrium at temperature T_{kin} , we can thus obtain the total CS column density N_{CS} .

$$N_{CS} = N_{CS_1} \left(1 + \frac{1}{3}e^{2.35/T_{\text{kin}}} + \frac{5}{3}e^{-4.7/T_{\text{kin}}} + \dots \right) \quad (\text{B.3})$$

B.2 Mass and density

$$M_{\text{H}_2} = \mu m_{\text{H}} \pi a b N_{\text{H}_2} \quad (\text{B.4})$$

with $\mu = 2.8$ being the averaged atomic weight (accounting for 20% Helium), m_{H} the hydrogen mass and a, b the semi-minor and semi-major axis of the selected elliptic regions.

$$n_{\text{H}_2} = \frac{M}{4/3(\mu m_{\text{H}}) \pi a b^2} \quad (\text{B.5})$$

B.3 Physical parameters of individual sources

C Column densities and distance studies

D HESS J1809–193 additional figures

D.1 Nanten CO(1–0)

Figure D.1 shows the different CO(1–0) detections shown in the line of sight overlaid by the CS(1–0) detections shown in white contours. We remind that the SNR G011.2–0.3 distance range between $d = 4.4 - 7$ kpc (Borkowski et al. 2016). In order to further constraint its distance, we require to study ISM morphology near SNR G011.2–0.3 between $v_{\text{lsr}} = 40$ to 150 km/s (whose detections are shown in panels a-e). The ISM gas at the velocity range $v_{\text{lsr}} = 40$ to 50 km/s (near/far distance $d \sim 4.6/12.1$ kpc) appears to coincide with the SNR position. The near distance $d \sim 4.6$ kpc is thus a viable candidate for the position of SNR G011.2–0.3.

D.2 HC₃N(5–4,F=4–3) and C³⁴S(1–0)

Table A.1 Position, size and fitting parameters of the emission traced by the tracers CS(1–0), its isotopologue C³⁴S(1–0), CO(1–0) and HC₃N(5–4,F=4–3) towards HESS J1809–193. T_A^* denotes the peak temperature at $v_{lsr} = v_{cent}$, Δv indicates the full width half maximum (FWHM) of a Gaussian fit. W represents the main beam integrated intensity. A main beam efficiency factor η_{mb} (see [Urquhart et al. 2010](#) and text). Finally, the { indicates that two the two components with little velocity separation are physically connected.

Molecular tracer	Region	Position (RA, Dec) (J2000.0)	Area ^a (arcsec ²)	T_A^* (K)	v_{cent} (km/s)	Δv (km/s)	$W = \int T_{mb} dv$ (K km/s)	
Nanten CO(1–0)	1	(272.61°, -19.38°)	819×373	6.5	30.7	8.7	67.6	
	2	(272.36°, -19.71°)	663×437	6.9	31.0	13.6	111.8	
	3	(272.90°, -19.55°)	127×127	7.1	32.0	13.5	114.0	
Mopra CS(1–0)	1	(272.43°, -19.74°)	819×373	0.2	30.2	4.6	2.1	
	1-1	(272.61°, -19.38°)	146×45	0.6	29.4	3.1	4.6	
	1-2	(272.62°, -19.46°)	30×30	0.3	30.0	2.3	1.9	
	1-3	(272.57°, -19.46°)	30×30	0.3	29.5	2.6	2.2	
	1-4	(272.54°, -19.47°)	30×30	0.5	29.1	3.6	4.3	
	2	(272.61°, -19.39°)	663×437	0.2	29.2	3.9	2.0	
	2-1	(272.57°, -19.46°)	30×30	{	0.5	31.5	2.7	3.3
					0.3	31.7	1.1	0.8
	2-2	(272.53°, -19.72°)	30×30	{	0.5	29.4	3.9	4.4
					0.1	31.7	1.2	0.4
	2-3	(272.41°, -19.77°)	30×30	{	0.5	30.8	2.6	3.0
					0.3	28.6	2.2	1.3
	3	(272.76°, -19.61°)	127×127	{	0.1	34.2	3.6	1.3
				0.1	31.3	1.5	0.4	
Mopra C ³⁴ S(1–0) ^a	1-1	(272.61°, -19.38°)	146×45	0.1	30.0	3.7	0.9	
	1-2	(272.62°, -19.46°)	30×30	0.2	30.0	1.2	0.5	
	1-3	(272.57°, -19.46°)	30×30	0.2	29.4	0.8	0.4	
	1-4	(272.54°, -19.47°)	30×30	0.2	29.3	0.8	0.4	
	2-1	(272.57°, -19.46°)	30×30	{	0.2	31.6	1.0	0.4
					0.1	30.1	1.0	0.3
	2-2	(272.53°, -19.72°)	30×30	0.1	30.5	1.6	0.6	
2-3	(272.41°, -19.77°)	30×30	0.2	30.8	1.0	0.4		
Mopra HC ₃ N(5–4,F=4–3)	HC1	(272.69°, -19.27°)	187×60	0.2	31.7	1.8	1.0	
	HC2	(272.61°, -19.38°)	205×67	0.2	29.3	2.1	1.1	
	HC3	(272.53°, -19.46°)	88×88	0.2	29.2	2.1	1.2	
	HC4	(272.49°, -19.74°)	257×214	0.1	29.1	5.1	1.3	

^a:The values represent the semi-major and semi-minor axes respectively.

Table A.2 Position, size and fitting parameters of the emission traced by the tracers CS(1–0) and CO(1–0) towards HESS J1026–582. T_A^* denotes the peak temperature at $v_{\text{lsr}} = v_{\text{cent}}$, Δv indicates the full width half maximum (FWHM) of a Gaussian fit. W represents the main beam integrated intensity using a main beam efficiency factor η_{mb} (see Urquhart et al. 2010 for 7mm tracers).

Molecular tracer	Region	Position (RA, Dec) (J2000.0)	Area ^a (arcsec ²)	T_A^* (K)	v_{cent} (km/s)	Δv (km/s)	$W = \int T_{\text{mb}} dv$ K km/s
Nanten CO(1–0)	A	(157.47°, -58.58°)	1096×1096	1.1	-15.2	4.3	5.7
	B	(156.35°, -58.20°)	773×773	2.3	3.2	4.3	11.9
Mopra CS(1–0)	1	(156.36°, -58.16°)	67×67	0.2	-19.2	1.4	0.6
	2	(156.15°, -58.11°)	59×59	0.2	-16.5	1.4	0.5
	3	(156.80°, -57.80°)	39×39	0.2	13.1	2.1	0.9
	4	(156.66°, -57.79°)	33×33	0.1	12.9	1.1	0.4
	5	(156.57°, -57.89°)	280×280	0.1	11.9	2.0	0.7
	6	(156.46°, -58.11°)	100×100	0.2	1.3	1.8	0.7
	7	(156.49°, -58.20°)	110×110	0.1	2.3	1.5	0.4
	8	(156.34°, -58.24°)	98×98	0.3	3.6	1.6	1.1
	9	(156.90°, -57.82°)	178×178	< 0.1	-1.1	1.5	0.2

^a:The values represent the semi-major and semi-minor axes respectively.

Table A.3 Position, size and fitting parameters of the emission traced by the tracers CS(1–0) and CO(1–0) towards HESS J1119–582. T_A^* denotes the peak temperature at $v_{\text{lsr}} = v_{\text{cent}}$, Δv indicates the full width half maximum (FWHM) of a Gaussian fit. W represents the main beam integrated intensity using the main beam efficiency factor η_{mb} (see Urquhart et al. 2010 for 7mm tracers). Finally, the { indicates that two the two components with little velocity separation are physically connected.

Molecular tracer	Region	Position (RA, Dec) (J2000.0)	Area ^a (arcsec ²)	T_A^* (K)	v_{cent} (km/s)	Δv (km/s)	$W = \int T_{\text{mb}} dv$ (K km/s)
Nanten CO(1–0)	A	(170.20°, -61.35°)	522×522	1.4	-12.3	5.9	9.6
	B	(169.40°, -61.48°)	495×159	0.6	-19.1	5.1	3.8
	C	170.08°, -61.19°)	219×219	{ 1.1	20.4	8.2	4.1
	D	(169.38°, -61.44°)	705×480	{ 1.0	35.1	2.2	1.5
Mopra CS(1–0)				1.7	30.2	4.7	4.4
	1	(169.96°, -61.32°)	30×30	0.2	13.5	0.8	0.4
	2	(169.44°, -61.37°)	30×30	0.2	28.9	1.3	0.6
	3	(169.56°, -61.55°)	30×30	0.3	34.1	1.0	0.6

^a:The values represent the semi-major and semi-minor axes respectively.

Table A.4 Position, size and fitting parameters of the emission traced by the tracers CS(1–0) and CO(1–0) towards HESS J1418–609 and HESS J1420–607. T_A^* denotes the peak temperature at $v_{lsr} = v_{cent}$, Δv indicates the full width half maximum (FWHM) of a Gaussian fit. W represents the main beam integrated intensity using the main beam efficiency factor η_{mb} (see [Urquhart et al. 2010](#) for tracers). Finally, the $\{$ indicates that two the two components with little velocity separation are physically connected.

Molecular tracer	tracer	Regions	Position (RA, Dec) (J2000.0)	Area ^a (arcsec ²)	T_A^* (K)	v_{cent} (km/s)	Δv (km/s)	$W = \int T_{mb} dv$ (K km/s)
Nanten	CO(1–0)	A	(214.47°, -61.11°)	752×411	1.1	-4.8	6.0	7.6
		1	(214.51°, -60.80°)	30×30	0.4	-39.0	1.4	1.3
		2	(214.21°, -60.86°)	30×30	0.2	-56.6	0.8	0.4
		3	(214.12°, -60.99°)	30×30	0.4	-62.4	1.7	1.7
		4	(214.37°, -60.85°)	198×198	0.2	-44.9	1.4	0.5
		5	(215.07°, -60.68°)	124×124	0.2	-46.6	2.2	1.0
Mopra	CS(1–0)	6	(215.07°, -60.84°)	52×52	0.2	-49.7	3.3	1.2
		7	(214.73°, -61.00°)	30×30	0.2	-51.0	1.2	0.8
		8	(214.47°, -61.02°)	70×70	0.2	-47.2	2.4	1.0
		9	(214.21°, -61.14°)	30×30	0.3	-45.1	1.8	1.3
		10	(214.87°, -60.85°)	135.2×135.2	$\left\{ \begin{array}{l} 0.2 \\ 0.2 \end{array} \right.$	$\left\{ \begin{array}{l} -3.3 \\ -5.0 \end{array} \right.$	$\left\{ \begin{array}{l} 1.6 \\ 1.3 \end{array} \right.$	$\left\{ \begin{array}{l} 0.7 \\ 0.5 \end{array} \right.$
		11	(214.22°, -61.06°)	30×30	0.2	-5.5	1.7	0.9
		12	(215.23°, -60.67°)	30×30	0.2	-12.1	1.1	0.4

^a:The values represent the semi-major and semi-minor axes respectively.

Table A.5 Position, size and fitting parameters of the emission traced by the tracer CS(1–0) transition towards HESS J1303–631. T_A^* denotes the peak temperature at $v_{\text{lsr}} = v_{\text{cent}}$, Δv indicates the full width half maximum (FWHM) of a Gaussian fit. W represents the main beam integrated intensity using the main beam efficiency factor η_{mb} (see Urquhart et al. 2010 for 7mm tracers). Finally, the { indicates that two the two components with little velocity separation are physically connected.

Molecular tracer	Region	Position (RA, Dec) (J2000.0)	Area ^a arcsec ²	T_A^* (K)	v_{cent} (km/s)	Δv (km/s)	$W = \int T_{\text{mb}} dv$ K km/s	
Nanten CO(1–0)	A	(195.63°, -63.46°)	512×300	2.8	-30.0	10.3	34.7	
	B	(196.06°, -63.21°)	438×438	3.8	-19.7	7.9	35.6	
	C	(195.89°, -63.18°)	191×191	{	5.6	33.4	5.4	36.6
					1.0	24.7	3.1	3.8
D	(195.18°, -63.145°)	395×395	{	2.2	32.7	7.4	19.4	
				1.6	26.3	4.2	8.2	
Mopra CS(1–0)	1	(195.52°, -63.23°)	65×65	0.2	-30.9	2.1	1.3	
	2	(195.38°, -63.21°)	30×30	0.2	-30.1	0.9	0.5	
	3	(195.61°, -63.18°)	30×30	0.2	-30.0	1.5	0.7	
	4	(195.36°, -62.98°)	30×30	0.2	-19.2	1.7	0.9	
	5	(195.59°, -63.01°)	30×30	0.2	-18.0	0.9	0.5	
	6	(195.37°, -63.10°)	30×30	0.1	-24.6	1.6	0.6	
	7	(195.80°, -63.23°)	30×30	0.3	-23.1	2.4	2.1	
	8	(195.46°, -63.07°)	92×92	0.1	30.7	2.7	0.9	
	9	(195.48°, -62.95°)	47×47	0.2	24.1	3.1	1.5	
	10	(195.20°, -63.14°)	36×36	0.2	25.9	1.6	0.9	

^a:The values represent the semi-major and semi-minor axes respectively.

Table A.6 Position, size and fitting parameters of the emission traced by the tracers CS(1–0) and CO(1–0) towards HESS J1018–589B. T_A^* denotes the peak temperature at $v_{\text{lsr}} = v_{\text{cent}}$, Δv indicates the full width half maximum (FWHM) of a Gaussian fit. W represents the main beam integrated intensity using a main beam efficiency factor η_{mb} (see Urquhart et al. 2010 for 7mm tracers).

Molecular tracer	Region	Position (RA, Dec) (J2000.0)	Area ^a arcsec ²	T_A^* (K)	v_{cent} (km/s)	Δv (km/s)	$W = \int T_{\text{mb}} dv$ K km/s
Nanten CO(1–0)	A	(154.68°, -58.82°)	400×400	0.9	-15.9	12.0	13.8
Mopra CS(1–0)	1	(154.37°, -58.98°)	30×30	0.2	29.4	2.8	1.6
	2	(154.35°, -59.01°)	30×30	0.4	45.4	1.6	1.7
	3	(154.49°, -58.97°)	30×30	0.4	35.2	1.1	1.1

^a:The values represent the semi-major and semi-minor axes respectively.

Table B.1 Physical parameters obtained from our CS and CO analysis from the different selected regions located towards HESS J1809–193. In the case where C³⁴S(1–0) is detected, the derived optical depth $\tau_{\text{CS}(1-0)}$ is shown as superscript next to the CS column density N_{CS} . Otherwise, an optical thin scenario and the derived column densities N_{H_2} and N_{CS} , mass $M_{\text{H}_2}(\text{CS})$ and H₂ averaged density $n_{\text{H}_2}(\text{CS})$ act as lower limits.

HESS J1809–193					
Reg.	Distance (kpc)	$N_{\text{CS}} [10^{12}]^a$ (cm ⁻²)	CS(1–0)	$M_{\text{H}_2}(\text{CS})^{abc}$ (M _⊙)	$n_{\text{H}_2}(\text{CS})^{abc}$ (cm ⁻³)
			$N_{\text{H}_2} [10^{20}]^{ab}$ (cm ⁻²)		
1	3.6	20	52	3.2×10^4	1.7×10^2
1-1	3.6	210 ⁽⁴⁾	520	7.5×10^3	4.8×10^3
1-2	3.6	270 ⁽⁷⁾	670	1.3×10^3	3.2×10^4
1-3	3.6	180 ⁽⁴⁾	460	6.0×10^3	2.2×10^4
1-4	3.6	190 ⁽²⁾	460	9.0×10^4	2.2×10^4
2	3.6	13	33	1.2×10^4	1.9×10^2
2-1	3.6	380 ⁽⁵⁾	950	1.7×10^3	4.4×10^4
2-2	3.6	290 ⁽³⁾	720	1.3×10^3	3.3×10^4
2-3	3.6	200 ⁽²⁾	510	1.0×10^3	2.3×10^4
3	3.6	15	30	5.3×10^3	2.6×10^2

CO(1–0)			
Reg.	Distance (kpc)	$M_{\text{H}_2}(\text{CO})^{cd}$ (M _⊙)	$n_{\text{H}_2}(\text{CO})^{cd}$ (cm ⁻³)
1	3.6	8.1×10^4	4.4×10^2
2	3.6	2.3×10^5	1.7×10^2
3	2.5	4.3×10^4	1.1×10^3

^a:Parameters have been derived using the LTE assumption.

^b:The H₂ physical parameters derived using a CS abundance ratio $\chi_{\text{CS}} = 4 \times 10^{-9}$

^c:A prolate geometry have been used in order to derive the mass and density.

^d:The $X_{\text{CO}} = 2.0 \times 10^{20} \text{ cm}^{-2}/(\text{K km/s})$ have been used to convert the integrated intensity W_{CO} into H₂ column density N_{H_2}

Table B.2 Physical parameters obtained from our CS and CO analysis from the different selected regions located towards HESS J1026–582. In the case of our CS analysis, we assumed a optically thin scenario and the derived column densities N_{H_2} and N_{CS} , mass M_{H_2} (CS) and H_2 averaged density n_{H_2} (CS) act as lower limits.

HESS J1026–582					
Reg.	Distance (kpc)	$N_{\text{CS}} [10^{12}]^a$ (cm^{-2})	CS(1–0)		
			$N_{\text{H}_2} [10^{20}]^{ab}$ (cm^{-2})	$M_{\text{H}_2}(\text{CS})^{abc}$ (M_{\odot})	$n_{\text{H}_2}(\text{CS})^{abc}$ (cm^{-3})
1	2.1	7	17	4.9×10^1	6.3×10^2
2	2.1	6	14	3.0×10^1	5.9×10^2
3	6.1	19	47	2.6×10^2	1.3×10^3
4	6.1	7	18	1.0×10^2	5.0×10^2
5	6.1	7	18	1.0×10^4	5.2×10^1
6	4.9	7	18	7.0×10^2	1.9×10^2
7	4.9	4	10	4.2×10^2	1.0×10^2
8	4.9	11	28	1.0×10^3	3.0×10^2
CO(1–0)					
Reg.	Distance (kpc)	$M_{\text{H}_2}(\text{CO})^{cd}$ (M_{\odot})	$n_{\text{H}_2}(\text{CO})^{cd}$ (cm^{-3})		
A	2.1	9.7×10^3	2.5×10^1		
B	4.9	5.4×10^4	3.2×10^1		

^a:Parameters have been derived using the LTE assumption.

^b:The H_2 physical parameters derived using a CS abundance ratio $\chi_{\text{CS}} = 4 \times 10^{-9}$

^c:A prolate geometry have been used in order to derive the mass and density.

^d:The $X_{\text{CO}} = 2.0 \times 10^{20} \text{ cm}^{-2}/(\text{K km/s})$ have been used to convert the integrated intensity W_{CO} into H_2 column density N_{H_2}

Table B.3 Physical parameters obtained from our CS and CO analysis from the different selected regions located towards HESS J1119–582. In the case of our CS analysis, we assumed a optically thin scenario and the derived column densities N_{H_2} and N_{CS} , mass M_{H_2} (CS) and H_2 averaged density n_{H_2} (CS) act as lower limits.

HESS J1119–582					
Reg.	Distance (kpc)	$N_{\text{CS}} [10^{12}]^a$ (cm^{-2})	CS(1–0)		
			$N_{\text{H}_2} [10^{20}]^{ab}$ (cm^{-2})	$M_{\text{H}_2}(\text{CS})^{abc}$ (M_{\odot})	$n_{\text{H}_2}(\text{CS})^{abc}$ (cm^{-3})
1	8.0	7	17	8.0×10^1	3.5×10^2
2	9.4	11	27	1.7×10^2	4.8×10^2
3	10.0	12	31	2.3×10^2	5.2×10^2
CO(1–0)					
Reg.	Distance (kpc)	$M_{\text{H}_2}(\text{CO})^{cd}$ (M_{\odot})	$n_{\text{H}_2}(\text{CO})^{cd}$ (cm^{-3})		
A	5.0	2.2×10^4	5.0×10^1		
B	4.2	7.1×10^3	5.0×10^1		
C	8.6	1.3×10^4	6.1×10^1		
D	9.7	1.3×10^5	1.4×10^1		

^a:Parameters have been derived using the LTE assumption.

^b:The H_2 physical parameters derived using a CS abundance ratio $\chi_{\text{CS}} = 4 \times 10^{-9}$

^c:A prolate geometry have been used in order to derive the mass and density.

^d:The $X_{\text{CO}} = 2.0 \times 10^{20} \text{ cm}^{-2}/(\text{K km/s})$ have been used to convert the integrated intensity W_{CO} into H_2 column density N_{H_2}

Table B.4 Physical parameters obtained from our CS and CO analysis from the different selected regions located towards HESS J1026–631. In the case of our CS analysis, we assumed an optically thin scenario and the derived column densities N_{H_2} and N_{CS} , mass $M_{\text{H}_2}(\text{CS})$ and H_2 averaged density $n_{\text{H}_2}(\text{CS})$ act as lower limits.

HESS J1303–631					
Reg.	Distance (kpc)	$N_{\text{CS}} [10^{12}]^a$ (cm^{-2})	CS(1–0)		
			$N_{\text{H}_2} [10^{20}]^{ab}$ (cm^{-2})	$M_{\text{H}_2}(\text{CS})^{abc}$ (M_{\odot})	$n_{\text{H}_2}(\text{CS})^{abc}$ (cm^{-3})
1	6.7	13	33	5.5×10^2	3.6×10^2
2	6.7	9	23	8.0×10^1	5.5×10^2
3	6.7	13	31	1.1×10^2	7.5×10^2
4	8.0	10	25	1.1×10^2	5.3×10^2
5	8.0	11	28	1.3×10^2	5.9×10^2
6	8.0	17	43	2.0×10^2	9.0×10^2
7	8.0	24	59	7.5×10^2	7.4×10^2
8	12	9	22	2.3×10^3	9.7×10^1
9	12	19	48	1.3×10^3	4.1×10^2
10	12	18	44	5.0×10^2	6.0×10^2

CO(1–0)			
Reg.	Distance (kpc)	$M_{\text{H}_2}(\text{CO})^{cd}$ (M_{\odot})	$n_{\text{H}_2}(\text{CO})^{cd}$ (cm^{-3})
A	2.5	1.0×10^4	4.8×10^2
B	8.1	1.4×10^5	1.0×10^2
C	12.6	6.8×10^4	1.8×10^2
D	12.6	2.2×10^5	5.4×10^1

^a:Parameters have been derived using the LTE assumption.

^b:The H_2 physical parameters derived using a CS abundance ratio $\chi_{\text{CS}} = 4 \times 10^{-9}$

^c:A prolate geometry have been used in order to derive the mass and density.

Table B.5 Physical parameters obtained from our CS and CO analysis from the different selected regions located towards HESS J1420-607 and HESS J1418-609. In the case of our CS analysis, we assumed a optically thin scenario and the derived column densities N_{H_2} and N_{CS} , mass M_{H_2} (CS) and H_2 averaged density n_{H_2} (CS) act as lower limits.

HESS J1420-607+HESS J1418-609					
Reg.	Distance (kpc)	$N_{\text{CS}} [10^{12}]^a$ (cm^{-2})	CS(1-0) $N_{\text{H}_2} [10^{20}]^{ab}$ (cm^{-2})	M_{H_2} (CS) ^{abc} (M_{\odot})	n_{H_2} (CS) ^{abc} (cm^{-3})
1	5.5	25	63	1.4×10^2	1.9×10^3
2	5.5	8	21	4.6×10^1	6.3×10^2
3	5.5	33	84	1.9×10^2	2.6×10^3
4	9.0	6	14	2.6×10^3	4.4×10^1
5	9.0	10	25	1.0×10^3	1.2×10^2
6	9.0	14	36	5.0×10^2	4.3×10^2
7	9.0	13	34	1.1×10^2	7.2×10^2
8	9.0	11	42	7.0×10^2	2.4×10^2
9	10.5	26	64	2.1×10^2	1.3×10^3
10	10.5	12	21	6.0×10^3	1.0×10^2
11	10.5	23	56	5.5×10^2	8.2×10^2
12	10.5	9	23	2.3×10^2	3.4×10^2

CO(1-0)			
Reg.	Distance (kpc)	M_{H_2} (CO) ^{cd} (M_{\odot})	$n_{\text{H}_2}^{cd}$ (cm^{-3})
A	10.5	9.4×10^4	1.6×10^1

^a:Parameters have been derived using the LTE assumption.

^b:The H_2 physical parameters derived using a CS abundance ratio $\chi_{\text{CS}} = 4 \times 10^{-9}$

^c:A prolate geometry have been used in order to derive the mass and density.

^d:The $X_{\text{CO}} = 2.0 \times 10^{20} \text{ cm}^{-2}/(\text{K km/s})$ have been used to convert the integrated intensity W_{CO} into H_2 column density N_{H_2}

Table B.6 Physical parameters obtained from our CS and CO analysis from the different selected regions located towards HESS J1018-589B. In the case of our CS analysis, we assumed a optically thin scenario and the derived column densities N_{H_2} and N_{CS} , mass M_{H_2} (CS) and H_2 averaged density n_{H_2} (CS) act as lower limits.

HESS J1018-589B					
Reg.	Distance (kpc)	$N_{\text{CS}} [10^{12}]^a$ (cm^{-2})	CS(1-0) $N_{\text{H}_2} [10^{20}]^{ab}$ (cm^{-2})	M_{H_2} (CS) ^{abc} (M_{\odot})	n_{H_2} (CS) ^{abc} (cm^{-3})
1	8.0	33	82	3.8×10^2	1.7×10^3
2	9.6	33	83	5.5×10^2	1.4×10^3
3	8.0	22	54	2.5×10^2	1.1×10^3

CO(1-0)			
Reg.	Distance (kpc)	M_{H_2} (CO) ^{cd} (M_{\odot})	n_{H_2} (CO) ^{cd} (cm^{-3})
A	2.0	2.9×10^3	175

^a:Parameters have been derived using the LTE assumption.

^b:The H_2 physical parameters derived using a CS abundance ratio $\chi_{\text{CS}} = 4 \times 10^{-9}$

^c:A prolate geometry have been used in order to derive the mass and density.

^d:The $X_{\text{CO}} = 2.0 \times 10^{20} \text{ cm}^{-2}/(\text{K km/s})$ have been used to convert the integrated intensity W_{CO} into H_2 column density N_{H_2}

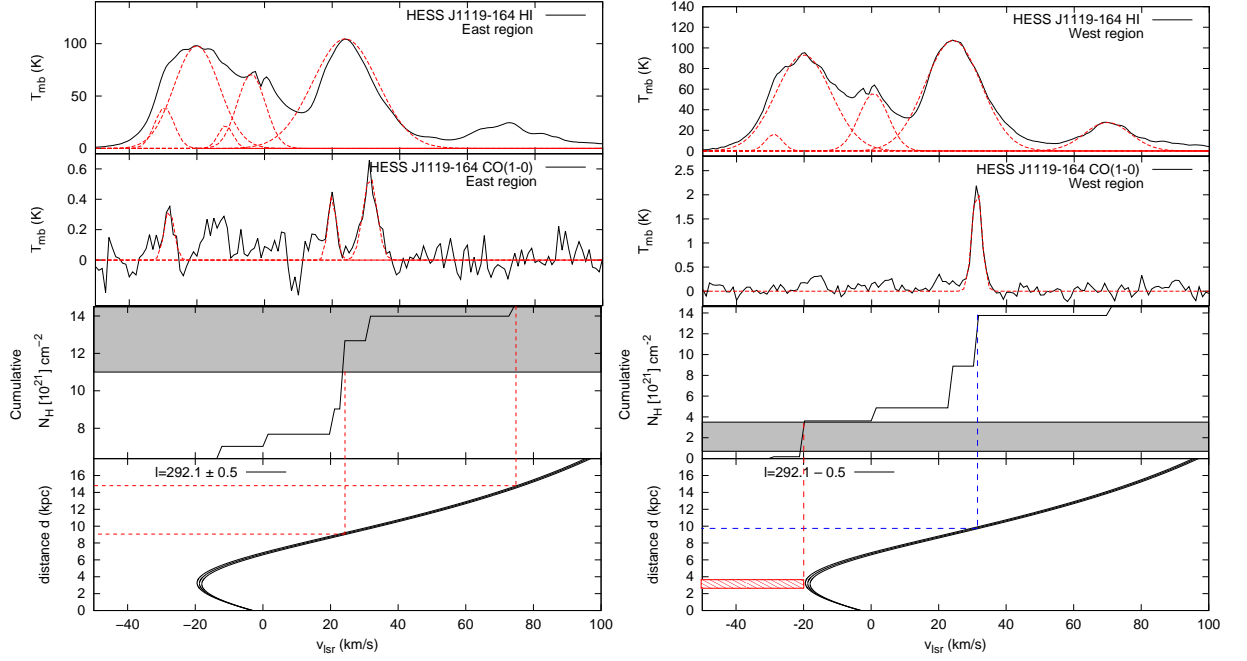


Figure C.1. Averaged SGPS (*first panels*) and Nanten CO(1–0) emission (*second panels*) towards the region ‘A’ (*left*) and the western part of the SNR (*right*) (see Figure 7). The different Gaussian fits are shown as red dashed lines. At each Gaussian peaks, the HI and CO(1–0) emission have been integrated and converted into column density, N_{H} (*third panel*), via the X_{CO} and the X_{HI} factors (see text). Here, all emission are assumed to be in the far distance. The grey regions show the X-ray absorbed column density range obtained by Pivovarov et al. (2001). The *fourth panels* indicate the Galactic rotation curve towards the position (RA, Dec)=(291.1 \pm 0.5, –0.3) with the red dashed lines delimiting the distance where our column densities match with the X-ray column densities while the blue dashed line indicates the distance where the column density in the western region roughly equals the column density in the eastern region.

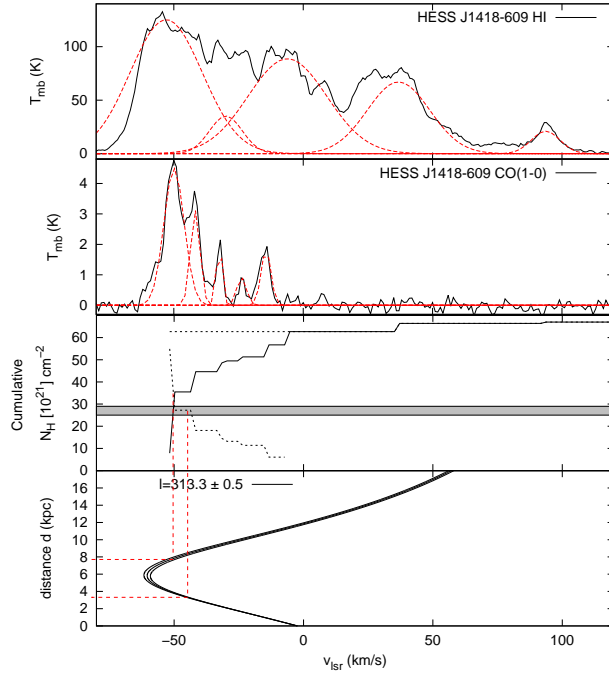


Figure C.2. Averaged SGPS HI and Nanten CO(1–0) emission towards HESS J1418–609 (see Fig. 9) in black solid lines. In both panels, the Gaussian fits are shown as red dashed lines. At each Gaussian peaks, the HI and CO(1–0) emission have been integrated and converted into N_{H} column density via the X_{CO} and X_{HI} respectively (see text). The bottom panel indicates the evolution of the distance towards the position ($313 \pm 0.5, 0.1$) as a function of kinematic velocity.

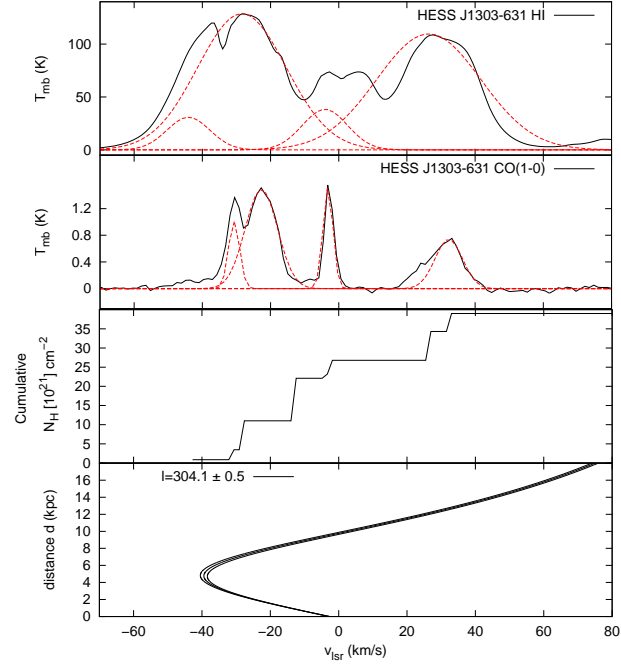


Figure C.3. Averaged SGPS HI and Nanten CO(1–0) emission towards HESS J1303–631 (see Fig. 11) in black solid lines. In both panels, the Gaussian fits are shown as red dashed lines. At each Gaussian peaks, the HI and CO(1–0) emission have been integrated and converted into N_{H} column density via the X_{CO} and X_{HI} respectively (see text). The bottom panel indicates the evolution of the distance towards the position ($301 \pm 0.5, -0.1$) as a function of kinematic velocity.

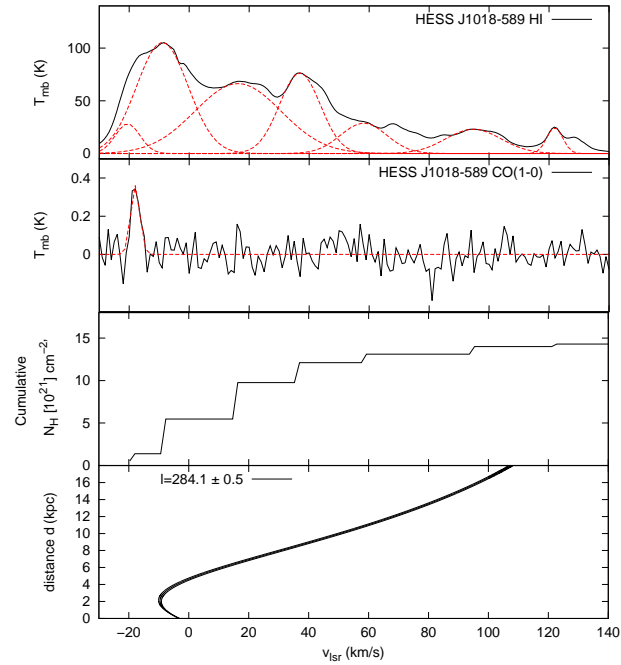


Figure C.4. Averaged G.A.S.S HI and Nanten CO(1–0) emission towards HESS J1018–589 (see Fig. 14) in black solid lines. In both panels, the Gaussian fits are shown as red dashed lines. At each Gaussian peaks, the HI and CO(1–0) emission have been integrated and converted into N_{H} cumulative column density via the X_{CO} and X_{HI} respectively (see text). The bottom panel indicates the kinematic distance towards the position (RA, Dec)=($284 \pm 0.5, -1.7$) as a function of kinematic velocity v_{lsr} .

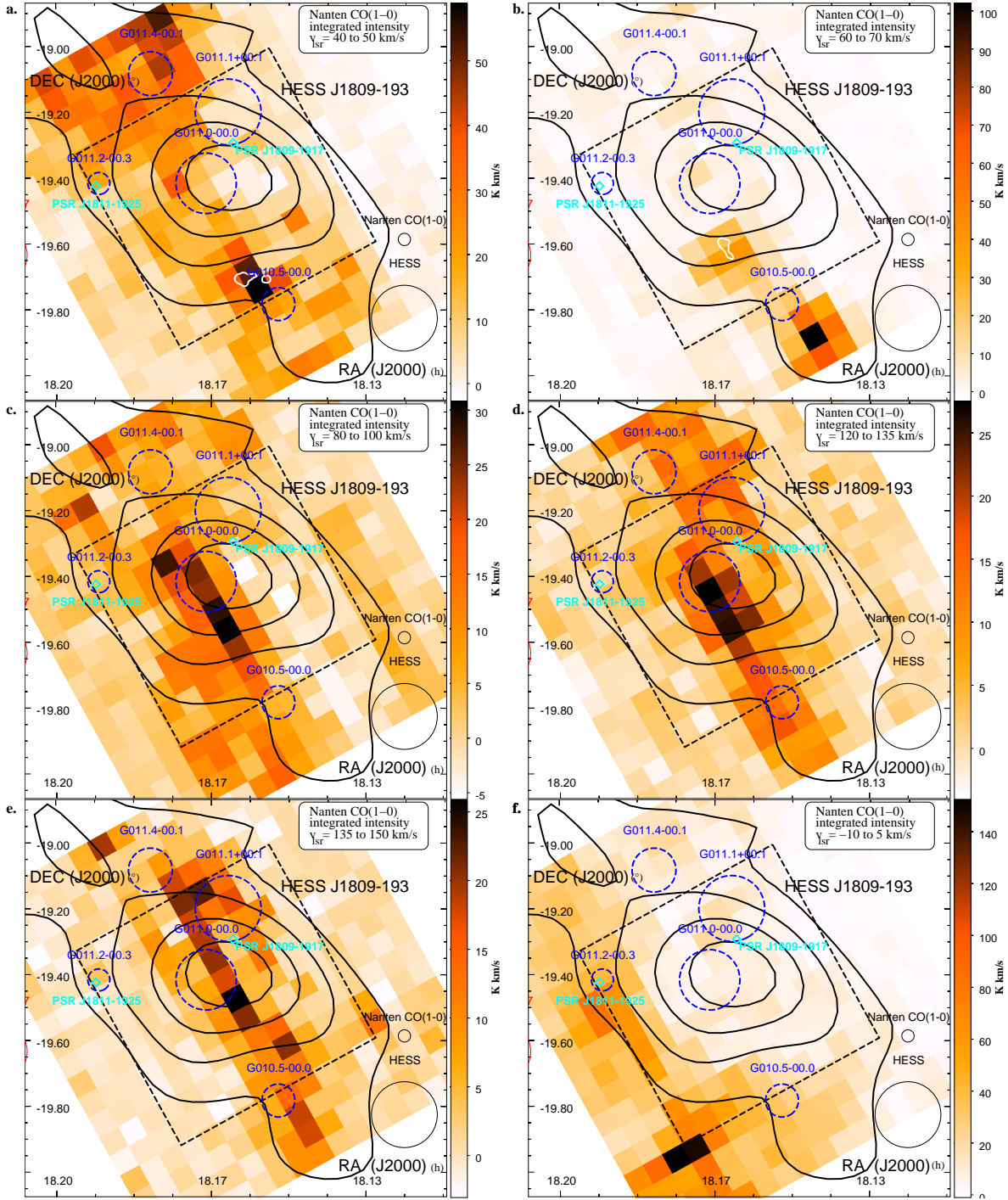


Figure D.1. Nanten CO(1-0) integrated intensity maps towards HESS J1809-193 across the velocity bands $v_{lsr} = 40$ to 50 km/s (near/far distance $d \sim 4.6/12.1$ kpc), 60 to 70 km/s (near/far distance $d \sim 5.4/11.2$ kpc), 80 to 100 km/s (near/far distance $d \sim 6.2/10.4$ kpc), 120 to 135 km/s (near/far distance $d \sim 7.2/9.5$ kpc), 135 to 150 km/s (near/far distance $d \sim 7.9/9.1$ kpc), -10 to 5 km/s (distance $d \sim 17.0$ kpc) overlaid by the CS(1-0) integrated intensity emission shown in white contours. The dashed black box represents the area covered during our 7mm survey. The SNRs are shown in blue solid circles while the pulsars are illustrated as blue diamonds.

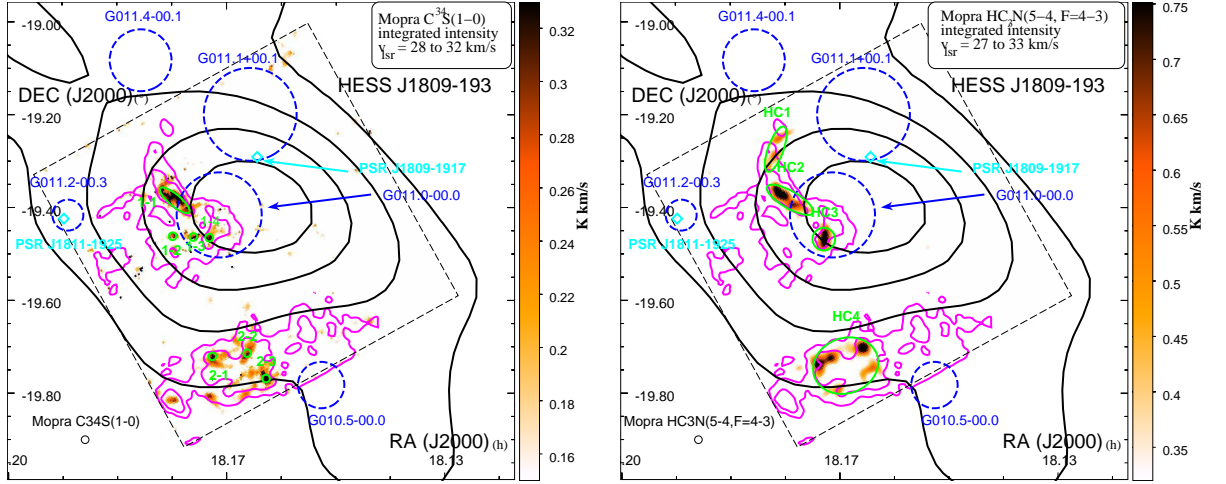


Figure D.2. Mopra $C^{34}S(1-0)$ (Left panel) and $HC_3N(5-4, F=4-3)$ (right panel) integrated intensity between $v_{lsr} = 28$ to 32 km/s and $v_{lsr} = 27$ to 32 km/s respectively towards HESS J1809-193. The various $C^{34}S$ detections labeled '1-1 to 1-4' and '2-1 to 2-3' (left panel) and the HC_3N detections labeled 'HC1 to HC4' are shown in green ellipses. In both panels, the $CS(1-0)$ integrated intensity between $v_{lsr} = 25$ to 38 km/s are shown in purple. The SNRs are shown as dashed blue circles while the position of the pulsars PSR J1809-1917 and PSR J1811-1925.

Chapter 8

Summary and Future Works

This thesis tackled one of the most important questions in high energy astrophysics : are pulsar wind nebulae (PWNe) capable to accelerate high energy cosmic-rays (proton and nuclei) to very high energies. Answering this question would provide constraints on the particle composition inside PWNe as well as the mechanisms of particle acceleration in the pulsar environment. One main method to detect cosmic-rays is to search for TeV gamma-ray emission produced from the interaction between cosmic-rays and the surrounding target materials. On one hand, both the low particle density inside PWNe and the overlapping TeV gamma-ray emission produced by high energy electrons up-scattering soft photons via inverse-Compton, make such a direct approach impossible. On the other hand, the presence of dense molecular gas, with sufficient target materials, could in principle, highlight the presence of cosmic-rays that escaped the PWNe. In this thesis, I have thus investigated how the inhomogeneous ISM could affect the morphological properties of the TeV emission produced by both cosmic-rays and high energy electrons as they the PWN and its progenitor supernova remnants (SNR).

Searching for physical associations between PWNe and nearby molecular clouds was thus the mandatory first step to test this hypothesis. To do so, I combined the SGPS HI and Nanten CO(1–0) surveys, tracing both the atomic and molecular gas, with our recent Mopra observations, which probes dense molecular gas (CS and NH₃ tracers), as well as star forming regions (traced by e.g CH₃OH, recombination lines, HC₃N), and shocked gas (traced by SiO). This thesis first focused on the gas study towards TeV source HESS J1826–130, located north to the TeV source PWN HESS J1825–137, powered by the ~ 40 kyr old pulsar PSR J1826–1334. The PWN G018.5–0.4, powered by the radio-quiet pulsar PSR J1826–1256, is spatially coincident to the TeV source, and is consequently one suitable candidate to explain the origin of the HESS J1826–130 TeV emission. However, our gas studies have revealed the presence of dense and turbulent molecular clouds overlapping HESS J1826–130, located at a pulsar PSR J1826–1334 dispersion measure distance $d \sim 4$ kpc. I have notably shown that, inside this molecular complex, the required cosmic-ray energy density in this molecular complex to significantly contribute to the TeV emission towards HESS J1826–130 could be achieved by the progenitor SNR of PSR J1826–1334. Finally, based on the morphology of the gas distribution, I have finally argued an association between the PWN G018.5–0.4 and the surrounding molecular gas at a far distance $d \sim 11.4$ kpc, thus leaving the question about the origin of HESS J1826–130 open.

This region thus appeared to be a suitable candidate to test how the molecular gas would shape the TeV emission as the high energy electrons and cosmic-rays, escaping both the PWN HESS J1825–137 and its progenitor SNR, propagate inside these molecular clouds, and test whether I could isolate the

TeV emission produced by CRs escaping the PWN HESS J1825–137 from the one produced by CRs escaping the progenitor SNR. To quantify the possible contribution of the CRs/high energy electrons from the PWN and its progenitor SNR to the observed photon flux towards HESS J1826–130, I have built a numerical code, which models the morphology and photon spectral energy distribution (SED), based on the diffusion properties of CRs/high energy electrons in the ISM, and accounting for all radiative energy losses. This code notably uses a template 3D description of the ISM, based on our aforementioned gas studies, to predict the TeV gamma-ray morphology as accurately as possible for any given scenarios. After the calculating the spatial and energy distribution of CRs and high energy electrons, the numerical code outputs the morphology of the TeV emission as would be seen by the upcoming ground based gamma-ray observatory CTA, whose sensitivity is expected to be ten times better than HESS and whose angular resolution would match that of our Mopra surveys.

In chapter 6, I have thus modelled the hadronic and leptonic TeV emission produced by the PWN HESS J1825–137 and explored various scenarios (e.g slow and fast diffusion, shift of the molecular cloud in the line of sight). I have found that only a slow diffusion ($D(E) = 10^{26} \sqrt{E/10 \text{ GeV}} \text{ cm}^2 \text{ s}^{-1}$) of cosmic-rays escaping the SNR would result in a significant contribution of the hadronic TeV emission from HESS 1825–137 towards HESS J1826–130. I have also highlighted that high energy electrons from both the PWN HESS J1825–137 and its progenitor SNR are not expected to contribute to the aforementioned TeV source due to the spectral steepening of the TeV gamma-ray emission caused by severe energy losses from synchrotron radiation. The results have finally shown that potential CRs escaping the PWN HESS J1825–137 would not be detected as its resulting hadronic TeV component is considerably lower compared to the one produced by CRs escaping the SNR. However, as PWNe and SNRs can be considered as a continuous and impulsive injector respectively (for a system age greater than $\sim 10^4$ yr), these results indicate that older PWNe, powered by powerful pulsar, may offer better chances for the detection of CRs escaping PWNe.

Thus, in an effort to find more suitable candidates, gas studies were also conducted towards seven other TeV sources thought to be PWN candidates. Among these TeV sources, HESS J1809–193 has appeared to be a viable region for future work. Indeed, I have discovered the presence of a shocked molecular cloud matching the pulsar PSR J1809–1917 kinematic distance, and showing good spatial correspondence with the SNR G011.0–0.0, which may thus suggest SNR-MC interaction. If the molecular cloud was indeed physically associated with the progenitor SNR of the pulsar PSR J1809–1917, I have derived that, inside this molecular cloud, the required CR energy density to contribute to the TeV emission could be achieved by both the PWN powered by the aforementioned pulsar, and its progenitor SNR. As the pulsar PSR J1809–1917 characteristic age is ~ 2.5 times higher than that of PSR J1826–1334, I have argued that HESS J1809–193 may be another laboratory to test with our numerical code, the presence of CRs inside the PWN.

8.1 Future work

8.1.1 Upgrading the numerical code

In its current form, the numerical code outputs FITS cube showing the gamma-ray distribution as a function of position and energy. I have demonstrated that such numerical code can be useful to discriminate leptonic from hadronic gamma-ray emission. The current limitation of this version is however the fixed spatial resolution which requires large computational time. Indeed, if I increase the grid resolution by a factor of two, the computational time is expected to increase by a factor of $\sim 2^5 = 32$. This method is

also highly inefficient as the distribution of CRs/high energy electrons inside large void regions (i.e no molecular gas) does not need to be as detailed as in clumpy regions. Consequently, I aim to implement an Octree algorithm (see Chapter 6), which will optimize the number of cells and their distribution inside the grid. Notably, this algorithm will produce more accurate results towards complex molecular regions with no drastic cost in computational time. This new algorithm will also enable a much deeper analysis of the variation of the results as I explore through the parameter space, which will be useful to visualize which parameters impact the results the most and provide important constraints on the physical properties of PWNe and their progenitor SNRs.

Another important upcoming upgrade is the modeling the synchrotron X-ray morphology. I have already shown in Chapter 6 that the non thermal radiation produced by high energy electrons were very sensitive to the position of molecular clouds with respect to the PWNe. In order to obtain an accurate model of the X-ray emission, an accurate column density maps would then be required to account for X-ray absorption. Adiabatic losses and a time dependent PWN magnetic field would also have to be implemented, as early high energy electrons are expected to suffer from both, which would eventually affect the resulting X-ray emission for young PWNe.

The current numerical code also assumes an isotropic diffusion of CRs/high energy electrons. However, the magnetic field distribution may affect the directionality of their propagation in the ISM. As a detailed structure of the magnetic field in our Galaxy is to be expected soon (see next section), the implementation of a new algorithm solving the anisotropic, and possibly non-linear, diffusion of CRs/high energy electrons would be the next challenge.

By combing an upgraded version of the numerical code with the sensitivity and angular resolution of CTA, a powerful application of this numerical code would also be to obtain further information about the nature of unidentified TeV sources with several high energy sources close to the TeV peak (e.g see HESS J1809–193 in Chapter 7). By comparing the expected morphology of the TeV gamma-ray emission produced by each source at various energies with the upcoming results from CTA, one could disentangle the contribution of each high energy source.

8.1.2 Towards a more detailed multi wavelength studies

A very accurate description of the ISM surrounding the high energy source is a primary requirement to study the propagation of CRs. In this thesis, I have mostly combined my line emission study with existing X-ray data to search for possible physical association between molecular clouds and progenitor SNRs. However, additional information can be obtained from a more complete multi wavelength analysis. In our gas study towards HESS J1826–130, I have included optical $H\alpha$ surveys in my line emission study, and have found that the SNR $H\alpha$ rim reported by Stupar et al. (2008) might be associated with the progenitor SNR of PSR J1826–1334. This association would notably be consistent with the expected progenitor SNR radius $R_{\text{SNR}} \sim 120 \text{ pc}$ (de Jager & Djannati-Ataï, 2009), and would therefore infer stringent conditions on the ambient density surrounding HESS J1825–137. Including optical observations (e.g from UK Schmidt telescope) could then additional highlight additional clues to find the progenitor SNR of a given pulsar thought to contribute to the TeV emission.

At radio wavelength, the combination between The new HI, OH, Recombination line survey (THOR, Anderson et al. 2017), with the VGPS continuum data, the Spitzer MIPS GAL 24 μm and GLIMPSE 8 μm surveys, have revealed an additional 76 Galactic SNRs candidates. The low frequency images of the Murchison Widefield Array (MWA, Bowman et al. 2013) are also expected to unveil fainter SNRs. As

a consequence, these radio surveys will reduce the discrepancy between the number of pulsar and SNR detections, providing valuable information for our high energy studies.

Finally, the Polarisation Sky Survey of the Universe's Magnetism (POSSUM, Gaensler et al. 2010) with ASKAP aims to provide a 3D view of our Galactic magnetic field, which, in our case, could be used to better model the propagation of CRs in the ISM.

8.1.3 Study of the SNRs in the Large Magellanic Cloud (LMC)

With a high Galactic latitude and a “face-on” orientation, the LMC offers great advantages for the study of the evolution and structure of SNRs and their interaction with the ISM. The recent TeV gamma-ray detections in the LMC with HESS (H.E.S.S. Collaboration et al., 2015), notably towards the core-collapse N132D, are promising news for additional detections at TeV energies by the upcoming CTA. Additionally, Sano et al. (2017) recently reported good spatial correspondence between CO(1–0) emission and X-ray data towards six SNRs, which suggests SNR-MC interaction. Therefore, my numerical code could ultimately be used to model the TeV emission produced by CRs/high energy electrons escaping the SNR and predict which ones could be detected by CTA.

Appendix A

Diffusive shock acceleration

I derive here the energy gain from a test particle crossing the shock and the resulting cosmic-ray differential flux resulting from the first-order Fermi acceleration. In our scenario, I make the following assumptions:

- I assume a test particle which does not change the shock properties
- The flow is perpendicular to the shock.
- The shock is supersonic
- The shock is not relativistic.

Let v_s be the shock speed, v_d the speed of the *shocked* flow downstream and v_u the speed of the *unshocked* flow upstream. In the upstream frame S_u , $v_s = U$, $v_u=0$, and therefore $v_d = 3U/4$. Finally, in the downstream frame S_d , $v'_s = U/4$, $v'_d = 0$ and $v'_u = 3U/4$ (see Fig A.1).

Let us start with a particle upstream with energy E_0 , velocity v and angle θ_0 with respect to the shock normal. Using the Lorentz transformation, the energy of the particle in the downstream frame is

$$E'_0 = \gamma_d (E_0 - v_d \bar{p} \cos \theta'_0) \quad (\text{A.1})$$

where \bar{p} is the particle momentum $\bar{p} = \gamma m v$ and γ_d is the downstream flow Lorentz factor. If I assume the particle to be mildly relativistic then $p = E/c$, I obtain :

$$E'_0 = \gamma_d E_0 \left(1 - \frac{v'_d}{c} \cos \theta'_0 \right) \quad (\text{A.2})$$

Let the particle trajectory be deviated, its energy remain the same in the downstream region $E'_1 = E'_0$. The particle then crosses the shock again and I obtain :

$$E'_1 = \gamma_u E_1 \left(1 + \frac{v_u}{c} \cos \theta_1 \right) \quad (\text{A.3})$$

$$E'_1 = \gamma_u \gamma_d E_0 \left(1 + \frac{v_u}{c} \cos \theta_1 \right) \left(1 - \frac{v'_d}{c} \cos \theta'_0 \right) \quad (\text{A.4})$$

The velocity of both frame being the same I can omit the subscript for the Lorentz factor $\gamma = \gamma_u = \gamma_d$, and $v'_d/c = v_u/c = \beta$, Eq. A.4 thus becomes :

$$E'_1 = \gamma^2 E_0 (1 + \beta \cos \theta_1) (1 - \beta \cos \theta'_0) \quad (\text{A.5})$$

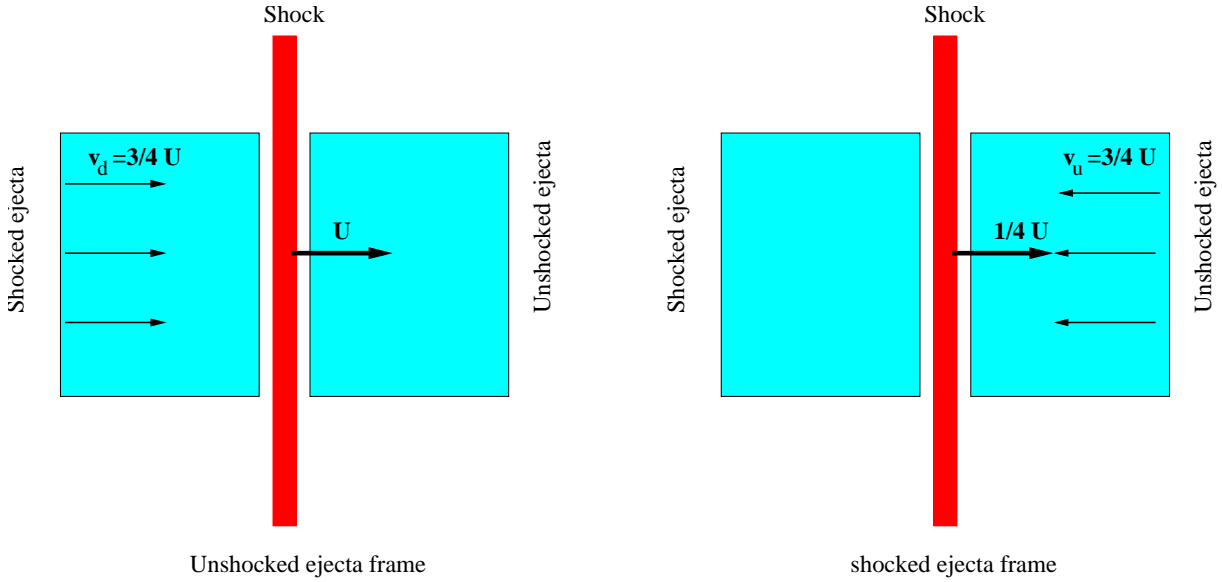


Figure A.1: Sketch illustrating the change of frame in order to obtain the energy gain for a cosmic-ray to cross a strong shock. U represent the shock speed.

Thus, the fraction of energy gain per crossing:

$$\frac{\Delta E}{E_0} = \frac{E_1 - E_0}{E_0} = \gamma (1 + \beta \cos \theta_1) (1 - \beta \cos \theta'_0) - 1 \quad (\text{A.6})$$

$$\frac{\Delta E}{E_0} = \frac{1 + \beta \cos \theta_1 - \beta \cos \theta'_0 - \beta^2 \cos \theta_1 \cos \theta'_0}{1 - \beta^2} - 1 \quad (\text{A.7})$$

Now, the probability $P(\theta)$ for a particle to reach the shock with an angle θ depends on $\cos \theta$. Assuming an isotropic distribution of particles entering the shock, The average angle θ'_0 to which they cross the frame is defined by :

$$\langle \cos \theta'_0 \rangle = \frac{2\pi n v \int_{\pi}^{\pi/2} \cos^2 \theta \sin \theta d\theta}{2\pi n v \int_{\pi}^{\pi/2} \cos \theta \sin \theta d\theta} \quad (\text{A.8})$$

$$\langle \cos \theta'_0 \rangle = \frac{-1/3}{1/2} = -\frac{2}{3} \quad (\text{A.9})$$

I use the same reasoning to determine the average angle at which the cosmic-ray crosses downstream to upstream

$$\langle \cos \theta_1 \rangle = \frac{2\pi n v \int_0^{\pi/2} \cos^2 \theta \sin \theta d\theta}{2\pi n v \int_0^{\pi/2} \cos \theta \sin \theta d\theta} \quad (\text{A.10})$$

$$\langle \cos \theta_1 \rangle = \frac{1/3}{1/2} = \frac{2}{3} \quad (\text{A.11})$$

I can thus determine the average fraction of energy gained per crossing

$$\frac{\langle \Delta E \rangle}{E_0} \sim \frac{4/3\beta + 4/9\beta^2 + \beta^2}{1 - \beta^2} \quad (\text{A.12})$$

As I assumed a non relativistic shock, I deduce the flow speed is non relativistic $\beta \ll 1$, I can neglect the second order term.

$$\frac{\langle \Delta E \rangle}{E_0} \sim \frac{4}{3}\beta = \frac{U}{c} \quad (\text{A.13})$$

Therefore, after crossing the shock twice the test particle increased its initial energy by a factor of U/c . The computation of the differential cosmic-ray spectrum relates to how many times the cosmic-ray crosses the shock before escaping the system. Assuming an isotropic distribution of particle, I can compute the average density of particle crossing the shock :

$$\frac{2\pi}{4\pi} N \int_0^{\pi/2} \cos \theta \sin \theta d\theta = \frac{N}{4} \quad (\text{A.14})$$

Therefore the rate at which the cosmic-rays cross the shock is $\sim Nc/4$. Bell (1978b) also remarked that in the shock frame, particles are removed to downstream at a speed $U/4$ and the rate of loss of particle is therefore $NU/4$. The probability of particles escaping the shock region is therefore U/c . The probability of remaining confined inside the shock is thus $1-U/c$ and after k times $(1 - U/c)^k$. Consequently, the number of particle $N(> k)$ remaining in the shock after k crossing is :

$$\frac{N(> k)}{N_0} = (1 - U/c)^k \quad (\text{A.15})$$

From Eq.A.13, the resulting energy E of a particle, with initial energy E_0 , from crossing the shock k times :

$$\frac{E}{E_0} = \left(1 + \frac{\Delta E}{E}\right)^k \quad (\text{A.16})$$

I now assume that number of particle with energy greater than E follows a power-law $N(> E) \propto E^{-\alpha}$, the spectral index α is then obtained from the following equation :

$$\alpha = \frac{\log(N/N_0)}{\log(E/E_0)} = \frac{\log(1 - U/c)}{\log(1 + U/c)} \sim -1 \quad (\text{A.17})$$

Consequently, I find $N(> E) \propto E^{-1}$. The differential cosmic-ray distribution is therefore $N(E) \sim E^{-2}$.

Appendix B

Probing Non-thermal emission

In this section, I first list the common non-thermal interactions found in dilute gas. I mostly focus on the general properties of these emission on the observed *spectral energy distribution* (SED), and how they could affect the the evolution of the energy distribution of both protons and electrons. If needed, I refer to Blumenthal & Gould (1970) for a detailed review of the leptonic non thermal radiations in dilute gas, and Kelner et al. (2006) and Kafexhiu et al. (2014) for a review of the proton-proton hadronic interaction. My SED modeling code produces photon SED for a given impulsive/continuous source with an arbitrary energy distribution of protons and electrons, accounting for the various radiation losses listed below. I will then compare the results of my SED modeling code with published results.

B.1 Synchrotron radiation

Charged particles (protons or electrons) gyrate around a magnetic field. The resulting frequency of gyration or *cyclotron frequency* is given (in cgs units) by :

$$\omega_{\text{cycl}} = \frac{qB}{mc} \quad (\text{B.1})$$

where q is the charge of the particle and m its mass. If the particle travels with a pitch angle α with respect to the magnetic field, the *cyclotron frequency* is multiplied by $\sin \alpha$.

Another important formula is the Larmor's formula of radiation. The total power radiated by a non relativistic single particle is

$$\frac{dP}{d\Omega} = \frac{q^2 v^2 \sin^2 \theta}{4\pi c^3} \text{ erg str}^{-1} \text{ s}^{-1} \quad (\text{B.2})$$

Consequently, the particle shows dipole radiation pattern where the radiation is maximum for $\theta = \pi/2$, and therefore maximum towards the trajectory of the particle. Integrating over the solid angle gives the total power

$$P = \frac{q^2 \dot{v}^2}{2c^3} \int_{\theta=0}^{\theta=\pi} \sin^3 \theta d\theta \quad (\text{B.3})$$

$$P = \frac{2q^2 \dot{v}^2}{3c^3} \quad (\text{B.4})$$

with q being the charge of the particle, \dot{v} being the averaged acceleration of the particle and c being the speed of light.

For non relativistic gyrating particle , the power radiated is observed at the cyclotron frequency ν_{cycl} . However, for high energy particles, the beaming effects alters the pattern of the previous dipole radiation and the power radiated spreads across the frequency range. The averaged acceleration generated by the particle in its rest frame is

$$\bar{v} = \frac{\gamma q B \sin \alpha}{m} \quad (\text{B.5})$$

Therefore the total power loss becomes :

$$P = \frac{2q^4 \gamma^2 B^2 \sin^2 \alpha}{3m^2 c^3} \quad (\text{B.6})$$

Introducing the Thompson cross section σ_{T} and the magnetic energy density U_{B} :

$$\sigma_{\text{T}} = \frac{8\pi}{3} \left(\frac{q}{mc^2} \right)^2 U_{\text{B}} = \frac{B^2}{8\pi} \quad (\text{B.7})$$

I thus obtain the power loss of a particle via synchrotron radiation :

$$P = -2\sigma_{\text{T}} \gamma^2 c U_{\text{B}} \sin^2 \alpha \quad (\text{B.8})$$

In this thesis, I assume the particle distribution and velocity to be isotropic. Therefore the mean power loss $\langle P \rangle$ is

$$\langle P \rangle = -\frac{4}{3} \sigma_{\text{T}} \gamma^2 c U_{\text{B}} \quad (\text{B.9})$$

I notice here several important points, the energy loss rate is proportional to γ^2 which leads to interesting features regarding the evolution of the energy distribution of particles over time (see chapter 4). The power radiated is very sensitive to the magnetic field strength of the medium. Finally, the efficiency of the synchrotron loss is also dependent on the mass of the particle. Therefore, the synchrotron emission from protons is negligible compared by the one generated by electrons.

The flux produced from synchrotron radiation for isotropic distribution of electron follows this relation :

$$P(\nu) = \frac{\sqrt{3}e^3 B \nu}{mc^2 \nu_c} \int_{x=\nu/\nu_c}^{\infty} K_{5/3}(x) \quad (\text{B.10})$$

$$\nu_c = \frac{3eB\gamma^2}{4\pi mc} \quad (\text{B.11})$$

where $K_{5/3}(x)$ is the modified Bessel function whose value drops when $x > 1$ and ν_c is the critical frequency of the emission dependent on the particle energy. As in Fig B.1, if the cosmic-ray follows a power law distribution $E^{-\alpha}$, the spectral energy distribution (SED) of photons follows :

$$E_{\gamma}^2 \frac{dN}{dE_{\gamma}} = E_{\gamma}^{(3-\alpha)/2} \quad (\text{B.12})$$

The synchrotron radiation spectrum covers from radio to X-rays up and generally illustrates a cutoff at $E_{\gamma} \sim 20 \text{ MeV}$ (de Jager & Djannati-Ataï, 2009) and therefore cannot be observed at VHE γ -ray. However, its importance is crucial as the electrons mostly lose their energy via synchrotron radiations. Therefore, the morphology of the VHE emission becomes greatly affected by the magnetic field. Finally, a simple parametrization enable to estimate the possible photon energy E_X radiated from an electron with energy E_e (Kargaltsev et al., 2013) :

$$E_X = 4 \left(\frac{E_e}{100 \text{ TeV}} \right) \left(\frac{B}{10 \mu\text{G}} \right)^2 \text{ keV} \quad (\text{B.13})$$

B.2 Inverse Compton

The inverse Compton radiation refers to the scattering caused by a *soft* photon and a high energy particle. As opposed to the Compton interaction where the particle gains energy from high energy photons, it is possible to observe VHE γ -ray emission from the interaction between a low energy photon (e.g CMB) and a high energy electron.

In the rest frame of the electron, the particle energy loss depends on the Thompson cross section and the energy density of photons U_{rad}

$$\frac{dE'}{dt} = -\sigma_{\text{T}}cU'_{\text{rad}} \quad (\text{B.14})$$

In the laboratory frame, I assume the photon radiation is isotropic, therefore the energy density in the frame where the particle is at rest is given by:

$$U'_{\text{rad}} = \frac{U_{\text{rad}}}{2} \int_1^{-1} \gamma^2 \left(1 - \frac{v \cos \theta}{c}\right)^2 d(\cos \theta) \quad (\text{B.15})$$

$$U'_{\text{rad}} = \frac{4}{3}U_{\text{rad}} \left(\gamma^2 - \frac{1}{4}\right) \quad (\text{B.16})$$

Combining Eq B.16 with Eq B.14 I obtain :

$$\frac{dE'}{dt}_{\text{loss}} = -\frac{4}{3}\sigma_{\text{T}}cU_{\text{rad}} \left(\gamma^2 - \frac{1}{4}\right) \quad (\text{B.17})$$

By conservation of energy , the energy *gained* by the incident photon are also given by Eq B.17. The energy loss by photon due to scattering being $\sigma_{\text{T}}cU_{\text{rad}}$, the net energy gained by a photon per collision is :

$$\frac{dE}{dt} = \frac{4}{3}\sigma_{\text{T}}cU_{\text{rad}} \left(\gamma^2 - \frac{1}{4} - \frac{3}{4}\right) \quad (\text{B.18})$$

$$\frac{dE}{dt} = \frac{4}{3}\sigma_{\text{T}}cU_{\text{rad}}\beta^2\gamma^2 \quad (\text{B.19})$$

where $\beta = v/c$. In the relativistic case and in the Thompson regime, I thus notice that the energy loss rate of the electron is similar to the one from synchrotron radiation. Therefore, in the Thompson regime, it is possible to determine the magnetic field (Aharonian et al., 1997).

$$\frac{|B|^2}{8\pi U_{\text{rad}}} = \frac{\int P_{\text{sync}}(\nu) d\nu}{\int P_{\text{IC}}(\nu) d\nu} \text{ in cgs unit} \quad (\text{B.20})$$

However, in the case where the initial energy of the soft photon ϵ_γ follows $E_e\epsilon \sim (m_e c^2)^2$, the Thompson cross section do not remain valid and I need to use the Klein Nishina cross section σ_{KN} to correct for the recoil effects :

$$\sigma_{\text{KN}} = \frac{3}{4}\sigma_{\text{T}} \left(2q \ln q + (1+2q)(1-q) + \frac{1}{2} \frac{(pq)^2}{1+pq} (1-q) \right) \quad (\text{B.21})$$

$$q = \frac{4\epsilon_\gamma\gamma}{mc^2} \quad (\text{B.22})$$

$$p = \frac{E_\gamma}{qE_p \left(1 - \frac{E_\gamma}{E_p}\right)} \quad (\text{B.23})$$

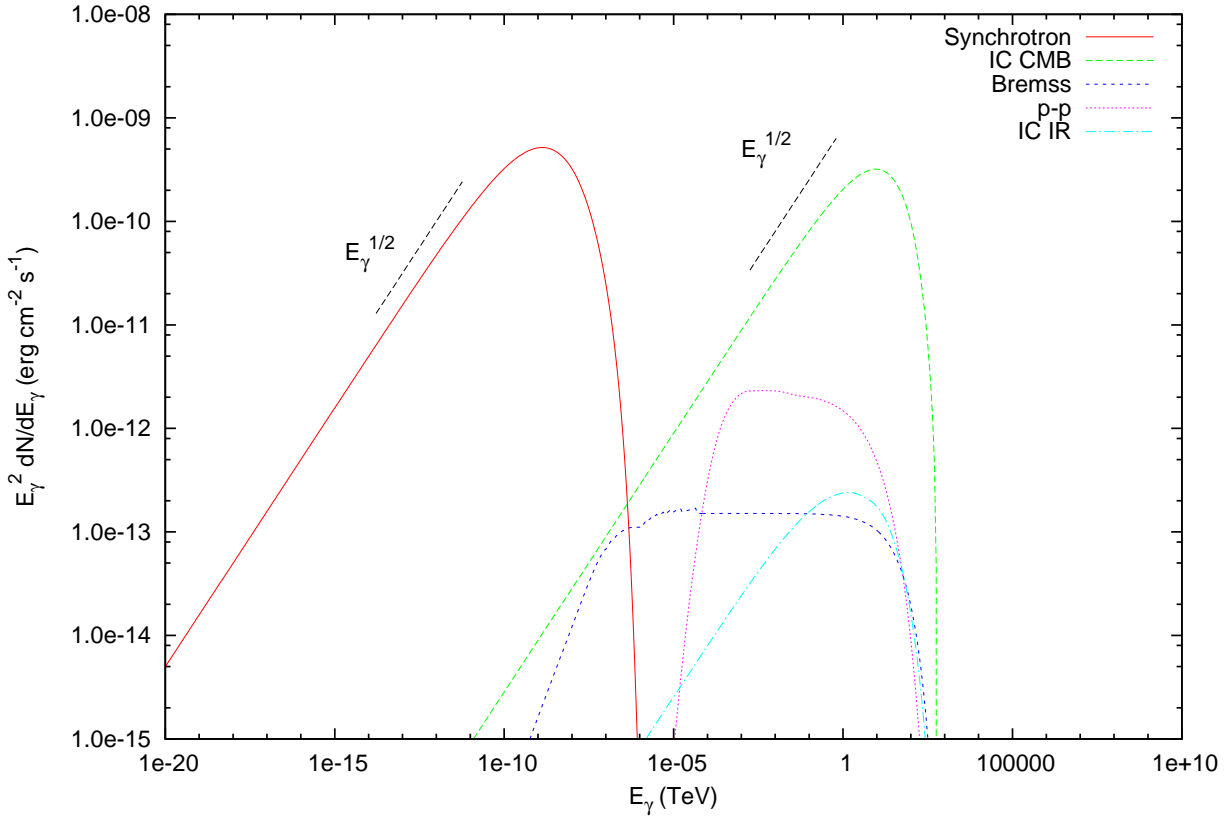


Figure B.1: Spectral energy distribution of the different interaction assuming an electron and proton power-law distribution E^{-2} with an energy cutoff at 100 TeV. I assumed a total output energy $E_{\text{tot}} = 3 \times 10^{49}$ erg where 90% goes to the protons' energy budget. The magnetic field of the system is set to $3\mu\text{G}$ and the target density is fixed to 1 cm^{-3} . Additional IC component from IC scattering of IR photons with energy density $U_{\text{IR}} = 0.01 \text{ eV/cm}^3$ is shown in cyan. The system is located 1 kpc away.

For highly relativistic particle cooling rate thus becomes $\propto \ln E$. I can approximate the particle energy loss by the following

$$\frac{dE}{dt} = \frac{4}{3} \sigma_{\text{T}} c U_{\text{rad}} \gamma^2 \left(1 + \frac{4\gamma\epsilon_{\text{eff}}}{mc^2} \right)^{-\beta} \quad (\text{B.24})$$

$$f_{\text{KN}}(\gamma) = \left(1 + \frac{4\gamma\epsilon_{\text{eff}}}{mc^2} \right)^{-\beta} \quad (\text{B.25})$$

with $\beta = -3/2$ and $\epsilon_{\text{eff}} = 2.8kT$ for the Planck distribution of soft photons (see Manolakou et al. (2007) and reference therein). The photon flux generated by inverse Compton radiation by a single electron.

$$\frac{dN}{dE_{\gamma}} = \frac{3}{4} \sigma_{\text{T}} c \int \frac{n(\epsilon) d\epsilon}{\epsilon} F_{\text{KN}}(Ee, E_{\gamma}, \epsilon) \quad (\text{B.26})$$

In the Thompson limit, from a power-law distribution of electrons, the IC spectrum follow the same trend as the synchrotron spectrum. Finally, I can link the energy of the gamma-ray photon with energy E_{γ} produced by the energy E_e of the emitting electron via the following equation (Hinton & Hofmann, 2009) :

$$E_{\gamma} = 4 \left(\frac{E_e}{1 \text{ TeV}} \right)^{1/2} \quad (\text{B.27})$$

B.2.1 Bremsstrahlung

MeV to TeV gamma-rays can also be emitted from the interactions of a electron with a nucleus. Bremsstrahlung is dependent on the impact parameter b between the two electrons and the target particle (proton, electron, nuclei), defined as the perpendicular distance between the nucleus and the electron trajectory.

Blumenthal & Gould (1970) stated that in the high energy limit, the differential cross bremsstrahlung of an electron transitioning from an initial energy E_i to a final energy E_f , and thus producing a photon with energy $E_\gamma = E_i - E_f$ is

$$d\sigma = \frac{4\alpha r_0^2}{E_\gamma} \left(1 + \left(\frac{E_f}{E_i} \right)^2 \phi_1 - \frac{2}{3} \frac{E_f}{E_i} \phi_2 \right) \quad (\text{B.28})$$

where $\alpha = 1/137$ is the fine structure constant, r_0 is the classical radius of the particle and in the case of a unshielded nucleus with atomic number Z , I have :

$$\phi_1 = \phi_2 = 4Z \left(\ln \left(\frac{2E_i E_f}{E_\gamma} \right) - \frac{1}{2} \right) \quad (\text{B.29})$$

Several corrections are however generally added due to shielding of the electrons in the high energy regime (Koch & Motz, 1959). From Eq. B.28, I also notice that the differential cross section roughly decreases as a function of $1/E_\gamma$. The photon flux at energy E_γ can then be derived by integrating the total differential cross section across all electron energies $E_e \geq E_\gamma$ with distribution $N(E)$.

$$\frac{dN}{dE_\gamma} = nc \int d\sigma(E_e, E_\gamma, Z) dE_e \quad (\text{B.30})$$

As $d\sigma \sim 1/E_\gamma$ at high energies, I find that the photon SED, produced by a power-law distribution of electrons $N(E) \propto E^{-\alpha}$, also follows a power-law with spectral index $\Gamma = 2 - \alpha$ at $E_\gamma \sim$ a few GeV. In the case of E^{-2} spectrum, the differential energy flux $E^2 dN/dE_\gamma$ will be flat in the GeV-TeV band.

where n is the target density of the nucleus. Thus, the photon energy spectrum produced by a power-law distribution of electron $E_e^{-\alpha}$ should follow $\beta = 2 - \alpha$. Therefore, for a typical E_e^{-2} distribution of electron, I should expect a flat energy distribution of photons.

Finally, the cooling rate of an electron in a neutral medium is given by the following relation :

$$\frac{dE_e}{dt} = - \frac{n_z Z (Z + 1.3) e^6}{16\pi^3 \hbar \epsilon_0^3 m_e c^4} E_e \left(\ln \left(\frac{183}{Z^{1/3}} + \frac{1}{8} \right) \right) \quad (\text{B.31})$$

Unlike inverse Compton and synchrotron losses, the bremsstrahlung cooling rate only evolves as a function of E_e and is generally not dominant for high energy electrons. As the total power lost from Bremsstrahlung is inversely proportional to the mass of the high energy particle, protons are also unlikely to produce significant photons compared to electrons.

B.2.2 proton-proton interaction

One important interaction is the production of secondary γ -ray from the decay of neutral pions produced by a CR and a target particle (proton, nuclei). Unlike electrons, protons are not *elementary* particles and there exists several products resulting from this inelastic scattering (See chapter 3). Although the

energy of the two γ -ray photons produced should match the pion of energy, the energy of the neutral pion π^0 ranges from its rest mass to the total kinetic energy available between the two protons. Differential cross section of the p-p interaction producing γ -ray have been parametrised Dermer (1986), Kelner et al. (2006), Kamae et al. (2006) and more recently Kafexhiu et al. (2014). The total proton-proton cross section parametrisation is:

$$\sigma_{\text{inel}}(E) = \left(34.3 + 1.88 \ln \left(\frac{E_p}{1 \text{ TeV}} \right) + 0.25 \ln \left(\frac{E_p}{1 \text{ TeV}} \right)^2 \right) \left(1 - \left(\frac{E_{\text{th}}}{E_p} \right)^4 \right)^2 \quad (\text{B.32})$$

where $E_{\text{th}} = 1.2 \text{ GeV}$ represents the minimal CR energy required to create a neutral pion. The energy loss rate of a proton from inelastic collision is given by

$$\frac{dE_p}{dt} = - \frac{1}{n \sigma_{\text{inel}}(E) c} \quad (\text{B.33})$$

The inelastic cross section weakly depends on the proton energy, therefore it is sometimes easier to assume σ_{inel} as a constant :

$$\frac{dE_p}{dt} = \frac{6 \times 10^7}{n \text{ cm}^{-3}} \text{ yr} \quad (\text{B.34})$$

Kafexhiu et al. (2014) modelled the photon SED dN/dE_γ emitted by one proton via this following equation :

$$\frac{dN}{dE_\gamma} = n \int_{E_p=E_\gamma}^{\infty} A_{\text{max}}(T_p) F(E_\gamma, T_p) dE_p \quad (\text{B.35})$$

where A_{max} represents the multiplicity of neutral pions π^0 produced during the p-p collision and $F(E_\gamma, T_p)$ a parametrisation function. One does expect the photon flux to be symmetrical around $E_\gamma = m\pi^0 c^2/2 \sim 0.6 \text{ GeV}$ as a result from the conservation of energy and momentum when the neutral pion decayed. From a power-law distribution distribution of protons $N(E_p) \propto E_p^{-\alpha}$, I expect the photon differential energy flux to follow a power-law distribution with spectral index $\Gamma = 2 - \alpha$ for energies $E_\gamma >$ a few GeV (see purple line in Fig. B.1). For a proton energy distribution $N(E_p) \propto E_p^{-2}$, $E_\gamma^2 dN/dE_\gamma$ will thus have a flat spectrum in these energy range as per the Bremsstrahlung radiation.

B.3 SED modelling Code

My modelling code consists to solve Eq.4.10 for the case of both impulsive and continuous sources, accounting for all radiation losses listed above, and then obtain the resulting SED. I first derive the normalisation factor A of the energy distribution of protons/electrons from the total energy budget $W_{p,e}$ ($\dot{W}_{p,e}$ for continuous sources) :

$$A = \begin{cases} \frac{W_{p,e}}{\int \mathcal{N}(E) E dE} & \text{for impulsive source} \\ \frac{\dot{W}_{p,e}}{\int \mathcal{N}(E) E dE} & \text{for continuous source} \end{cases} \quad (\text{B.36})$$

where $\mathcal{N}(E)$ is the denormalised distribution of protons/electrons (e.g $\mathcal{N}(E) = E^{-\alpha}$ for a power-law distribution). In our modelling code, I use the fraction of the total energy (rate) transferred to protons η_p and to electrons $\eta_e = 1 - \eta_p$ in order to obtain $W_{p,e}$ or $\dot{W}_{p,e}$.

I then aim to obtain the final energy distribution of protons/electrons at t_{age} . In order to do so, I derive for each Lorentz factor γ , the Lorentz factor γ_0 at earlier epochs (or $t = 0$ for impulsive injector).

For the leptonic case, the total cooling rate $\dot{\gamma}(\gamma)$ is given by :

$$\dot{\gamma}(\gamma) = b_s \gamma^2 + b_c (3 \ln \gamma + 18.8) + 5.3 b_b \gamma + \sum_{i=\text{CMB, IR, Opt}} b_{\text{IC}}^i \gamma^2 F_{\text{KN}}^i(\gamma) \quad (\text{B.37})$$

where $b_s = 1.292 \times 10^{-15} (B/10^3 \mu\text{G})^2 \text{s}^{-1}$ is a constant for synchrotron losses, $b_{\text{IC}} = 5.204 \times 10^{-20} (u_0^i/eV) \text{s}^{-1}$ is a constant for IC losses with u_0 being the total energy density of the soft photons, $b_c = 1.491 \times 10^{-14} n_{\text{H}}/1 \text{cm}^{-3}$ is the Coulomb losses constant with n_{H} being the target density, and $b_b = 1.37 \times 10^{-16} n_{\text{H}} \text{s}^{-1}$ is a constant for Bremsstrahlung losses in neutral medium (see Manolakou et al. 2007 and references therein).

For the hadronic case, I simply use :

$$\dot{\gamma}(\gamma) = \frac{1}{n_{\text{H}} c \sigma_{\text{pp}}(\gamma)} \quad (\text{B.38})$$

Using the total cooling rate for a given Lorentz factor, the following methods is used to obtain γ_0

1. Derive $\Delta t = d\gamma/\dot{\gamma}(\gamma)$
2. Increment γ by $d\gamma$
3. Repeat (1) and (2) until the cumulative time t reach the system age t_{age}

The $d\gamma$ step is automatically adjusted so that the estimation of γ_0 remains accurate for any Lorentz factor.

I then use Eq. 4.10 to get the final distribution of electrons and protons. Finally, I use Eqs. B.10, B.26, B.30 and B.35 to obtain the final photon SED.

B.4 Comparison of Results

Here, I validate the results of my modelling code by comparing them with already published results. I used the package `g3data` to fetch data points from these published papers. As the calibration required to fetch the value is done manually, the data point values show some inaccuracies ($\sim 20 - 30\%$ uncertainties may be expected).

To test our leptonic emission model, I compare in Fig.B.4 our resulting SEDs with the results from Aharonian et al. (1997), which studied the evolution of the energy distribution of electrons continuously injected by pulsars, and accounting for synchrotron and IC radiation losses. The various plots show the contribution of time, the magnetic field strength, the energy cut-off of the energy distribution of electrons (defined as E_0 in Fig.B.4) and the spin down power (defined as L_0 in Fig.B.4) on the photons SED. I remark that our numerical code reproduces the published results. The slight discrepancy of the IC emission for the case of a small $E_0 = 10 \text{TeV}$ comes from the fact that the near IR soft photons was not included while computing the IC flux.

In Fig. B.3, I also compared the output of my code with the published results from Domainko & Ohm (2012), which studied the origin of the VHE gamma-ray source HESS J1507–622. For the case of leptonic scenario (left panel) and hadronic-leptonic scenario (right), our results match with theirs. I note however

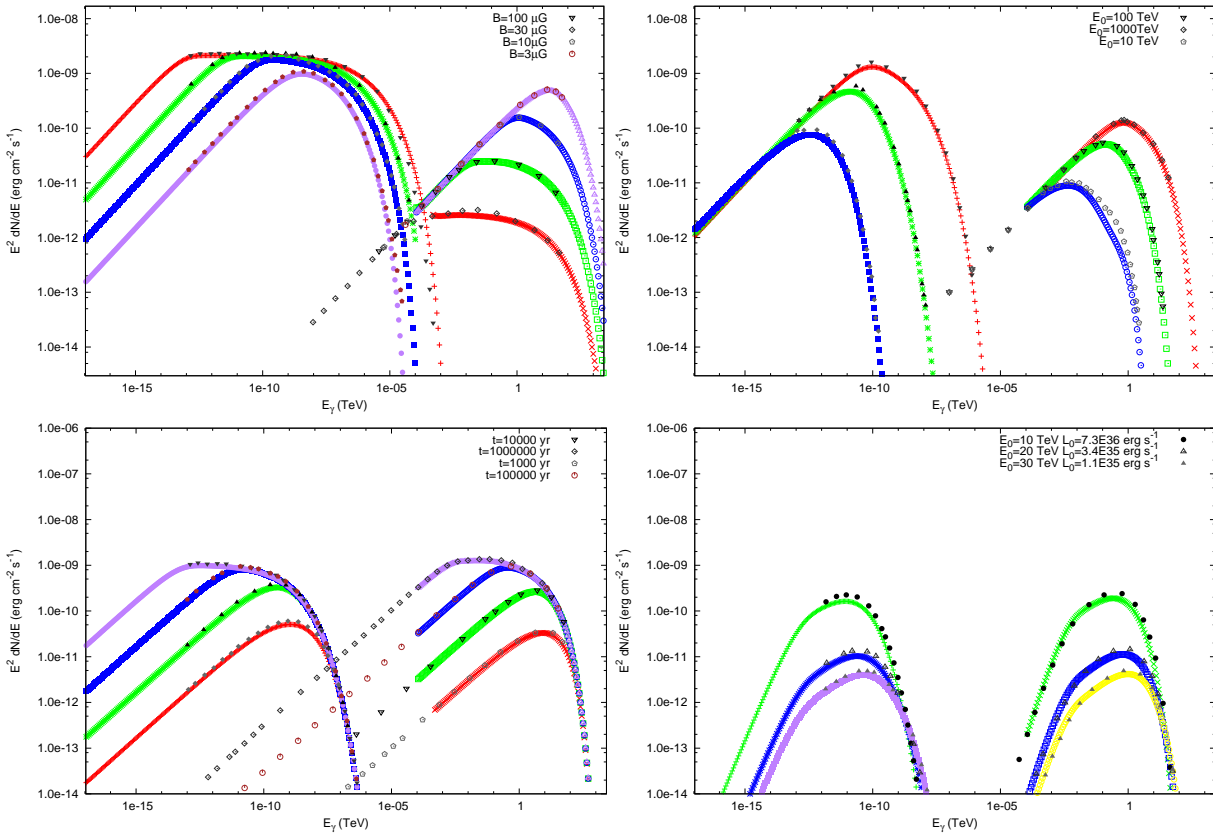


Figure B.2: Comparison of the modelling code results (in purple, blue, green and red) with the published results from Aharonian et al. (1997) (in grey and brown dotted points) for the case of continuously injected electrons whose energy distribution obeys a power-law with spectral index $\alpha = 2$. (*Top Left*) Photons SEDs for a magnetic field strength $B = 3\mu\text{G}$ (purple), $10\mu\text{G}$ (blue), $30\mu\text{G}$ (green) and $100\mu\text{G}$ (red) assuming a 10^4 yr old pulsar with spin down power $L_0 = 10^{37}$ ergs $^{-1}$. (*Top right*) Photons SEDs for a power-law distribution of electrons with energy cut-off $E_0=10$ TeV (blue), $E_0=100$ TeV (green) and $E_0=1000$ TeV (red). (*Bottom left*) Evolution of the SED at $t = 1,000$ yr (red), $t = 10,000$ yr (green), $t = 100,000$ yr (blue) and $t = 1,000,000$ yr (purple) for a power-law distribution of electrons with energy cut-off $E_0=100$ TeV. (*Bottom right*) Photons SED produced a pulsar with $L_0 = 7.3 \times 10^{36}$ ergs $^{-1}$ and $E_0=10$ TeV, a second with $L_0 = 3.5 \times 10^{35}$ ergs $^{-1}$ and $E_0=20$ TeV and a third with $L_0 = 1.1 \times 10^{35}$ erg and $E_0 = 30$ TeV.

that, compared to the *GEANT* model (in red, see Kafexhiu et al. 2014), the *GGSJET* model (in green) shows a slight overestimation of the gamma-ray flux between $E_\gamma = 10 - 10000$ GeV.

Finally, Fig. B.4 illustrates the gamma-ray SED towards DorC located in the Large Magellanic Cloud (LMC) using the same initial parameters as the one from H.E.S.S. Collaboration et al. (2015) (auxiliary informations). Our model reproduces the published results.

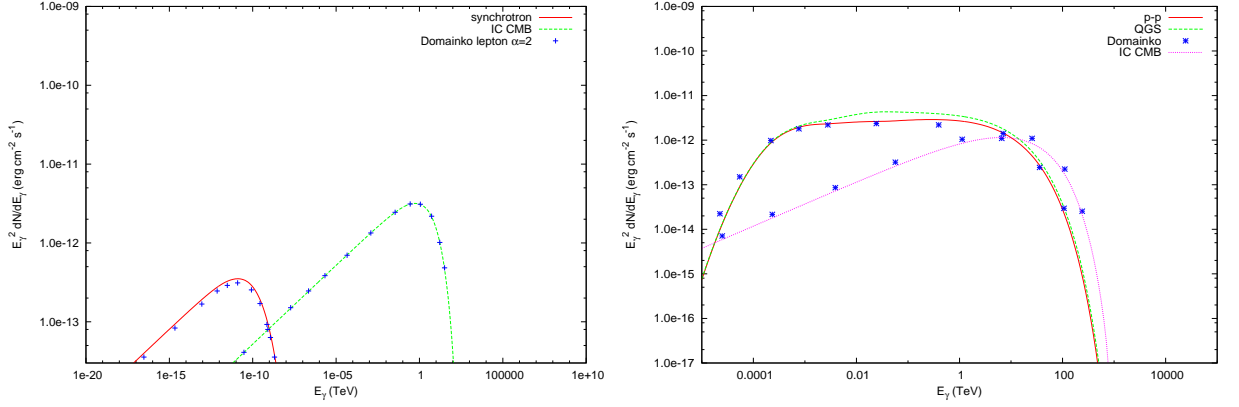


Figure B.3: Comparison of the numerical code results with the published results from Domainko & Ohm (2012) regarding the origin of HESS J1507–622. For the leptonic scenario (left panel), a power-law distribution with spectral index $\alpha=2.0$ and an energy cut-off $E_0 = 60$ TeV was continuously injected. A total electron energy budget $W_e = 2.7 \times 10^{47}$ erg, a magnetic field strength $B = 1 \mu\text{G}$ and a pulsar age $t_{\text{age}} = 3 \times 10^5$ yr were assumed. The synchrotron radiation is shown in red while the IC (CMB) radiation is shown in green. For the hadronic-leptonic scenario (right panel), 99.95% of the total energy $W_0 = 1.0005 \times 10^{50}$ erg was transferred to protons and the remaining 0.0005% to electrons. Both the proton and electrons energy distribution obey a power-law distribution with spectral index $\alpha = 2.0$, with an energy cut-off $E_{0,p} = 100$ TeV for protons and $E_{0,e} = 60$ TeV for electrons. The gamma-ray emission using the GEANT model is here shown in red while the gamma-ray emission using QGSJET model is shown in green. Finally, the IC up-scattering of CMB photons is here shown in purple.

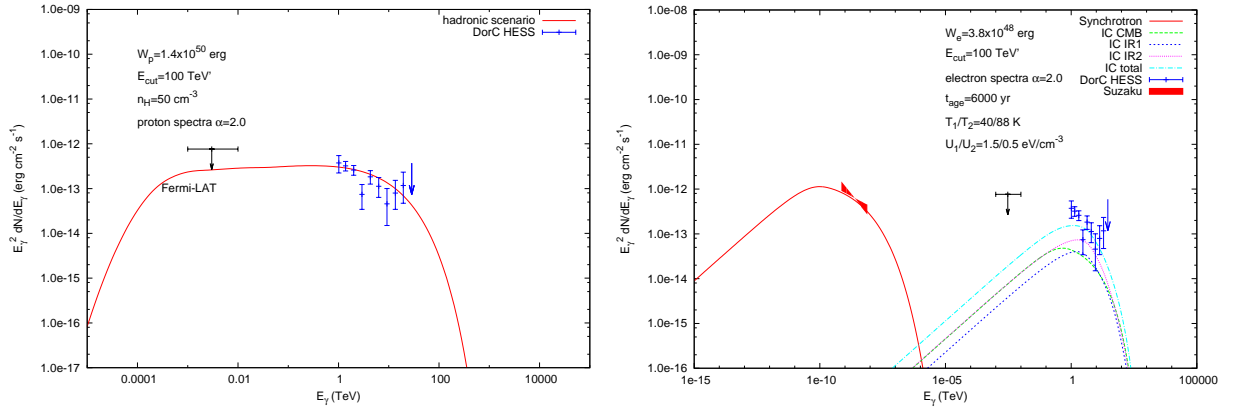


Figure B.4: photons SED towards 30DorC located in the Large Magellanic Cloud (LMC). The HESS data points are shown in blue. The red cross indicate the energy flux observed by Suzaku and the down arrow represents the upper-limit obtained from Fermi observations. The left panel shows the hadronic scenario where a total proton energy $W_p = 1.4 \times 10^{50}$ erg has been injected. The proton energy distribution follows a power-law with spectral index $\alpha = 2.0$ and a energy cut-off $E_{\text{cut}} = 100$ TeV, the density of the surrounding ISM is here assumed to be $n_{\text{H}} = 50 \text{ cm}^{-3}$. The right panel illustrates the leptonic scenario with a total energy transferred to electrons $W_e = 3.0 \times 10^{48}$ erg. The electron distribution follows a power-law spectra with spectral index $\alpha = 2.0$ and energy cut-off $E_{\text{cut}} = 100$ TeV. The contribution of IC radiation from the up-scattering of two IR soft photons regions with energy density $U_1 = 1.5 \text{ eV cm}^{-3}$ and $U_2 = 0.5 \text{ eV cm}^{-3}$ and with radiation temperature $T_1 = 40$ K and $T_2 = 80$ K are shown in dashed blue and sold purple respectively. Combined with the IC up-scattering of soft CMB photons (in dashed green), the total IC radiation is here displayed in dashed blue. Finally, the SED from synchrotron radiation is shown in red.

Appendix C

Diffusion code

Combining analysis of astrophysical high energy sources at various wavelength can provide additional constraints about its physical properties (e.g energy, magnetic field strength, shape of the electron and CR energy distribution). For instance, one zone model have been used to predict the physical properties of PWNe (Amato, 2014). Here, the modeling code aims to model the diffusion of high energy CRs and electrons into an *inhomogeneous* interstellar medium and predict the morphology of the electromagnetic radiation at various wavelengths. It aims to provide additional morphological distinctions between hadronic and leptonic scenario as the cooling rate of protons and electrons are different (see Chapter 4). The presence of dense molecular regions in the vicinity is expected to affect the gamma-ray morphology. Here, I describe our modeling code used to understand the origin of the TeV emission towards the north of HESS J1825–137. The model accounts for the diffusion of CRs/electrons as they lose energy via the different interactions outlined in Appendix B. Fig. C.1 briefly sketches the different steps of the program.

C.1 Numerical solution

Implementing a template description of the gas density distribution means I can only solve the diffusion equation numerically. To do so, each position x, y, z has been discretized using a grid composed of cells with size Δx (see Fig. 6.3 for basic illustration). To obtain the energy density of CRs/high energy electrons $n(\gamma, x, y, z, t)$ at a given discrete position (x, y, z) and time t , I increment the energy density $n(\gamma, x, y, z, t - \Delta t)$ obtained from the previous time step with the net density of CRs/high energy electrons (with Lorentz factor γ_0 at $t - \Delta t$) transferred from this cell to its neighbour cells. This net transfer is notably dependent on the energy density gradient between the two cells at $t - \Delta t$ and the unitless diffusion coefficient $D = D\Delta t/\Delta x^2$. The diffusion equation (Eq. 4.25) thus becomes :

$$n \left| \begin{array}{c} \gamma \\ t \\ x, y, z \end{array} \right. = \sum_{i=x, y, z} \left[\frac{\dot{\gamma}_0}{\dot{\gamma}} D \left| \begin{array}{c} \gamma_0 \\ t - \Delta t \\ i + \Delta i/2 \end{array} \right. \left(n \left| \begin{array}{c} \gamma_0 \\ t - \Delta t \\ i + \Delta i \end{array} \right. - n \left| \begin{array}{c} \gamma_0 \\ t - \Delta t \\ i \end{array} \right. \right) \right. \\ \left. + \frac{\dot{\gamma}'_0}{\dot{\gamma}} D \left| \begin{array}{c} \gamma'_0 \\ t - \Delta t \\ i - \Delta i/2 \end{array} \right. \left(n \left| \begin{array}{c} \gamma'_0 \\ t - \Delta t \\ i - \Delta i \end{array} \right. - n \left| \begin{array}{c} \gamma'_0 \\ t - \Delta t \\ i \end{array} \right. \right) \right] \quad (\text{C.1})$$



Figure C.1: sketch summarizing the different steps of the program I have created to obtain the SED of the gamma-rays produced by the protons/electrons diffusing in a ISM with varying density, magnetic field and diffusivity.

C.1.1 Obtaining the time step Δt

To numerically solve the diffusion equation, several important rules must be followed :

- The density distribution must remain positive at all points.
- For a given Lorentz factor γ , the position of the maximum value must remain constant as a function of time (in the absence of external source).

I now compute the maximum value of D to follow the aforementioned rules :

$$n_{\max}(1 - 6D) \geq n_{\max}D \quad (\text{C.2})$$

$$n_{\max} - 6Dn_{\max} \geq n_{\max}D \quad (\text{C.3})$$

$$n_{\max} \geq 7Dn_{\max} \quad (\text{C.4})$$

$$D \leq \frac{1}{7} \quad (\text{C.5})$$

In order to comply to these rules, the unitless diffusion factor must not exceed $D < 1/7$ (for Cartesian configuration). As a rule of thumb, I always use $D < 0.1$ while numerically solving the diffusion equation so as to avoid any problems. Consequently, the required time step Δt becomes :

$$\Delta t = \frac{\Delta x^2}{D_{\max}} \quad (\text{C.6})$$

As in our case, the diffusion equation increases with energy, the implied time step becomes very small. Consequently, the Cartesian configuration, despite being flexible, becomes very computationally intensive. To circumvent this issue, the program allows the spatial resolution to gradually decrease by a factor of 2 and 4 (generally used for particles with energy $E_e > 200 \text{ TeV}$) in order to keep the value of Δt to a reasonable level. Using this method, solving the numerical equation over such a wide region does not become as computationally intensive.

C.1.2 Obtaining γ_0

An important step to account for is the radiation losses (see Chapter 4 and Appendix B) which eventually affects the evolution of the energy density distribution of particles $n(x, y, z, E, t)$. The initial Lorentz factor γ_0 at a previous step time $t - \Delta t$ must be acquired :

$$\Delta t = \int_{\gamma}^{\gamma_0} \frac{d\gamma''}{\dot{\gamma}(\gamma'')} \quad (\text{C.7})$$

where $\dot{\gamma}(\gamma'')$ is the cooling rate of a particle with Lorentz factor γ'' . Accordingly, the cooling time from radiation $t_{\text{cool}}(\gamma) = \gamma/\dot{\gamma}(\gamma)$ represents the required time for a particle to lose half its energy. The cooling rate of each interactions are very smooth. Thus in the case where $\Delta t \ll t_{\text{cool}}$, I can approximate Eq. C.7 by

$$\Delta t \sim \frac{\gamma_0 - \gamma}{\dot{\gamma}(\gamma)} \quad (\text{C.8})$$

$$\gamma_0 \sim \gamma + \dot{\gamma}(\gamma) \Delta t \quad (\text{C.9})$$

However for very high energy particles where $\Delta t \sim t_{\text{cool}}$, I find γ_0 using the numerical methods shown in Appendix B.

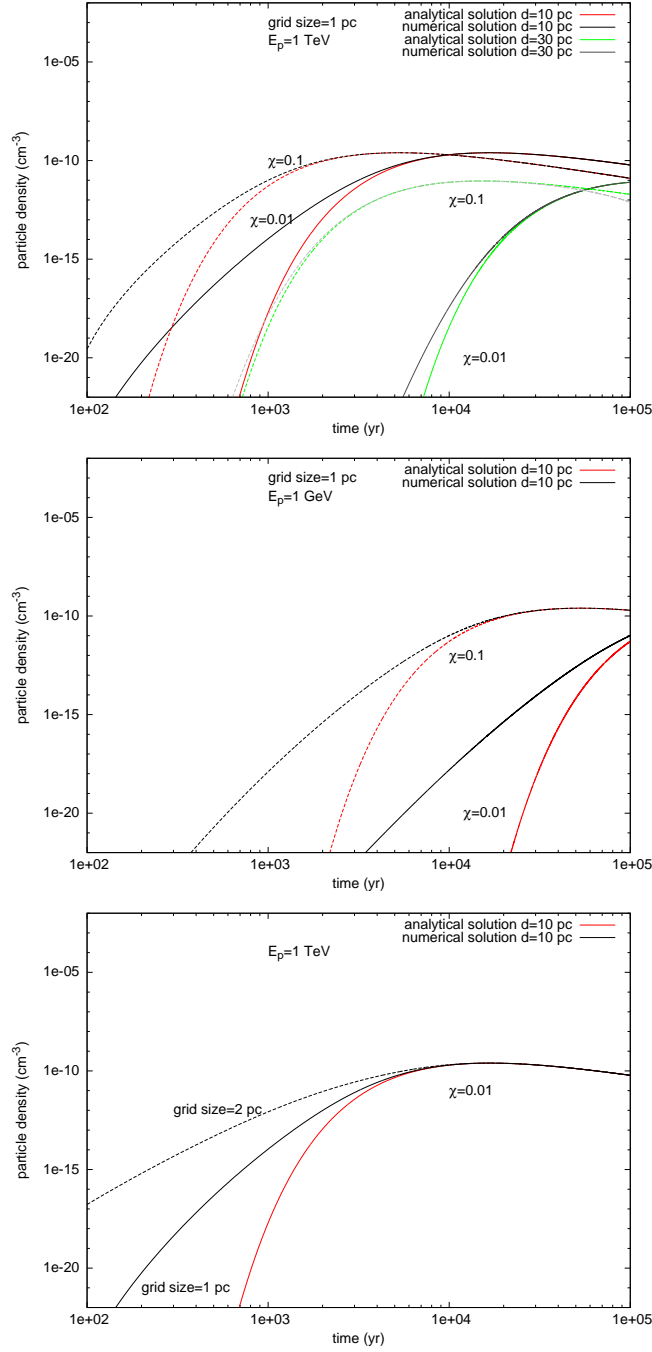


Figure C.2: (Top) Comparison between the analytical solution shown in red and green for a distance $d = 10 \text{ pc}$ and 30 pc away from the impulsive source and their respective numerical solution in black ($d = 10 \text{ pc}$) and grey ($d = 30 \text{ pc}$) as a function of the system age for a particle with energy $E_p = 1 \text{ TeV}$. In both cases, scenarios where the diffusion coefficient suppression factor $\chi=0.01$ and $\chi=0.1$ are shown in solid and dashed lines respectively. (Middle) Same as top for a distance $d = 10 \text{ pc}$ for particle energy $E_p = 1 \text{ GeV}$. (Bottom) Comparisons of the analytical solutions (in red) with the numerical solutions (in blue) as a function of time at distance $d = 10 \text{ pc}$ for a particle energy $E_p = 1 \text{ TeV}$ for two different grid sizes.

C.1.3 Convergence to exact solution

Fig. C.2 indicates the time required for the numerical methods to converge towards the *exact* solution for a given particle energy E_p , located at a distance d from the CR accelerator, and with a diffusion coefficient suppression factor χ . I first note that the slower diffusion ($\chi = 0.01$) from lower energy particles at 1 GeV strongly impedes on the convergence to the *exact* solution at a distance $d = 10$ pc with convergence time $t_{\text{conv}} \sim 10^5$ yr for $\chi = 0.01$ compared to $E_p = 1$ TeV with $t_{\text{conv}} \sim 5000$ yr. Similarly, I find that the convergence time for a suppression factor $\chi=0.01$ is a factor of 3 slower than the case where $\chi = 0.1$, likely caused by the reduction of the diffusion radius R_{diff} (see Chapter 4) by a factor of 3. Additionally, the time required for the numerical method to reach the analytical solution also increases as a function of the distance d from the CR accelerators because of the longer time required for CRs/high energy electrons to reach this distance. A bigger spatial resolution also *increases* the discrepancy between the numerical and analytical solutions but *do not increase* the time for the numerical method to reach the analytical solution. As a conclusion, as I increase the distance with the high energy source, an overestimation of the particle energy density at low energy is to be expected. Consequently, at large distance, the spectra predicted by our numerical model will be slightly softer than what is expected.

C.1.4 Boundary condition

In Fig. C.2 I noted that for the case $d = 30$ pc, $\chi = 0.1$ and $E_p = 1$ TeV (see grey dashed line), the numerical solution appears to *diverge* from the analytical one at $t > 10^5$ yr. This is caused by the boundary conditions here which impose the condition $n(\gamma)=0$ at the edge of the grids and thus act as a *sink*. The more R_{diff} gets closer to the grid boundaries, the more our numerical solutions suffer particle escape losses. To circumvent this issue in our numerical code, I impose that the density $n_b(\gamma)$ at the edge of our grid follows this condition :

$$n_b \Big|_{x,y,z}^{\gamma} = \sum_{i=x,y,z} \left(\frac{\dot{\gamma}_0}{\dot{\gamma}} \mathbf{D} \Big|_i^{\gamma_0} \left(n_b \Big|_i^{\gamma_0} - n \Big|_{i-\Delta i}^{\gamma_0} \right) + \frac{\dot{\gamma}'_0}{\dot{\gamma}} \mathbf{D} \Big|_{i-\Delta i/2}^{\gamma'_0} \left(n \Big|_{i-\Delta i}^{\gamma'_0} - n_b \Big|_i^{\gamma'_0} \right) \right) \quad (\text{C.10})$$

This equation extrapolates the value of the particle density past the grid boundary using the energy density of the last cells. I then use the diffusion coefficient at the boundary to obtain the new energy density at the boundaries.

C.1.5 Obtaining the SED

Once I obtained the CR/high energy electron energy distribution in each grid, I derive the SED from leptonic and hadronic interaction using Eqs. B.10, B.26, B.30 and B.35. From Appendix B, I already showed that our numerical methods used to obtain the SED from an arbitrary energy distribution of protons and electrons matched with published results.

C.1.6 test result

Analytical solution

One method to test the robustness of our numerical solutions is to compare our results in a scenario where the analytical solution is found. Here, I consider an impulsive injector, and use the diffusion of particles from a finite size source of volume $V = (4 \text{ pc})^3$. To obtain the analytical solution from this scenario, I convolve the Green function for the diffusion equation (see Eq. 4.30 in Chapter 4) with the size of the CR source here assumed to be the $4 \text{ pc} \times 4 \text{ pc} \times 4 \text{ pc}$ (i.e. grid size at lowest resolution) :

$$n_{\text{exact}}(\gamma, x, y, z, t) = \int_{-2}^2 \int_{-2}^2 \int_{-2}^2 \frac{n_0}{64\pi^{3/2} R_{\text{diff}}^3} \exp\left(-\frac{(x-s_1)^2}{R_{\text{diff}}^2}\right) \exp\left(-\frac{(y-s_2)^2}{R_{\text{diff}}^2}\right) \exp\left(-\frac{(z-s_3)^2}{R_{\text{diff}}^2}\right) ds_1 ds_2 ds_3 \quad (\text{C.11})$$

where $n_0 = n(0, 0, 0, \gamma_0, 0)$. I first start by a change of variable $u_1 = (x - s_1)/R_{\text{diff}}$, $u_2 = (y - s_2)/R_{\text{diff}}$ and $u_3 = (z - s_3)/R_{\text{diff}}$ leading to $ds_1 = -R_{\text{diff}} du_1$, $ds_2 = -R_{\text{diff}} du_2$ and $ds_3 = -R_{\text{diff}} du_3$:

$$n_{\text{exact}}(\gamma, x, y, z, t) = - \int_{-2}^2 \int_{-2}^2 \int_{-2}^2 \frac{n_0}{64\pi^{3/2}} \exp(-u_1) \exp(-u_2) \exp(-u_3) du_1 du_2 du_3 \quad (\text{C.12})$$

Using the definition of the error function :

$$\text{erf}(a) = \frac{2}{\sqrt{\pi}} \int_0^a \exp(-x) dx \quad (\text{C.13})$$

I then solve Eq. C.12 :

$$n_{\text{exact}}(\gamma, x, y, z, t) = \frac{n_0}{512} \prod_{i=x,y,z} \left(\text{erf}\left(\frac{i+2}{R_{\text{diff}}}\right) - \text{erf}\left(\frac{i-2}{R_{\text{diff}}}\right) \right) \quad (\text{C.14})$$

Leptonic case

Fig. C.3 (top panel) shows the different particle density energy distribution as a function of distance d from the injector, at the plane $z = 0$. The magnetic field strength is uniform and fixed at $B = 10\mu\text{G}$. At these distances, I find that our the energy distribution of electrons appears similar to the analytical solution. The resulting photon SEDs shown in Fig. C.3 bottom panel are also consistent with the SEDs predicted from the analytical solution. Therefore, our numerical code appears to be robust as long as the age of the system exceeds the convergence time (see previous section).

Hadronic case

CRs do not usually lose significant amount of energy from radiation losses. The drawback is that CRs are likely to propagate past the boundary regions. However, from Fig. C.4, I show that the photon SEDs produced by our numerical solution match with the one predicted by our analytical solution. I thus remark that the boundary conditions used in our modelling code prevents the loss of particle density at high energies.

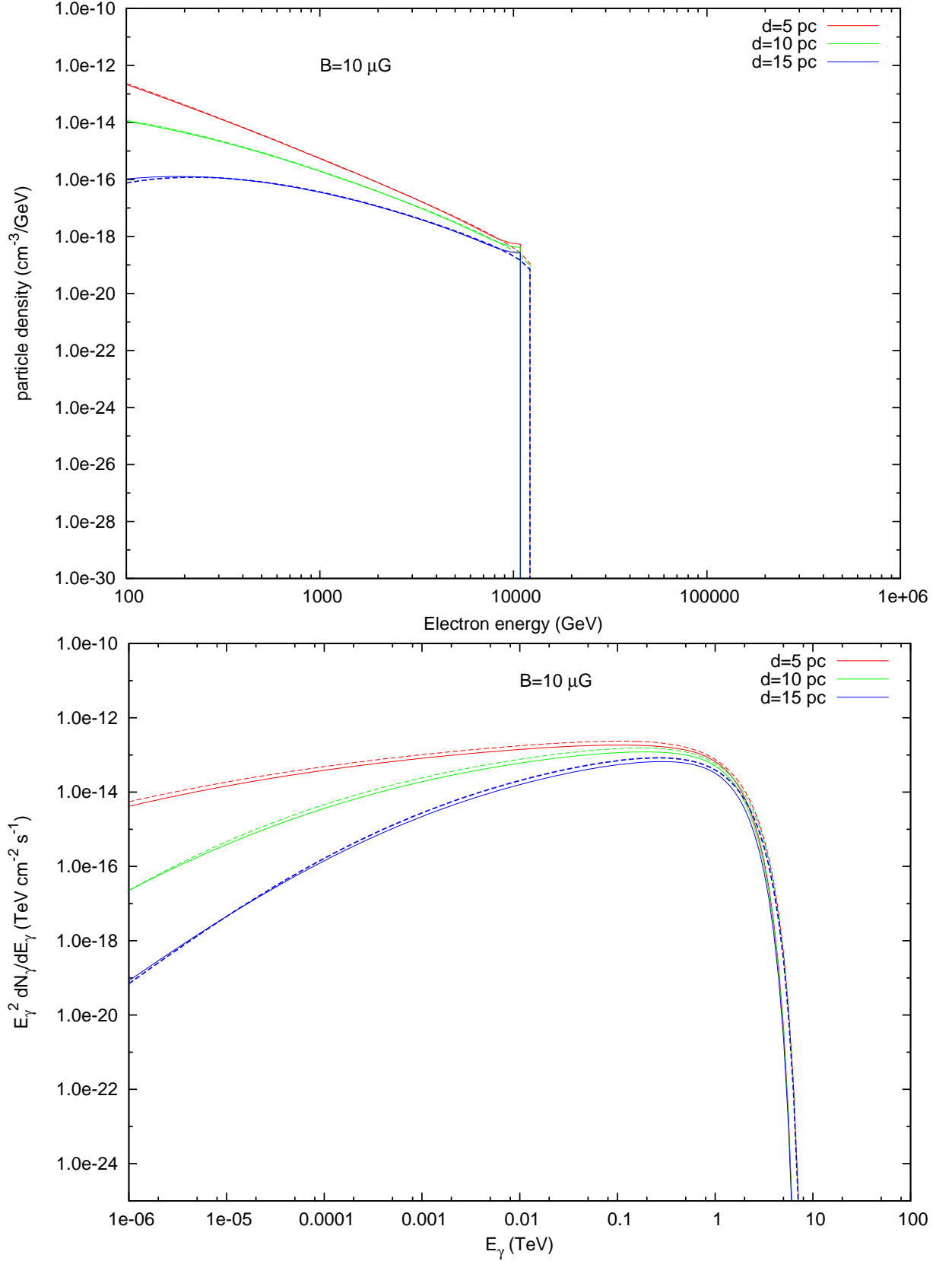


Figure C.3: (Top) Electron density distribution as a function of density at $d = 5$ pc (red), $d = 10$ pc (green), $d = 15$ pc (blue) in the case of a uniform magnetic field $B = 10\mu\text{G}$. The solid lines indicate our numerical solution while the analytical solution are shown in dashed lines. (Bottom) Gamma-ray spectral energy distribution at the aforementioned distances. the numerical solutions (in solid lines) are compared with the SED from the analytical energy density distribution (in dashed lines).

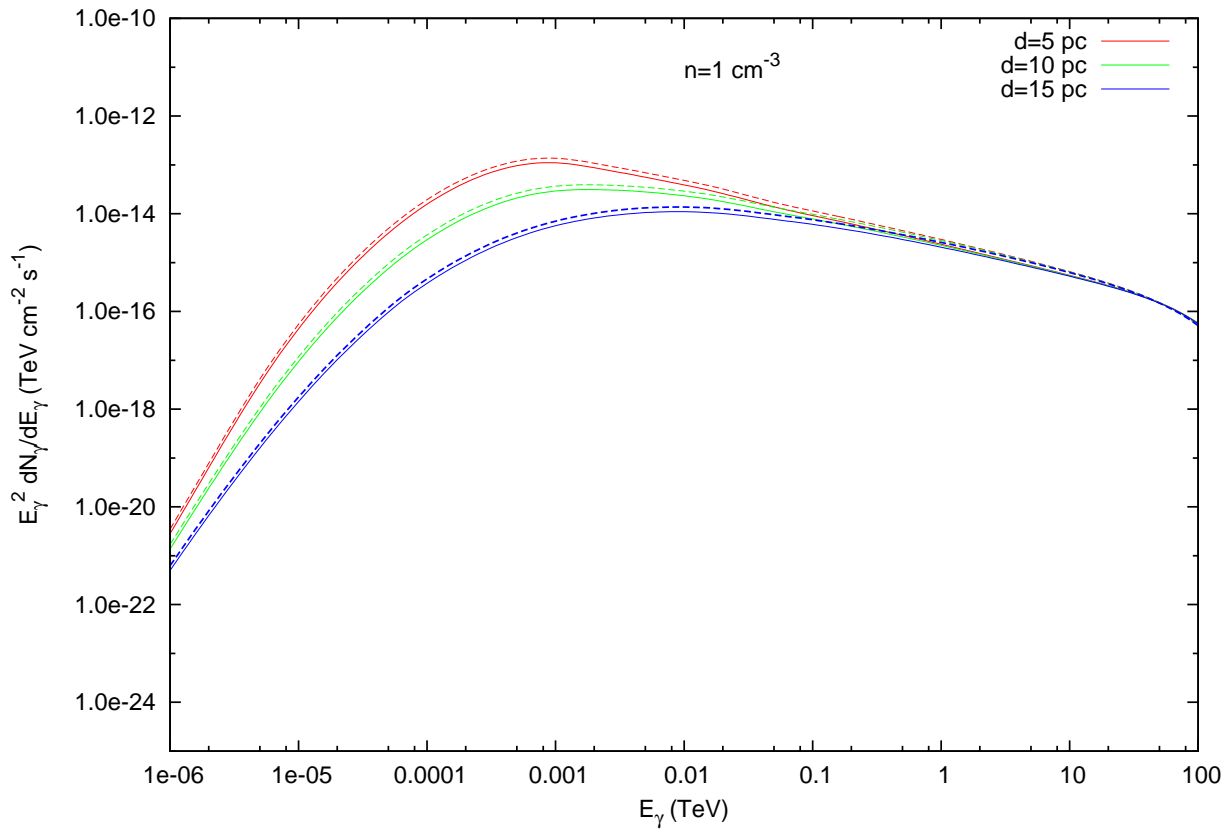


Figure C.4: Gamma-ray spectral energy distribution from hadronic p-p interactions at the distance $d = 5 \text{ pc}$ (red), $d = 10 \text{ pc}$ (green), $d = 15 \text{ pc}$ (blue). The numerical solutions (in solid lines) and compared with the SED from the analytical energy density distribution (in dashed lines).

Appendix D

Additional gamma-ray modelled emission towards HESS 1826–130

In this appendix, I show the modelled morphology of the gamma-ray emission contributed by the PWN HESS J1826–130 or its progenitor SNR for the scenarios P2, P3 (Hadronic scenarios) and scenarios E1 and E4 (leptonic scenarios, see Section 6.3.3 and Tables 6.1 and 6.2 for description of these scenarios.)

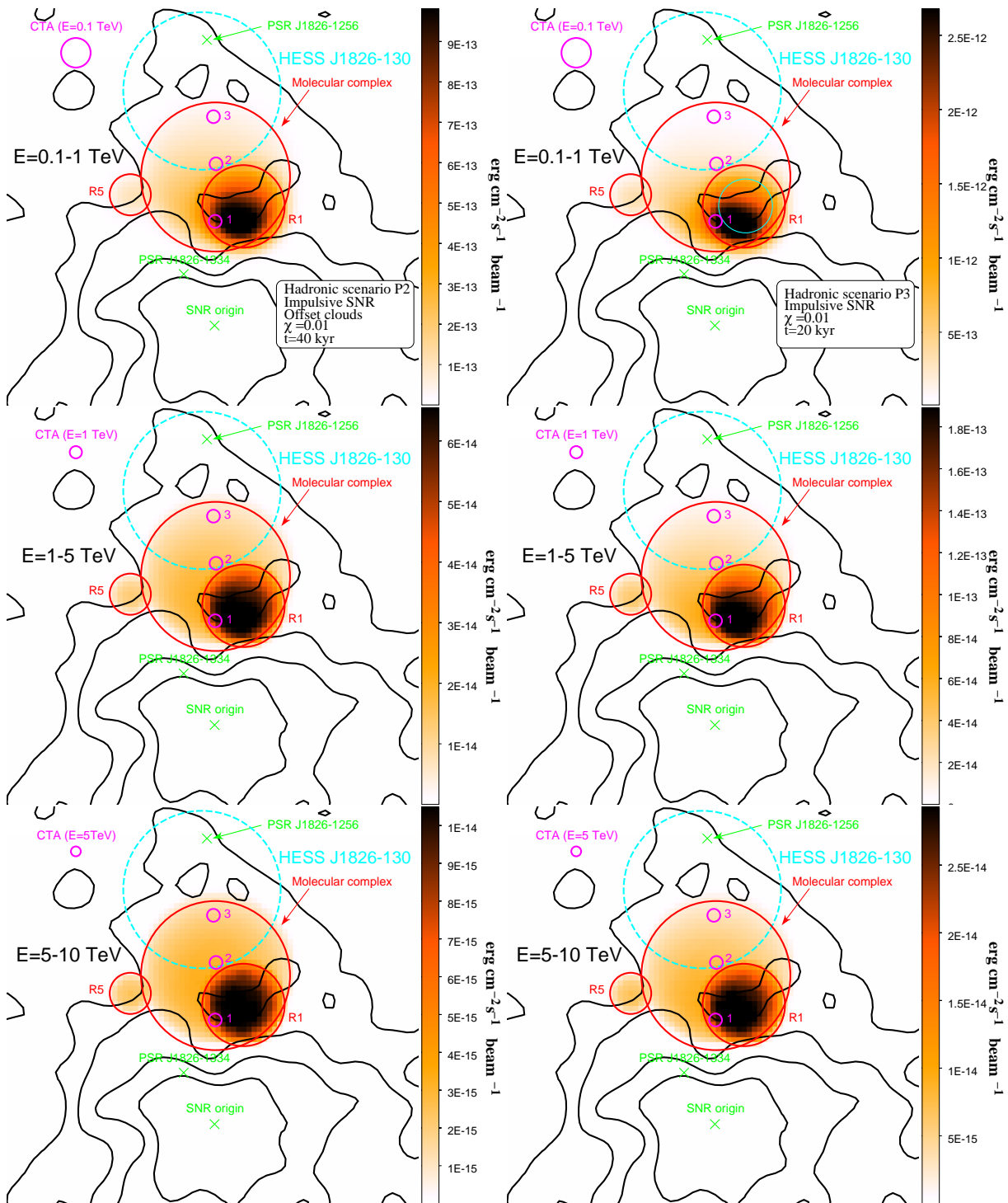


Figure D.1: Integrated energy flux of gamma-rays between the energy ranges $E_\gamma = 0.1 - 1$ TeV (top), $1 - 5$ TeV (middle), $5 - 10$ TeV (bottom) produced by cosmic rays from the *progenitor* SNR of PSR J1826–1334 using a diffusion coefficient suppression factor $\chi=0.01$, overlaid by the observed TeV emission in black contours. Compared to scenario P1 (see Table 6.1), the scenario P2 (left panels) shows the effect of the offset position of molecular clouds in the line of sight with respect to the SNR origin while the scenario P3 uses the characteristic age of the pulsar PSR J1826–1334 $t_c = 20$ kyr as age of the system. The assumed origin of the SNR is shown in green cross. The position, sizes and densities of the three molecular clouds shown as red circles are displayed in Table 6.1. The thick cyan circle represents the area used to obtain the flux towards HESS J1826–130.

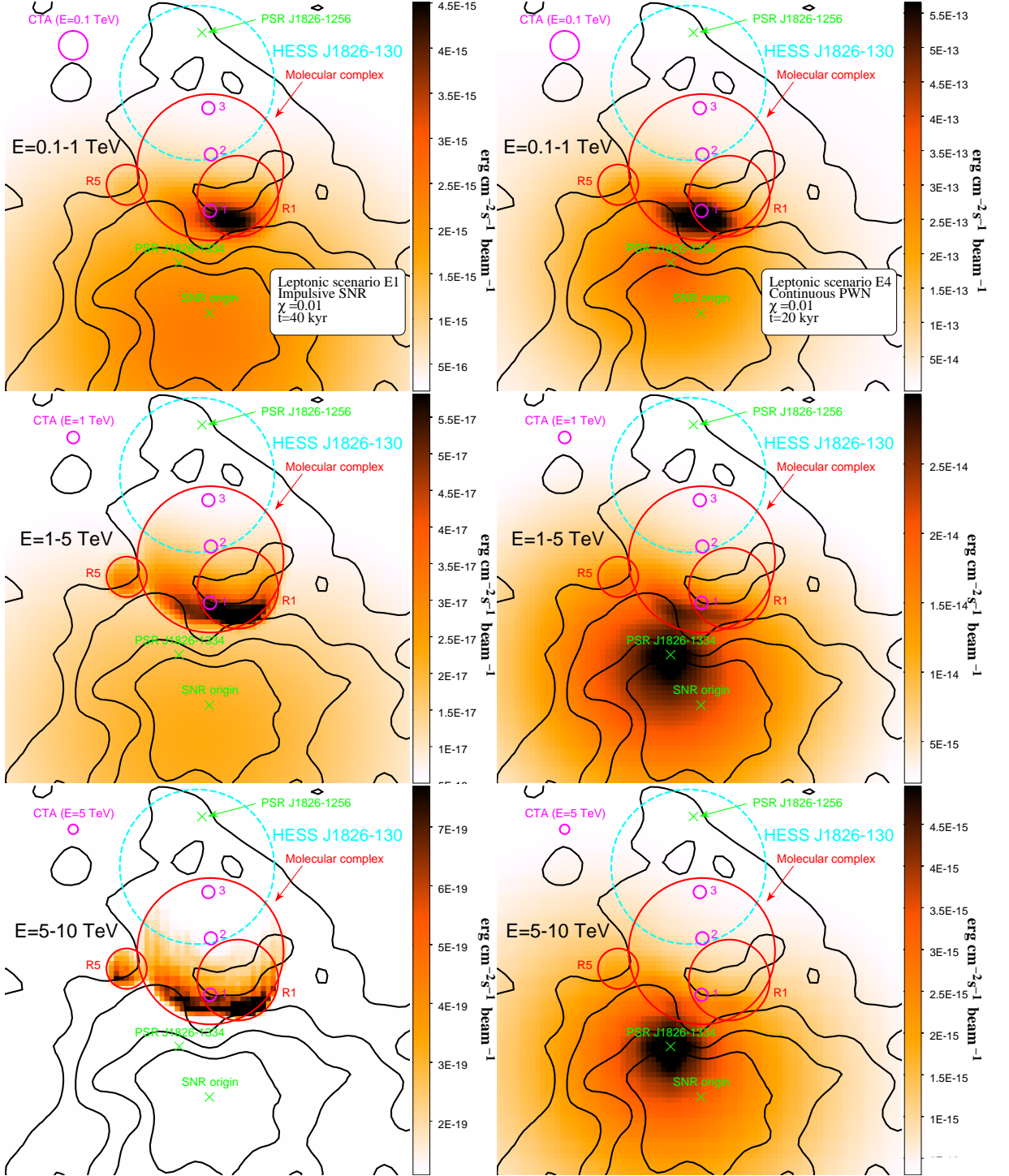


Figure D.2: (*Left panels*) Integrated energy flux of gamma-rays between the energy ranges $E_\gamma = 0.1 - 1$ TeV (top), $1 - 5$ TeV (middle), $5 - 10$ TeV (bottom) produced by high energy electrons escaping the progenitor SNR of PSR J1826–1334 using a diffusion coefficient suppression factor $\chi=0.01$ at $t = 40$ kyr (scenario E1). (*Right panels*) Integrated energy flux of gamma-rays between the energy ranges $E_\gamma = 0.1 - 1$ TeV (top), $1 - 5$ TeV (middle), $5 - 10$ TeV (bottom) produced by high energy electrons escaping the pulsar PSR J1826–1334 using a diffusion coefficient suppression factor $\chi=0.01$ at $t = 20$ kyr (scenario E4). In both panels, the observed TeV emission is illustrated in black contours. The assumed origin of the SNR is shown in green cross. The position, sizes and densities of the three molecular clouds shown as red circles are displayed in Table 6.1. The thick cyan circle represents the area used to obtain the flux towards HESS J1826–130.

Bibliography

- Abeysekara A. U., et al., 2013, [Astroparticle Physics](#), 50, 26
- Acharya B. S., et al., 2013, [Astroparticle Physics](#), 43, 3
- Adriani O., et al., 2009, [Nature](#), 458, 607
- Aharonian F. A., Atoyan A. M., 1996, [A&A](#), 309, 917
- Aharonian F. A., Drury L. O., Voelk H. J., 1994, [A&A](#), 285, 645
- Aharonian F. A., Atoyan A. M., Kifune T., 1997, [MNRAS](#), 291, 162
- Aharonian F., et al., 2006a, [A&A](#), 457, 899
- Aharonian F., et al., 2006b, [A&A](#), 460, 365
- Aharonian F., et al., 2006c, [A&A](#), 460, 743
- Aharonian F., et al., 2007, [A&A](#), 467, 1075
- Aharonian F., et al., 2008, [A&A](#), 481, 401
- Amato E., 2014, [International Journal of Modern Physics Conference Series](#), 28, 60160
- Anderson L. D., Bania T. M., 2009, [ApJ](#), 690, 706
- Anderson L. D., et al., 2017, preprint, ([arXiv:1705.10927](#))
- Angüner E. O., Aharonian F., Bordas P., Casanova S., Hoischen C., Oya I., Ziegler A., 2017, [AIP Conference Proceedings](#), 1792, 040024
- Apel W. D., et al., 2010, [Nuclear Instruments and Methods in Physics Research A](#), 620, 202
- Arons J., 1983, [ApJ](#), 266, 215
- Atoyan A. M., Aharonian F. A., Völk H. J., 1995, [Phys. Rev. D](#), 52, 3265
- Atwood W. B., et al., 2009, [ApJ](#), 697, 1071
- Auger P., 1941, *Rayons cosmique*. Presses universitaire de France
- Auger P., Ehrenfest P., Maze R., Daudin J., Fréon R. A., 1939, [Reviews of Modern Physics](#), 11, 288
- Barbot C., Drees M., 2003, [Astroparticle Physics](#), 20, 5
- Bednarek W., 2007, [Ap&SS](#), 309, 179
- Bednarek W., Sitarek J., 2007, [MNRAS](#), 377, 920
- Bednarek W., Sobczak T., 2014, [MNRAS](#), 445, 2842

- Bell A. R., 1978a, *MNRAS*, 182, 147
- Bell A. R., 1978b, *MNRAS*, 182, 147
- Berezinskii V. S., Bulanov S. V., Dogiel V. A., Ptuskin V. S., 1990, *Astrophysics of cosmic rays*
- Bignami G. F., et al., 1975, *Space Science Instrumentation*, 1, 245
- Bird D. J., et al., 1994, *ApJ*, 424, 491
- Blandford R., Eichler D., 1987, *Phys. Rep.*, 154, 1
- Blondin J. M., Chevalier R. A., Frierson D. M., 2001, *ApJ*, 563, 806
- Blumenthal G. R., Gould R. J., 1970, *Reviews of Modern Physics*, 42, 237
- Bogovalov S. V., Aharonian F. A., 2000, *MNRAS*, 313, 504
- Bolatto A. D., Wolfire M., Leroy A. K., 2013, *ARA&A*, 51, 207
- Bowman J. D., et al., 2013, *PASA*, 30, e031
- Brand J., Blitz L., 1993, *A&A*, 275, 67
- Brogan C. L., Gelfand J. D., Gaensler B. M., Kassim N. E., Lazio T. J. W., 2006, *ApJ*, 639, L25
- Bucciantini N., Arons J., Amato E., 2011, *MNRAS*, 410, 381
- Burton M. G., et al., 2015, *ApJ*, 811, 13
- Caraveo P. A., 2014, *ARA&A*, 52, 211
- Cesarsky C. J., Voelk H. J., 1977, in Wills R. D., Battrock B., eds, *ESA Special Publication Vol. 124, Recent Advances in Gamma-Ray Astronomy*.
- Cheng K. S., Ho C., Ruderman M., 1986, *ApJ*, 300, 500
- Cioffi D. F., McKee C. F., Bertschinger E., 1988, *ApJ*, 334, 252
- Cocconi G., 1960, *International Cosmic Ray Conference*, 2, 309
- Crutcher R. M., Wandelt B., Heiles C., Falgarone E., Troland T. H., 2010, *ApJ*, 725, 466
- Daum A., et al., 1997, *Astroparticle Physics*, 8, 1
- Deil C., Brun F., Carrigan S., Chaves R., Donath A., Gast H., Marandon V., Terrier R., 2015, in *34th International Cosmic Ray Conference (ICRC 2015)*. PoS
- Dermer C. D., 1986, *A&A*, 157, 223
- Dermer C. D., Powale G., 2013, *A&A*, 553, A34
- Domainko W., Ohm S., 2012, *A&A*, 545, A94
- Drury L. O., 1983, *Reports on Progress in Physics*, 46, 973
- Fichtel C. E., Hartman R. C., Kniffen D. A., Thompson D. J., Ogelman H., Ozel M. E., Tumer T., Bignami G. F., 1975, *ApJ*, 198, 163
- Fukuda T., Yoshiike S., Sano H., Torii K., Yamamoto H., Acero F., Fukui Y., 2014, *ApJ*, 788, 94
- Fukui Y., et al., 2014, *ApJ*, 780, 36

- Gabici S., Aharonian F. A., Blasi P., 2007, *Ap&SS*, 309, 365
- Gabici S., Aharonian F. A., Casanova S., 2009, *MNRAS*, 396, 1629
- Gabici S., Casanova S., Aharonian F. A., Rowell G., 2010, in Boissier S., Heydari-Malayeri M., Samadi R., Valls-Gabaud D., eds, SF2A-2010: Proceedings of the Annual meeting of the French Society of Astronomy and Astrophysics. p. 313 ([arXiv:1009.5291](https://arxiv.org/abs/1009.5291))
- Gaensler B. M., Slane P. O., 2006, *ARA&A*, 44, 17
- Gaensler B. M., Arons J., Kaspi V. M., Pivovarov M. J., Kawai N., Tamura K., 2002, *ApJ*, 569, 878
- Gaensler B. M., Landecker T. L., Taylor A. R., POSSUM Collaboration 2010, in American Astronomical Society Meeting Abstracts #215. p. 515
- Gaisser T. K., 1990, Cosmic rays and particle physics
- Galbraith W., Jelley J. V., 1953, *Nature*, 171, 349
- Garden R. P., Hayashi M., Hasegawa T., Gatley I., Kaifu N., 1991, *ApJ*, 374, 540
- Gelfand J. D., Slane P. O., Zhang W., 2009, *ApJ*, 703, 2051
- Giuliani A., et al., 2010, *A&A*, 516, L11
- Gold T., 1969, *Nature*, 221, 25
- Goldreich P., Julian W. H., 1969, *ApJ*, 157, 869
- Goldsmith P. F., 1972, *ApJ*, 176, 597
- Greisen K., 1966, *Physical Review Letters*, 16, 748
- Gusdorf A., Cabrit S., Flower D. R., Pineau Des Forêts G., 2008, *A&A*, 482, 809
- H.E.S.S. Collaboration et al., 2011, *A&A*, 531, L18
- H.E.S.S. Collaboration et al., 2012, *A&A*, 548, A46
- H.E.S.S. Collaboration et al., 2015, *Science*, 347, 406
- HESS Collaboration et al., 2016, *Nature*, 531, 476
- HESS website 2017, HESS website, <https://www.mpi-hd.mpg.de/hfm/HESS/pages/about/telescopes/images/>
- Habe A., Ohta K., 1992, *PASJ*, 44, 203
- Heitler W., 1954, The Quantum Theory of Radiation. Dover Books on Physics and Chemistry, Dover Publications, <https://books.google.com.au/books?id=L7w7UpecbKYC>
- Hess V. F., 1913, *Z. Phys.*, 14, 610
- Hillas A., 1972, Cosmic rays. The Commonwealth and International Library, Pergamon Press, <http://books.google.com.au/books?id=9gEvAAAAIAAJ>
- Hillas A. M., 1984, *ARA&A*, 22, 425
- Hillas A. M., 1985, International Cosmic Ray Conference, 3
- Hinton J. A., Hofmann W., 2009, *ARA&A*, 47, 523
- Hinton J. A., the HESS Collaboration 2004, *New A Rev.*, 48, 331

- Ho P. T. P., Townes C. H., 1983, *ARA&A*, 21, 239
- Hoshino M., Arons J., Gallant Y. A., Langdon A. B., 1992, *ApJ*, 390, 454
- Irvine W. M., Goldsmith P. F., Hjalmarsen A., 1987, in Hollenbach D. J., Thronson Jr. H. A., eds, *Astrophysics and Space Science Library Vol. 134, Interstellar Processes*. pp 561–609
- Kafexhiu E., Aharonian F., Taylor A. M., Vila G. S., 2014, *Phys. Rev. D*, 90, 123014
- Kamae T., Karlsson N., Mizuno T., Abe T., Koi T., 2006, *ApJ*, 647, 692
- Kanbach G., et al., 1988, *Space Sci. Rev.*, 49, 69
- Kargaltsev O., Rangelov B., Pavlov G. G., 2013, preprint, ([arXiv:1305.2552](https://arxiv.org/abs/1305.2552))
- Kelner S. R., Aharonian F. A., Bugayov V. V., 2006, *Phys. Rev. D*, 74, 034018
- Kennel C. F., Coroniti F. V., 1984, *ApJ*, 283, 694
- Kildea J., et al., 2007, *Astroparticle Physics*, 28, 182
- Kirk J. G., Skjæraasen O., Gallant Y. A., 2002, *A&A*, 388, L29
- Koch H. W., Motz J. W., 1959, *Reviews of Modern Physics*, 31, 920
- Ladd N., Purcell C., Wong T., Robertson S., 2005, *PASA*, 22, 62
- Larionov G. M., Zinchenko I., Val'tts I. E., 2006, *Astronomy Reports*, 50, 107
- Lemiere A., Terrier R., Djannati-Ataï A., 2006, *ArXiv Astrophysics e-prints*,
- Lemoine-Goumard M., Degrange B., Tluczykont M., 2006, *Astroparticle Physics*, 25, 195
- Leroy A. K., et al., 2011, *ApJ*, 737, 12
- Li H., Chen Y., 2010, *MNRAS*, 409, L35
- Li T.-P., Ma Y.-Q., 1983, *ApJ*, 272, 317
- Malkov M. A., Diamond P. H., Sagdeev R. Z., Aharonian F. A., Moskalenko I. V., 2013, *ApJ*, 768, 73
- Manolakou K., Horns D., Kirk J. G., 2007, *A&A*, 474, 689
- Matthews J., 2005, *Astroparticle Physics*, 22, 387
- McClure-Griffiths N. M., Dickey J. M., Gaensler B. M., Green A. J., Haverkorn M., Strasser S., 2005, *ApJS*, 158, 178
- McClure-Griffiths N. M., et al., 2009, *ApJS*, 181, 398
- Meyer M., Horns D., Zechlin H.-S., 2010, *A&A*, 523, A2
- Millikan R. A., Cameron G. H., 1926, *Physical Review*, 28, 851
- Mizuno A., Fukui Y., 2004, in Clemens D., Shah R., Brainerd T., eds, *Astronomical Society of the Pacific Conference Series Vol. 317, Milky Way Surveys: The Structure and Evolution of our Galaxy*. p. 59
- Nava L., Gabici S., 2013, *MNRAS*, 429, 1643
- Nava L., Gabici S., Marcowith A., Morlino G., Ptuskin V. S., 2016, *MNRAS*, 461, 3552
- Nicholas B., Rowell G., Burton M. G., Walsh A., Fukui Y., Kawamura A., Longmore S., Keto E., 2011, *MNRAS*, 411, 1367

- Ohira Y., Yamazaki R., Kawanaka N., Ioka K., 2012, *MNRAS*, 427, 91
- Ohm S., van Eldik C., Egberts K., 2009, *Astroparticle Physics*, 31, 383
- Oort J. H., 1951, in *Problems of Cosmical Aerodynamics*. p. 118
- Patterson J. R., Hillas A. M., 1983, *Journal of Physics G Nuclear Physics*, 9, 1433
- Pierre Auger Collaboration 2015, *Nuclear Instruments and Methods in Physics Research A*, 798, 172
- Prosekin A. Y., Kelner S. R., Aharonian F. A., 2015, preprint, ([arXiv:1506.06594](https://arxiv.org/abs/1506.06594))
- Protheroe R. J., Ott J., Ekers R. D., Jones D. I., Crocker R. M., 2008, *MNRAS*, 390, 683
- Ptuskin V. S., Zirakashvili V. N., 2005, *A&A*, 429, 755
- Reynolds S. P., Keohane J. W., 1999, *ApJ*, 525, 368
- Roberts M. S. E., Gotthelf E. V., Halpern J. P., Brogan C. L., Ransom S. M., 2007, in Becker W., Huang H. H., eds, *WE-Heraeus Seminar on Neutron Stars and Pulsars 40 years after the Discovery*. p. 24 ([arXiv:astro-ph/0612631](https://arxiv.org/abs/astro-ph/0612631))
- Roman-Duval J., Jackson J. M., Heyer M., Rathborne J., Simon R., 2010, *ApJ*, 723, 492
- Rowell G. P., 2003, *A&A*, 410, 389
- Sano H., et al., 2017, *AIP Conference Proceedings*, 1792, 040038
- Sedov L. I., 1959, *Similarity and Dimensional Methods in Mechanics*
- Skilling J., 1975, *MNRAS*, 173, 245
- Slane P., Bykov A., Ellison D. C., Dubner G., Castro D., 2014, *Space Sci. Rev.*,
- Stanev T., 2010, *High Energy Cosmic Rays*. Springer Praxis Books, Springer, <https://books.google.com.au/books?id=1y9YEHAFBMC>
- Strong A. W., Mattox J. R., 1996, *A&A*, 308, L21
- Strong A. W., Moskalenko I. V., 1998, *ApJ*, 509, 212
- Strong A. W., Moskalenko I. V., Reimer O., Digel S., Diehl R., 2004, *A&A*, 422, L47
- Strong A. W., Moskalenko I. V., Ptuskin V. S., 2007, *Annual Review of Nuclear and Particle Science*, 57, 285
- Stupar M., Parker Q. A., Filipović M. D., 2008, *MNRAS*, 390, 1037
- Sturrock P. A., 1971, *ApJ*, 164, 529
- Tafalla M., Myers P. C., Caselli P., Walmsley C. M., 2004, *A&A*, 416, 191
- Takahashi Y., JEM-EUSO Collaboration 2009, *New Journal of Physics*, 11, 065009
- Tavani M., 1993, *ApJ*, 407, 135
- Tavani M., et al., 2009, *A&A*, 502, 995
- Torii K., et al., 2015, *ApJ*, 806, 7
- Torres D. F., Cillis A., Martín J., de Oña Wilhelmi E., 2014, *Journal of High Energy Astrophysics*, 1, 31
- Ungerechts H., Winnewisser G., Walmsley C. M., 1986, *A&A*, 157, 207

- Urquhart J. S., et al., 2010, [PASA](#), 27, 321
- Voisin F., Rowell G., Burton M. G., Walsh A., Fukui Y., Aharonian F., 2016, [MNRAS](#), 458, 2813
- Voronkov M. A., Caswell J. L., Ellingsen S. P., Green J. A., Breen S. L., 2014, [MNRAS](#), 439, 2584
- Weekes T. C., et al., 2002, [Astroparticle Physics](#), 17, 221
- Wilson T. L., Bieging J., Downes D., 1978, [A&A](#), 63, 1
- Wilson T. L., Henkel C., Huttemeister S., Dahmen G., Linhart A., Lemme C., Schmid-Burgk J., 1993, [A&A](#), 276, L29
- Zatsepin G. T., Kuz'min V. A., 1966, *ZhETF Pisma Redaktsiiu*, 4, 114
- Zinchenko I., Forsstroem V., Lapinov A., Mattila K., 1994, [A&A](#), 288, 601
- de Jager O. C., Djannati-Ataï A., 2009, in Becker W., ed., *Astrophysics and Space Science Library* Vol. 357, *Astrophysics and Space Science Library*. p. 451 ([arXiv:0803.0116](#)), [doi:10.1007/978-3-540-76965-1_17](#)
- de Naurois M., Rolland L., 2009, [Astroparticle Physics](#), 32, 231
- van Haarlem M. P., et al., 2013, [A&A](#), 556, A2
- van der Swaluw E., Achterberg A., Gallant Y. A., Tóth G., 2001, [A&A](#), 380, 309